Karlsruhe Institute of Technology

Volcano monitoring with bistatic TanDEM-X SAR interferometry

INAUGURAL DISSERTATION

for the fulfillment of the requirements
for the academic degree of

DOCTOR OF ENGINEERING
(Dr.-Ing.)

Accepted by
the Department of Civil Engineering,
Geo and Environmental Sciences
of the
Karlsruhe Institute of Technology

Submitted by

Dipl.-Geogr. Julia Kubanek

from
Neustadt am Rübenberge
Lower Saxony, Germany

Day of examination: 24.05.2016

Main referee:	Prof. Dr.-Ing. Dr. h.c. Bernhard Heck
First Co-referee:	Prof. Dr.-Ing. habil. Alberto Moreira
Second Co-referee:	Priv. Doz. Dr. Thomas R. Walter

Karlsruhe 2017

Members of the doctoral committee

Prof. Dr.-Ing. Dr. h.c. Bernhard Heck
Geodetic Institute
Karlsruhe Institute of Technology
Karlsruhe, Germany

Priv. Doz. Dr. Thomas R. Walter
Section 2.1: Physics of Earthquakes and Volcanoes
German Research Centre for Geosciences
Potsdam, Germany

Prof. Dr.-Ing. Maria Hennes
Geodetic Institute
Karlsruhe Institute of Technology
Karlsruhe, Germany

Prof. Dr. rer. nat. Frank Schilling
Insitute for Applied Geosciences
Karlsruhe Institute of Technology
Karlsruhe, Germany

Prof. Dr.-Ing. habil. Alberto Moreira
Microwaves and Radar Institute
German Aerospace Center
Oberpfaffenhofen, Germany

Prof. Dr.-Ing. Stefan Hinz
Institute of Photogrammetry and Remote Sensing
Karlsruhe Institute of Technology
Karlsruhe, Germany

Prof. Dr. rer. nat. Martin Breunig
Geodetic Institute
Karlsruhe Institute of Technology
Karlsruhe, Germany

Kubanek, Julia

Volcano Monitoring with bistatic TanDEM-X SAR interferometry

Department of Civil Engineering, Geo and Environmental Sciences,
Karlsruhe Institute of Technology (KIT)

Keywords: TanDEM-X, InSAR, topographic changes, volcanoes, digital elevation models, lava domes, lava flows

This work is simultaneously published in:
German Geodetic Commission, series C, No. 793
Bavarian Academy of Sciences and Humanities, Munich, 2017
ISBN 978-3-7696-5205-5

Insanity:
doing the same thing
over and over again
and expecting
different results.

(Albert Einstein)

Parts of this thesis have been published in the following proceedings and journal articles:

Kubanek J, Westerhaus M, Heck B (2013a) On the potential of TanDEM-X to assess complex topography. In: Proc. of ESA Living Planet Symposium, 9.-13. Sep. 2013, Edinburgh, Scotland

Kubanek J, Westerhaus M, Heck B (2013b) Topographic changes at Volcán de Colima observed by double differential InSAR using TanDEM-X. In: Proc. of ESA Living Planet Symposium, 9.-13. Sep. 2013, Edinburgh, Scotland

Kubanek J, Westerhaus M, Varley N, James MR, Heck B (2014) On using bistatic TanDEM-X data for volcano monitoring. In: Proc. of 10th European Conference on Synthetic Aperture Radar (EUSAR), 3.-5. June 2014, Berlin, Germany

Kubanek J, Richardson JA, Charbonnier SJ, Connor LJ (2015a) Lava flow mapping and volume calculations of the 2012-13 Tolbachik, Kamchatka fissure eruption using bistatic TanDEM-X InSAR. Bulletin of Volcanology 77(106):1–13, DOI 10.1007/s00445-015-0989-9

Kubanek J, Westerhaus M, Heck B (2015b) On the use of bistatic TanDEM-X images to quantify volumetric changes of active lava domes. In: International Association of Geodesy Symposia, Springer International Publishing Switzerland, DOI 10.1007/1345_2015_172

Kubanek J, Westerhaus M, Schenk A, Aisyah N, Brotopuspito KS, Heck B (2015c) Volumetric change quantification of the 2010 Merapi eruption using TanDEM-X InSAR. Remote Sensing of Environment 164:16–25, DOI 10.1016/j.rse.2015.02.027

Abstract

Estimating the amount of erupted material during a volcanic crisis provides valuable insights into the eruption dynamics and its hazard, but is at the same time one of the major challenges in volcano research. One way to estimate erupted volumes is to assess topographic changes before and after an eruption while using digital elevation models. However, collecting topographic data is difficult, especially when topography is changing fast due to volcanic activity.

An innovative way to acquire 3-D information of volcanoes repeatedly is using data from the German TanDEM-X satellite mission. TanDEM-X consists of two nearly identical radar satellites that fly in a close formation, building a large single-pass synthetic aperture radar interferometer with adaptable spatial baselines. The short repeat interval allows generating digital elevation models of the area under investigation every 11 days, or multiples of this – depending on the availability of data – through the use of the interferometric phase.

The present thesis deals with the application of the bistatic TanDEM-X data in volcano research. A new data processing approach is developed in which TanDEM-X data are used to generate digital elevation models before, during, and after volcanic activity. A differential analysis of the digital elevation models allows to estimate the topographic and volumetric changes caused by the volcanic activity.

For developing and testing the differential TanDEM-X digital elevation model approach, three test sites are chosen. They are characterized by different types of volcanic activity all of which cause a topographic change. Two test sites, Merapi in Indonesia and Volcán de Colima in Mexico, are dome-building volcanoes whereas Tolbachik in Kamchatka is a volcanic complex composed of a shield volcano and a stratovolcano.

The focus at Merapi is on the quantification of the topographic changes in the summit area caused by its 2010 eruption. Using bistatic TanDEM-X data, three digital elevation models are generated before and after the eruption to reveal the large topographic losses of about 200 m.

The second study focuses on mapping and measuring lava flow extent and volume during the fissure eruption of Tolbachik in Kamchatka which occurred in 2012-13.

During the eruption which lasted for about nine months, 18 TanDEM-X data pairs are analyzed. The differencing of digital elevation models enables to estimate the amount of basaltic lava that was extruded over time and results in a final lava flow volume of $0.53\,\mathrm{km}^3$.

The third study at Volcán de Colima demonstrates the ability of the TanDEM-X differential approach to observe much smaller topographic changes. Altogether, 26 bistatic data pairs are analyzed to reveal the volumetric change due to a small explosive event in June 2011 which led to a topographic loss of up to 20 m.

The studies of all test sites indicate that TanDEM-X is suitable for revealing topographic changes at active volcanoes with a high accuracy. A comparison with aerophotogrammetric observations corroborates the TanDEM-X-based results. An extensive validation in areas where no topographic change is expected results in errors for the mean offset over all elevation differences of $\pm\,0.21\,\mathrm{m}$ for the Tolbachik test site and between $\pm\,0.13\,\mathrm{m}$ and $\pm\,0.59\,\mathrm{m}$ for Volcán de Colima, depending on the slope. The good accuracy corroborates that differencing digital elevation models from TanDEM-X results in reliable estimates of topographic and volumetric changes due to various kinds of volcanic activity, which allows – in the case of Tolbachik – to calculate lava extrusion rates.

Ausführliche Zusammenfassung

Vulkanmonitoring mittels bistatischer TanDEM-X SAR-Interferometrie

Die Bestimmung von Eruptionsvolumina während vulkanischer Aktivität ist in vielen Regionen für die ansässige Bevölkerung von großer Bedeutung, da sie hilfreiche Anhaltspunkte für die Gefährdung des jeweiligen Gebietes liefern können. Eine Möglichkeit zur Bestimmung der Menge des ausgestoßenen Materials ist die Abbildung der Topographie vor, während und nach einer Eruption. Die Differenzbildung digitaler Geländemodelle ermöglicht die Ableitung von Höhen- und Formänderungen des Geländes, woraus das Volumen des eruptierten Materials bestimmt werden kann.

Digitale Geländemodelle mit Auflösungen im Meterbereich lassen sich unter anderem über eine interferometrische Auswertung von Radar-Daten mit synthetischer Apertur (SAR-Daten) ableiten. Ein wesentlicher Vorteil der Nutzung von Radarsatelliten ist, dass die Datenaufnahme global erfolgen kann. Ein weiterer Vorteil bei der Beobachtung aktiver Vulkane ist die Eigenschaft, dass die genutzten Wellenlägen im Gegensatz zum optischen Bereich die mit Eruptionen häufig einhergehenden Rauchwolken durchdringen können. Da Radarsatelliten aktive Systeme sind, senden sie ihre eigene Strahlung aus und können somit zu jeder Tages- und Nachtzeit Daten aufnehmen.

Die komplexen SAR-Daten bestehen aus der Rückstreumagnitude und der Phase. Aus der Phasendifferenz von zwei SAR-Bildern, die üblicherweise mit einem bestimmten zeitlichen Abstand von dem gleichen Satelliten mit gleicher Aufnahmegeometrie aufgenommen werden (Repeat-Pass Interferometrie), lässt sich die Höhe des Geländes bestimmen.

Ein wesentlicher Nachteil der Nutzung von Radarbildern, die zu unterschiedlichen Zeiten aufgenommen werden, sind die zeitlich variablen Phasenterme. Solange die Rückstreueigenschaften am Boden stabil sind, kann eine interferometrische Auswertung gute Ergebnisse liefern. Das Hauptproblem ergibt sich aus den langen Wiederholintervallen heutiger Satellitenmissionen. Obwohl die italienische Mission COSMO-SkyMED Aufnahmen mit nur einem Tag Abstand ermöglicht, können schon

kleinere Veränderungen am Boden zu starken Dekorrelationen zwischen den zwei Radarbildern führen, die eine klassische interferometrische Auswertung verhindern. Gerade Vulkangebäude verändern sich jedoch häufig auch in kurzen Zeitintervallen deutlich, sodass die Repeat-Pass Interferometrie hier an ihre Grenzen stößt.

Eine innovative Möglichkeit, um die Topographie von Vulkanen abbilden zu können, bietet die TanDEM-X Satellitenmission des Deutschen Zentrums für Luft- und Raumfahrt. Die Satellitenmission besteht aus den zwei nahezu baugleichen Radarsatelliten TerraSAR-X und TanDEM-X, die im engen Helix-Formationsflug die Erde umfliegen und dabei als großes SAR-Interferometer agieren. Primäres Ziel der Mission ist die Generierung eines globalen digitalen Geländemodells mit einer Auflösung von 12 m und einer vertikalen Genauigkeit von 2 - 4 m.

Während des Überfluges sendet einer der Satelliten elektromagnische Wellen aus und beide Satelliten empfangen das von der Erdoberfläche zurückgestreute Signal (Single-Pass Interferometrie). Als Ergebnis entstehen zwei nahezu zeitgleich aufgenommene komplexe SAR-Bilder, die jeweils aus der Rückstreuamplitude und der Phaseninformation bestehen. Dieser Aufnahmemodus wird auch als bistatisch bezeichnet, im Gegensatz zur Aufnahme eines einzigen Bildes, dem monostatischen Aufnahmemodus. Über die interferometrische Auswertung der Laufzeitdifferenz beider Bilder können anhand der Phaseninformation hochaufgelöste digitale Geländemodelle generiert werden.

Ein ähnliches System wurde im Jahr 2000 mit der Shuttle Radar Topography Mission (SRTM) umgesetzt. Im Gegensatz zur TanDEM-X-Satellitenmission befanden sich bei der SRTM-Mission die zwei Antennen auf der gleichen Plattform und die Mission konnte in ihrem elf-tägigem Überflug fast die komplette Erdoberfläche einmal abbilden. Die Missionsparameter von TanDEM-X ermöglichen im Gegensatz zur SRTM-Mission wiederholte Aufnahmen eines Gebietes. Der innovative Charakter der TanDEM-X-Mission besteht in ebendieser Möglichkeit wiederkehrender Aufnahmen. Das Widerholintervall der Mission ist elf Tage – oder ein Vielfaches davon – sodass bei regelmäßiger Aufnahme alle elf Tage ein digitales Geländemodell generiert werden kann.

Das Ziel der vorliegenden Arbeit ist die Untersuchung und Bewertung der Nutzbarkeit der TanDEM-X-Daten in der Vulkanforschung. Ein neuer Ansatz zur Verarbeitung der bistatischen Daten wird vorgestellt und für die Ableitung vulkanologischer Parameter getestet. Dabei wird aus den TanDEM-X-Daten die Topographie vor, während und nach einem vulkanologischen Ereignis abgebildet. Anhand einer differentiellen Analyse der abgeleiteten digitalen Geländemodelle können topographische und volumetrische Änderungen quantifiziert werden.

Um einen möglichst allgemeingültigen Ansatz entwickeln zu können, wurden drei Testgebiete ausgewählt. Diese unterscheiden sich in der Art der vulkanologischen Aktivität, die jedoch in allen drei Testgebieten topographische Änderungen verursacht.

Der Merapi auf der indonesischen Insel Java ist ein dombildender Vulkan mit wechselnder Aktivität. Dombildende Vulkane sind durch effusive Eruptionen charakterisiert, die sich über sehr lange Zeiträume erstrecken können. Alle paar Jahre treten Explosionen und Domzerstörungen mit einhergehenden pyroklastischen Strömen auf. Am Merapi fand eine solche Zerstörung des Doms von Oktober bis November 2010

statt. Zu Beginn der Eruption ist der alte Lavadom kollabiert. Der neugebildete Dom wurde nach zwölf Tagen wiederum zerstört. Insgesamt führte die Aktivität am Merapi zur kompletten Zerstörung des Kraterbereichs und hinterließ zwei steile Kraterwände und einen kleinen Dom im Innern des heute nach Südosten geöffneten Kraters. Die Nutzung eines bistatischen TanDEM-X Datenpaares, das im Oktober 2010 kurz vor der Eruption aufgezeichnet wurde, bildet die Prä-Eruptionstopographie ab. Zwei Datensätze, die etwa ein Jahr später im Oktober und November 2011 aufgezeichnet wurden, werden zur Abbildung der posteruptiven Topographie genutzt. Durch die Differenzbildung der Datensätze lässt sich der Materialverlust im Gipfelbereich bestimmen, der am Merapi mit bis zu 200 m sehr groß ist.

Als zweites Untersuchungsgebiet wurde der Tolbachik in Kamtschatka in Russland gewählt. Der Tolbachik unterscheidet sich stark von den anderen zwei Untersuchungsgebieten. Der Vulkankomplex besteht aus zwei überlappenden, morphologisch verschiedenen Vulkanen. Während der Plosky Tolbachik im Osten ein basaltischer Schildvulkan ist, handelt es sich bei seinem Nachbarn im Westen, Ostry Tolbachik, um einen steilen Stratovulkan. Nachdem über 35 Jahre keine Aktivität registriert werden konnte, wurde der Vulkankomplex im November 2012 aktiv. Die vulkanische Aktivität bestand aus basaltischen Lavaflüssen, die südlich des Vulkanmassivs entlang der von Nordost nach Südwest verlaufenden Spalten austraten. Die Spalteneruption dauerte etwa neun Monate bis August 2013. Während der Eruption wurden elf bistatische TanDEM-X Datensätze aufgezeichnet, die, in Kombination mit einem Datensatz, der kurz vor der Eruption aufgezeichnet wurde, sehr gut den fortdauernden Ausfluss neuer Lavamassen kartieren sowie die Berechnung des ausgestoßenen Volumens ermöglichen. Aus der Zeit nach dem Ende der Eruption wurden sechs weitere Datensätze genutzt, um die Wiederholbarkeit der Ergebnisse zu validieren.

Der Volcán de Colima in Mexiko ist, wie auch der Merapi, ein dombildender Vulkan. Am Colima wird untersucht, ob auch kleinere topographische Änderungen mit dem entwickelten Ansatz quantifiziert werden können. Die Studie konzentriert sich auf eine kleine Explosion, die sich im Juni 2011 am westlichen Rand des Kraters ereignet hat. Die Explosion wurde durch den plötzlichen Stopp des aufsteigenden Magmas ausgelöst, was bis dahin zur Bildung des Doms führte. Aus der Zeit vor der Explosion können zwei Datenpaare aus dem absteigenden Orbit verwendet werden. Nach der Explosion sind sehr viele Datensätze vorhanden. Zur Quantifizierung des Volumenverlustes im Gipfelbereich werden sieben digitale Geländemodelle generiert, die die Post-Explosions-Topographie abbilden. Zur Analyse der Genauigkeit der abgeleiteten Geländemodelle und Ergebnisse werden 19 weitere Datensätze prozessiert. Die sich ergebenden 26 digitalen Geländemodelle, die nach der Explosion zwischen Ende Juni 2011 und Ende Dezember 2012 aufgezeichnet wurden, eignen sich hervorragend zur weiteren Fehlerabschätzung, da in dieser Zeit keine weitere vulkanische Aktivität registriert wurde. Die topographischen Änderungen am Volcán de Colima sind mit maximal -20 m wesentlich kleiner als am Merapi.

Alle Studien der drei Untersuchungsgebiete bestätigen, dass der auf TanDEM-X basierende Ansatz gute Ergebnisse liefert. Dies wird durch den Vergleich mit photogrammetrischen Beobachtungen bestätigt. Das Hauptproblem des entwickelten Ansatzes sind am Merapi und am Volcán de Colima die geometrischen Dekorrelationen, die durch die steile und zerklüftete Topographie an Stratovulkanen entstehen.

Am Tolbachik hingegen verursacht die Interaktion zwischen Lavaflüssen und der sich jahreszeitlich ändernden Vegetation die größten Probleme.

Eine interne Validierung zur Fehlerabschätzung in Gebieten, in denen keine topographische Änderung durch Vulkanismus zu erwarten ist, ergibt am Tolbachik im eher flacheren Gelände mittlere Abweichungen für die aus den digitalen Geländemodellen gebildeten Differenzen von $\pm\,0.21\,\mathrm{m}$ und am Volcán de Colima zwischen $\pm\,0.13\,\mathrm{m}$ und $\pm\,0.59\,\mathrm{m}$ in Abhängigkeit von der Geländeneigung. Die Genauigkeitsanalysen bestätigen die Eignung von TanDEM-X, wiederholte digitale Geländemodelle von Vulkanen zu generieren, die über eine Differenzbildung eine verlässliche Quantifizierung der topographischen und volumetrischen Änderungen erlauben. Die Anwendung der Methodik an unterschiedlichen Vulkanen und zur Untersuchung unterschiedlicher Ausprägungen der vulkanischen Aktivität zeigen das Potential und die Vielfältigkeit des entwickelten Ansatzes.

Contents

1. Introduction

1.1 Motivation

Measuring the volume of erupted material during a volcanic event is one of the major challenges in volcano research but is at the same time of particular importance as it allows assessment of the hazard and risk during an eruption. One way to measure erupted volumes – regardless of the type of volcanic activity – is the generation and differencing of pre-, syn-, and/or post-eruption digital elevation models (DEMs).

Among other methods, synthetic aperture radar (SAR) interferometry (InSAR) allows the generation of DEMs with meter-level accuracy using the phase difference between two radar images of the same target area. In addition to the possibility of global acquisitions, one of the major advantages of InSAR is its cloud-penetrating characteristic, which is especially important with regard to studies at active volcanoes.

A widespread method is using spaceborne radar images acquired at different times to derive the interferometric phase (repeat-pass InSAR). As long as the backscattering conditions on the ground and the atmospheric conditions remain unchanged, repeat-pass InSAR provides appropriate results (Bignami et al., 2013; Wadge, 2003; Wadge et al., 2011). The main problem is due to the repeat-interval of current radar satellite missions. Although the Italian COSMO-SkyMed (Constellation of small Satellites for Mediterranean basin Observation) mission has the potential for 1-day repeats, repeat-times are, under normal conditions, one to several weeks. Major surface changes in very short time intervals that commonly occur during volcanic crises due to ashfall, lava flows, lava dome collapse, or explosions, deteriorate the coherence and hinder or even prevent interferometric analysis (Lu and Freymueller, 1998; Stevens et al., 2001; Stevens and Wadge, 2004; Wadge, 2003). Former studies therefore conclude that data acquired simultaneously (single-pass, bistatic mode) are required to extract topographic information from InSAR at fast-changing environments like volcanoes.

The innovative German Earth observation mission TanDEM-X (**T**erraSAR-X **a**dd-o**n** for **D**igital **E**levation **M**easurement) is of great importance to overcome some

of the problems of the repeat-pass interferometric approach. The two almost identical radar satellites TerraSAR-X (TSX) and TanDEM-X (TDX) fly in close helix formation and concurrently acquire images of the same place on the Earth's surface from slightly different positions in a single pass. It is the first time that DEMs of low coherent and highly dynamic areas (i.e., volcanoes) can be generated repeatedly (with an interval of 11 days or multiples) using InSAR, even with cloud cover or during nighttime. Differencing of TanDEM-X DEMs therefore opens the opportunity to assess topographic and volume changes at active volcanoes using spaceborne InSAR.

The advantage of using InSAR to study decorrelation-prone volcanic phenomena and the innovative TanDEM-X satellite mission are the background of the present study. The thesis deals with the application of bistatic TanDEM-X imagery to study active volcanism, aiming to answer the general research question:

Can TanDEM-X InSAR serve as a basis to quantify topographic and volumetric changes in non-coherent areas around volcanoes and thus overcome the limitations of ground-based, optical, and repeat-pass interferometric methods?

The research question requires to develop and test a methodology that is able to observe different volcanic processes that lead to a topographic change and cause a decorrelation in repeat-pass InSAR data. To ensure that volcanic activity could be studied, three test sites showing different volcanological characteristics were selected. Merapi on Java, Indonesia, and Volcán de Colima in Mexico are both steep-sided stratovolcanoes with varying lava-dome activity. Long terms of dome extrusion with intermittent explosions and gravitational dome failure culminate in complete dome destruction. The third test site, the Tolbachik volcanic complex in Central Kamchatka, Russia, is different. Composed of a shield volcano in the east and a stratovolcano in the west, its recent eruptive activity took place from the central crater and along a fissure zone south of the complex. The extruded lava is basaltic and very fluid.

1.2 Contributions

The contributions of the thesis can be split into two main fields: (1) the development and test of a strategy to process bistatic TanDEM-X data with the open source software DORIS (Delft Object-oriented Radar Interferometric Software, Kampes et al., 2003) and (2) the application of the developed methodology in volcano research. As the application of the TanDEM-X data to study, e.g., steep-sided environments like dome-building volcanoes requires special processing considerations, both research topics influence each other. The following list summarizes the main topics of the conducted research:

1. Interferometric processing of bistatic TanDEM-X data to generate high-resolution DEMs, including format conversion of the raw data.
2. Using radar shadow masks to enhance volume estimates in steep topography.
3. Accuracy assessment of TanDEM-X-based DEMs and derived products with and without using external data sources.

4. Application of the strategy to assess large topographic changes at steep-sided stratovolcano Merapi due to its 2010 eruption.

5. Application of TanDEM-X bistatic data to study lava flows that were emplaced during the 2012-13 Tolbachik fissure eruption.

6. Application of the developed processing strategy to assess topographic changes at a 20 m level at Volcán de Colima due to an explosion in June 2011.

1.3 Thesis roadmap

The second chapter summarizes the basic principles and applications of SAR interferometry. In addition to an introduction to the SAR measurement principle, the chapter gives an overview of the main interferometric processing steps necessary to generate DEMs using the DORIS software package. The chapter further introduces the TanDEM-X satellite mission and summarizes the general data processing considerations of the bistatic TanDEM-X data. It concludes with a characterization of the main errors in digital elevation models generated from SAR interferometric data. The second chapter provides the basic knowledge for the following chapters, which are the core of the present thesis. Chapter 3 gives an overview of the state of the art of topographic change estimation at volcanoes. Previous studies that used TanDEM-X to analyze active volcanism are further described. The last two parts of Chapter 3 provide the methodological background of the thesis and explain why the three test sites mentioned above were selected to develop and test the TanDEM-X-based approach. The following three chapters (Chap. 4, 5, and 6) include the application of the bistatic TanDEM-X data to study various volcanological phenomena. In Chapter 4, the 2010 eruption of Merapi in Indonesia is investigated. The TanDEM-X-based study is underpinned by results that were acquired during fieldwork. Chapter 5 provides the results of a temporal TanDEM-X-based approach that was developed to study the lava flows that were emplaced during the 2012-13 fissure eruption of Tolbachik in Kamchatka, Russia. For validation, the TanDEM-X-based results are compared to photogrammetric data. The accuracy is further validated using reference areas where no topographic change is expected. In Chapter 6, small lava-dome changes at Volcán de Colima in Mexico are analyzed. Like at Tolbachik, the chapter provides a comparison of the TanDEM-X-based results to photogrammetric data, and also a validation using data pairs from a period when Volcán de Colima remained quiet. Finally, Chapter 7 – conclusions and outlook – summarizes the most important results and gives an extensive outlook raising a number of questions for further research.

2. SAR interferometry: basic principles and data processing

This chapter gives a short introduction to spaceborne InSAR and its application in earth sciences. It is not an attempt to give a comprehensive explanation of the entire methodology, as several authors have done this before (e.g., Curlander and McDonough, 1991; Hanssen, 2001). The objective is to provide an overview of the interferometric measurement principle and the processing steps necessary for DEM generation and commonly faced difficulties.

Section 2.1 of this chapter describes the principles of the SAR measurement and explains the imaging geometry of SAR systems (Sec. 2.1.1). The geometric effects resulting from the side-looking characteristic of SAR systems are described in Section 2.1.2. In Section 2.1.3, the synthetic aperture is shortly described, as well as resolution considerations of SAR images.

In Section 2.2, the SAR interferometric technique is explained including a description about the formation of interferograms (Sec. 2.2.1). The different components that build the interferometric phase are further described (Sec. 2.2.2).

Section 2.3 describes the main steps of the interferometric (repeat-pass) processing chain to generate DEMs based on the DORIS software (Kampes et al., 2003).

The innovative TanDEM-X mission is presented in Section 2.4 and an overview of mandatory changes to process bistatic data is given in Section 2.5. The chapter concludes with the most important error sources that have an effect on the accuracy of DEMs generated by repeat-pass and single-pass InSAR (Sec. 2.6).

2.1 SAR measurement principle

Imaging radar systems, such as SAR, emit electromagnetic pulses and receive the signal that is reflected from the ground. The two-way travel time from the antenna to the target is used to measure its distance. The backscattering on the ground allows to derive physical quantities of the surface, i.e., its roughness, the topography, and the dielectric characteristics. Monostatic systems use a single antenna whereas bistatic

systems employ two physically separated antennas for transmission and reception (Hanssen, 2001; Bamler and Hartl, 1998).

Spaceborne SAR systems operate in the microwave (cm to dm wavelength) band of the electromagnetic spectrum and are therefore able to penetrate clouds. While being active sensors, SAR systems provide their own illumination and can operate almost independently from the sun during day- and nighttime. This, as well as the potential to acquire information globally, makes them suitable for operational monitoring tasks (Bamler and Hartl, 1998). SAR is therefore capable to monitor dynamic phenomena like earthquakes (Massonnet et al., 1993), ocean currents (Fu and Holt, 1982), ice sheet motion (Goldstein et al., 1993), and volcanic activity (Massonnet et al., 1995).

2.1.1 Imaging geometry

The imaging geometry of SAR systems mounted on an aircraft (airborne) or a satellite (spaceborne) is side-looking. The sensor S moves with a velocity v at a height H (Fig. 2.1). The antenna transmits microwave pulses to the ground to illuminate the antenna's footprint at the rate of the *pulse repetition frequency* (PRF) and receives the backscattered pulses. The sensor transmits to the side (*range*) of the satellite's path (*azimuth*) (Bamler and Hartl, 1998). Transmitting in range allows to discriminate targets with a different distance to the sensor and generates a reflectivity map of the Earth's surface in 2D (Bamler, 2000).

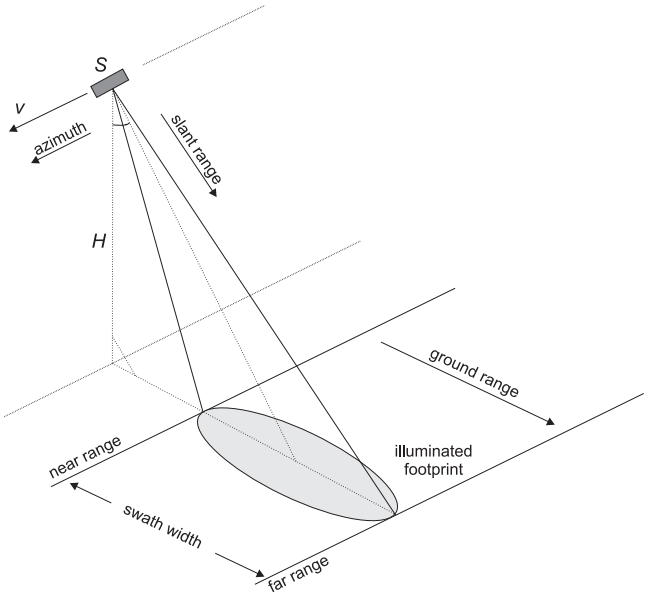

Figure 2.1 – SAR imaging geometry based on Bamler (2000).

Figure 2.2 shows a cross section of the acquisition geometry where the sensor images a target T that is elevated by a local topography to a height h above the reference surface. *Slant range* R is the distance between S and T and thus the natural product of the range measurement. *Ground range* r is the distance between the ground track of S and T on the correct position of the reference surface (see also Fig. 2.1). To transform R to r, every point needs to be corrected using the local terrain height (see Sec. 2.3.8) (Olmsted, 1993).

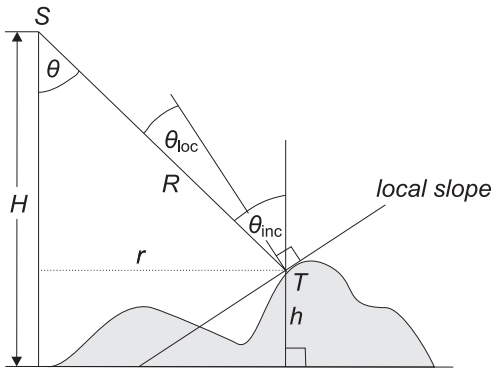

Figure 2.2 – Cross section of terrain imaging with SAR based on Olmsted (1993).

The angle between nadir and the range vector that is defined by the antenna orientation and the height of the platform is the *look angle* θ. The *incidence angle* θ_{inc} is defined as the angle between the local vertical (ellipsoidal normal) and the slant range vector. For a flat earth, $h = 0$, $\theta_{\text{inc}} = \theta$ holds. The *local incidence angle* θ_{loc} is defined as the angle between the local topographic surface normal and the slant range vector.

The SAR illumination results in a reflectivity map based on the slant range measurement. Considering a smooth surface, a non-linear relationship characterizes the distance from the sensor to the target and its cross-track position in the image. The side-looking characteristic of the SAR instrument causes a variation of the incidence angle in ground range. The spacing of two points with the same cross-track distance therefore appears compressed in near range compared to points with the same cross-track spacing in far range (Fig. 2.3a). From this property, it becomes also apparent that the resolution depends on the range distance.

2.1.2 Terrain induced distortions

Due to the side-looking imaging geometry, variations in terrain height can further cause distortions that depend on the local incidence angle (*terrain induced distortions*). The look angle θ must be chosen large enough to achieve a reasonable ground range resolution, but choosing it too large in turn causes grazing incidence with low backscatter (Fig. 2.4). It is usually chosen between 20° and 50° for spaceborne SAR systems (Olmsted, 1993).

Given the terrain inclination angle α, three different types of terrain induced distortions (also referred to as *geometric effects*) can be distinguished: (1) *foreshortening*, (2) *layover*, and (3) *shadowing*. They are explained in the following:

Foreshortening
Forshortening occurs when the slope that is directed towards the sensor is smaller than the look angle ($\alpha < \theta$). The slope will be imaged smaller than it is compared to the flat-earth-scenario (Fig. 2.3a). This situation can be seen at points A' and B' in the image plane of the radar (Fig. 2.3b).

Layover
If the slope is faced towards the sensor and is very steep with $\alpha \geq \theta$, the summit will be displayed closer to the sensor than the foot of the hill in the radar image plane, resulting in a strongly decorrelated image (Fig. 2.3c). Additionally, the backscatter

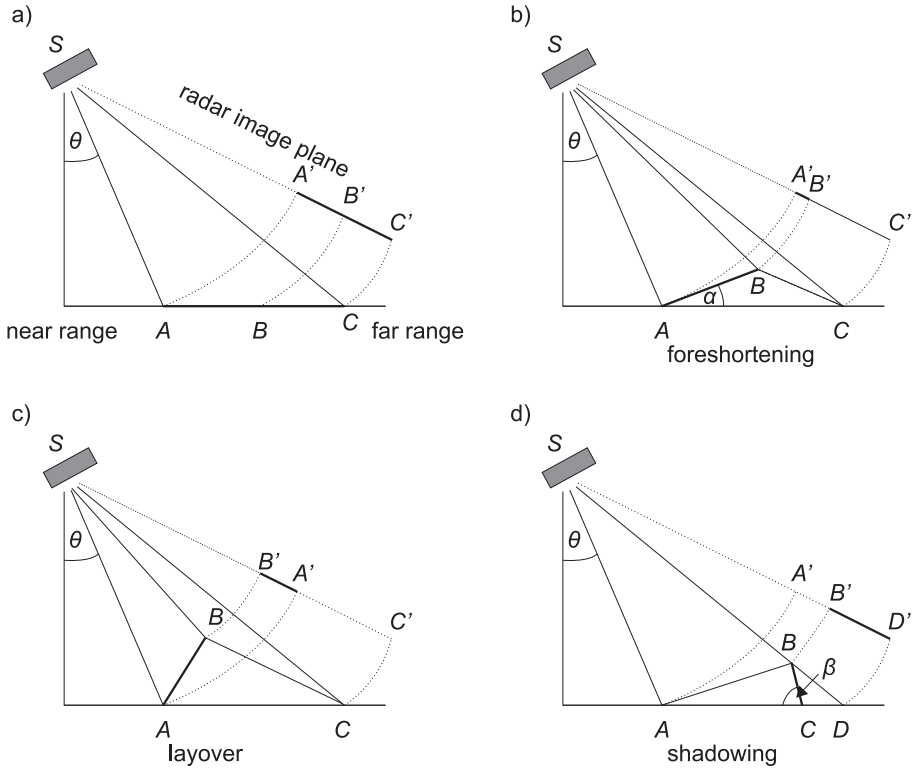

Figure 2.3 – Geometric effects in SAR images based on Olmsted (1993). (a) Relationship between slant range and ground range, (b) foreshortening, (c) layover, and (d) shadowing.

from positions on the ground that are located at different places, but in the same slant range distance, is received simultaneously, which affects assigning the received signal to the corresponding backscatter on the ground. This can be clearly seen in the amplitude information of SAR data, where layover areas commonly appear very bright (Fig. 2.4).

Shadowing
Shadowing can be considered as the opposite to layover. It occurs, when the slope is greater than or equal to the look angle ($\beta \geq \theta$) but with the slope normal pointing away from the sensor. Regarding Figure 2.3d, the area between points B and D cannot be seen by the sensor, shown by the absence of point C' on the image plane. For the reason that no backscatter is received, shadow areas appear dark in the amplitude image (Fig. 2.4).

2.1.3 Resolution

Whereas the radar principle that scans the surface with the speed of light is used in range, a continuously moving antenna beam with velocity v is used in azimuth. This imaging constellation requires transmitting subsequent pulses at a defined PRF (Bamler, 2000).

The resolution in range direction depends on the bandwidth of the transmitted pulses and is usually between 1 and 50 m. The bandwidth of TanDEM-X data for the Merapi test site is, for instance, 100 MHz for the pre-eruption data pair and 150 MHz for the post-eruption data pairs, leading to a ground range resolution of 2.9 m and

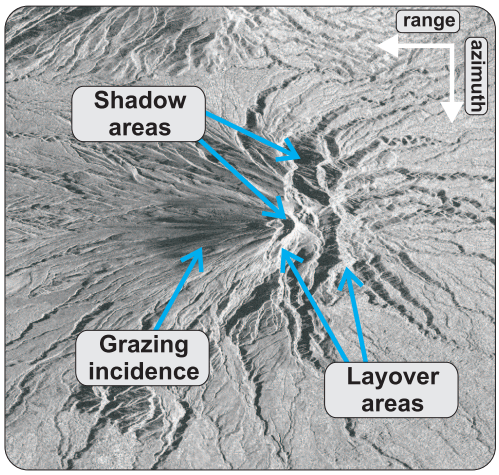

Figure 2.4 – Geometric effects in a TanDEM-X amplitude image of Merapi. Shadow areas and areas with a low backscatter due to grazing incidence on slopes tilted away from the SAR sensor appear dark, layover areas are bright.

1.9 m, respectively. The azimuth resolution is limited by the antenna length and decreases with increasing distance to the target. Regarding a real aperture system, the antenna would require several kilometers of length to achieve meter-level resolution in azimuth for a platform in space, i.e., a satellite in several hundreds of kilometers height (Moreira, 2000). The solution is the imaging with a synthetic aperture which enables an azimuth resolution independent from the distance to the ground (Albertz, 2009). SAR is based on the fact that each object is seen by the sensor over a certain amount of time, i.e., as long as it is within the flight track of the satellite. The received echoes are then correlated, which means that independent pixels on the ground are imaged several times. The larger their distance to the sensor, the more often they are imaged. Since the SAR antenna is moving relative to the ground, the echoes are subject to the Doppler-effect (Moreira, 2000). This means that higher frequencies are observed when the object is moving towards the sensor, and lower frequencies are given when the object is moving away. During processing, the variation of the Doppler frequency of every point in the image is correlated and its correct relative position can be calculated. The movement of the platform in addition to a coherent reception of the echoes thus leads to a synthetic aperture. Coherent receiving of the echoes means that amplitude and phase information are detected from the backscattered signal by quadrature demodulation. The pre-processed (focused) radar image consists of a complex-valued raw data matrix which is organized in pixels (in range) and lines (in azimuth). Every pixel is composed of a real (in-phase) and an imaginary (quadrature) component (Bamler, 2000). After image acquisition, a SAR processor is employed to simulate a long antenna and to correct the phase of the echo lines of the raw data matrix.

The length of the synthetic aperture is defined by the radiation pattern of the real aperture and the distance to the target. The resolution in azimuth is a consequence of the synthetic aperture length (Moreira, 2000) and is, for example, 3.3 m for TanDEM-X.

2.2 SAR interferometry

InSAR uses the phase difference between two (or more) SAR images of the same target area acquired at different times (repeat-pass InSAR) to monitor ground displacements of the surface, e.g., at active volcanoes, on a mm to cm scale. As a second application, DEMs with meter-level resolution can be generated. The basic requirement for both approaches – the DEM generation and the deformation monitoring – is that the backscattering properties on the ground must be stable over time. It is defined by the coherence γ, as the normalized complex spatial cross-correlation of the interferometric signal (see Sec. 2.3.4). Regarding DEM generation, using images acquired at the same time (single-pass InSAR) reveals the best results (see Sec. 2.6).

One image (in repeat-pass mode usually the one that was acquired first) is commonly referred to as *master* (or *master image*) and the other one as *slave* (or *slave image*). To receive an interferometric phase change between the two image acquisitions, at least one imaging parameter of the slave must be different compared to the master. Regarding the deformation approach, the movement of the pixel in the line-of-sight (LOS) direction of the satellite leads to a phase change. In contrast, DEM generation using *across-track* interferometry commonly requires that the terrain is viewed from a slightly different position in each acquisition but without changing the look angle θ. The difference in observation point from master and slave acquisition is the *baseline* B, which can be split into its component perpendicular to the look direction (*perpendicular baseline*, $B_\perp$) and its component in look direction (*parallel baseline*, $B_\parallel$) (Fig. 2.5).

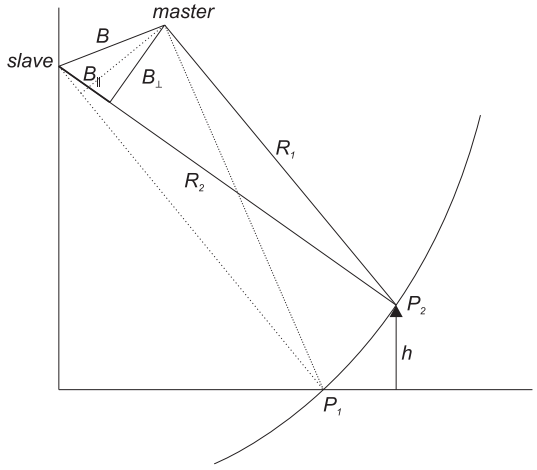

Figure 2.5 – Principle of interferometric SAR after Hein (2004).

2.2.1 Interferogram formation

Each complex SAR image consists of complex values that are aligned along a regular grid. Each complex signal y_1 (master image) and y_2 (slave image) can be split into an amplitude and a phase component (Hanssen, 2001):

$$y_1 = |y_1| \exp(j\psi_1) \tag{2.1}$$

$$y_2 = |y_2| \exp(j\psi_2). \tag{2.2}$$

The complex multiplication of y_1 and y_2 yields the complex interferogram:

$$y_1 y_2^* = |y_1| \exp(j\psi_1)|y_2| \exp(-j\psi_2) = |y_1||y_2| \exp(j(\psi_1 - \psi_2)). \tag{2.3}$$

With one SAR image, it is not possible to distinguish between the two points P_1 and P_2 in Figure 2.5 that are at the same slant range. Using only a single SAR image, the points would be mapped into the same resolution cell. However, since P_2 is elevated at h, the points obviously have a different ground range. Using a second SAR image, the difference in both echo signals leads to the phase which can be used to reveal the change in look angle θ between the two points. This change in combination with the range R_1 and the height of the satellite enables to determine the height h of point P_2. Regarding DEM generation, the second image must be acquired from a slightly different position to derive the interferogram and to reveal the change in look angle (Hein, 2004). The phase values ψ_1 and ψ_2 for point P_2 in both images are according to Hanssen (2001):

$$\psi_{1,P_2} = -\frac{2\pi 2R_1}{\lambda} + \psi_{1_{\text{scat}}} \tag{2.4}$$

$$\psi_{2,P_2} = -\frac{2\pi 2R_2}{\lambda} + \psi_{2_{\text{scat}}}, \tag{2.5}$$

with range R_1 and R_2 for P_2 in the master and slave acquisitions, respectively, the radar wavelength λ, and the scattering phases $\psi_{1_{\text{scat}}}$ and $\psi_{2_{scat}}$ for P_2. If $\psi_{1_{\text{scat}}}$ and $\psi_{2_{\text{scat}}}$ equal each other, the difference of both phase values results in the interferometric phase ϕ, as a sensitive measure for the range difference (Hanssen, 2001; Bamler and Hartl, 1998):

$$\phi = -\frac{4\pi \Delta R}{\lambda}, \tag{2.6}$$

where $\Delta R = R_2 - R_1$ is the difference in the path length of the signal. The factor 4π results from the range distance for the transmitted and received signal, while the satellite transmits and receives during both fly-overs.

2.2.2 Interferometric phase contributions

According to Hooper et al. (2004), the interferometric phase (or differential phase) ϕ is composed of the reference phase ϕ_{ref}, the topographic phase ϕ_{topo}, the phase change due to the displacement of the ground scatterer in the LOS of the satellite ϕ_{def}, the phase contribution due to atmospheric phase delay ϕ_{atm}, the phase contribution due to orbital errors ϕ_{orb}, a phase portion due to the changing backscattering properties on the ground ϕ_{bs}, and the portion of phase noise ϕ_{noise}:

$$\phi = \phi_{\text{ref}} + \phi_{\text{topo}} + \phi_{\text{def}} + \phi_{\text{atm}} + \phi_{\text{orb}} + \phi_{\text{bs}} + \phi_{\text{noise}}. \tag{2.7}$$

Several studies successfully applied repeat-pass InSAR to detect and monitor ground displacement at active volcanoes (e.g., Massonnet et al., 1995; Pritchard and Simons,

2002; Parks et al., 2012). For deriving surface displacement ϕ_{def} on a cm to mm scale, a (high-resolution) DEM is required during processing to subtract the topographic phase portion ϕ_{topo}. When no deformation occurs between two overflights, repeat-pass InSAR also allows the generation of DEMs with meter-level accuracy.

2.3 InSAR processing

For the reason that the present research focuses on the derivation of DEMs from interferometric SAR, the following section gives an overview of the processing steps necessary to generate DEMs from monostatic (repeat-pass) SAR data using DORIS. A flowchart of the basic processing steps is given in Figure 2.6. The flowchart lists the steps in the order they are executed in DORIS.

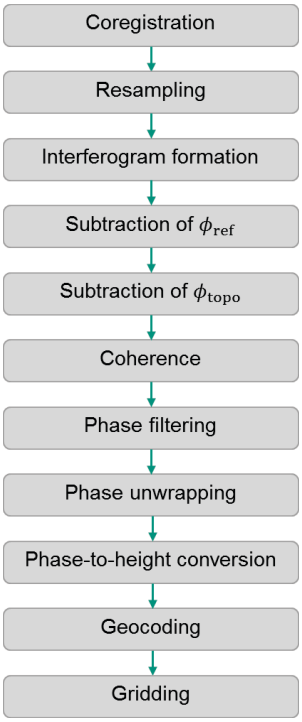

Figure 2.6 – Processing chain of the basic steps for DEM generation using DORIS.

2.3.1 Coregistration and resampling

Different start- and stop-times during image acquisition result in varying imaging geometries for different scenes, which means that the SAR images are shifted against each other and distorted. Interferometric processing therefore requires the sub-pixel registration of the slave image with respect to the master as first step. The accuracy of the coregistration affects not only the quality of the final interferogram but also of the generated DEM.

The coregistration is usually done in two steps. The *coarse registration* first applies the precise satellite orbit data and timing to approximate the offsets between the two images. The relative shifts between slave and master image are estimated within a few pixels in range and tens of pixels in azimuth (Hanssen, 2001). The coarse registration itself consists of two steps. Given an arbitrary point on the master's orbit and an arbitrary range, the coarse coregistration starts with determining the

corresponding position of the pixel on the reference ellipsoid. In the next step, the correct Doppler position of the pixel is iteratively found for the slave orbit. The timing of both orbit positions enables derivation of the shifts in azimuth and further also the shifts in range.

In the subsequent *fine registration*, evenly distributed correlation windows are used to estimate the offsets for each window. Only the amplitude information is commonly used to determine the relative shifts between the master and slave image in azimuth and range direction. The calculated relative shifts of a set of windows can be used to estimate a two-dimensional polynomial which in turn can be used to calculate the displacement vectors for every single pixel in the slave image. Oversampling enables determination of the coregistration offsets on a subpixel level (Hanssen, 2001).

Resampling is afterwards required because the geometrical transformation usually does not result in integer values. The resampling is, therefore, nothing else than transferring the derived shift from the distorted to the rectified image using an interpolation between discrete points. Different interpolation kernels like nearest neighbor, bilinear interpolation, cubic convolution, or truncated sinc function were tested (Hanssen and Bamler, 1999; Li and Bethel, 2008). Both studies conclude that the resampling preference depends on the SAR data type and (correlation) quality as well as on the terrain type. Therefore, there may not be just one 'best' resampling algorithm for coregistering complex SAR data.

2.3.2 Reference phase computation and subtraction

After interferogram formation (see Sec. 2.2.1), the phase caused by the reference surface, i.e., WGS 84 (World Geodetic System 1984) ellipsoid, is simulated and subtracted from the interferogram. The reference phase ϕ_{ref} is – as is the topographic phase ϕ_{topo} – a result of the different slant ranges when $B \neq 0$. The subtraction of the geometric phase ϕ_{ref} which results from the known SAR acquisition geometry is common to derive the full information of the interferogram. The resulting fringe pattern of the *flattened interferogram* already resembles iso-height contours, but is still ambiguous (Fig. 2.7) (Bamler and Hartl, 1998).

2.3.3 Reference topography computation and subtraction

This step is not mandatory, especially when the aim is generating a DEM itself. However, including a reference DEM during processing decisively simplifies phase unwrapping (Sec. 2.3.6). A reference DEM, such as SRTM (Shuttle Radar Topography Mission), is radar coded, which means it is converted from geographical to radar coordinates while using the acquisition geometry of the master satellite. It is, therefore, the reverse procedure of geocoding (Sec. 2.3.8). The reference topography phase ϕ_{topo} can be used in different steps of the processing. In the present work, it is subtracted from the complex interferogram after subtracting the reference phase ϕ_{ref}, resulting in the residual wrapped phase φ. After unwrapping, the reference topography ϕ_{topo} has to be added again to the residual (unwrapped) phase φ_{unw} as the geocoding step requires real height values.

2.3.4 Coherence

The (local) coherence γ is a measure of the accuracy of the interferometric phase and is used to estimate the phase noise of the complex interferogram (Hanssen, 2001; Ferretti et al., 2007a). The coherence of two SAR images is defined as:

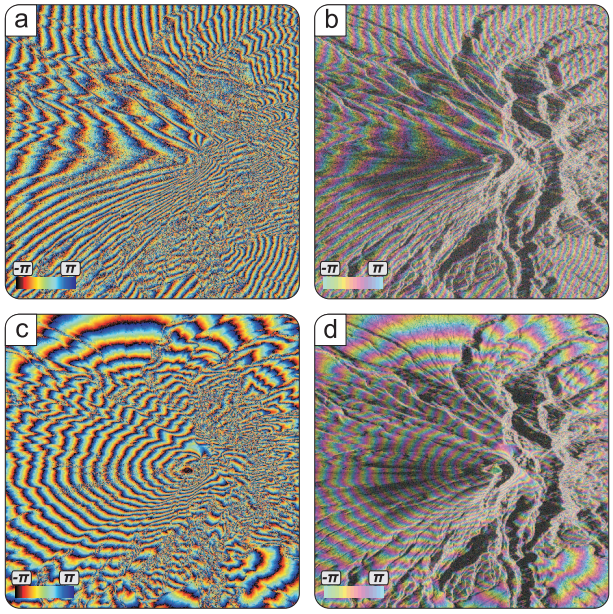

Figure 2.7 – Complex interferogram of Merapi before and after subtracting the reference phase ϕ_{ref}. (a) Phase information before reference phase subtraction, (b) phase information before reference phase subtraction plotted on top of the amplitude image, (c) phase information after reference phase subtraction, and (d) phase information after reference phase subtraction plotted on top of the amplitude image.

$$\gamma = \frac{E\{y_1 y_2^*\}}{\sqrt{E\{|y_1|^2\}E\{|y_2|^2\}}}, \qquad 0 \leq |\gamma| \leq 1, \tag{2.8}$$

where $E\{.\}$ is the expectation and * denotes the complex conjugated variable (DORIS Manual, 2009; Hanssen, 2001). With Equation (2.8), the coherence of every single pixel can be estimated. In practice, however, uniform regions are assumed to have consistent coherence values. The pixels surrounding the pixel of interest are, therefore, included in the analysis by the spatial average over N pixels (Hanssen, 2001):

$$|\hat{\gamma}| = \frac{|\sum_{n=1}^{N} y_1^{(n)} y_2^{*(n)}|}{\sqrt{\sum_{n=1}^{N} |y_1^{(n)}|^2 \sum_{n=1}^{N} |y_2^{(n)}|^2}}, \tag{2.9}$$

with $|\hat{\gamma}|$ as the estimation value of $|\gamma|$. The replacement of the expectation by spatial averaging is related to the assumption of an ergodic stochastic process. The spatial averaging is conducted over a shifting window including a few pixels in range and azimuth. The amount of pixels that are used for averaging determines the accuracy of the estimation (Hanssen, 2001).

The coherence can be estimated with or without prior subtraction of the reference phase ϕ_{ref} (see Sec. 2.3.2). If only phase statistics are derived from γ, Equation (2.9) can be used. However, noise ϕ_{noise} in the data and/or a systematic phase change in the estimation window due to topographic ϕ_{topo}, atmospheric ϕ_{atm}, or deformation signals ϕ_{def} which lead to variations in the effective path length over the scene decrease the estimated coherence. The *phase corrected coherence* $\hat{\gamma}_{\text{pc}}$

should, therefore, be preferred if the phase noise is, e.g., used to classify terrain types (Hanssen, 2001):

$$|\hat{\gamma}_{\mathrm{pc}}| = \frac{|\sum_{n=1}^{N} y_1^{(n)} y_2^{*(n)} \exp(-j\phi^{(n)})|}{\sqrt{\sum_{n=1}^{N} |y_1^{(n)}|^2 \sum_{n=1}^{N} |y_2^{(n)}|^2}} \tag{2.10}$$

with $\phi^{(n)}$ as the systematic phase component for each pixel.

Considering mountainous terrain, a reference DEM phase ϕ_{topo} should be subtracted for a proper estimation of γ (DORIS Manual, 2009).

Identical acquisitions lead to an entirely coherent signal, which is in reality not true as several factors influence the signal. For repeat-pass systems, these are among others thermal noise ϕ_{noise}, changed atmospheric conditions between two overflights ϕ_{atm}, changes in the backscattering properties on the ground ϕ_{bs}, and geometric decorrelation (Schwäbisch, 1995; Hanssen, 2001). Figure 2.8 shows a coherence image of Merapi as example.

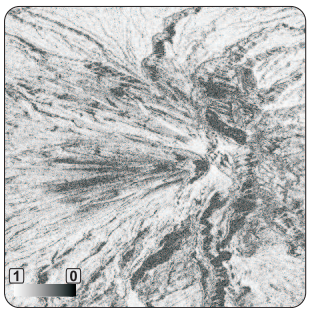

Figure 2.8 – Example showing the coherence image of Merapi. Dark colors show low and bright colors indicate high coherence.

2.3.5 Filtering

Filtering is done to reduce phase noise ϕ_{noise} and can be employed at different times during processing. The two filtering approaches that were used in this thesis are complex multilooking and phase filtering which are described in the following:

Complex multilooking
One way to reduce noise is *complex multilooking*, which is usually applied during interferogram generation/reference phase subtraction ϕ_{ref}. It aims to increase the radiometric accuracy by spatial averaging of the complex interferogram. Subsequently, the image resolution is decreased (Ferretti et al., 2007b).

Phase filtering
Filtering after interferogram generation is usually employed before phase unwrapping. A widely used filter that can also be applied within the DORIS software packages is the *adaptive filter* developed by Goldstein and Werner (1998). A second option, *spatial convolution* (Schowengerdt, 1983), is also implemented within DORIS to filter the complex interferogram.

2.3.6 Phase unwrapping

The phase is always ambiguous in terms of integer values of 2π. Resolving the ambiguous phase is called *phase unwrapping*. *Wrapping* the absolute phase to the $[-\pi, \pi)$-interval is a forward problem that is solved easily. The phase unwrapping as the inverse problem is not, especially in presence of phase noise ϕ_{noise} and geometric problems in the data (see Sec. 2.1.2, Hanssen, 2001).

Different phase unwrapping algorithms exist (see Ghiglia and Pritt (1998), for an overview). As the unwrapped phase ϕ_{unw} contains information that cannot be found in the wrapped phase ϕ, phase unwrapping is according to Chen and Zebker (2001) an extremely difficult problem which forces all algorithms to rely on assumptions. The most common one is that the unwrapped phase information of adjacent pixels varies less than π. If this property holds, the unwrapping can be performed by integrating the wrapped phase differences of adjacent pixels. The problem is here, among others, the already mentioned geometric effects. Shadow and layover areas transgress the assumption, leading to bigger phase jumps in the data. A maximum likelihood approach is necessary to resolve the problem.

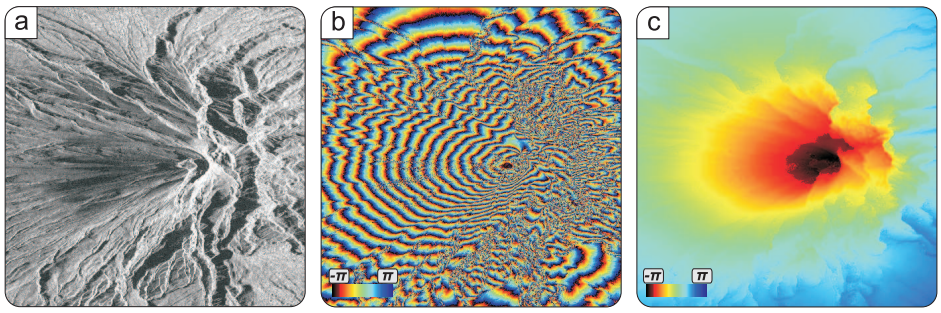

Figure 2.9 – Example images showing intermediate products of Merapi. (a) Amplitude image, (b) ambiguous wrapped phase ϕ, and (c) interferometric phase after unwrapping ϕ_{unw}.

Within DORIS, the Statistical Cost-Flow Network algorithm (SNAPHU) developed by Chen and Zebker (2001) is recommended. The approach employs nonlinear cost functions and treats the unwrapping problem as a maximum a posteriori probability problem. This enables to use the expected characteristics of the interferometric SAR signals and their statistics to develop approximation models to solve the ambiguous phase (Chen and Zebker, 2001). Figure 2.9 shows the complex interferogram (b) before and (c) after phase unwrapping for the Merapi test site.

2.3.7 Phase-to-height conversion

In this step, which is also called slant-to-height conversion, the solved unambiguous phase is converted to topographic height.

The measured height h above the reference body is according to Hanssen (2001) defined as

$$h = -\frac{\lambda R \sin\theta}{4\pi B_{\perp}} \phi_{\text{unw}}. \tag{2.11}$$

λ, R, $\sin\theta$, and $B_{\perp}$ are known, ϕ_{unw} is the unwrapped phase. An initial value based on a reference surface such as an ellipsoid is used for $\sin\theta$. A change in the height

above the reference body leads to a change in the look angle and a change of the perpendicular baseline (see Fig. 2.5). The phase-to-height conversion therefore needs to be solved iteratively until a satisfying accuracy is reached for h (Hanssen, 2001).

The height of ambiguity h_{amb} is the height difference between two adjacent discontinuities. It can be computed from the interferometric parameters. Inserting 2π for the unwrapped phase ϕ_{unw} in Equation (2.11) yields

$$h_{\text{amb}} = -\frac{\lambda R \sin\theta}{2B_{\perp}}, \tag{2.12}$$

which is the height of ambiguity as the height difference corresponding to an interferometric phase of 2π. The height of ambiguity allows assessing the interferometric performance while providing information on the height of the terrain that can unambiguously be resolved within a 2π phase change (Gonzáles et al., 2010).

2.3.8 Geocoding

The described phase-to-height conversion already results in a DEM which is still in the SAR-specific slant range imaging geometry. To make it useful for different applications, e.g., for scientific analyses, it has to be transformed to common geodetic coordinates. Geocoding is therefore nothing else than a transformation from the radar coordinates (range, azimuth, height) into coordinates of a geodetic reference system (longitude, latitude, height) such as WGS 84 or ITRF (International Terrestrial Reference Frame) (Hanssen, 2001; Schwäbisch, 1995).

For SAR, the range to the target as well as the Doppler centroid, which is the Doppler shift at the antenna beam center, of the backscattered signal is known. This enables determination of the precise position of the satellite and the properties of the Earth surface (Olmsted, 1993). Geocoding is, therefore, implemented in DORIS using the Range-Doppler algorithm. To determine the position of a target on Earth, three equations need to be solved simultaneously, containing the positioning parameters x, y, and z with respect to an ITRF (geocentric, equatorial reference frame) (Curlander and McDonough, 1991; Olmsted, 1993; Bähr, 2013):

1. The range equation indicates that the range measurement R equals the distance to the target:
$$|\boldsymbol{R_s} - \boldsymbol{R_t}| - R = 0, \tag{2.13}$$
with $\boldsymbol{R_s}$ and $\boldsymbol{R_t}$ as the sensor and target positioning vectors, respectively.

2. The Doppler equation expresses that the distance between the object point related to the pixel is located perpendicular to the flight track of the satellite (Doppler centroid):
$$f_{DC} - \frac{2\boldsymbol{V_s}(\boldsymbol{R_s} - \boldsymbol{R_t})}{\lambda|\boldsymbol{R_s} - \boldsymbol{R_t}|} = 0, \tag{2.14}$$
where f_{DC} is the Doppler centroid frequency, $\boldsymbol{V_s}$ is the sensor velocity vector, and

3. the Earth model equation

$$\frac{x^2+y^2}{(R_e+h)^2}+\frac{z^2}{(1-f)(R_e+h)^2}-1=0, \tag{2.15}$$

with h the height above the reference ellipsoid and R_e the Earth radius at the equator. f is the geometrical flattening of the ellipsoid.

Geocoding means the direct transformation, i.e., from image to object. The location equations can be solved for every pixel to convert to Cartesian coordinates x, y, z in a geodetic coordinate system:

$$(i,j) \longleftrightarrow (x,y,z), \tag{2.16}$$

where i and j are the range/azimuth coordinates of the pixel. The geocoding procedure is usually implemented as an iterative procedure to solve the location and conversion equations (DORIS Manual, 2009; Geudtner, 1995).

2.3.9 Gridding

The next step involves the conversion to geographic coordinates:

$$(x,y,z) \longleftrightarrow (\Phi,\Lambda,h), \tag{2.17}$$

where Φ and Λ are geographic latitude and longitude, respectively. The geographic coordinates can further be transformed to a metric map projection, e.g., UTM (Universal Transverse Mercator):

$$(\Phi,\Lambda,h) \longleftrightarrow (X,Y,h), \tag{2.18}$$

with X as easting and Y as northing (see Heck, 2003).

2.4 TanDEM-X mission concept

One example for acquiring SAR data in a single-pass was the SRTM-mission in February 2000. During the 11-day-long space shuttle flight, two radar antennas separated by 60 m were used to map the Earth's land surface in bistatic acquisition mode, resulting in a 30 m (1 arc second) resolution DEM and a 90 m (3 arc seconds) resolution DEM between about 60° north and 57° south (Rabus et al., 2003).

In contrast to the single-pass acquisition and static DEM of the SRTM mission, the TanDEM-X mission enables the acquisition of bistatic data repeatedly with a temporal baseline of 11 days, or multiples, in ascending and descending orbit for the first time.

The satellite mission consists of the two nearly identical radar satellites, TerraSAR-X (TSX) and TanDEM-X (TDX), which fly at an altitude of about 510 km in a sun-synchronous orbit. Table 2.1 gives an overview of the mission parameters used for acquiring the data for the global DEM as the primary mission goal. The parameters

Table 2.1 – TanDEM-X mission parameters based on Lachaise et al. (2007).

Mean orbit altitude	511.5 km
Orbit	Sun-synchronous
Inclination	97.44°
Effective across track baseline	300 - 500 m
Along track baseline	< 1 km
Baseline knowledge	< 1 mm
Radar wavelength	3.1 cm (X-band)
Incidence angle	ca. 31° - 48°
Range bandwidth	100 MHz
PRF	ca. 3 kHz
Range swath width	26 - 31 km
Scene length in azimuth direction	ca. 100 km
Expected coherence	0.70 - 0.85

are also valid for the data used in this thesis. However, characteristics given in other publications may vary due to the different mission objectives and phases. For instance, during the TanDEM-X science phase, the pursuit monostatic phase that started in autumn 2014 was characterized by a set of drifting across track baselines ranging between 0 m and 750 m (Hajnsek et al., 2014). This is suitable for SAR tomography or large baseline investigations in the polar regions.

Both satellites carry high performance SAR systems, operating in the microwave spectrum using X-band (9.6 GHz). Whereas in monostatic mode only one data pair is acquired during a fly-over, a TanDEM-X fly-over in bistatic mode acquires two radar images simultaneously, which form a single-pass interferogram (Moreira et al., 2003). Either TSX or TDX can be used as transmitter and both satellites receive the backscattered signal simultaneously (Krieger et al., 2007). Since the temporal changes in the backscattering properties on the ground ϕ_{bs} are negligible and the atmospheric conditions during image acquisition are the same, the coherence is remarkably increased compared to repeat-pass data sets (Stevens and Wadge, 2004). According to Martone et al. (2012b), the coherence of all acquisitions processed between December 2010 and April 2012 for the global TanDEM-X DEM is 0.75. Table 4.1 gives an overview of measured coherences for the analyzed data pairs of the Merapi test site, Table 5.1 for the Tolbachik test site, and Table 6.1 for Volcán de Colima.

Moreira et al. (2003) developed the HELIX formation to coordinate the close formation flight of the two satellites and to ensure interferometric performance. The specific configuration enables acquisition of images of the entire Earth's surface with adaptable across (300 - 500 m) and along track (almost zero to several kilometers) baselines. This allows different applications at the same time, e.g, sensing of elevation with a stable height of ambiguity and sensing of velocity, e.g., wind speed, or detection of moving targets. Whereas the maximum across track baseline occurs over the equator, the trajectories of the two satellites intersect over the poles. For global DEM acquisition (and thus also for the data used in this thesis), the along track baseline needs to be smaller than 1 km.

Whereas ascending and descending acquisition geometries are always suitable to map equatorial regions (including the Merapi and Volcán de Colima test sites), only one geometry is suitable to map northern and southern latitudes (including the Tolbachik test site) at the same time. It depends on the crossing orbits of TSX and TDX at the poles due to the HELIX configuration. This leads to short effective baselines for the complementary acquisition geometry and results in a low height sensitivity. The effective baseline B_{eff} is defined as half the length of the perpendicular baseline $B_{\perp}$ for the TanDEM-X products (see Sec. 2.5).

Since the start of the satellite mission in 2010, the ascending orbit has been the favorable orbit with suitable baselines for the northern hemisphere (i.e., the Tolbachik test site, see Chap. 5). For the possibility to use both acquisition geometries and different effective baselines B_{eff} for the global DEM generation – which is especially required in difficult terrain like, e.g., valleys, mountains, high vegetation – the satellite formation was swapped from August 2013 until April 2014 (Borla Tridon et al., 2013; Zink, 2014). This was done by a 180° shift of the libration phase in the HELIX formation (Krieger et al., 2007). During this period, the descending orbit was the favorable orbit for northern latitudes and the ascending orbit for southern latitudes.

Table 2.2 – Comparison of TanDEM-X and SRTM specifications after Krieger et al. (2007).

Requirement	Specification	SRTM DTED-2 (Digital terrain elevation data)	TanDEM-X HRTI-3 (High-resolution terrain information)
Relative vertical accuracy	90 % linear point-to-point error over a 1° x 1° cell	12 m (slope < 20%) 15 m (slope > 20%)	2 m (slope < 20 %) 4 m (slope > 20 %)
Absolute vertical accuracy	90 % linear error	18 m	10 m
Relative horizontal accuracy	90 % circular error	15 m	3 m
Horizontal accuracy	90 % circular error	23 m	10 m
Spatial resolution	Independent pixels	30 m (1 arc sec at equator)	12 m (0.4 arc sec at equator)

The primary mission goal is the acquisition of a global DEM with unprecedented accuracy according to the high-resolution terrain information (HRTI)-3 standard. This requires a spatial resolution of 12 m, a relative vertical accuracy of 2 to 4 m depending on the slope, and a relative horizontal accuracy of 3 m. To fulfill these requirements, data segments from successive TanDEM-X satellite passes are combined to improve the DEM accuracy (Krieger et al., 2007). Table 2.2 compares the specifications of the TanDEM-X DEM with those of the 30 m SRTM DEM. The DEM quality of an exemplary 12 m resolution TanDEM-X DEM compared to a 90 m SRTM DEM covering the Tolbachik test site is further shown in Figure 2.10. 90 m SRTM data were chosen here since 30 m SRTM data were not available for the selected test site. SRTM data were acquired in 2000 and the TanDEM-X data were acquired about 12 years later at the end of 2012, but before the Tolbachik fissure eruption investigated in Chapter 5 occurred. The topography in both DEMs should

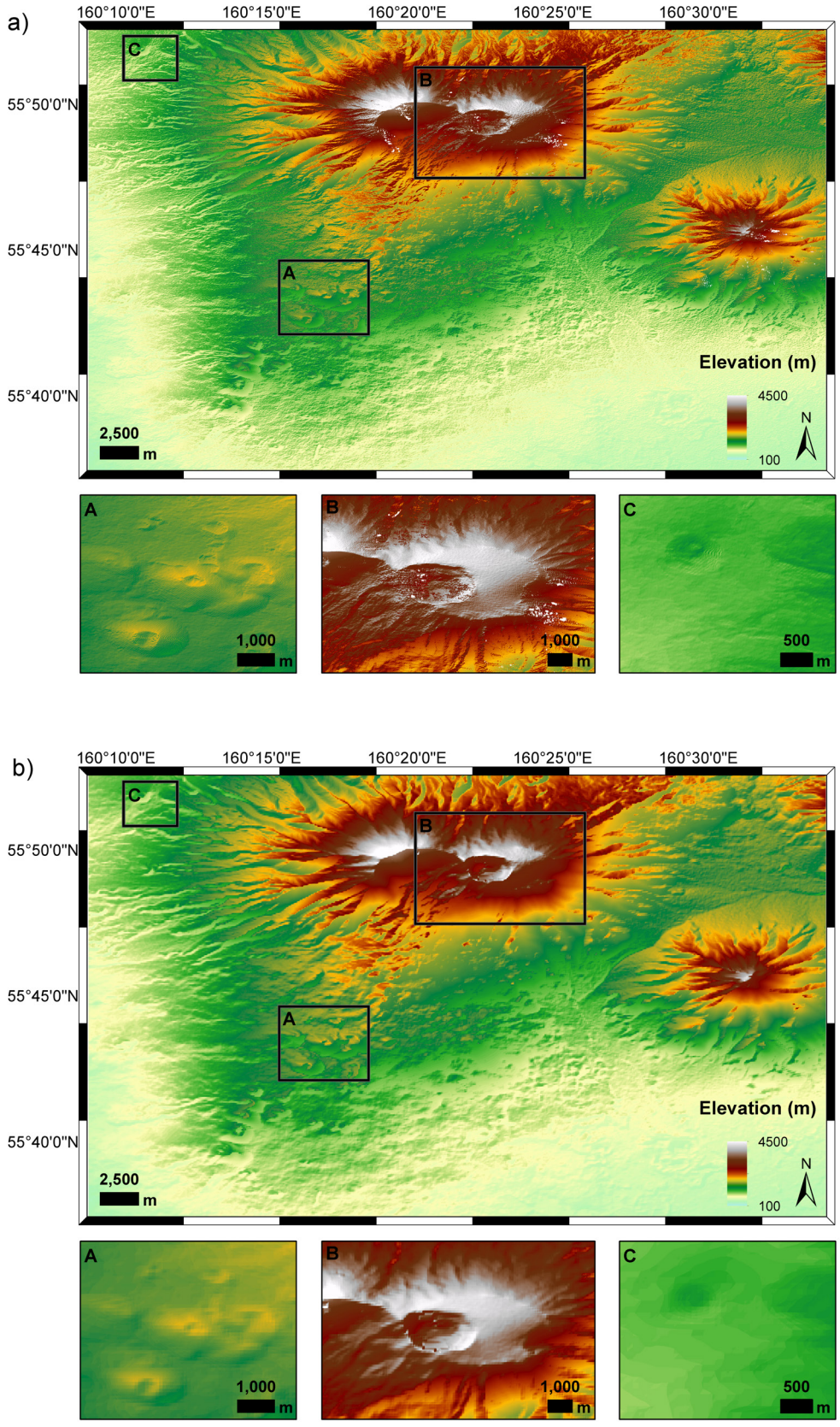

Figure 2.10 – Comparison of (a) 12 m resolution TanDEM-X DEM and (b) 90 m resolution SRTM DEM for the Tolbachik test site. Clippings A, B, and C show details of the scene.

therefore be comparable. The image on top of each part shows a wider area of the Tolbachik volcanic complex. The clippings A to C below both images show different topographic features in detail. Clippings A and C show smaller cones, whereas clipping B shows the shield volcano Plosky Tolbachik.

2.5 Considerations for bistatic InSAR data processing

Based on Section 2.3 where generating DEMs using monostatic repeat-pass SAR data was introduced, this section focuses on the general processing performed to generate DEMs from the bistatic TanDEM-X data. Similar processing steps of both approaches are identified and the required specialties for processing bistatic data are addressed. As the characteristics of the test sites differ, the processing was adapted to the varying requirements and applications of the data. The modifications in the processing are therefore described in more detail for each test site in the corresponding chapter.

The processing workflow of the bistatic TanDEM-X data is as follows (Fig. 2.11): Two radar images are recorded simultaneously during each fly-over of the satellite pair (Fig. 2.11b). The phase information of both images enables the calculation of the interferometric phase ϕ (Fig. 2.11c), from which the terrain height h is calculated according to Equation (2.11).

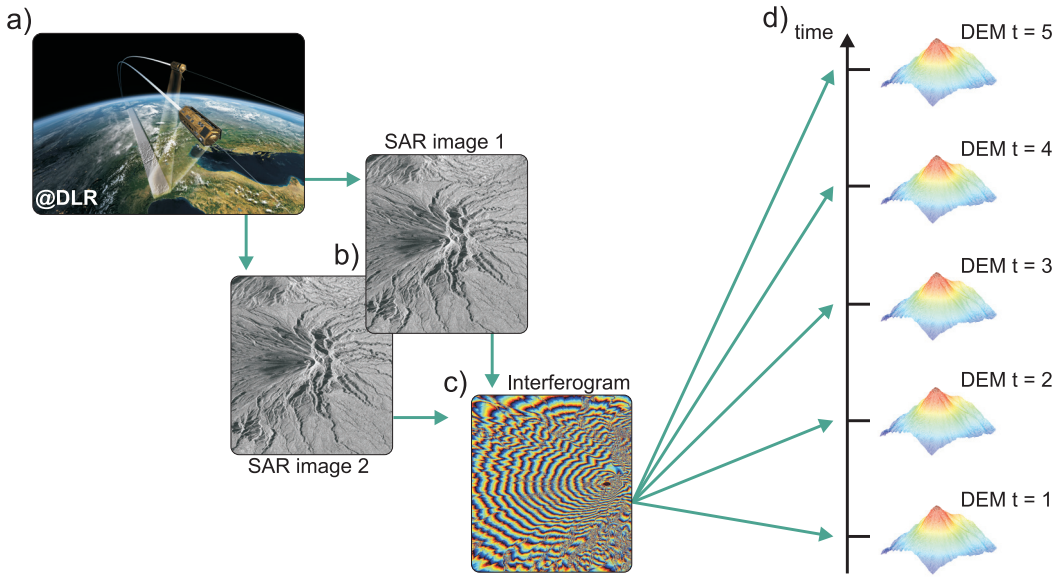

Figure 2.11 – General workflow of bistatic TanDEM-X data processing. (a) Formation flight of the two satellites TSX and TDX. (b) Two radar images are recorded simultaneously during every overflight. (c) The phase information of both radar images is used to calculate the interferometric phase, from which a DEM is generated for each acquisition time. (d) Differencing the DEMs calculated over time enables the assessment of topographic changes.

Interferometric analysis was performed using the DORIS software package (Kampes et al., 2003). Since the temporal baseline is zero days, the interferometric phase ϕ

only consists of the reference phase ϕ_{ref}, the topographic phase ϕ_{topo}, and the phase noise ϕ_{noise}. This means that neither deformations of the Earth surface ϕ_{def}, nor changes of the water vapor content of the atmosphere ϕ_{atm} nor a change in the backscattering properties on the ground ϕ_{bs}, e.g., due to volcanic activity, affect the interferometric signal.

Furthermore, the phase component due to errors in estimating the orbit trajectories ϕ_{orb} was neglected for the reason already explained in Section 2.6: Wermuth et al. (2009) proved that the TerraSAR-X science orbits are determined with an accuracy of about 4 - 5 cm. Additionally, to guarantee interferometric performance of the TanDEM-X mission, both satellites are further equipped with geodetic-type GPS (Global Positioning System) receivers (Montenbruck et al., 2011) which enable the determination of the spatial baseline between the two satellites with millimeter accuracy.

The formula commonly used for repeat-pass interferometry (Eq. 2.7) is accordingly simplified in the bistatic case to

$$\phi = \phi_{\text{ref}} + \phi_{\text{topo}} + \phi_{\text{noise}}. \tag{2.19}$$

The complex raw data of the TanDEM-X mission are provided as Coregistered Single look Slant range Complex (CoSSC) files stored in half-precision format (Fritz et al., 2012). As this format is unknown to the DORIS software package, the data had to be converted from half-precision to floating point precision using the Half Precision Floating Point Converter in Matlab developed by Tursa (2009). Interferograms of each bistatic TanDEM-X pair were then generated using DORIS. Since the two radar images are already coregistered, the processing steps concerning coregistration were not required (Fig. 2.12). The interferometric processing started directly with computing the complex interferograms (Sec. 2.2.1).

After interferogram generation, the reference phase ϕ_{ref} was subtracted (Sec. 2.3.2). This step was performed for the data pairs of all test sites. The processing was first tested without using a reference DEM phase ϕ_{topo} (Sec. 2.3.3) for the Merapi test site. Due to the spatially limited but large topographic changes, the processing without a reference DEM phase led to adequate results at Merapi. The application of TanDEM-X data to study larger spatially extents like at Tolbachik (see Sec. 5.2.2) as well as the derivation of topographic changes of less than 20 m like at Volcán de Colima (see Sec. 6.3.2) required an improved alignment of the DEMs. This was done by subtracting a reference topography phase ϕ_{topo} during processing. Prior to phase unwrapping, the complex interferograms of all test sites were filtered with either the adaptive filtering approach of Goldstein and Werner (1998) or spatial convolution (Sec. 2.3.5). The Goldstein filter implemented in DORIS is based on the fact that a higher relative weight is given to the peak in the spectrum which is caused by the fringes, leading to sharper fringes. The second commonly employed method implemented in DORIS is spatial convolution with a certain kernel function, e.g., a 3 point moving average (DORIS Manual, 2009). The filtering is basically employed to smoothen the interferometric signal to facilitate unwrapping. Since the interferograms from data of the TanDEM-X mission already contain very clear fringes with little disruption, the results did not show appreciable differences. The filtered interferogram was unwrapped using the SNAPHU algorithm (Sec. 2.3.6). Slant-to-height

conversion and geocoding was done using the Schwabisch algorithm implemented in DORIS (Sec. 2.3.7). Gridding was performed afterwards using the Generic Mapping Tool (GMT, Wessel et al. (2013)), where the grid spacing was adapted to the resolution of the data in azimuth and range in combination with the implemented multilooking. The post-processing of the DEMs to derive topographic changes over time was performed using Matlab. Differencing the DEMs from data acquired before, during, and after volcanic activity allowed estimating and quantifying large topographic changes at volcanoes.

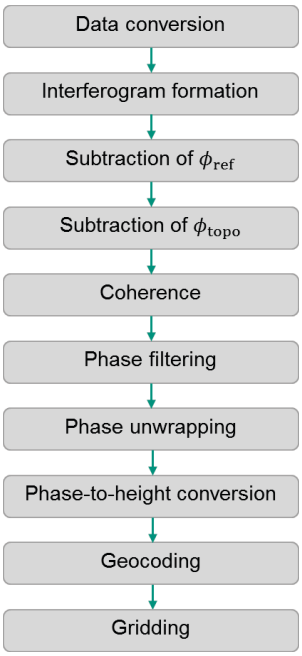

Figure 2.12 – Processing chain of the basic steps for DEM generation from bistatic data using DORIS.

In monostatic mode, the same satellite transmits and receives the signal, considering the run-time from the satellite to the surface and vice versa (Sec. 2.2.1). In bistatic mode, the active (master) satellite transmits and both satellites receive the signal.

In this study, the difference between monostatic and bistatic acquisition mode is approximated using half the length of the perpendicular baseline $B_{\perp}$, which is also called effective baseline B_{eff} for the TanDEM-X products. Since in bistatic mode only one satellite emits the electromagnetic wave while both satellites receive it, the numerator of the formula to derive the interferometric phase (Eq. 2.6) reduces to 2π:

$$\phi = -\frac{2\pi}{\lambda}\Delta R. \tag{2.20}$$

This was changed in the DORIS software code to process the bistatic data. It leads to an increased height of ambiguity and thereby reflects the decreased sensitivity of the bistatic mode compared to monostatic data. It is assumed that the approximation of the bistatic acquisition geometry does not have a significant effect on the results. Although the effects were not validated within the present thesis, ideas for analyzing the influence of the approximation are given in Section 7.2.

2.6 Errors in digital elevation models

Getting back to Equation (2.7), the interferometric phase ϕ is a summation of different phase terms. For DEM generation, the topographic phase ϕ_{topo} is the phase term of interest. All other phase terms are therefore seen as error sources and are tried to be eliminated during processing. The phase term due to the reference phase ϕ_{ref} was already mentioned in Section 2.3.2.

The accuracy of DEMs derived from monostatic repeat-pass InSAR is influenced by various factors described in the following. The errors resulting from the repeat-pass approach are in each section compared to the errors resulting from the single-pass TanDEM-X mission to show the major differences between repeat-pass and single-pass InSAR for DEM generation.

1. **Orbit errors** ϕ_{orb}. Orbit errors ϕ_{orb} result from an inaccurate determination of antenna positions during data acquisition and influence the baseline determination. This error source is included in ϕ_{orb} in Equation (2.7). Equation (2.12) indicates that the phase-to-height conversion depends on the perpendicular baseline $B_{\perp}$, which in turn determines the height resolution. Errors in baseline estimation therefore propagate into large systematic errors for the terrain height h. However, regarding current spaceborne SAR systems like TerraSAR-X, the satellite orbits are estimated with a 3-D orbit accuracy of better than 10 cm for the precise science orbits (Yoon et al., 2009; Wermuth et al., 2009). This means that the error is very small for repeat-pass InSAR analyses.

   Krieger et al. (2007) distinguish three different components of baseline estimation errors: (1) along-track errors, (2) across-track errors, and (3) radial errors. Errors in along-track are generally uncritical as they are resolved during coregistration. Across-track errors as well as radial errors can lead to both, errors in the LOS $B_{\parallel\text{err}}$ and errors that are perpendicular to the LOS $B_{\perp\text{err}}$. The errors perpendicular to the LOS lead to a bias in the phase-to-height conversion, producing a height error h_{err} of

$$h_{\text{err}} = h * \frac{B_{\perp\text{err}}}{B_{\perp}}, \tag{2.21}$$

   with h as the topographic height. Regarding TanDEM-X data, perpendicular baseline errors $B_{\perp\text{err}}$ result in DEM height errors h_{err} in the order of a few centimeters (Krieger et al., 2007; Gonzáles et al., 2010).

   Errors in LOS direction $B_{\parallel\text{err}}$ lead to a displacement of the DEM in vertical direction:

$$h_{\text{err}} = \frac{h_{\text{amb}}}{\lambda} * B_{\parallel\text{err}}. \tag{2.22}$$

   Regarding TanDEM-X data, a perpendicular baseline $B_{\perp}$ of 87.5 m and an incidence angle θ_{inc} of 33° that corresponds to a slant range R of 600 km (Krieger et al., 2007), the height of ambiguity h_{amb} is calculated with 57.8 m using Equation (2.12). Assuming an error in estimating the parallel baseline $B_{\parallel\text{err}}$ of 1 mm, the corresponding height error h_{err} is 1.9 cm.

As the incidence angle θ_{inc} varies from near to far range, also h_{amb} varies, causing the DEM to be tilted in ground range with

$$\epsilon_{\text{tilt}} = \frac{h_{\text{err}}}{\Delta s} = \frac{B_{\parallel \text{err}}}{B_{\perp}}, \tag{2.23}$$

with Δs the distance in ground range based on a reference point. Assuming again a perpendicular baseline $B_{\perp}$ of 87.5 m, the resulting DEM will be tilted with 11.4 mm/km.

2. **Thermal noise** ϕ_{noise}. Thermal noise ϕ_{noise} is modeled to be additive, which means that both, master and slave image, consist of a deterministic part plus a random noise component. It can generally lead to phase measurement errors. The quality of an image can be described by the signal-to-noise-ratio (SNR) which estimates how much a signal has been corrupted by noise. According to Zebker and Villasenor (1992), the effects of thermal noise ϕ_{noise} are easily evaluated and removed.

   Regarding TanDEM-X, Martone et al. (2012b) report a SNR higher than 6 dB for most land cover types and a coherence $\gamma > 0.6$. Regarding this value, the authors conclude that in most analyzed cases the images could sufficiently be unwrapped (Martone et al., 2012a,b).

3. **Geometric effects**. The described terrain induced distortions (Sec. 2.1.2) influence the quality of the derived DEMs, especially in mountainous terrain and can lead to artifacts (Eineder, 2003). As height errors h_{err} caused by phase errors are inversely proportional to the perpendicular baseline $B_{\perp}$, interferograms with short baselines are less sensitive to topography than interferograms with long baselines, meaning that long baselines should be chosen for proper generation of accurate DEMs. However, DEMs generated using longer baselines are stronger affected by geometric distortions, leading to an increased amount of phase errors and thus also the amount of height errors is increased. Lu and Dzurisin (2014) suggest to choose interferograms with the largest available baseline within the limit of correlation.

   According to Ferretti et al. (2007b), the following statements can be made (see also Sec. 2.1.2): (1) foreshortening areas become non-coherent when the baseline is greater than a few meters, and (2) oppositely located slopes show the best coherence values, as long as they are not subject to shadowing. γ is generally high in urban environments and areas that are characterized by exposed rocks, and low in highly vegetated areas and on water surfaces (Ferretti et al., 2007b).

   Regarding bistatic data such as TanDEM-X, geometric effects have the strongest influence on the coherence γ and thus on the interferometric performance. An analysis about the relationship between the spatial baseline and the DEM accuracy is given in Chapter 6.3.8.

4. **Temporal decorrelation** ϕ_{bs}. Phase measurement errors caused by decorrelation due to changes in the backscattering properties on the ground ϕ_{bs} that generally increase over time (temporal decorrelation) cause the coherence γ to decrease (Zebker and Villasenor, 1992). Repeat intervals of current radar

satellite missions are, for example, 11 days for TerraSAR-X (Werninghaus, 2004) and 12 days for Sentinel-1A (Torres et al., 2012; Berger et al., 2012). With the start of Sentinel-1B in April 2016, repeat-interval of the mission decreased to 6 days. The nominal repeat interval of COSMO-SkyMED is 16 days (Bianchessi and Righini, 2008), however, 1-day-repeats are also possible (Covello et al., 2010). Temporal decorrelation ϕ_{bs} is probably the most critical point regarding DEM generation from repeat-pass interferometric analysis. Here, one of the major advantages of single-pass data is clearly shown, where temporal decorrelation ϕ_{bs} does not influence the interferometric phase. This point is further discussed in Section 3.1.

5. **Atmospheric and ionospheric disturbances** ϕ_{atm}. Atmospheric and ionospheric disturbances ϕ_{atm} in the LOS of the SAR satellite can lead to unexpected phase changes (Goldstein, 1995). Regarding the troposphere, this can be caused by, e.g., varying water vapor contents. Ionospheric effects have a higher effect on longer wavelengths like L-band and are caused by varying electron density (Lu and Dzurisin, 2014). The effects can be minimized using a stack of interferograms (as the effects are generally uncorrelated over time) or with using long baselines, as the baseline length is inversely proportional to the effect the atmosphere has on the DEM height. The alternative of using single-pass data for DEM generation clearly shows the advantage here as the atmospheric composition in both of the two simultaneously acquired radar images will be nearly equal.

6. **Deformation** ϕ_{def}. Deformation of the Earth surface between two image acquisitions leads to an additional phase term ϕ_{def} and can be caused among others by tectonics, volcanic activity, or by ground water variations. To circumvent that ϕ_{def} has an influence on the interferogram, short temporal baselines are recommended for DEM generation. However, strong episodic motions by earthquakes exist and DEM generation can fail, even if temporal baselines of only a few hours are used.

   Also here, the single-pass TanDEM-X data provide a clear advantage compared to repeat-pass data. More information is given in Chapter 3.

It becomes apparent that orbit errors (ϕ_{orb}) and errors due to thermal noise (ϕ_{noise}), as well as errors due to geometric effects are an issue regarding DEM generation from both, repeat-pass and single-pass InSAR, respectively. Regarding current radar satellite missions, it is expected that the error values are comparable for repeat-pass and single-pass studies, assuming the system parameters are similar.

Whereas temporal decorrelation (ϕ_{bs}), atmospheric and ionospheric disturbances (ϕ_{atm}), and deformation (ϕ_{def}) have very strong effects in repeat-pass studies, they do not influence single-pass data in any form. This makes the TanDEM-X data suitable to generate high resolution digital elevation models from every overflight of the satellite pair, which is one of the main prerequisites for the present thesis.

3. Observation of topographic changes at active volcanoes

This chapter gives an overview of the developed methodology. The first section summarizes the state of the art of topographic change estimation at volcanoes and highlights advantages and disadvantages of field methods and remote sensing methods to reveal topographic changes. Section 3.2 then introduces different studies which used repeat-pass SAR data for DEM generation. Section 3.3 summarizes the recently conducted studies that used TanDEM-X in volcano research. In Section 3.4, the double-differential TanDEM-X approach to study active volcanism is presented and an overview of the major requirements the approach should fulfill is given. Based on these prerequisites, the chapter ends with a description of the selected test sites (Sec. 3.5).

3.1 State of the art of topographic change estimation at volcanoes

Growth rates and volumes of active lava domes and lava flows are key parameters in volcano monitoring (e.g., Stevens et al., 1999; Baldi et al., 2005; Schilling et al., 2008; Vallance et al., 2008; Wadge et al., 2008; Coppola et al., 2010; Ryan et al., 2010; Wadge et al., 2010; Diefenbach et al., 2013). They are used in combination with many other parameters like surface deformation rates (Dvorak and Dzurisin, 1997; Stevens and Wadge, 2004), geochemical composition of gas (Casadevall et al., 1983; Saepuloh et al., 2013), or seismicity (Brenguier et al., 2008; Luckett et al., 2008) to reveal insights into the eruption dynamics.

A quantitative knowledge of the mass transport through the volcanic system is essential to assess eruption dynamics as well as the hazard of lava and pyroclastic flows often accompanied by surges, and secondary phenomena such as lahars. Surges are hot gas and ash clouds which destroy everything on their way. Pyroclastic flows are a mixture of hot gases, volcanic ash, and lava dome fragments up to several meters in size, traveling down the flanks at velocities of more than 100 km/h, reaching distances of several kilometers. They often cause severe destruction and

death (Calder et al., 2002; Abdurachman et al., 2000; Gertisser et al., 2011). Lahars – as secondary phenomena – consist of a mixture of rock fragments and water which travels down the slopes (Grotzinger et al., 2008). They can occur, for instance, when a pyroclastic flow strikes a river or – which is the case for Merapi volcano – if the pyroclastic deposits are sweeping away in the rainy season (Pierson et al., 1990). Also lahars have enough energy to transport big blocks over several kilometers and lead to severe destruction (de Bélizal et al., 2013; Solikhin et al., 2015).

The volume of extruded material – or collapsing material in the case of dome-building volcanoes – correlates with the damage potential. Although crucial for eruption forecasting, quantitative data on mass transport is not easily determined.

Lava flows as well as lava domes can be monitored in the field with ground-based methods or with remote sensing/airborne methods. Ground-based methods may give direct information about magma ascent rates at vents as well as thickness, density, and composition of flow deposits and volcanic tephra, but these observations may be spatially limited by obstructions which limit visibility, by smoke and cloud cover, or by limited access to proximal areas. Another problem is due to the fact that analyzing single sections of a lava flow may not be representative for the entire lava flow field (Calvari et al., 2003). The most severe disadvantage regarding the field measurements is, however, the possible danger resulting from active lava flows for equipment and ground-based personnel (Calvari et al., 2003). These challenges make remote sensing methods a safer and more robust alternative. Remote sensing has the ability to map the extent and volume of erupted material in a spatially comprehensive and continuous way.

Ebmeier et al. (2012) distinguish the remote-sensing methods into (1) thermal and (2) volumetric methods. Thermal methods use a simple heat budget and lava heat loss properties for estimating lava fluxes. The assumption is a linear relationship between heat flux and lava flow, which is reasonable when cooling controls the flow area, but fails when volume or topography limit the lava flux (Harris et al., 2007). In contrast, the volumetric methods use the difference of DEMs recorded at least prior and after an eruption to analyze the topographic change and to derive the lava flow characteristics such as length, thickness, and flow volume.

Several studies use photogrammetric methods to generate high-resolution DEMs for volcano monitoring (e.g., James and Varley, 2012; Diefenbach et al., 2012). The 2004-2008 activity of Mount St. Helens is an outstanding example in which periodical topographic measurements were successfully employed to observe the eruptive activity and especially the lava dome growth. The volcano was monitored over its 3-year-long activity, and three LiDAR (Light Detection And Ranging) DEMs as well as more than 20 DEMs from vertical aerial photogrammetry were generated to analyze topographic changes of the growing volcano dome and deforming glacier. LiDAR data acquired in 2003 provided initial datum control (Vallance et al., 2008; Schilling et al., 2008). Vertical aerial photographs and derived DEMs were used to determine extruded volumes and magmatic ascent rates. They served as a means to help assess volcanic hazards (Schilling et al., 2008).

The Mount St. Helens example demonstrated that topographic information in the form of a time series of DEMs can be successfully employed to gain insight in eruption dynamics while observing topographic changes at dome-building volcanoes. How-

ever, high-precision data acquisition was only possible due to the fact that the topographic control had been in place before the eruption started. The high costs of the air photo and LiDAR acquisitions and the time needed for a photogrammetric data processing procedure requiring manual identification of many control points limited the frequency of data acquisition and reporting.

Although the rapid progress in automated image analysis and photogrammetry has significantly reduced the processing time recently (Diefenbach et al., 2012, 2013), the requirement of good visibility is still an issue (Diefenbach et al., 2013). Especially the observation of active volcanic areas is frequently hindered by clouds and fume, which remains a main disadvantage of photogrammetric methods for volcano monitoring.

3.2 State of the art of digital elevation model generation using InSAR

Spaceborne radar satellite missions that are operated in a repeat-pass mode and revisit the volcano at regular intervals have the potential to overcome the disadvantages of photogrammetric approaches, since the propagation of microwaves is much less affected by clouds or volcanic plumes (although the variable atmospheric water vapor content still is an issue for InSAR (e.g., Goldstein, 1995; Rao et al., 2006; Zebker et al., 1997)). The main advantages for using InSAR to derive DEMs are that no or only few ground control points are required, and images may be obtained during periods of cloud cover and during night. In addition, the technique can generate near-real-time and reliable DEMs with global access (Bürgmann et al., 2000). However, the derivation of DEMs from the interferometric phase requires a specific constellation of satellites, especially when data acquisition takes place during volcanic activity.

During 1995-2000, the European Space Agency (ESA) operated the two European Remote Sensing (ERS) satellites, ERS-1 and ERS-2, in a tandem constellation to collect radar images from the Earth's surface with a spatial resolution of 25 m in range and 5 m in azimuth. The satellite formation was characterized by a comparably large perpendicular baseline of the two satellite orbits (up to 500 m) combined with a short temporal baseline of only 24 hours which allowed acquiring topographic information. In this case, the temporal baseline was short for the reasons discussed in Section 2.6: long temporal baselines lead to temporal decorrelation ϕ_{bs}. Furthermore, deformation ϕ_{def} of the Earth surface and changes in the atmospheric composition ϕ_{atm} can cause decorrelation of the interferometric phase.

Wadge (2003) used ERS-1/-2 tandem data to generate DEMs of Soufrière Hills, Montserrat, to continuously monitor its growing/changing lava dome, and of Arenal volcano, Costa Rica, to monitor the lava flow field. Regarding the application of ERS-1/-2 tandem data to study the active lava dome at Soufrière Hills, Wadge (2003) concluded that even temporal baselines of only one day were too long to achieve reasonable results. Mapping the lava flow field at Arenal worked well, however, Wadge (2003) concluded that surface decorrelation at the long-lived lava flow together with flow motion occurring between two image acquisitions were apparent. More severe, residual differential flow motion which appeared in parts of the flow was not large enough to produce full decorrelation, but the anomalous fringes were prone to be misinterpreted as topography (Wadge, 2003; Stevens et al., 2001).

Regarding current radar satellite missions, also the Italian COSMO-SkyMed mission has the potential for 1-day repeats. Bignami et al. (2013) used a one-day COSMO-SkyMed data pair with a short spatial baseline (104 m) to generate a DEM of Merapi on Java, Indonesia, after its 2010 eruption and compared it to a pre-eruption DEM from airborne SAR data. The accuracy of the post-eruption COSMO-SkyMed DEM was analyzed based on the pre-eruption, airborne DEM only considering unchanged areas. The standard deviation along selected isohypses was calculated with 10.9 m. A second validation was conducted with respect to the correlation of the pre- and post-eruption DEMs. Therefore, a pre-eruption optical satellite image from QuickBird (www.digitalglobe.com/resources) with a resolution of 60 cm was compared to a post-eruption optical image from Google. The mean values of DEM differences at defined control points was -1.4 m. To validate the volume estimates for the pyroclastic density current deposits, Bignami et al. (2013) compared the remote sensing based results to fieldwork. Although the remote sensing based approach resulted in twice the volume calculated during fieldwork, the authors denote their volume estimates as acceptable results – considering the uncertainties of both methods and the difficulty to assess erupted volumes in general.

The COSMO-SkyMed-based study shows the high importance of SAR data to study volcanological phenomena, but also highlights the need for a special acquisition of SAR data. Also Wadge (2003) already concluded that short repeat-intervals would be best to observe topographic changes at active volcanoes. Regarding the monitoring of dome-growth, he outlined the need of using single-pass InSAR data.

3.3 Recent studies using TanDEM-X in volcano research

Some studies dealing with using TanDEM-X in volcano research have already been published and will be summarized in the following. Poland (2014) for example used TanDEM-X data to quantify the time-averaged discharge rate at Kilauea Volcano on Hawaii. 11 TanDEM-X data pairs were used during 2011-13 to measure the lava effusion rate at Kilauea by means of DEM differencing. TanDEM-X played a crucial role as other methods were useless: whereas in former activity phases SO_2 could be linked well to the lava effusion rate (Sutton et al., 2001, 2003), this relationship broke down when pre-eruptive degassing began in 2008 (Elias and Sutton, 2012). In addition, lava tubes or channels were not observable during the eruption which prevented other analyses. The DEM differencing allowed the calculation of the mean dense-rock equivalent (DRE) lava discharge rate between mid-2011 and mid-2012 with approximately 2 m^3/s. DRE is the volume of magma calculated after the volume of interparticle pore space vesicles has been subtracted (Schmincke, 2004). The uncertainty of the DEM differences was estimated in areas where no topographic change occurred. The mean in those areas was generally calculated with a precision of $\pm$ 2 m. The standard deviation amounted to up to 3 m on recent lava flows where no vegetation was present and to more than 8 m in heavily vegetated regions (Poland, 2014).

Xu and Jónsson (2014) combined a pre-eruption DEM derived using multiple ALOS (Advanced Land Observing Satellite) SAR interferograms with a post-eruption DEM from TanDEM-X to analyze lava flow volumes and flow coverage linked to the

2007-08 volcanic activity on Jebel at Tair Island in the Red Sea. DEM differencing resulted in the topographic change caused by the eruption. Topographic change mainly consisted of deposited lavas and the formation of a new scoria cone in the summit area. Scoria cones are cone-shaped, regular volcanoes of 50 - 200 m height. They develop in locally confined eruptions of small volume in a few weeks or months (Schmincke, 2004). Scoria cones were also developed during the Tolbachik 2012-13 fissure eruption, see Section 5.1.2.

Basaltic lava flows are more common on Earth than lava flows of other composition. They can be subdivided in two major structural types: pahoehoe lava and 'a'a lava. Pahoehoe lava flows are about 1 - 10 m thick and can travel many kilometers. They are characterized by their smooth surface and bulbous structure. In contrast, 'a'a lava is highly spinose (Schmincke, 2004). The average thickness of the lava flows that were extruded at Jebel at Tair Island was calculated by Xu and Jónsson (2014) with 3.8 m, leading to a bulk volume of $2.2 \pm 1.1 \times 10^7$ m^3. Considering that most of the flows are 'a'a, assuming a vesicularity of 25 %, which expresses the portion of bubbles within the lava, leads to a DRE volume of $1.7 \pm 0.8 \times 10^7$ m^3.

The uncertainty was again estimated in areas where no topographic change occurred during the eruption. In addition, areas prone to geometrical decorrelation were masked out. The calculated standard deviation of 1.9 m proved the good alignment of the DEMs and confirmed the accuracy of the volume estimate.

More recently, Albino et al. (2015) estimated the erupted volumes of Nyamulagira and Nyiragongo, two of Africa's most active volcanoes, using a time-series comparison of 5 m resolution TanDEM-X-derived DEMs. Also in this study, TanDEM-X data are of special importance because political instabilities in the region often hindered field measurements. For the eruptive episodes in 2011-12 of Nyamulagira, the erupted volume was calculated with $305.2 \pm 36.0 \times 10^6$ m^3. Furthermore, TanDEM-X and SRTM DEMs were used to reveal estimates of erupted volumes for five other eruptions which occurred since 2001. The quality of the TanDEM-X DEMs was analyzed in three different ways:

1. Analysis of the vertical accuracy of each pixel using the corresponding interferometric parameters. A final DEM which was merged from DEMs acquired with different baselines using a weighted mean resulted in an elevation uncertainty smaller than 0.78 m for 90 % of all pixels.

2. Analysis of the vertical accuracy of the DEMs by comparison with GPS measurements. During two field campaigns, 42 GPS positions were measured and the height values were compared to TanDEM-X height values. The mean error for TanDEM-X was 1.58 m and the standard deviation was 0.98 m.

3. Point-to-point comparison with high-resolution optical images to assess the horizontal accuracy. Local targets in a TanDEM-X amplitude image were compared to a 1 m resolution IKONOS image which was orthorectified and georeferenced using the GPS points. Measuring the distance between selected points in both images resulted in a standard deviation of 5.4 m in the east and 1.9 m in the north component, and in a total root-mean square error of 12.6 m.

3.4 Double-differential TanDEM-X approach to study active volcanoes

The previous section has demonstrated that TanDEM-X data can be employed to study active volcanism successfully, which is also the idea of the present thesis. The developed TanDEM-X approach is illustrated in Figure 2.11 in a flow diagram: As two radar images are acquired simultaneously by the two satellites, the coherence of each data pair is comparably high. This enables generating high-quality interferograms and resulting high-resolution DEMs. A subsequent comparison of the DEMs generated from data pairs acquired at different times allows the study of different volcanological phenomena (Fig. 3.1). The developed methodology is also called double-differential TanDEM-X approach in the following. The first differential part is due to the interferometric analysis of two SAR images to generate one DEM. The double-differential then results from differencing two or more DEMs over time.

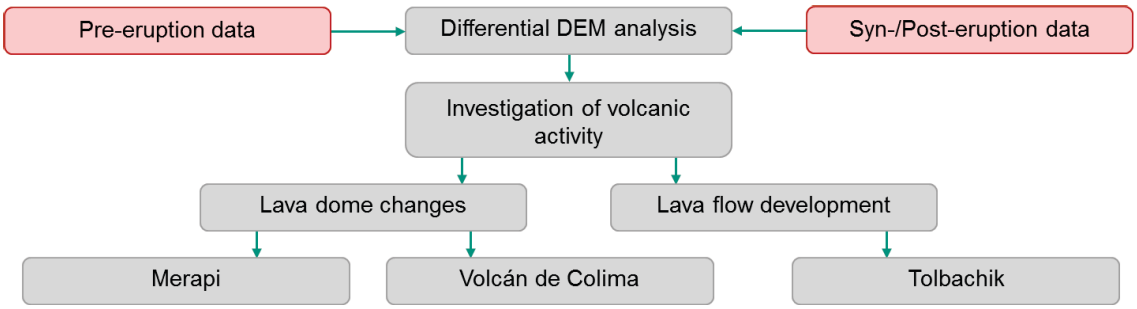

Figure 3.1 – Two main fields of study.

The conducted research can be subdivided into two main fields of study: dome-building volcanoes (1) and basaltic lava flows (2).

(1) The first focus is on dome-building volcanoes. Lava dome formation is a significant volcanic hazard as collapse events due to explosions and/or gravitational failure can trigger surges and pyroclastic flows. The rate of lava-dome growth can differ fundamentally, reaching from some cubic meters per year to cubic meters per second in active phases (Sparks et al., 1998). Since different phases of lava-dome activity can lead to differing amounts of topographic change, two different studies are conducted to investigate lava-dome activity. Whereas the first study is related to immense lava dome growth and intermediate explosions with massive topographic change, the second study focuses on a smaller explosive event which indicated the end of magma ascent to the summit.

(2) The second focus is on fluid (basaltic) lava flows. Lava flows are composed of molten rock which extrude non-explosively or explosively at any kind of volcanic vents. They flow in streams and destroy everything on their way, but are mostly slow enough to let people escape.

Measuring the changing topography of a volcanic edifice and the surrounding area enables quantification of mass flows and contributes to analyzing hazards in different ways. The major requirements of using TanDEM-X to study both, dome-building volcanoes as well as fluid lava flows, are listed in the following:

1. The developed methodology should be independent of space, time, and weather conditions and should allow to analyze different volcanological phenomena.

2. The approach should overcome the limitations of ground-based, optical, and repeat-pass interferometric methods.

3. The approach should enable to observe growing lava domes and extruding lava flows with high-resolution DEMs.

4. Topographic and volumetric changes at active lava domes and due to emplacement of lava flows should be revealed.

5. The approach should give important insight into the mass transport in volcanic systems and should enable the derivation of magma ascent rates.

6. The approach should contribute to numerical flow models (lava flows, pyroclastic flows, lahars) requiring up-to-date and high-resolution topographic information as well as information about topographic changes which occurred during an eruption.

7. The generated DEMs and derived volcanological parameters should be reliable.

3.5 Test site selection

The different requirements of the TanDEM-X mission did not enable the acquisition of time-series of all volcanoes globally. Therefore, several active volcanoes were defined as super test sites by the scientific community (Tab. 3.1).

Table 3.1 – TanDEM-X super test sites: volcanoes. Changed after Hajnsek and Busche (2013).

Volcano	Region
Bezymianny	Kamchatka, Russia
Volcán de Colima	Mexico
Etna	Italy
El Hiero	Canary Islands, Spain
Grímsvötn	Iceland
Kilauea	Hawaii
Merapi	Indonesia
Piton de la Fournaise	La Réunion, France
Shiveluch	Kamchatka
Soufrière Hills	Montserrat, the Carribean

To ensure the observation of volcanic activity during TanDEM-X acquisitions as an indispensable requirement and to study the properties of the chosen methodology, three different test sites were chosen (Fig. 3.2). When the research project started in spring 2011, **Merapi** on Java, Indonesia as well as **Volcán de Colima** in Mexico were promising objects as they are both dome-building volcanoes with varying activity that had shown major eruptions in recent times. Both volcanoes are stratovolcanoes and were designated as one of the 16 Decade Volcanoes by the International Association of Volcanology and Chemistry of the Earth's Interior (IAVCEI). The activity of both volcanoes is characterized by the effusive and primarily quiet phases of dome growth, which are intermitted by faster growing rates and destruction due

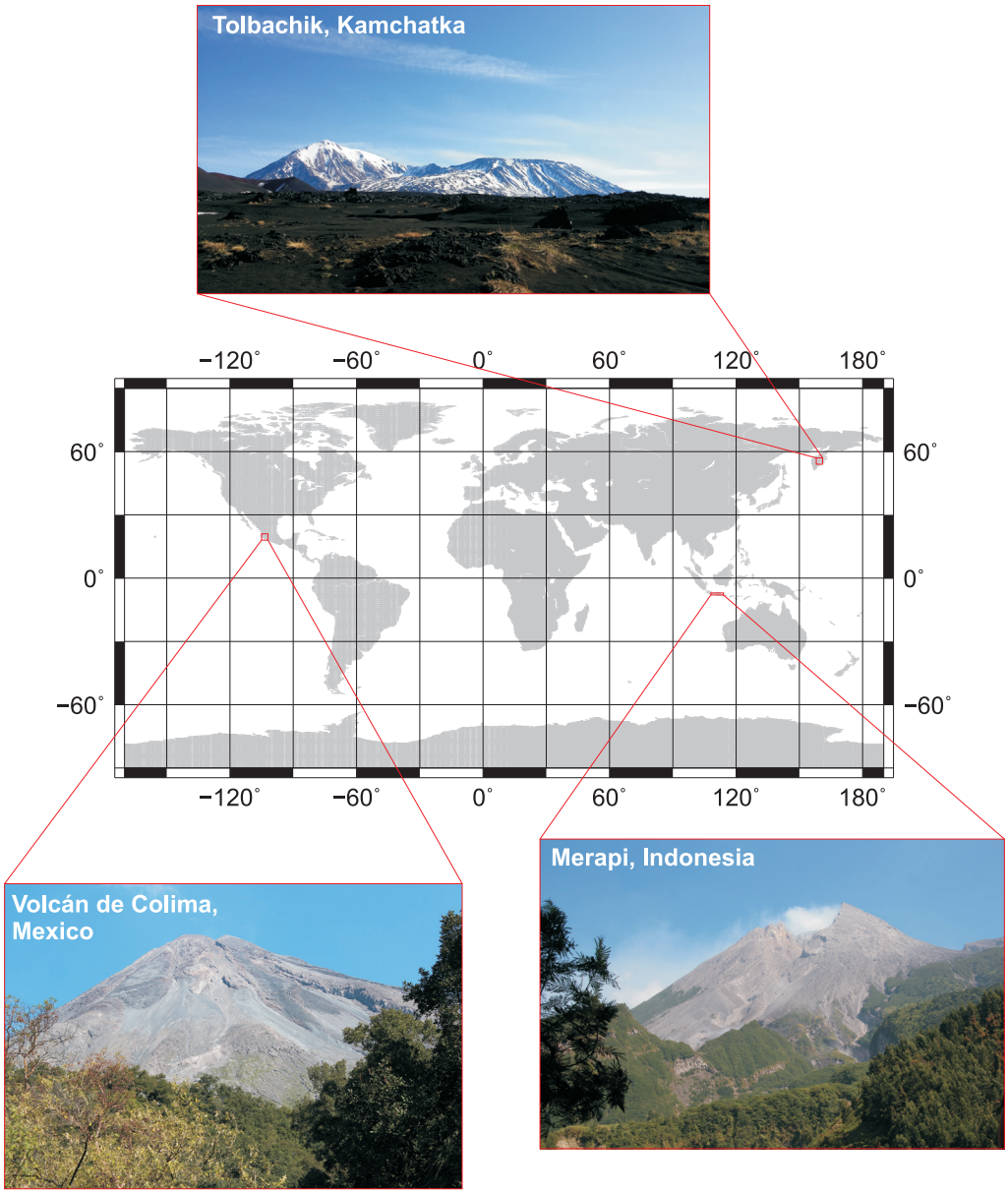

Figure 3.2 – World map showing the locations of the chosen test sites and corresponding photographs. The photographs of Merapi and Volcán de Colima were taken during fieldwork. The photograph of Tolbachik was taken in June 2015 by Janine Krippner, Pittsburgh University.

to gravitational failure or explosions. The activity also frequently leads to absolute lava dome destructions, causing pyroclastic flows and surges.

Another important aspect for choosing these two volcanoes as test sites was the comprehensive monitoring strategy of the local volcano observatories as well as the extensive availability of reference data in both regions. This was seen as a major requirement for the successful validation of the generated products and results from the innovative TanDEM-X data.

As third test site, **Tolbachik** in Kamchatka was chosen to analyze the development of a basaltic lava flow. Tolbachik recommenced erupting after 35 years of quiescence. Although Tolbachik is not listed as super test site in Table 3.1, it is included in the descending orbit that is acquired for Bezymianny volcano which is about 25

kilometers in the north-northeast of Tolbachik. Because of the lava flows continuously extruding at Tolbachik for about nine months in combination with the high temporal resolution of TanDEM-X images in the region, the volcano was included as test site to study lava flow emplacements.

The following three chapters deal with the application of the double-differential TanDEM-X approach to study different types of volcanic activity at the chosen test sites. Chapter 4 starts with Merapi volcano where the basic methodology was developed. In Chapter 5, the TanDEM-X approach is extended to study the basaltic lava flow extrusion at Tolbachik. The approach is again adapted in Chapter 6 to study small topographic changes at Volcán de Colima.

4. Volumetric change quantification of the 2010 Merapi eruption

This chapter presents the application of TanDEM-X to quantify large topographic losses of up to 200 m in steep terrain through the use of the interferometric phase. Bistatic TanDEM-X data is utilized to generate DEMs before and after the 2010 Merapi eruption to measure the topographic and volumetric change in the summit area. With the 2010 eruption, Merapi suddenly changed its volcanic behavior, leading to its largest and most explosive eruption in more than a century. The eruption was characterized as 100-year event (Surono et al., 2012). As the main interest of this study is to reveal insights into the lava dome behavior, the study focuses on a small area of about 1.3 km^3 around the volcano dome (Fig. 4.1). The eruption produced a complex topography in the summit area of Merapi now composed of a deep crater surrounded by two steep flanks. Although the side-looking imaging characteristic of SAR systems is challenging, the topographic and volumetric changes in the summit area are measurable. To quantify the volumetric loss, the shadow-affected areas were masked out, leading to a conservative estimate for the volumetric change. The quality of the DEMs is analyzed using data from permanent GPS stations located within a 4 km radius around the summit. Parts of this chapter were published in Kubanek et al. (2013a, 2015b,c).

4.1 Geological setting

The Merapi volcano (7.542° S, 110.442° E), pre-2010 eruption summit 2968 m above sea level, in Central Java is Indonesia's most dangerous volcano and one of the most hazardous volcanoes in the world. The high risk results from the dense settlement in the region combined with the type of volcanic activity. Merapi is located about 25 - 30 km north of the metropolitan area of Yogyakarta with a population of about 1.6 million people (Surono et al., 2012), with several settlements along Merapi's flanks. According to Voight et al. (2000), 80,000 people lived in the so-called forbidden zone in 2000 – potentially being at risk during an eruption.

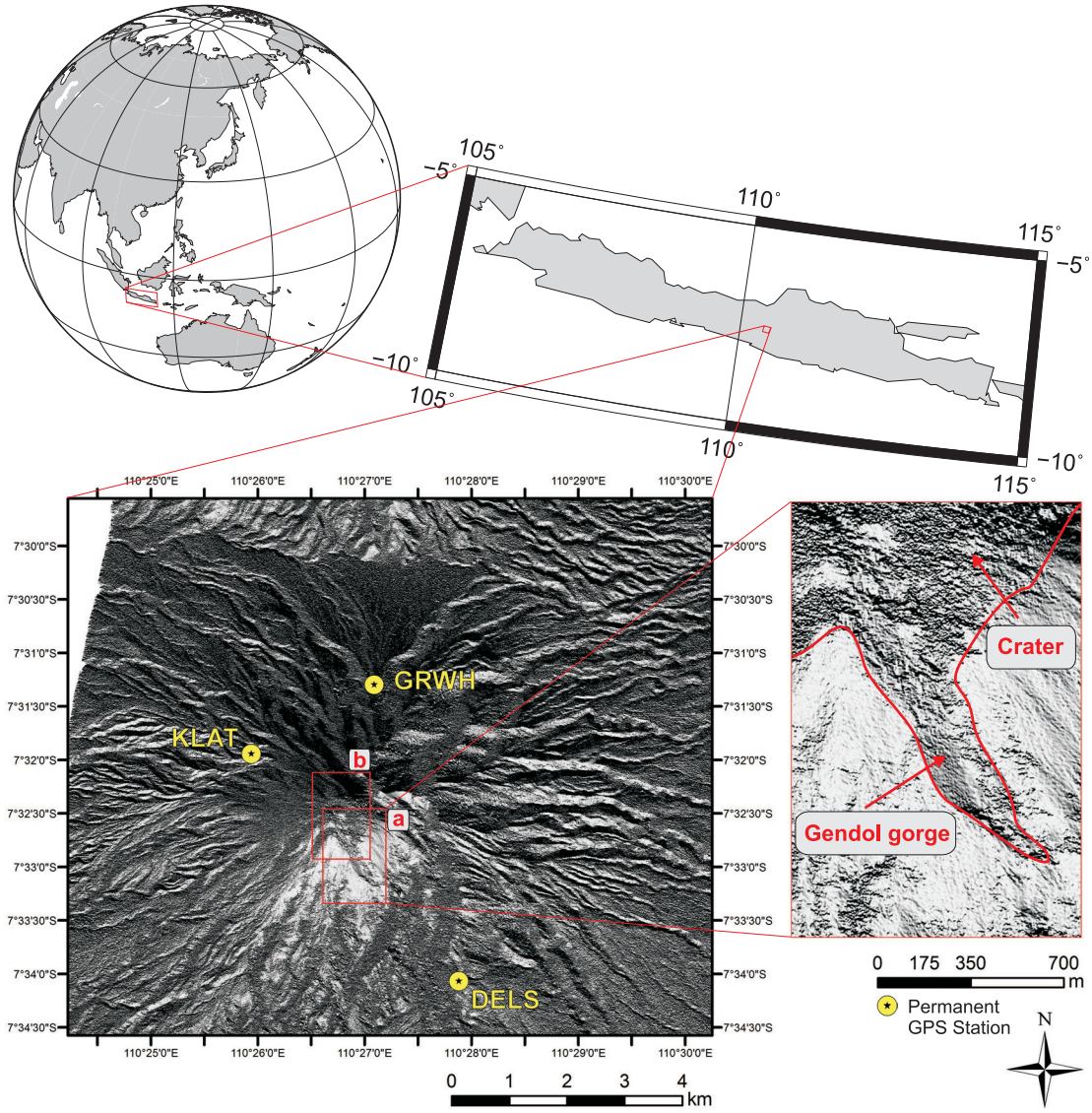

Figure 4.1 – Location of Merapi on Central Java, Indonesia. The upper right image shows Java, the lower left shows a map view of Merapi volcano including the locations of the permanent GPS stations around the summit. The section right to it (rectangle a) shows the post-2010 crater open to the south-east and the adjacent Gendol gorge. The area indicated by rectangle b is used in all following geocoded products (Fig. 4.8 and 4.10) for studying volume changes in the summit area of Merapi.

Merapi is the youngest and southernmost volcano of a chain of five volcanoes oriented from NNW to SSE. About 10 km north of Merapi is the currently dormant stratovolcano Merbabu. Volcanic activity in the region is due to the subduction of the oceanic Indo-Australian plate underneath the continental Eurasian plate (Aubert et al., 2000). Accordingly, Merapi is a stratovolcano with varying activity and highly explosive eruptions. The magmas of Merapi are basaltic to basaltic-andesitic and are too viscous to flow out at the surface. Instead, the magma accumulates in the summit and builds lava-domes – one of the most dangerous, but yet not completely understood volcanic phenomena.

Voight et al. (2000) give a descriptive overview of Merapi's historical eruptions. The stratovolcano has shown two different eruption styles in the past. The 20th cen-

tury activity was generally composed of effusive lava dome growth and gravitational collapses leading to the Merapi-specific *nuées ardentes*, pyroclastic flows produced by gravitational failure. Smaller eruptions with a Volcanic Explosivity Index (VEI) between 1 and 3 occurred every 4 to 6 years. In the 19th century, however, also larger explosive eruptions with a VEI of 4 occurred, with violent dome destructions and farther reaching pyroclastic flows. The last eruptions before the 2010 eruption occurred in 1992-93, 1994-98, and in 2006, and were all assigned a VEI of 1 to 2.

4.2 The 2010 Merapi eruption

The latest major eruption of Merapi started on 26 October 2010 with the first of six main explosive events (Surono et al., 2012). About one year earlier, a magma intrusion phase began which was characterized by a period of deflation turning into a period of inflation. In September 2010, strong inflation was revealed by Electronic Distance Measurement (EDM). However, the reflectors located close to the summit were destroyed during the eruption (Pallister et al., 2013). The first explosive event also destroyed the existing lava dome that had remained since the end of the 2006 eruption (Charbonnier and Gertisser, 2008). Next, a new dome was built from 01 to 04 November 2010 with an average magma ascent rate of 25 m^3s^{-1} (Pallister et al., 2013; Surono et al., 2012). This lava dome was destroyed on 04/05 November, which was followed by the formation of a new lava dome on 06 November with a minimum lava effusion rate of 35 m^3s^{-1}. The effusion rate decreased by 08 November together with the overall volcanic activity.

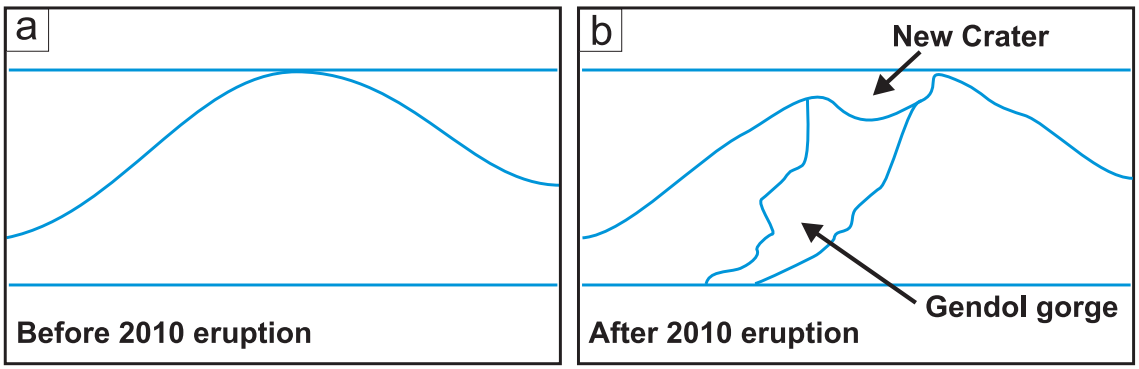

Figure 4.2 – Schematic contour showing the topography of Merapi (a) before and (b) after the 2010 eruption.

The summit of Merapi volcano changed fundamentally during the eruption (Fig. 4.2). Whereas before the 2010 eruption, Merapi's morphology looked like a cone with a small lava dome on top (Fig. 4.2a), the 2010-post-eruptive topography of the summit region is formed by a crater rim with two peaks at the eastern (higher) and western flanks (lower) and a deep nested crater of about 200 m depth (Fig. 4.2b, 4.3a and b) in its center. The newly formed crater is open to the south-east. The crater continues to the south-east into the Gendor gorge (also visible in Fig. 4.1, lower right image), which was deepened due to several explosions and pyroclastic flows accompanying the eruption. At the end of the eruption, a small lava dome was built and is still present in the crater today (Fig. 4.3b and c, Fig. 4.4d) (Pallister et al., 2013).

After Wadge et al. (2011) successfully used TerraSAR-X data to monitor the topographic changes of Soufrière Hills Volcano in July 2008 in near-real time to assist in

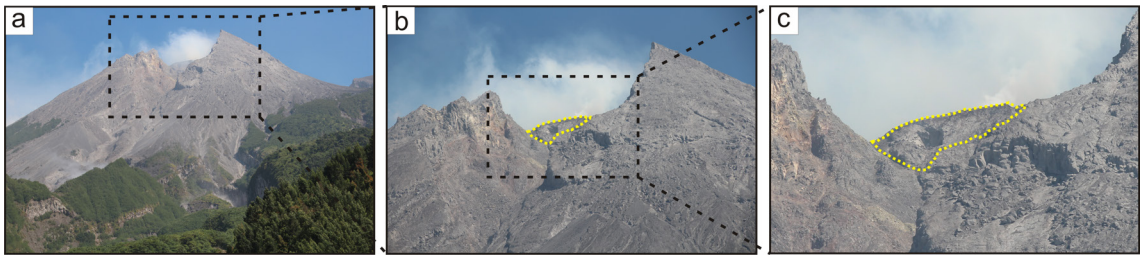

Figure 4.3 – Photographs of Merapi taken during fieldwork in September 2014 approximately 3.7 km away from the summit to the south-east. (a) Photography of Merapi showing the summit area; especially the steep slopes and the two peaks with the deep crater in the center are visible. (b) Zoom of the summit area shown in (a) and (c) zoom of the lava dome that was built in the end of the 2010 activity. The dome is surrounded by a yellow dotted line in (b) and (c).

evacuation decision making, the Merapi eruption in 2010 was one of the first eruptions in which satellite data including SAR data were analyzed in near-real-time to monitor topographic changes during a major volcanic crisis (Pallister et al., 2013). Although only the interpretation of the amplitude of the complex SAR data was used to observe changes at the volcano dome, the data were extremely useful for evacuation processes saving thousands of lives. A description about how this information was used in near-real-time to support evacuation plans during the eruption is given by Pallister et al. (2013).

4.3 Measuring topographic and volumetric changes during the 2010 eruption

The Merapi case study is the first test to utilize the bistatic TanDEM-X data to study active volcanism. The present section starts with the description of the data sets used to reveal the topographic and volumetric changes due to the 2010 eruption. The presentation of the results using amplitude and coherence information follows. The interferometric results are then used to reveal the volumetric change in the summit area of Merapi.

4.3.1 Data description and processing

For analyzing the topographic and volumetric changes in the summit area of Merapi linked to the 2010 eruption, three TanDEM-X data pairs, all recorded in descending orbit, were used. The TanDEM-X mission started acquiring data for scientific purposes in June 2011. However, one data pair was acquired during the commissioning phase of the satellite mission on 15 October 2010, 11 days before the eruption started. The data pair was used to reveal the pre-eruption topography and is also referred to as pre-eruption DEM in the following. The other two data pairs were acquired about one year after the eruption, on 24 October 2011 and 04 November 2011. They are denoted as first and second post-eruption DEM, respectively. Since the pre-eruption DEM was acquired in the commissioning phase, the bandwidth differs from the one used for the post-eruption data pairs. The resulting differences in the ground range resolution are given in Table 4.1 and are also visible in Figures 4.4a and b. Figures 4.4c and d as well as all parts of Figure 4.5 were scaled using the corresponding ground range resolution (Tab. 4.1).

Table 4.1 – Acquisition parameters for generated DEMs.

Acquisition date	15 Oct 2010	24 Oct 2011	04 Nov 2011
Orbit	Descending	Descending	Descending
Acquisition mode	StripMap	StripMap	StripMap
Effective baseline (m)	162.48	76.10	64.49
Height of ambiguity (m)	36.41	79.09	93.86
Incidence angle (°)	37.08	37.32	37.31
Bandwidth in range (MHz)	100	150	150
Ground range resolution (m)	2.9	1.9	1.9
Azimuth resolution (m)	3.3	3.3	3.3
Average coherence (whole scene)	0.68	0.79	0.81
Coherence (small section)	0.63	0.59	0.61

While the incidence angle of around 37° was similar in all satellite passes, the effective baseline decreased successively (Tab. 4.1). The height of ambiguity decreases with longer baselines. The effective baselines for the post-eruption DEMs are 64 m and 76 m and thus less than half of the length of the baseline of the pre-eruption DEM (162 m). The height of ambiguity amounts to 36.4 m for the pre-eruption DEM and 79.1 m and 93.9 m for the post-eruption DEMs, respectively (Tab. 4.1).

The TanDEM-X data pairs were processed according to the general processing considerations presented in Section 2.5. To preserve as many details as possible, the data was not multilooked. To simplify phase unwrapping, the interferograms were filtered using a Goldstein filter (Goldstein and Werner, 1998). A reference DEM phase ϕ_{topo} was not subtracted during processing because the generated DEMs and achieved results showed already a high quality. A reference DEM phase ϕ_{topo} was, therefore, not used for calculating the coherence γ, but the reference phase ϕ_{ref} was subtracted. For the final DEM products, a grid spacing of 3 m for each direction was chosen. The DEM differencing was conducted in the geocoded domain, where geographic coordinates related to WGS 84 were chosen. All analyses were carried out using a small section around the summit area amounting about 1.0 km from west to east and 1.3 km from north to south (marked as red box b in Fig. 4.1).

4.3.2 Amplitude results

The Merapi eruption in 2010 led to a major topographic change, which becomes obvious mainly in the summit area itself as well as in the area south-east of the summit. The summit appears as a cone in the radar coded pre-eruptive image (Fig. 4.4a and c), whereas it seems to be flattened in the radar coded post-eruptive image (Fig. 4.4b and d). The deepening of the crater and the opening of the Gendol gorge to the south-east as well as the lava dome itself are visible in the post-eruptive image (Fig. 4.4b and d). The black area right of the lava dome in the post-eruptive amplitude image was identified as radar shadow caused by the steep crater wall east of the crater which continues into the Gendol gorge to the south (Fig. 4.4d). Two small bright stripes running from north to south, one surrounding the lava dome in the west and the other one in the east of the shadow area, display the steep peaks of the remaining crater wall and continue into the flanks of the Gendol gorge. These bright stripes occur where the crater peaks are tilted towards the SAR sensor and were therefore identified as layover. In addition, the slope tilted away from the SAR

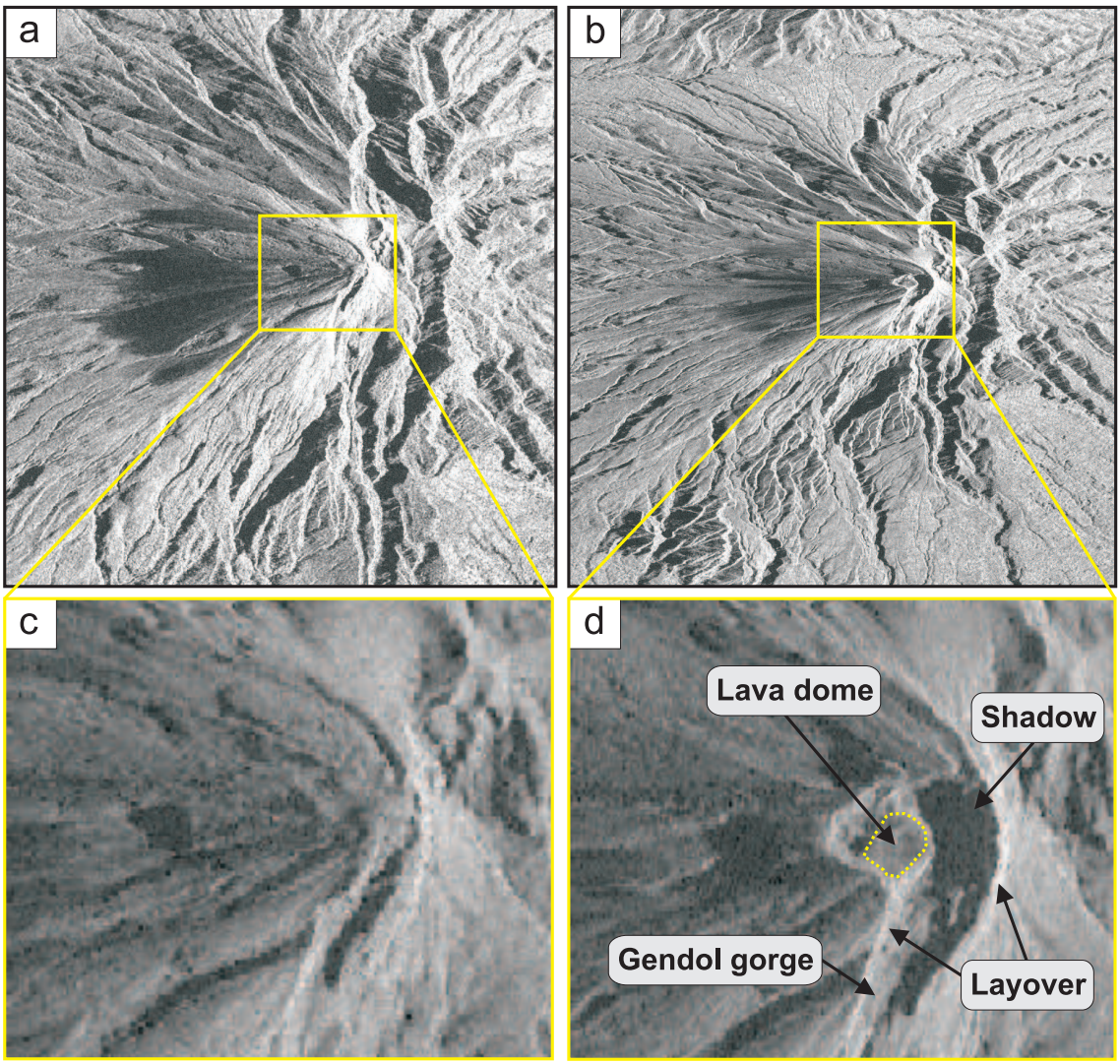

Figure 4.4 – Comparison of the backscatter magnitude of Merapi's summit area (a) before and (b) after the 2010 eruption. The data pair acquired on 24 October 2011 is used as example for the post-eruption topography. (c) is a zoom of the summit area before the eruption and (d) after the eruption. In (a) and (b), the different bandwidth is not corrected, whereas (c) and (d) are scaled using the corresponding bandwidth of the radar acquisitions (see Tab. 4.1) for comparison purposes.

sensor (the area west of the summit) is characterized by a low backscatter due to grazing incidence and therefore appears dark. The areas prone to shadow, layover, and grazing incidence hinder or even prevent the precise mapping of the steep crater walls in the generated DEMs (see Sec. 4.3.4 for further details).

4.3.3 Coherence results

The analyzed coherence images (Fig. 4.5a and b) corroborate the amplitude-based results. The coherence of the pre-eruption DEM again differs strongly from that of the post-eruption DEM. The shadow area identified in Section 4.3.2 is visible in Figure 4.5b as the dark area representing low coherence east of the center of the post-eruption radar coded coherence image.

The mean coherence of all images amounts to 0.61 for the shown section. This value is high compared to repeat-pass studies (Stevens and Wadge, 2004), but rather low

compared to a mean coherence of 0.75 obtained from the processing of a global TanDEM-X data set (Martone et al., 2012b). It has to be mentioned that the mean value of 0.61 reflects the coherence of a small region around the summit area prone to geometrical decorrelation, i.e., shadow, layover, and grazing incidence. Taking the average coherence of the whole SAR scenes into account (Tab. 4.1), the mean coherence of 0.76 equals the values published by Martone et al. (2012b).

4.3.4 Interferometric results

To quantify the topographic changes in the summit area, the interferometric phase of the three TanDEM-X data pairs was used to generate three DEMs. Figures 4.5c and d show the radar coded, wrapped phase images of the pre-eruptive data pair and the first post-eruptive data pair, respectively, after applying the adaptive filtering approach of Goldstein and Werner (1998). The quality of the fringes seems to be less affected in the pre-eruption DEM of Merapi, whereas it is more disrupted in the summit area by random noise in the post-eruption DEM.

To analyze the quality of the DEMs and to quantify the topographic changes due to the Merapi 2010 eruption, cross sections of the DEMs running from west to east at 7.5415° S latitude and from south to north at 110.446° E longitude, both passing the central vent of Merapi, were analyzed and compared. The DEMs were low-pass filtered in frequency domain using a moving average over a window of 5 x 5 pixel for smoothing the results (Fig. 4.6). The location of the cross sections is shown in Figure 4.8b.

Whereas the post-eruption DEMs follow a similar profile, the pre-eruption DEM differs strongly in both cross sections, reflecting the changes in the topography of the summit area. The main eruption resulted in collapse to the south-east and led to topographic changes of up to -200 m in the summit area and the opening of the Gendol gorge to the south-east.

Geometric distortions such as shadowing and layover as well as signal loss due to grazing incidence strongly affect the quality of the DEMs. Each DEM shows areas of different quality, which corresponds well with the identified geometric distortions. The varying signal quality for the differently oriented flanks can be explained using the cross section from west to east (Fig. 4.6a). The received signal at the western flank is characterized by a low signal-to-noise-ratio (SNR), which can be explained by the grazing incidence of the SAR system in descending orbit (Fig. 4.6a, section A). In section B, the recent crater floor including the new dome is displayed properly by the two post-eruptive DEMs. The new shadow area is visible in section C. The discrepancy between the two post-eruption DEMs gives evidence for an unwrapping error. The remaining part of the eastern flank shows again consistent height estimates for the DEMs (section D), although the spatial resolution is significantly reduced due to the steep incidence angle. An unwrapping error becomes also apparent in the cross-sections from south to north, shown in the large discrepancy between the two post-eruption DEMs.

Considering the cross sections of Merapi (Fig. 4.6) it is obvious that the profiles of the DEM recorded on 15 October 2010 are considerably smoother than those of the two post-eruption DEMs. This can be explained by the different effective baselines. The geometric decorrelation effects described above may have a minor additional effect.

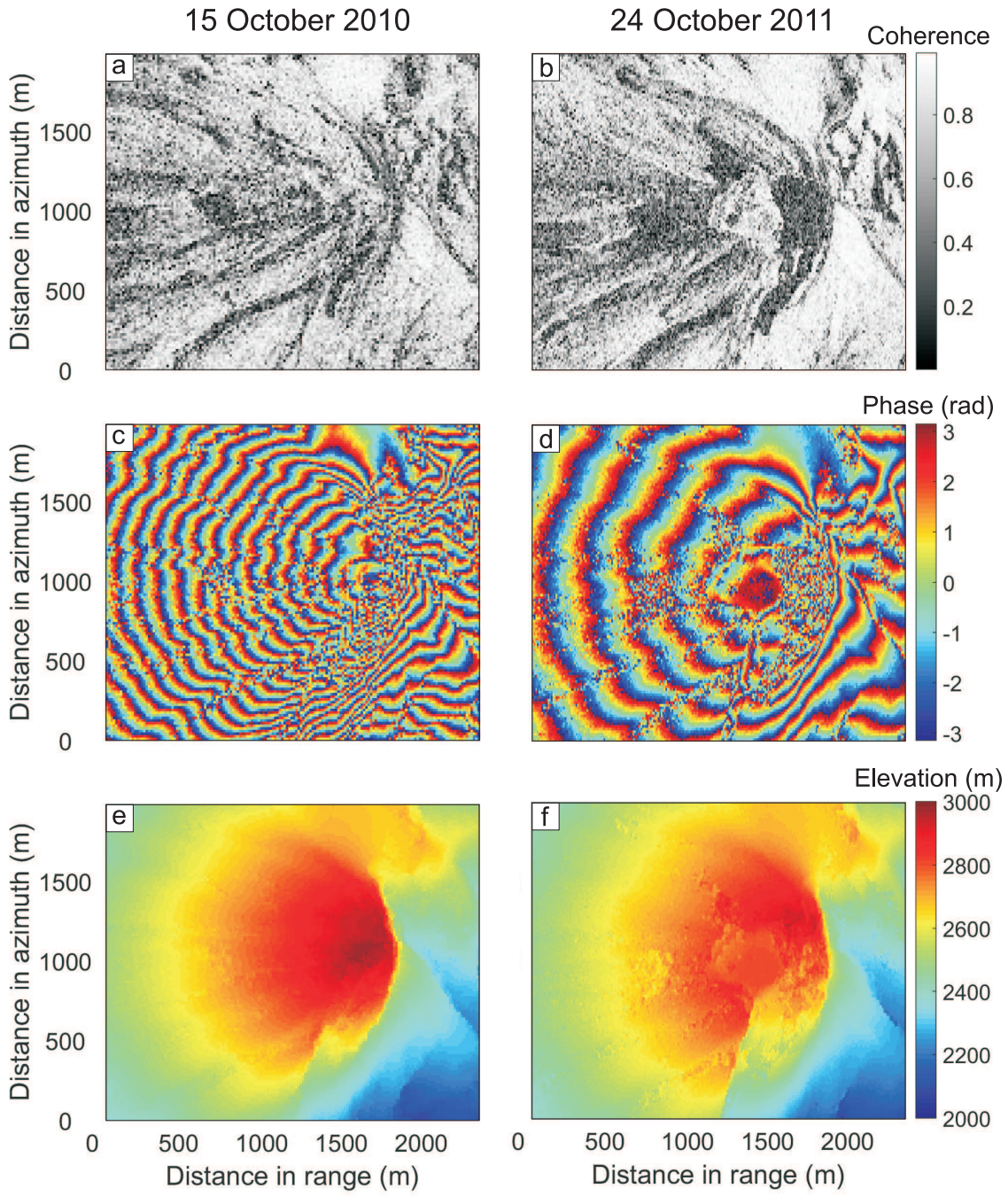

Figure 4.5 – Comparison of the derived products in radar coordinates from the pre-eruption DEM and the first post-eruption DEM. All sections show the same small area covering the summit of Merapi volcano as defined in Figures 4.4 c and d. (a) Radar coded coherence image of the pre-eruptive DEM, and (b) of the first post-eruptive DEM. Low coherence (dark) reflects the influence of geometrical decorrelation. While the black areas are indicative for a prevalence of random noise, the bright color characterizes areas where the radar signal hits the ground at nearly 90°. In these regions, the spatial resolution of the SAR images is strongly reduced. (c) Wrapped phase image of the pre-eruptive DEM after filtering, and (d) of the first post-eruptive DEM after filtering. The different fringe pattern results from different effective baselines during image acquisitions. (e) Elevation after unwrapping and slant-to-height conversion of the pre-eruptive DEM, and (f) of the post-eruptive DEM.

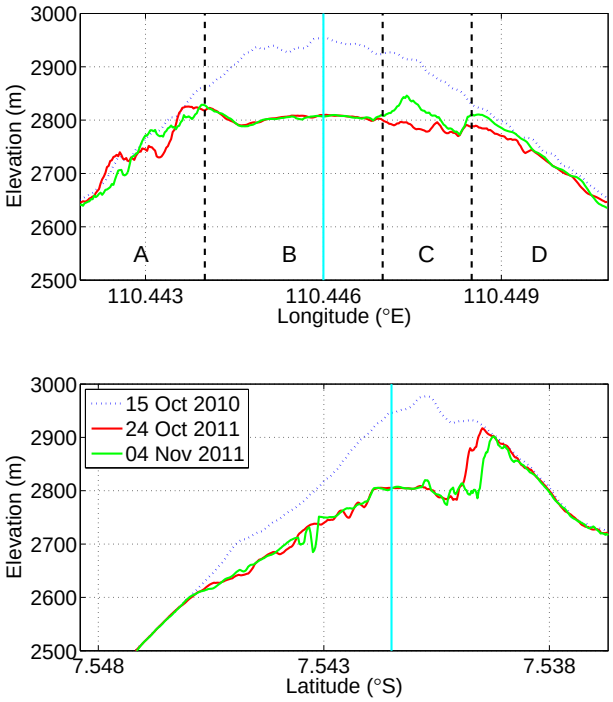

Figure 4.6 – Cross sections of the generated and low-pass filtered DEMs. The upper graphic shows the cross section from west to east at 7.5415° S. The cross section can be subdivided into four compartments providing different signal quality: the received signal at the western flank is characterized by random noise consisting of shadow zones and grazing signal (A). (B) shows the area where the received SAR signal displays the crater floor in a consistent way. The post-eruption DEMs illustrate the new shadow zone at the eastern flank in (C). (D) shows the area where the signal displays the eastern flank in a consistent way. The graphic below shows the cross section from north to south at 110.446° E. The topographic change caused by the 2010 eruption is visible in both cross sections. The light blue line in both cross sections shows the location of the other cross section, respectively.

Although the cross section from west to east shows that the geometric error sources affect the different DEMs similarly, some signal variations of the two post-eruption DEMs are detectable. The reason is the earlier described random phase noise on the flanks that is visible in Figure 4.5d as well as in the signal variations in the cross section from west to east (Fig. 4.6a). The transition of shadow to layover results in non-reliable height estimates of the steep crater walls in the post-eruptive DEMs to the east and west of the crater and the Gendol gorge. Nonetheless, the unwrapped DEMs display the crater floor and thus the volcanic dome in a plausible way (Fig. 4.5e and f). According to Surono et al. (2012), the depth of the post 2010 crater is about 200 m, which properly fits the observed topographic change. Unwrapping errors can be excluded in this case as the height of ambiguity of the two post-eruptive DEMs would cause a DEM-shift of 79 or 94 m or multiples, which is neither reasonable according to Surono et al. (2012), nor plausible from visual observations during fieldwork. Figure 4.7 on top shows an optical Digital Globe image of Merapi volcano in 3-D view that was acquired in 2015, where Merapi is seen from the south. The images below show the crater area itself and were both stitched from several photographs that were taken during fieldwork in September

2014. The red stick figure shows the place from where the photographs were taken. Whereas the image in the center focuses on the steep walls that surround the crater, the lower one shows in detail the small dome that remained after the 2010 eruption. A fracture in the center of the dome that was caused by a phreatic eruption on 18 November 2013 becomes also obvious (Walter et al., 2015).

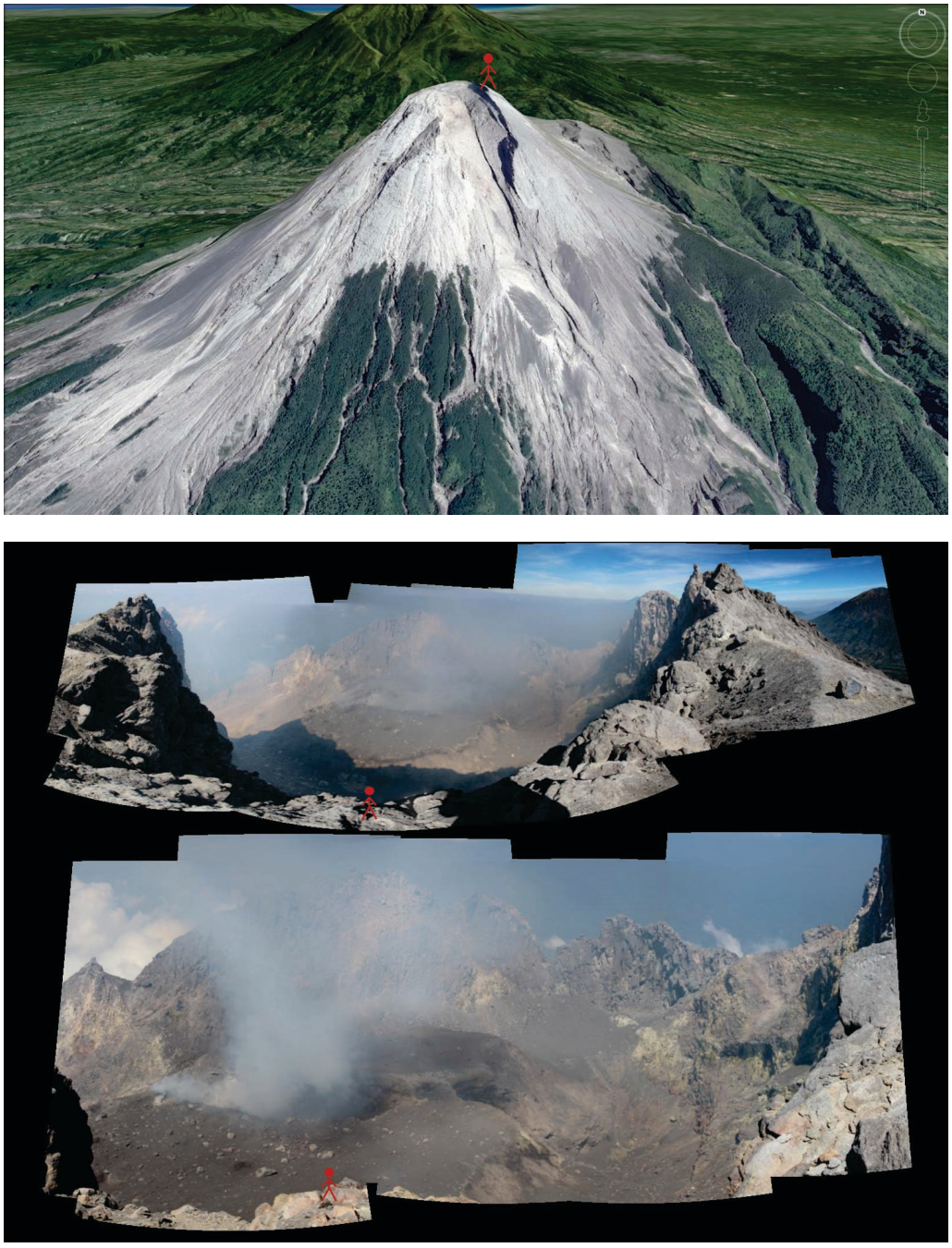

Figure 4.7 – The figure on top shows a Digital Globe image from Google Earth acquired in 2015 of Merapi volcano in 3-D view, seen from the south. The red stick figure shows the place that is possible to access for observing the lava dome in the field. The pictures below are both stitched from several photographies that were acquired during fieldwork in September 2014. The upper one focuses on the steep crater walls that surround the crater. The lower one shows the small remaining dome in detail.

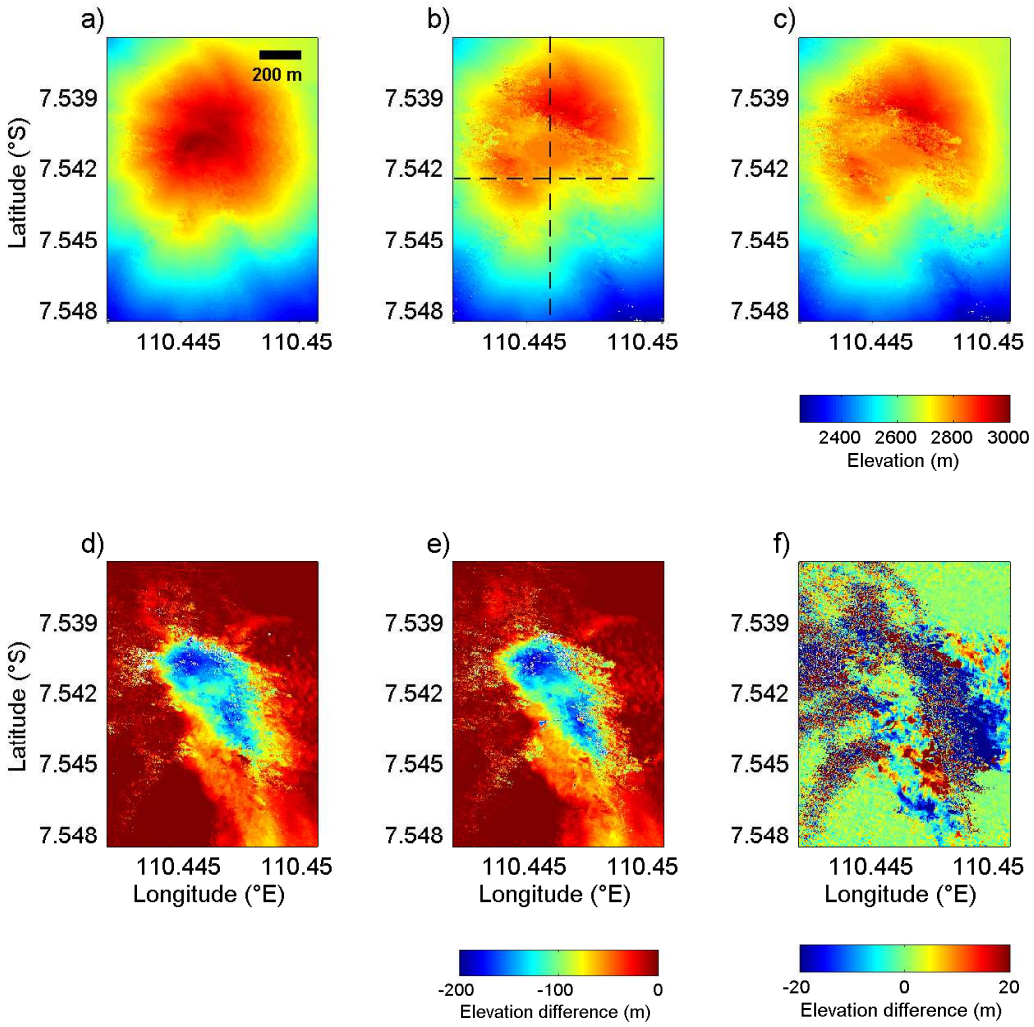

Figure 4.8 – Geocoded elevation maps and elevation differences of Merapi due to the 2010 eruption. All shown sections cover the same area highlighted as rectangle b in Figure 4.1. Map views on (a) the pre-eruption DEM recorded on 15 October 2010, (b) the first post-eruption DEM recorded on 24 October 2011, and (c) the second post-eruption DEM recorded on 04 November 2011. The dotted lines in (b) show the location of the cross sections presented in Figure 4.6. (d) Difference between the first post-eruption DEM and the pre-eruption DEM, (e) difference between the second post-eruption DEM and the pre-eruption DEM, and (f) difference between the two post-eruption DEMs.

4.3.5 Volumetry

Differencing each post-eruption DEM (Fig. 4.8b and c) and the pre-eruption DEM (Fig. 4.8a) results in the topographic change developed during the eruption (Fig. 4.8d and e). The difference between the two post-eruption DEMs was additionally calculated for comparison purposes. With a mean of -1.42 m, the difference (first post-eruption DEM – second post-eruption DEM) is very small, which indicates the quality of the generated DEMs (Fig. 4.8f). However, this elevation difference shows the unreliable elevation values in the shadow areas very well and uncovers the differences between the two post-eruption DEMs. This is also expressed in the standard deviation σ of the elevation values with 14.79 m.

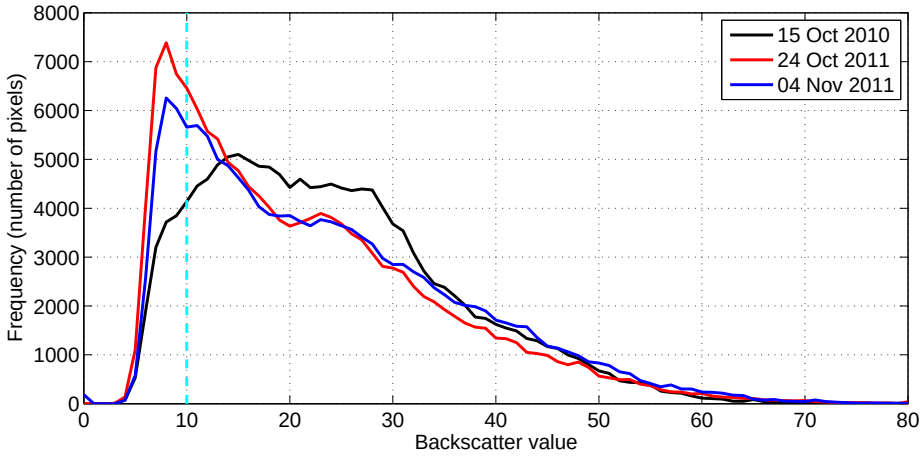

Figure 4.9 – Histogram of backscatter values. The light blue vertical line shows the threshold chosen to generate the individual shadow masks.

To exclude errors in the volume estimates due to geometrical decorrelation, shadow masks based on the amplitude information of the SAR data were generated. Figure 4.9 depicts the frequency of backscatter values of the three DEMs. Different values were tested as thresholds to generate the shadow masks. Choosing a threshold of 10 which is indicated in Figure 4.9 by the blue vertical line led to the most probable results. To generate the shadow mask for the two post-eruption DEMs individually, all amplitude values of the two data pairs smaller or equal to 10 were set to zero and all values equal or larger than 10 were set to one.

Figures 4.10a - c show the amplitude images of the Merapi data pairs. Whereas the pre-eruption DEM only contains very small shadow-affected areas close to the volcanic dome, the steep crater walls of the post-eruption topography caused a large shadow area east to the summit. Assuming that low amplitude values (black areas in the amplitude images) are shadow areas whereas bright areas are caused by layover, a shadow mask for each post-eruption DEM was generated because the portion and extent of geometrical decorrelation differs in both DEMs (see also Sec. 4.3.4).

The portion of the resulting shadow mask with respect to the total image is 20 % for the first post-eruption DEM, 16 % for the second post-eruption DEM, and the combined shadow mask has a portion of 25 % with respect to the total analyzed section. The shadow masks were then applied to the elevation difference maps individually. Figure 4.10d and e show the results for the two pre-post-eruption elevation differences and Figure 4.10f illustrates a combined shadow mask for the elevation difference from the two post-eruption DEMs. It becomes apparent that the shadow mask covers a bigger portion of the shadow area. The area prone to layover in the eastern part of the image is not covered. However, the area is not included in the calculation of the volumetric changes in the summit area. The area to the south indicates unwrapping errors in at least one of the DEMs.

The application of the shadow masks leads to the exclusion of a big portion of unreliable areas for calculating the volumetric loss. The volume change in the summit area due to the eruption was calculated using trapezoidal integration with $-18.7 \times 10^6\,\mathrm{m}^3$ for the difference between the first post-eruption DEM and the pre-eruption DEM. This result was reproduced using the difference between the second post-eruption

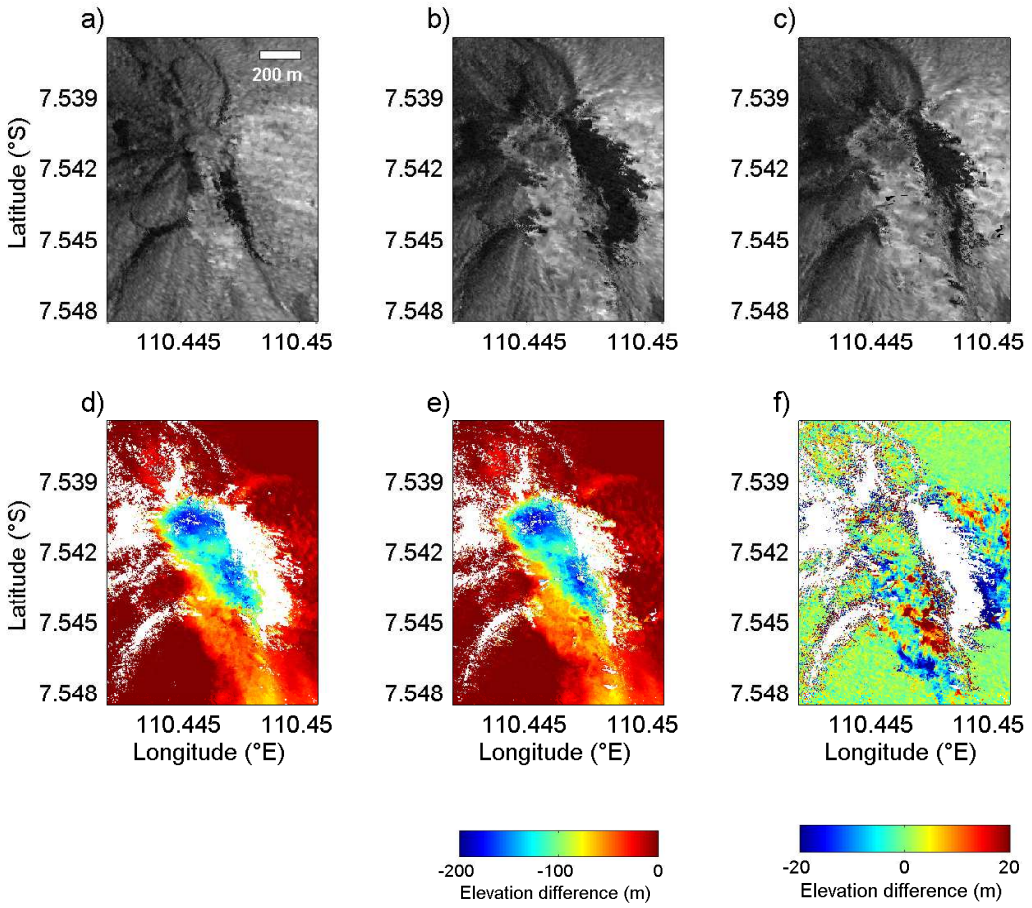

Figure 4.10 – Geocoded products derived from TanDEM-X data. All shown sections have the same size like rectangle b in Figure 4.1. (a) Amplitude information of the pre-eruptive DEM, (b) amplitude information of the first post-eruptive DEM, and (c) amplitude information of the second post-eruptive DEM. Black areas are decorrelated areas due to radar shadow and grazing incidence angles. (d) Corrected difference image of the first post-eruption DEM and the pre-eruption DEM using the corresponding shadow mask, (e) corrected difference image of the second post-eruption DEM and the pre-eruption DEM using the corresponding shadow mask, (f) corrected difference image of the two post-eruption DEMs using the combined shadow mask.

DEM and the pre-eruption DEM, resulting in a volume change of -19.1 x 10^6 m^3. Thus, the average volume change is -18.9 x 10^6 m^3. The difference in the dome volume change estimate from the two post-eruption DEMs is $\pm$ 0.4 x 10^6 m^3, which is 2 % of the average dome volume change. Introducing the shadow masks enables to exclude the error-prone, steep crater walls from the volumetric calculations but consequently leads to an underestimation of the volumetric change caused by the assumption that the masked areas contain zero values.

4.4 Discussion

The average volume change is estimated with -18.9 x 10^6 m^3, which responds to the volumetric change estimated by Pallister et al. (2013): the eruption of 26 October 2010 caused a loss of about 6 x 10^6 m^3 of non-juvenile material in the summit area.

The dome destruction of 04 to 05 November removed an additional portion of crater wall material of 10×10^6 m^3, resulting in a total loss of about 16×10^6 m^3 of non-juvenile material. To compare these findings with the TanDEM-X-based results, the volume of the new lava dome produced on 06 November 2010 in less than 12 hours has to be subtracted. Pallister et al. (2013) estimated this lava dome to have a volume of about 1.5×10^6 m^3, which results in a total volume change of $\sim$-14.5×10^6 m^3 for the corresponding time interval covered by the available bistatic TanDEM-X data.

It is most likely that the difference of 4.4×10^6 m^3 between the volume estimates of Pallister et al. (2013) and the TanDEM-X based volume estimates results from the different areas used for calculating the volumetric change. Whereas in this study, the summit area and part of the Gendol gorge (blue area in Fig. 4.8d and e) amounting to 30 % of the total volume were included in the analysis, it is assumed that Pallister et al. (2013) have only considered the crater region itself. Limiting the TanDEM-X-based analysis on the crater area results in an average volumetric change of -10.9×10^6 m^3. This underestimation of about 25 % compared to Pallister et al. (2013) is what can be expected considering that the TanDEM-X-based estimates are conservative. The generated shadow masks do not only exclude the crater wall to the east, but also parts of the crater itself, which leads to an underestimation of the volumetric change using TanDEM-X DEMs.

Data from three permanent GPS stations were employed to validate the precision of the generated DEMs. The stations KLAT, GRWH, and DELS are located within a 4 km radius around the summit of Merapi (Fig. 4.1), about 2 km north-west, 2.5 km north-east, and 4 km south-east to the summit, respectively.

The topographic heights at the GPS stations were compared with the topographic heights derived from the InSAR DEMs (Tab. 4.2). The mean elevation difference of the position KLAT amounts to 1 m and is rather small as is the mean deviation of all DEMs at position GRWH with 2 m. The pre-eruption DEM shows a large deviation for station DELS (-103 m) but reasonable values for both post-eruption DEMs (-2 and -1 m). The large deviation for the pre-eruption DEM can be explained by another unwrapping error, which is not the same as the one mentioned in Section 4.3.4. The height of ambiguity of the pre-eruption DEM of 36.4 m multiplied by three results in 109.2 m, which properly fits the elevation error of 103 m, considering the relative vertical accuracy of 2 to 4 m. As station KLAT was used as a tie point during the interferometric processing, the location of this GPS station is best comparable to the equivalent points in all DEMs. It is obvious that the mean elevation difference of the selected points in the generated DEMs (1 m) is small for all points, which corresponds to the expected relative vertical accuracy of 2 to 4 m specified by DLR (German Aerospace Center, Krieger et al., 2007). The outlier at station DELS was not included in the further investigations.

4.5 Conclusions and perspectives

As TanDEM-X is a new and innovative mission, the present study serves as a demonstration of its potential in volcano research. It is clear that the TanDEM-X data can be used to assess and quantify volumetric changes in the summit areas of dome-building volcanoes. The developed method bypasses the limitations of repeat-pass monostatic InSAR as it allows generating time series of differential DEMs

Table 4.2 – Elevation differences for GPS stations KLAT, DELS, GRWH.

	Elevation difference (m) to KLAT -7.532417° S 110.432324° E 1924.44496 m	Elevation difference (m) to DELS -7.567797° S 110.464685° E 1431.92366 m	Elevation difference (m) to GRWH -7.521613° S 110.4515503° E 2045.90973 m
15 October 2010	0	-103	-2
24 October 2011	2	-2	5
04 November 2011	2	-1	4
Mean with outlier			(-35)
Mean	1	-1	2

with meter-level accuracy. Using InSAR alone, it is possible to quantitatively assess large mass movements produced during the rapidly changing morphologies of volcanoes during eruptions. The calculated volume change due to the hazardous 2010 Merapi eruption fits well with the comparative data of Pallister et al. (2013) and highlights the potential of the innovative data to assist in disaster management during eruptions.

Employing InSAR at steep-sided stratovolcanoes is always challenging. When the present research project started, Merapi had a conical stratovolcano-like shape. Since the 2010 eruption, Merapi is characterized by a complex topography including two steep crater walls and a deep breached crater. This complex topography was challenging for developing the methodology presented here, but allowed at the same time to analyze the ability of the TanDEM-X method in complex topography and to highlight its limitations. As described in Section 2.1.2, a major issue regarding the interferometric DEM generation in complex topographic terrain is geometrical decorrelation caused by the side-looking geometry of slant-range SAR systems. Especially the extreme viewing conditions at steep Merapi volcano lead to severe shadow and layover effects. Geometrical decorrelation results in areas characterized by random, non-reliable interferometric phase information in the interferograms. This severely hampers phase unwrapping and can result in wrong height estimates. In contrast to repeat-pass interferometric analysis at volcanoes, very clear fringes with little disruption become visible at Merapi (see Fig. 4.5c and d). Especially in summit areas where the largest topographic changes due to volcanic activity are expected, repeat-pass interferograms often do not contain any useful signal due to lack of coherence (Lu et al., 2005; Lundgren et al., 2003). Geometric distortions were identified as the major error sources influencing the quality of the DEMs.

To further improve the DEM quality as well as the volume estimates, three approaches are suggested in the following:

Data fusion from ascending and descending orbits into a single DEM. Combining data from ascending and descending orbits will presumably improve the volume estimation in the summit area as shadow and layover areas are contrarily distributed in the DEMs of the two acquisition geometries. Although there is no pre-October 2010 ascending data pair available, several post-October 2010 data

pairs (starting in June 2011) can be analyzed to reduce the errors resulting from geometrical decorrelation.

Interpolation of shadow-affected areas. The introduction of shadow masks in Section 4.3.5 helped to minimize errors caused by geometrical decorrelation of the steep crater walls. The presented results are thus conservative. Another option would be to interpolate the areas excluded by the shadow masks to enhance the accuracy of the volume estimates. Eineder and Suchandt (2003) developed an approach based on using the radar shadow to unwrap and geocode objects in SAR data which cannot be reconstructed by the acquisition geometry and the commonly applied processing. Although developed for unwrapping and geocoding, the methodology can also be applied to interpolate the non-reliable areas related to the crater walls, leading to better volume estimates.

Using a reference DEM phase ϕ_{topo} during processing. The Merapi study was the first study in which the bistatic TanDEM-X data were used to analyze topographic and volumetric changes due to a major volcanic event. A reference DEM phase ϕ_{topo} was not used during processing since the processing without a reference topography phase already revealed promising results. In contrast, studying the lava flows extruded during the 2012-13 Tolbachik eruption in Chapter 5 as well as studying smaller topographic changes at Volcán de Colima in Chapter 6 did not reveal reliable results using the approach presented in this chapter due to an insufficient accuracy in the alignment of the DEMs. Therefore, the TanDEM-X approach was extended by means of using a reference DEM phase ϕ_{topo} during processing, which is presented in the two following chapters. Utilizing a reference DEM phase at Merapi was never tested, however, applying the approach developed at Tolbachik will probably solve the mentioned challenges and can avoid unwrapping errors.

5. Mapping lava flows of the 2012-13 Tolbachik, Kamchatka fissure eruption

Chapter 5 deals with the application of TanDEM-X data to study the lava flows emplaced during the 2012-13 fissure eruption of Tolbachik volcano in Kamchatka, Russia. The eruption was composed of very fluid basaltic lava flows which effused along a northeast-southwest trending fissure. TanDEM-X data were acquired before, during, and after the eruption. A new data processing approach is developed with which the TanDEM-X data are processed based on a pre-eruption reference topography. Thus, only the difference between the specific data pair acquired during or after the eruption and the reference topography is considered which enables the mapping of the lava flows and the measuring of the extruded lava flow volume over time. Based on this analysis, the lava extrusion rates for different time intervals are calculated. An uncertainty analysis is performed afterwards while analyzing the DEM differences in areas where no topographic change occurred. A comparison of the TanDEM-X-based results to volcanological parameters derived by Belousov et al. (2015) and Dvigalo et al. (2014) who used aerophotogrammetric observations as well as considerations to use the TanDEM-X data in near-real time to monitor volcanic activity ends the chapter. Parts of its content have been published in Kubanek et al. (2015a).

5.1 Geological setting

The Tolbachik volcanic complex is located in central Kamchatka, Russia (Fig. 5.1), at the southern end of the dominantly andesitic Klyuchevskaya volcano group. It is composed of two overlapping, but morphologically dissimilar volcanoes (Fig. 5.1 and 5.2). Ostry Tolbachik (55.831°N, 160.335°E, 3682 m above sea level) in the west is the older and higher sharp-topped stratovolcano. Plosky Tolbachik (55.824°N, 160.382°E, 3080 m above sea level) in the east is a basaltic shield volcano and one of the few volcanoes of the Hawaiian type in Kamchatka (Tokarev, 1978). On top of the truncated cone of Plosky Tolbachik is a central crater that hosts a caldera which is

3 km in diameter. It developed during the 1975-76 Great Tolbachik Fissure Eruption when the magmatic plumbing system emptied and the summit collapsed (Zelenski et al., 2014). The area southwest of the Tolbachik massif is called Tolbachinsky Dol and is composed of a lava plateau and a NNE-trending fissure, labeled as South Fissure in Figure 5.1. The cinder cones seen along the South Fissure are up to 300 m high and partly developed during the 1975-76 eruption.

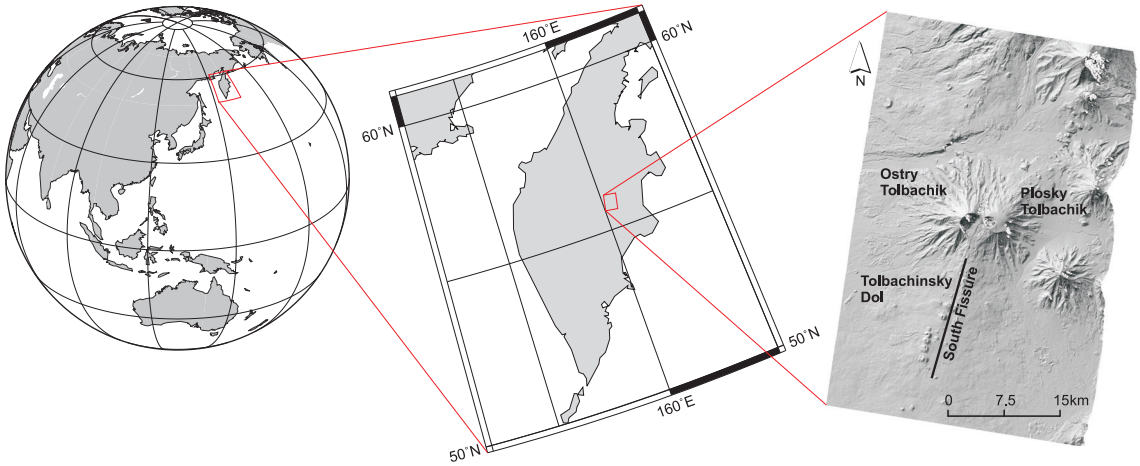

Figure 5.1 – Location of Tolbachik volcanic complex on the Kamchatka peninsula in Russia. The image on the right is a shaded relief generated from TanDEM-X data acquired on 15 November 2012. It shows the Tolbachik volcanic complex in the center. The schematically drawn South Fissure marks the fissure zone active during the 2012-13 eruption as well as during the 1975-76 Great Tolbachik Fissure Eruption.

According to Fedotov et al. (1980), more than 100 km^3 of basaltic lava erupted in the Tolbachinsky Dol during the Holocene. Eruptive activity took place from the central crater and along extensive rift zones extending northeast and southwest of Plosky Tolbachik up to 40 km from the central crater (Tokarev, 1978). The last major eruptions in 1941, 1975-76, and in 2012-13 were all located along the South Fissure (Fig. 5.1).

5.1.1 The 1975-76 eruption

Before the 2012-13 eruption occurred, the 1975-76 eruption was the youngest volcanic activity of the Tolbachik volcanic complex. It was located at the summit and at the south-flank fissures, respectively, and was part of the 10,000 year long episode of basaltic cinder cone activity extending south from Ostry and Plosky Tolbachik (Inbar et al., 2011). It is still the largest historical basaltic eruption in the Kurile-Kamchatka volcanic belt (Doubik and Hill, 1999).

The eruption was heralded by swarms of more than 300 earthquakes starting on 27 June 1975. On 06 July 1975, the volcanic activity started and lasted for about 17 months until 10 December 1976 (Doubik and Hill, 1999). The eruption extended about 30 km to the south with lava tubes and basalt sheets covering an area of more than 40 km^2 and up to 80 m thick (Tab. 5.12). The amount of new volcanic products was estimated by Fedotov et al. (1980) to be more than 2.0 km^3; lava covered an area of 44.73 km^2 (Gordeev et al., 2013b,a). Four big monogenetic scoria cones with heights of up to 300 m were built. The eruption additionally led to a subsidence of Plosky Tolbachik summit caldera of more than 400 m (Fedotov et al., 1980).

Figure 5.2 – The Tolbachik volcanic complex seen from the South on 26 July 2015, showing sharp Ostry Tolbachik on the left (W) and flat Plosky Tolbachik on the right (E). Photo courtesy of J. Krippner, University of Pittsburgh.

5.1.2 The 2012-13 eruption

After more than 35 years of quiescence, Tolbachik recommenced erupting on 27 November 2012. The eruption lasted for about nine months until 27 August 2013. Seismic data showed the first signs of unrest about five months before the eruption started in July 2012 when seismic activity slightly increased compared to the average level (Kugaenko et al., 2015). Since then, the amount and strength of earthquakes in the region around Tolbachik increased gradually. On 26 November 2012, frequent and strong earthquakes with a magnitude of 3 - 4 were measured. The seismic data gives evidence for the formation of the South Fissure (Belousov et al., 2015; Senyukov et al., 2015). On the same day, ash explosions and lava flows were reported in the area of the 1975 eruption, at the northern vents of the Tolbachinsky Dol (USGS, 2014; Senyukov et al., 2015). Lava fountained and effused from two eruptive centers, the Menyailov Vent and Naboko Vent, that are – compared to the 1975-76 eruption – located closer to Plosky Tolbachik (Gordeev et al., 2013b).

According to reports from the Institute of Volcanology and Seismology of the Far Eastern Branch of the Russian Academy of Sciences (IVS FEB RAS) and the Kamchatka Volcanic Eruption Response Team (KVERT), very fluid lava effused from two fissures along the western side of Tolbachinsky Dol and 17 - 20 km to different directions (west, south, and east) away from the fissure. Figure 5.3 shows an optical satellite image acquired by the Advanced Land Imager (ALI) on board the Earth Observing-1 (EO-1) Satellite on 22 December 2012. The image shows the lava flows

extruded to the east as well as the smoke clouds due to the ongoing eruption. Parts of the flow are already covered by snow. At least five new cones were built along the erupting fissure (USGS, 2014). From February through March 2013, continuous strombolian activity was observed at the main eruptive center, within a lava lake inside the cone (Zelenski et al., 2014).

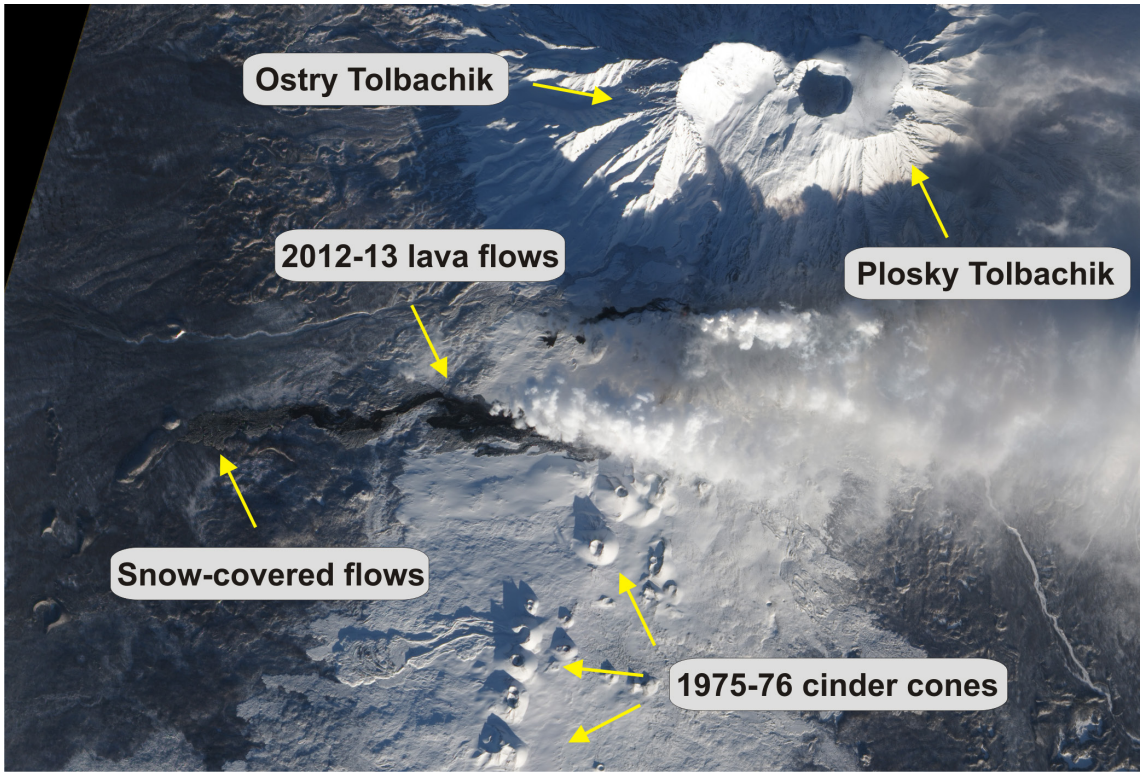

Figure 5.3 – Image showing the Tolbachik volcanic complex including the south fissure during the 2012-13 fissure eruption. The image was taken on 22 December 2012 by the ALI on board the EO-1 Satellite. Photo courtesy of Jesse Allen and Robert Simmon via Wikimedia Commons.

5.2 Mapping lava flows and measuring flow volume

This section presents the results of the double-differential TanDEM-X approach to study the lava flows emplaced during the 2012-13 Tolbachik fissure eruption. The section starts with a description of the analyzed TanDEM-X data pairs and the corresponding acquisition parameters. The newly developed data processing approach is presented in the following, showing also intermediate processing results. Subsequently, the mapping results of the lava flows extruded over time are analyzed based on the amplitude and coherence information, respectively, as well as on the DEM-differencing approach. To validate the derived results, the TanDEM-X measurements are first compared to aerophotogrammetric data. In addition, the accuracy of the repeatedly generated TanDEM-X DEMs is analyzed in reference areas where no topographic change is expected. Finally, a test with respect to utilizing the TanDEM-X data in near-real time is conducted.

5.2.1 Data description

The TanDEM-X mission recorded several data pairs before, during, and after the eruption. Regarding the TanDEM-X satellite configuration, the ascending orbit was the favorable orbit for northern latitudes before and during the eruption until August 2013 with respect to the effective baseline B_{eff} (see Chap. 2.4). After the eruption ended, the descending orbit was the favorable. As the ascending orbit only covered a small part of the extruded lava flows, data recorded in descending orbit were used in the present study, accepting the larger height of ambiguity due to very short effective baselines. Table 5.1 gives an overview of the analyzed data pairs including the main acquisition parameters.

Table 5.1 – Acquisition parameters of TanDEM-X data.

	Acquisition date	Effective baseline (m)	Height of ambiguity (m)	Average coherence	Multi-looking	Mean Incidence angle (°)
Pre-eruption	15 Nov 2012	31.6	-210.6	0.83	4 x 4	39.35
	07 Dec 2012	40.6	-162.0	0.84	4 x 4	39.36
	18 Dec 2012	41.3	-159.4	0.84	4 x 4	39.36
	09 Jan 2013	42.1	-155.9	0.84	4 x 4	39.36
	22 Feb 2013	53.8	-120.3	0.83	4 x 4	39.36
Syn-eruption	16 Mar 2013	53.5	-120.8	0.83	4 x 4	39.36
	10 May 2013	25.2	-261.1	0.84	4 x 4	39.33
	01 Jun 2013	31.8	-206.1	0.83	4 x 4	39.31
	23 Jun 2013	28.1	-233.8	0.85	4 x 4	39.31
	15 Jul 2013	37.9	-171.2	0.85	4 x 4	39.31
	17 Aug 2013	110.2	-58.9	0.81	4 x 4	39.33
	11 Oct 2013	92.9	69.5	0.81	4 x 4	39.31
	05 Dec 2013	83.7	-77.4	0.82	4 x 4	39.34
	16 Dec 2013	90.6	-71.5	0.81	4 x 4	39.33
Post-eruption	27 Dec 2013	105.3	-61.3	0.80	4 x 4	39.34
	07 Jan 2014	109.5	59.0	0.80	4 x 4	39.32
	29 Jan 2014	121.8	53.0	0.79	4 x 4	39.32
	09 Feb 2014	121.2	-53.3	0.78	4 x 4	39.34

All TanDEM-X data pairs were acquired in StripMap mode with an incidence angle between 39.31° and 39.36°. Figure 5.4 shows the filtered phase images of the pre-eruption DEM acquired on 15 November 2012 (a) and the post-eruption DEM acquired on 09 February 2014 (b). Both images are overlaid on the corresponding amplitude images. The interferograms still contain the topographic phase ϕ_{topo}, but not the reference phase ϕ_{ref}. The different effective baselines used during each image acquisition result in the different density of fringes seen in the interferograms. The fringe pattern contains minimal noise because the two radar images were acquired at the same time, which considerably increases the coherence (as noted above).

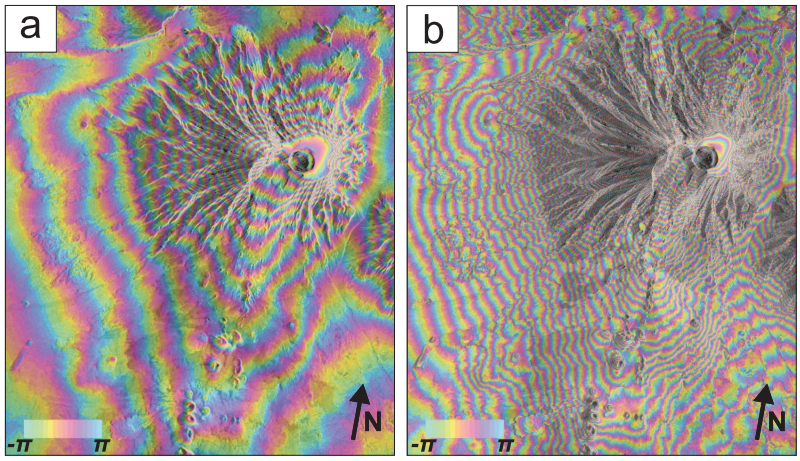

Figure 5.4 – TanDEM-X images of the Tolbachik complex including Tolbachinsky Dol. The filtered, wrapped interferograms processed from a TanDEM-X data pair acquired (a) before the eruption on 15 November 2012 and (b) after the eruption on 09 February 2014 are overlaid on the corresponding amplitude images. The difference in the number of fringes is due to the different effective baseline with which the satellite images were acquired (see Tab. 5.1).

5.2.2 Data processing

To study the emplaced lava flows of the 2012-13 eruption, the processing workflow of TanDEM-X bistatic data pairs had to be changed. This can be explained by the TanDEM-X specifications (see Sec. 2.4) combined with the geographical location of the study area in the high northern latitudes, which strongly affected the results using the processing employed for analyzing dome changes at Merapi (Sec. 4.3.1). In addition, whereas only a small area (covering only few square kilometers) was analyzed in the Merapi study, the Tolbachik lava flow field covered an area of about 40 km^2, which had to be considered during processing. Figure 5.5 shows the workflow of the developed data processing approach.

The processing can be divided into three major parts: (1) the pre-eruption DEM processing, (2) the syn- and post-eruption DEM processing, and (3) the differential DEM analysis. Parts (1) and (2) are shown in Figure 5.5. The pre-eruption DEM processing is performed only for one data pair, which was acquired on 15 November 2012 for the Tolbachik case (see Tab. 5.1). The final resulting DEM is then used as input to generate the syn- and post-eruption DEMs.

(1) Pre-eruption DEM processing
First, the pre-eruption TanDEM-X data pair is converted and used to build the interferogram with respect to the bistatic data processing considerations described in Section 2.5. The reference phase ϕ_{ref} is subtracted from the interferogram and afterwards also the reference topography phase ϕ_{topo}, resulting in the residual phase φ. In this case, SRTM3 is used for ϕ_{topo}. The residual phase φ is afterwards filtered using spatial convolution (DORIS Manual, 2009) and unwrapped using the SNAPHU approach (Chen and Zebker, 2001). The unwrapped residual phase φ_{unw} only contains the differential topography between SRTM and the pre-eruption TanDEM-X data pair as well as a planar offset together with a phase ramp. This was noted also by Poland (2014) but summed up as residual orbital phase. The planar offset and phase ramp are probably caused by approximating the effective baseline instead

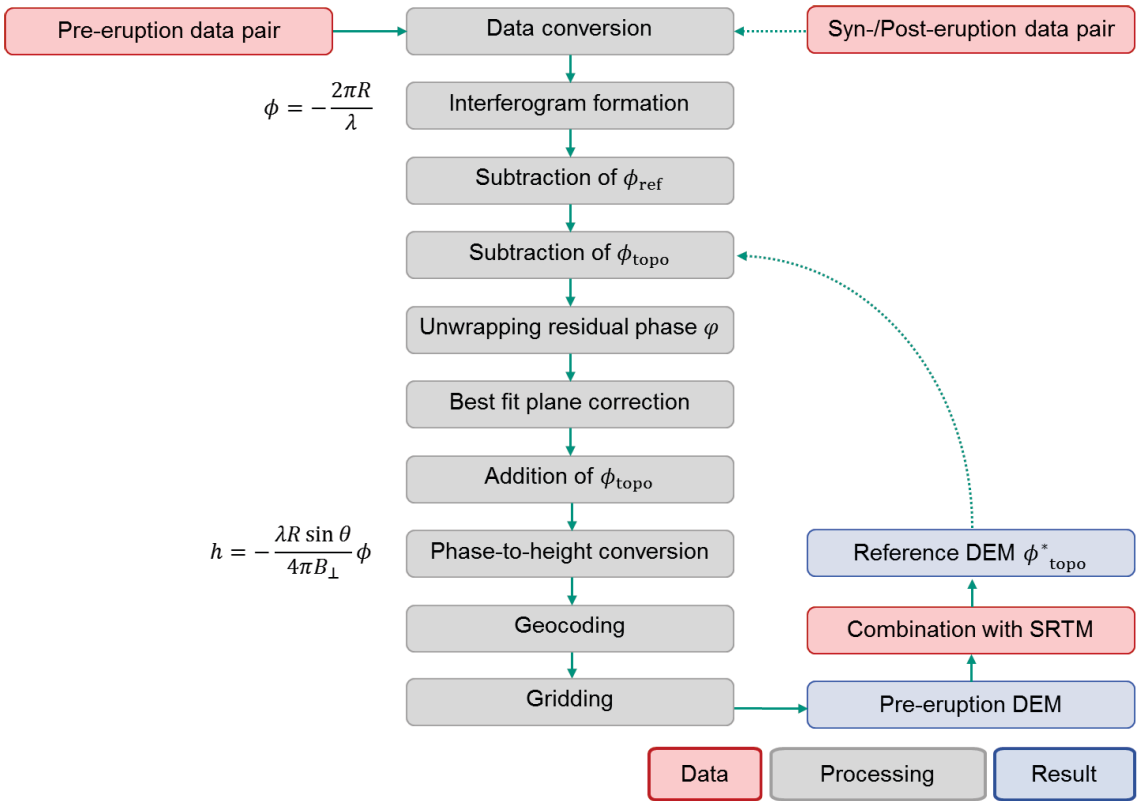

Figure 5.5 – Processing workflow for lava flow mapping at Tolbachik volcano.

of calculating it for each pixel separately (Duque et al., 2012). Assuming that this additional planar offset and phase ramp over the entire area are not real, a plane is fit using the deramping function implemented in the Automated DORIS Environment (ADORE-DORIS, Osmanoglu, 2012). Within this procedure, a first order polynomial is fit to the unwrapped residual phase φ_{unw} to account for the difference between the two DEMs and is subtracted (Fig. 5.7b). To exclude areas that are not reliable, the ramp is weighted using the coherence values. For this purpose, the coherence γ was calculated subtracting the reference phase ϕ_{ref} as well as the reference topography phase ϕ_{topo}.

Before slant-to-height conversion and geocoding using the Schwabisch algorithm implemented in DORIS, the reference topography phase ϕ_{topo} is added again to ensure a proper geocoding. The resulting pre-eruption DEM is gridded using GMT. According to the ground range spacing of 2.8 m and the azimuth spacing of 3.3 m combined with a multilooking of four in each direction, the final geocoded DEM has a pixel spacing of 11.2 m x 13.2 m, resulting in a pixel size of 147.84 m^2.

The resulting TanDEM-X-based pre-eruption DEM is then combined with an SRTM DEM to cover a larger area. This is required by DORIS to use it as input for subtracting the reference topography. Therefore, SRTM data with 90 m resolution were interpolated based on the TanDEM-X spacing. This allowed to replace the SRTM height values with TanDEM-X height values where available, based on geographic coordinates. In a final step, voids in the TanDEM-X data due to geometrical decorrelation were filled by the SRTM data. The resulting 'new' reference DEM phase is called ϕ^*_{topo} in the following to distinguish it from the SRTM reference DEM phase ϕ_{topo}.

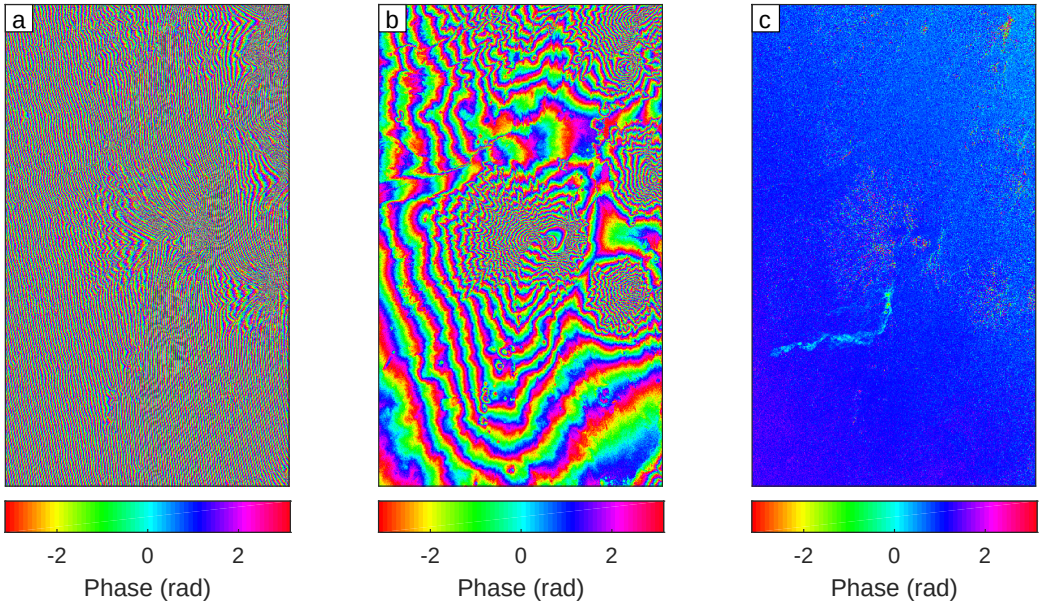

Figure 5.6 – TanDEM-X processing procedure used for differential DEM generation. The data pair acquired on 18 December 2012 is used as example. (a) Wrapped phase of complex interferogram, (b) wrapped phase after subtracting the reference phase ϕ_{ref}, (c) residual wrapped phase φ after subtracting the reference phase ϕ_{ref} and the new reference topography phase ϕ^*_{topo}.

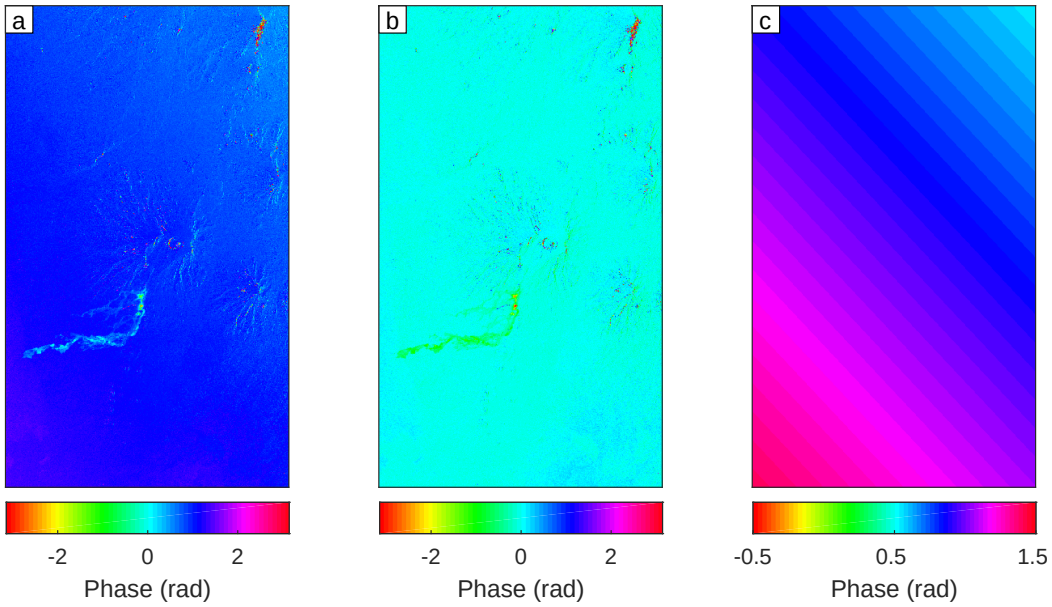

Figure 5.7 – Removal of planar function to correct phase information after unwrapping. The data pair acquired on 18 December 2012 is used again as example. (a) Filtered and unwrapped differential phase φ_{unw}, (b) phase-corrected unwrapped differential phase, (c) calculated best-fit-plane to correct unwrapped phase φ_{unw}.

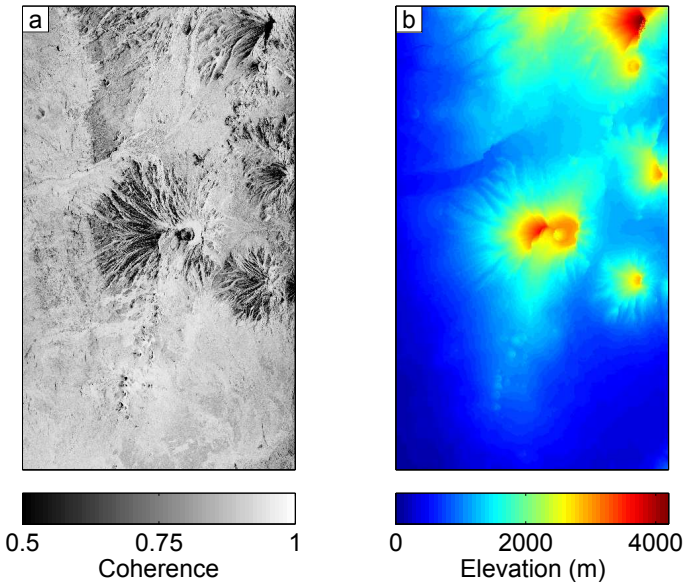

Figure 5.8 – Intermediate results of differential TanDEM-X data processing for Tolbachik. (a) shows the coherence that was used as mask for best-fit-plane subtraction. (b) shows the final DEM which consists of the residual unwrapped and deramped phase and the returned reference topography phase ϕ^*_{topo}. It is shown in the radar slant range geometry.

(2) Syn- and post-eruption DEM processing

Each syn- and post-eruption data pair listed in Table 5.1 is then processed in the same way, but using the newly generated reference DEM phase ϕ^*_{topo} to correct for topography (see Fig. 5.5). The intermediate results for a selected syn-eruption data pair acquired on 18 December 2012 are shown in Figures 5.6, 5.7, and 5.8. Also the pre-eruption DEM is processed again using ϕ^*_{topo} as reference DEM, which is required for the third part, the differential DEM analysis. It is called final pre-eruption DEM in Figure 5.9.

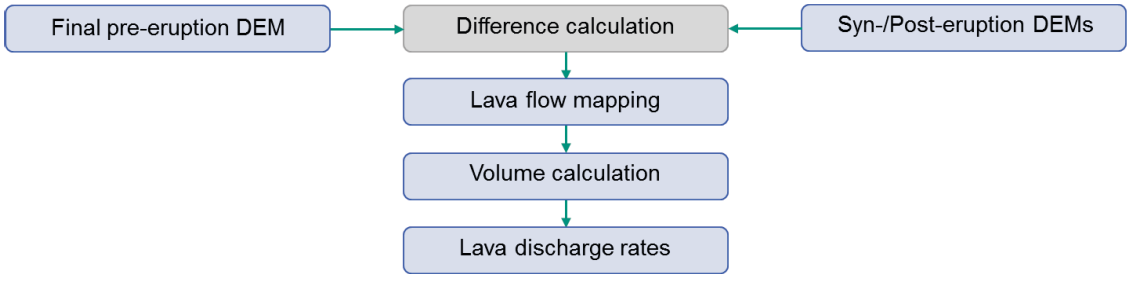

Figure 5.9 – Processing workflow for lava flow mapping at Tolbachik volcano.

(3) Differential DEM analysis

Part (3), the differential DEM analysis, is schematically shown in Figure 5.9. The final pre-eruption DEM is subtracted again from each processed syn- and post-eruption DEM in the geocoded domain. All presented results are therefore relative to this reference DEM. The DEM differencing enables the mapping of the lava

flows extruded between 15 November 2012 and the corresponding time the syn- and post-eruption data pairs were acquired (Sec. 5.2.3). In addition, the lava flow volume can be estimated (Sec. 5.2.4) and lava extrusion rates for different time intervals of the eruption can be calculated (Sec. 5.2.4).

5.2.3 Lava flow mapping

For mapping the lava flow fields formed during the 2012-13 eruption, a small area south of Plosky and Ostry Tolbachik, covering the entire new lava flow field, was selected. It measures about 150 km^2 (1.0×10^6 pixel) with an extension of 19 km (1701 pixel) from west to east and 8 km (601 pixel) from north to south. It is marked with a blue rectangle in Figure 5.10. All following analyses and results refer to this area.

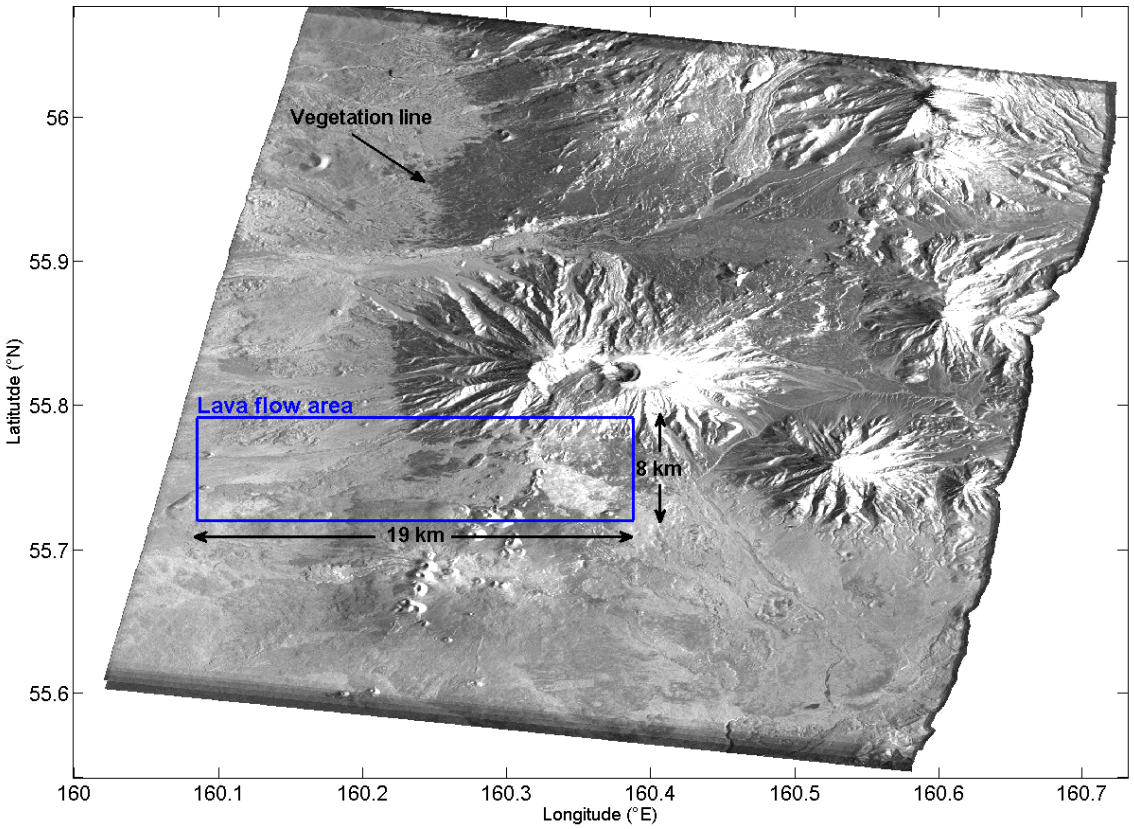

Figure 5.10 – Mean backscatter amplitude of all post-eruption data pairs. Bright values indicate a high and dark values a low backscatter. The blue rectangle shows the location and extension of the area analyzed to map the 2012-13 lava flows. Independent from the blue rectangle, a jump in the backscatter intensity from west to east at about 160.2/160.25° E is apparent in the image. It is labeled as vegetation line and will be discussed later in this section as well as in the discussion (Sec. 5.3).

5.2.3.1 Visual amplitude interpretations

As the amplitude information of the complex SAR data can rapidly be analyzed during eruptions to assist in evacuation procedures (e.g., Pallister et al., 2013) the amplitude information of the complex SAR data was analyzed first. In general, compared to analyzing the interferometric phase, the analysis of the amplitude is not

decisively faster. However, amplitude results are explicit and cannot be disrupted by unwrapping errors. They can therefore be used to confirm the interferometric results.

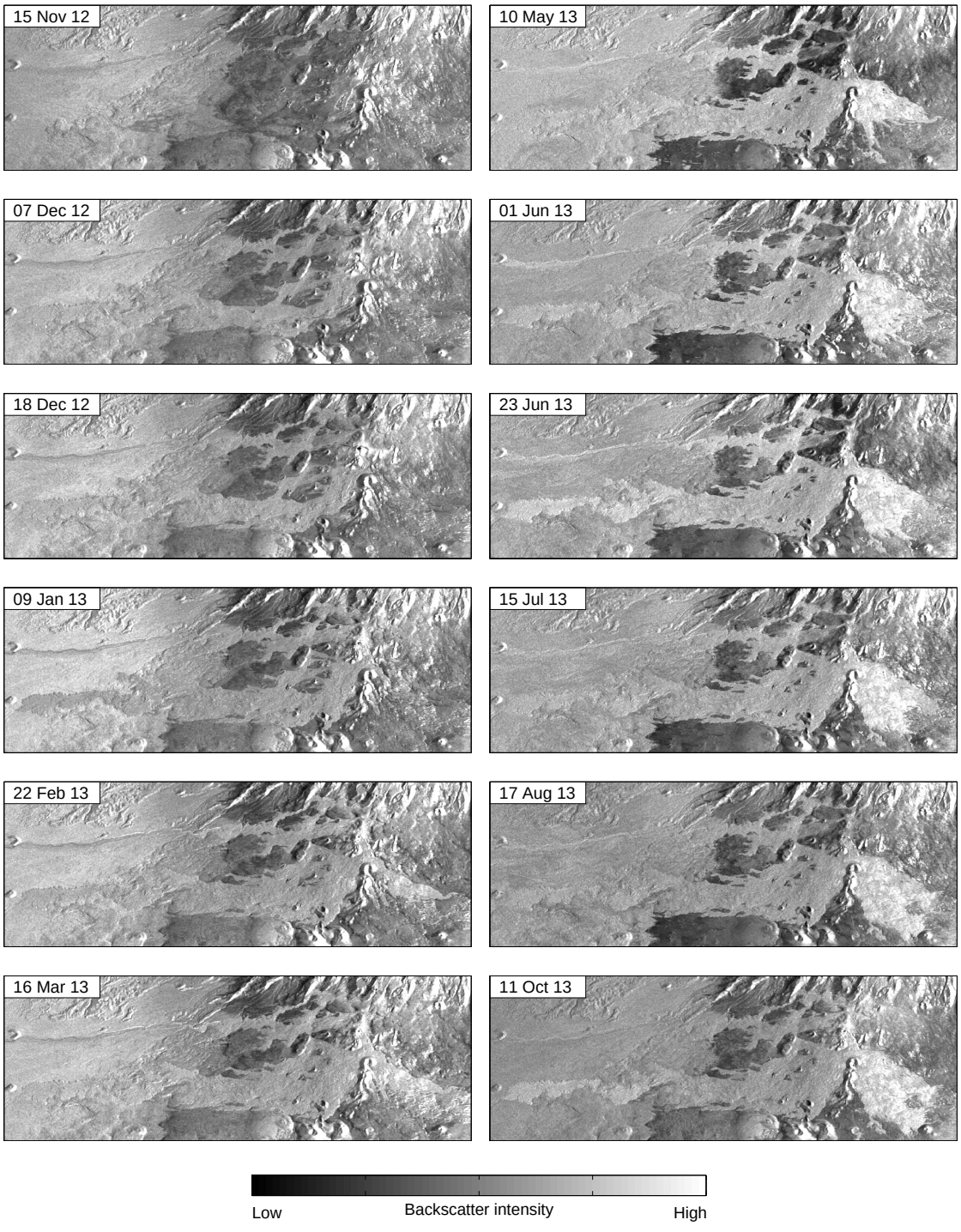

Figure 5.11 – Amplitude images: results for the pre-eruption data pair, for all syn-eruption data pairs, and for the first post-eruption data pair.

Figure 5.11 shows the geocoded intensity images of the lava flow area from selected TanDEM-X data pairs. Displayed are the results of the pre-eruption data pair acquired on 15 November 2012, of all syn-eruption data pairs acquired between

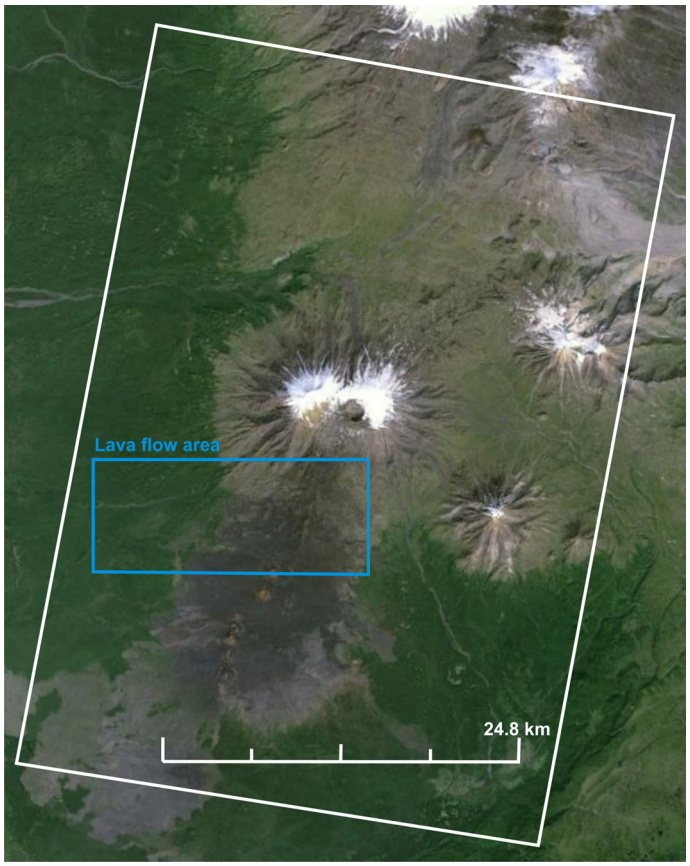

Figure 5.12 – Google Earth image showing the Tolbachik test site. The white rectangle marks the TanDEM-X scene, the blue rectangle the analyzed lava flow field. The transition from a vegetated area in the west to a barren area in the east is clearly visible.

December 2012 and August 2013, and of the first post-eruption data pair acquired on 11 October 2013. The results of the remaining post-eruption data pairs are comparable with the first post-eruption data pair and are shown in Appendix A.1 for completeness.

Whereas only older flows are visible in the reflectivity image of the pre-eruption DEM acquired on 15 November 2012, the syn-eruption images and the post-eruption image clearly show the more intense reflectivity of the new lava flows of the 2012-13 eruption. The different images give visual information about the area covered with new lava during a certain time of the eruption, i.e., which lava flow field (see Fig. 5.16) was formed when. The first selected syn-eruptive data pair was acquired on 07 December 2012 and only shows the flows effused to the south and west (Leningradskoe Lava Field and Vodopadnoe Lava Field), whereas the syn-eruptive data pair acquired on 22 February 2013 also shows the starting development of the Toludskoe Lava Field which later on effused to the east. This lava flow field is growing over time in the subsequent syn-eruption data pairs. The post-eruption data pair acquired on 11 October 2013 finally shows the entire lava flow. A temporal analysis of the development of the lava flow fields is given in Section 5.2.3.3.

In addition to the brighter reflectivity of the new lava flows, it becomes further obvious that the backscatter intensity in the western part of all images is higher than in the eastern part, separated by a sharp transition running from north to

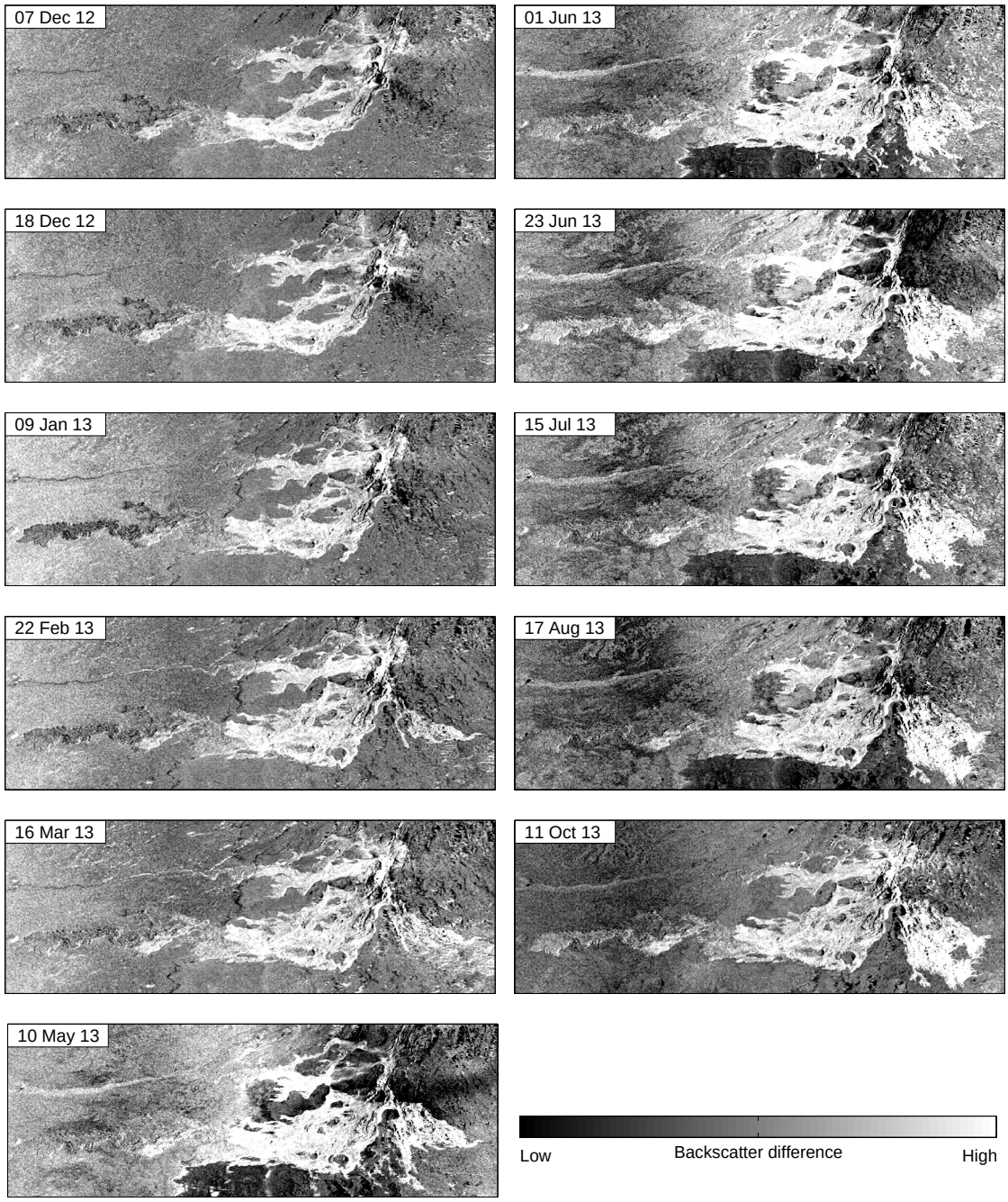

Figure 5.13 – Amplitude difference images of each syn-eruption and the first post-eruption data pair with respect to the pre-eruption data pair from 15 November 2012.

south. Its sharpness varies with the time of year the data was acquired. That is the reason why this border could not be identified using the amplitude images only. With the aid of optical images (i.e., Google Earth, see Fig. 5.12), however, it appeared as a transition in vegetation. The area to the west seems to be vegetated while the area east of the line appears barren. It is therefore labeled as vegetation line in Figure 5.10. The 'barren' area was covered by lava flows of the 1975-76 eruption which led to the absence of vegetation.

This vegetation line becomes obvious in all syn- and post-eruption data pairs and hinders the visual amplitude interpretations (Fig. 5.11). Whereas the flows that

were effused to the east are clearly distinguishable from the surrounding area, the backscatter intensity of the flows that were effused to the west resembles the backscatter of the surrounding surfaces. The flows to the west are only apparent in selected images, for instance in the 23 June 2013 amplitude image.

Since the general approach of this chapter is to map and measure lava flow extent and volume with DEM differencing, also the amplitude images were differenced. Within this process, the pre-eruption difference image is subtracted from each syn- and post-eruption amplitude image. Figure 5.13 shows the difference images for all syn-eruption data pairs and for the first post-eruption data pair acquired on 11 October 2013. The results for the remaining post-eruption images are depicted in Appendix A.2 for completeness.

Like the single amplitude images (without differencing) discussed above (Fig. 5.11), the differenced amplitude images (Fig. 5.13) clearly show the development of the lava flows over time to the different directions. It becomes further obvious that whereas the lava flows were hardly distinguishable from the surrounding surface in the single amplitude images, they are better represented in the difference images. It becomes also clear that the backscatter characteristic of the westernmost lava flow is different compared to the rest of the lava flow field.

In contrast to the single amplitude images where the vegetation line was obvious in all images, the amplitude differences only show the sharp transition during the summer months from May to August. This results from the fact that the pre-eruption data pair was acquired in winter on 15 November 2012. The vegetation in the western part therefore shows the same characteristic like in all winter images. In the summer images, however, the characteristics of the vegetation differ. Thus, the differencing of the summer images with the pre-eruption winter image leads to the sharp transition in the summer images, which also hinders to distinguish the western lava flows from the surrounding surface.

5.2.3.2 Visual coherence interpretations

The closer inspection of the coherence brings results comparable with the amplitude image interpretations. Figure 5.14 shows the coherence images of the same data pairs that were selected to interpret the amplitude images. The remaining post-eruption coherence images can be found in Appendix A.3. The newly effused lava flows are in some parts clearly visible in the syn- and the post-eruption data pairs. It becomes further obvious that the coherence differs throughout each image and from image to image. This can be caused by various factors. For the selected area, the differing coherence is most likely caused by decorrelation due to vegetation as explained in the previous section. Also snow cover may have an effect. The mean coherence for the analyzed subset ranges for all data pairs between 0.84 and 0.90. Table 5.2 shows the mean for each coherence image. The vegetation line marked in Figure 5.10 and explained above becomes also obvious in Figure 5.14, but shows a sharper transition in the summer images. In those images, the westernmost flow shows values comparable with its surrounding area.

As done before with the amplitude images, also the coherence images were differenced. The results are displayed in Figure 5.15. They are again comparable to those of the amplitude difference analysis. The newly extruded lava flows are visible in all

Table 5.2 – Statistics for the coherence images.

	Acquisition date	Mean
Pre-eruption	15 Nov 12	0.8935
	07 Dec 12	0.8862
	18 Dec 12	0.8799
	09 Jan 13	0.8741
	22 Feb 13	0.8869
Syn-eruption	16 Mar 13	0.8892
	10 May 13	0.8951
	01 Jun 13	0.8913
	23 Jun 13	0.8950
	15 Jul 13	0.8931
	17 Aug 13	0.8435
	11 Oct 13	0.8365
	05 Dec 13	0.8630
	16 Dec 13	0.8413
Post-eruption	27 Dec 13	0.8463
	07 Jan 14	0.8482
	29 Jan 14	0.8350
	09 Feb 14	0.8585
Mean	All data pairs	0.8698

coherence difference images but the westernmost flows are not easily recognizable in most of the images. Again, the vegetation transition becomes only apparent in the summer images acquired between May and August 2013. The westernmost lava flows are best displayed in the post-eruption images, again shown for the 11 October 2013 data pair as example. The remaining post-eruption difference images can be found in Appendix A.4.

Regarding both, coherence and amplitude analysis, as well as the corresponding differences between syn-/post-eruption and pre-eruption data pairs, it becomes apparent that lava flows are generally mappable from both. The vegetation obviously has a strong effect on the result and hinders a proper mapping of the lava flows in most cases. The hard transition from vegetation to barren area leads to different characteristics for areas surrounding different parts of the flow and also influences the flow backscatter itself. Differencing – especially of amplitude images – leads to better results, however, an extraction of the whole flow area is still not guaranteed. This also hinders the use of either the coherence or amplitude information to mask the lava flows, which would be helpful for further analyses (see Sec. 5.2.3.3). In addition, coherence and amplitude information do not enable measuring of the flow elevation and the revelation of the extruded volume of lava.

5.2.3.3 Interferometric results

The map on top of Figure 5.16 shows the elevation difference retrieved from the post-eruption TanDEM-X data pair acquired on 09 February 2014. The elevation difference directly reflects the lava flow thickness of all lava flows produced during the 2012-13 eruption. The outline of the lava flow shown in the map was manually digitized from the calculated elevation difference itself using ArcGIS.

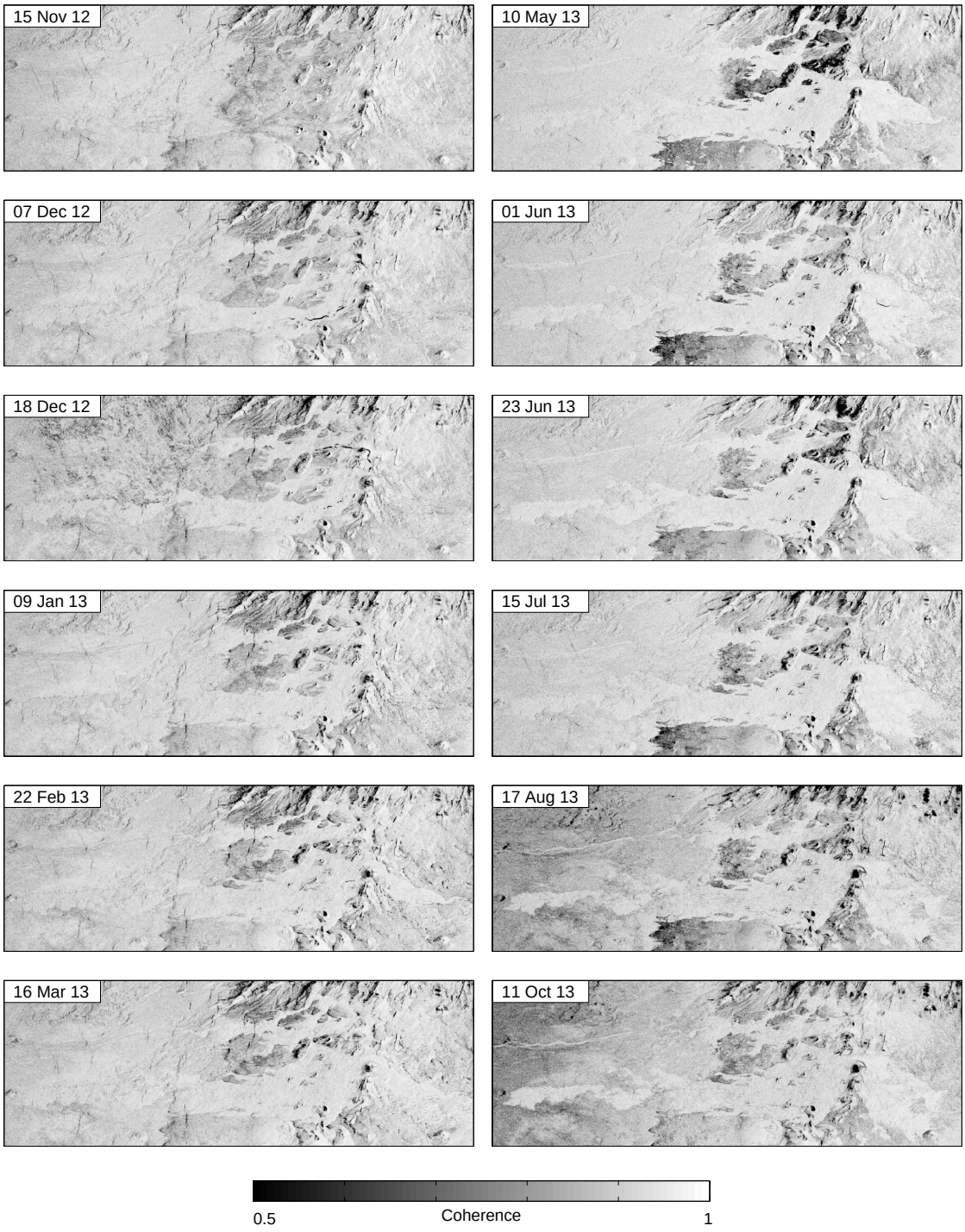

Figure 5.14 – Coherence images: results for the pre-eruption data pair, for all syn-eruption data pairs, and for the first post-eruption data pair.

The cross sections in the bottom of Figure 5.16 show the thickness at different locations of the elevation difference map. Cross section A - A' runs through the newly developed Menyailov Vent and amounts up to 70 m height. South to the Menyailov Vent, cross section B - B' crosses the Naboko Vent with a maximum height of 100 m. The lava effusion led to the development of those new cinder cones along the fissure. Cross sections C - C' crosses the Leningradskoe Lava Field close to the source with

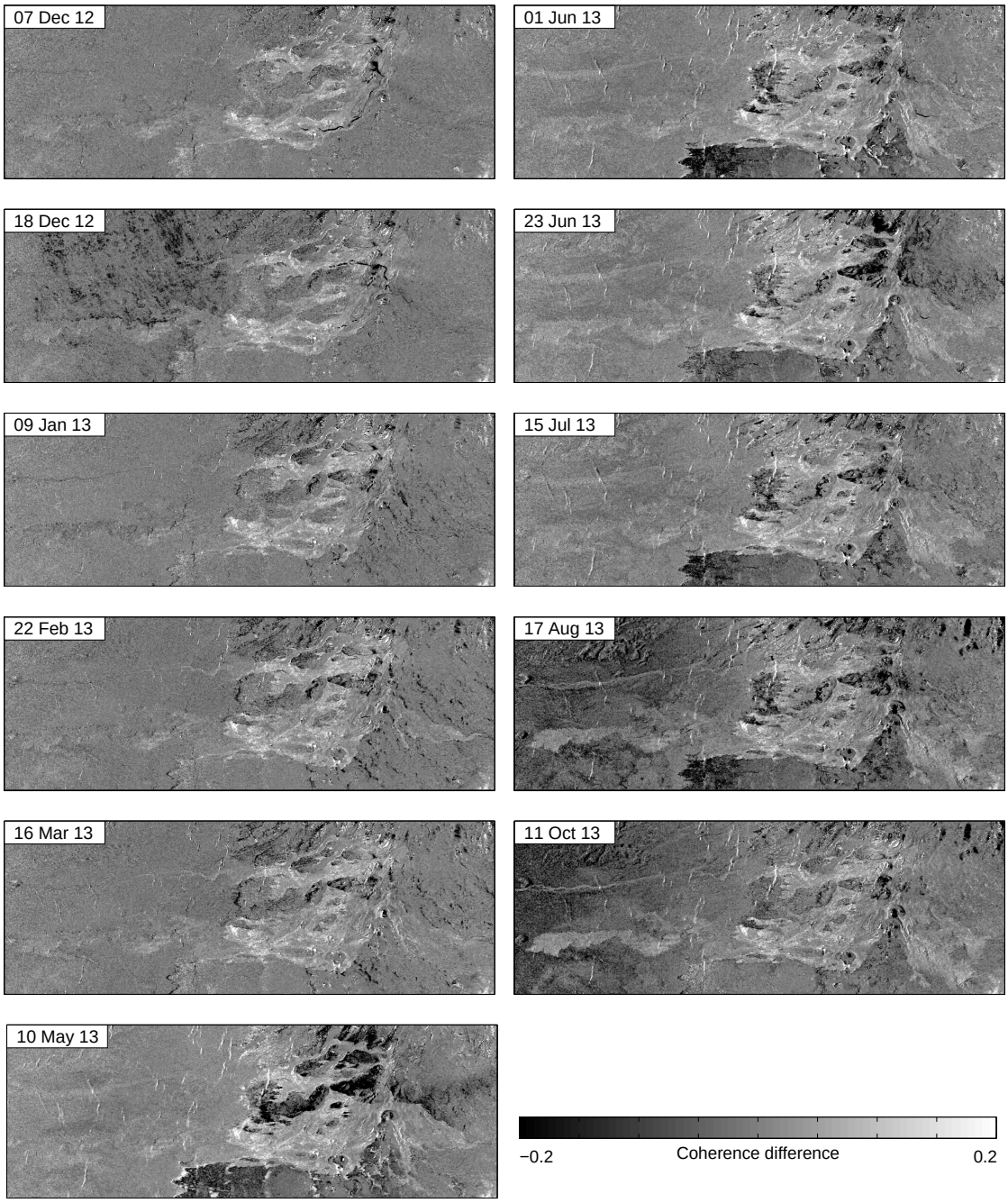

Figure 5.15 – Coherence difference images of each syn-eruption and the first post-eruption data pair with the pre-eruption data pair from 15 November 2012.

a maximum height of 65 m; cross section F - F' crosses the same flow field but in its tail, where the lava flow thickness measures only up to 20 m. Cross section D - D' shows the thickness at the chosen location of the Toludskoe Lava Field with up to 45 m. The primarily extruded Vodopadnoe Lava Field only shows a maximum elevation of 10 m (cross section E - E').

Figure 5.17 shows how the lava fields developed over time using all syn-eruptive TanDEM-X data pairs listed in Table 5.1 as well as the first post-eruption data pair acquired on 11 October 2013. The results for the remaining post-eruption data pairs are displayed in Appendix A.5 for completeness. All results are relative to

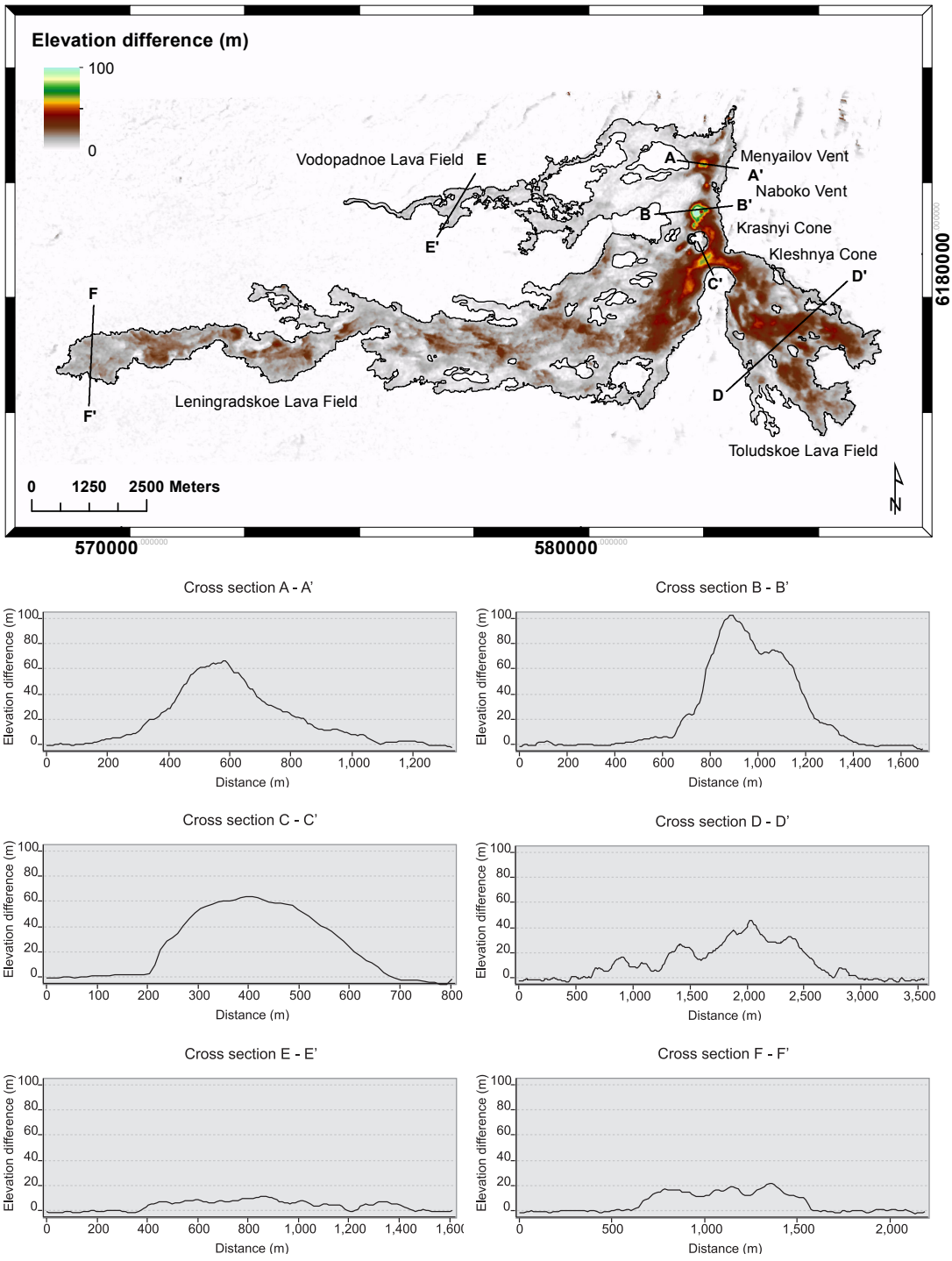

Figure 5.16 – Differencing the pre-eruption DEM (15 November 2012) and the post-eruption DEM (09 February 2014) results in an elevation map from which lava flow thickness and volume can be calculated. The image on top shows the lava flow extent outlined in black. The data was georeferenced to UTM zone 57 N. Lava thickness is indicated by color, and thickness profiles are calculated along each labeled black line intersecting the lava flow. Profiles A - A' (Menyailov Vent) and B - B' (Naboko Vent) indicate the locations of the two highest cinder cones close to 100 m in height built during the eruption. Profiles C - C', D - D', E - E', and F - F' show the flow thickness of the different lava flow fields. The names of the lava flow fields are based on Belousov et al. (2015).

the pre-eruption DEM from data acquired on 15 November 2012. The first three syn-eruptive data pairs were acquired on 07 and 18 December 2012 and on 09 January 2013. It becomes obvious that the lava flows effused during this phase only flew to the south and to the west, forming the Vodopadnoe as well as the Leningradskoe Lava Fields. This fits in well with other studies conducted to analyze the 2012-13 eruption: according to Dvigalo et al. (2014), lava was extruded mainly to the south and west at the beginning of the eruption, the Vodopadnoe Lava Field was mainly formed during the first two days. Also the Leningradskoe Lava Field started forming during the first eruptive episode. It becomes apparent that the main area of the Leningradskoe Lava Field was already defined by 22 February 2013. Later material flowing in the same direction was accumulated on top of the already existing flows.

According to the TanDEM-X-based elevation differences (Fig. 5.17), the Toludskoe Lava Field started forming between 18 December 2012 and 22 February 2013. It continued to grow till the end of the eruption on 27 August 2013. This is also in good agreement with Dvigalo et al. (2014), who mention that the first flow was poured eastwards around the old Kleshnya Cone on 25 December 2012. The difference images from 11 October 2013 until 09 February 2014 (Fig. 5.17 and A.5) all show the same shape regarding the lava flow fields as all data pairs were acquired after the end of the eruption. They were analyzed in the present study to prove the repeatability of the final lava flow extent and the lava flow volume.

How the Leningradskoe Lava Field and the Toludskoe Lava Field formed over time can also be seen in the cross sections shown in part (b) of Figure 5.18. Part (a) of the Figure shows the location of the cross section, passing both flow fields from west to east, close to the source. The flows went to the east and west here, and not directly to the south, which was hindered by the old Kleshnya Cone (see Fig. 5.16) which was built in a former eruption. This is a nice example of how topographic characteristics influence flow paths. From the cross sections shown in (b), it becomes clear that both flow fields grew until 10 May 2013 in the depicted location.

5.2.4 Lava flow area and volume calculation

The entire area extent of the lava flows could not be retrieved from the coherence or from the amplitude information of the TanDEM-X data pairs for the reasons discussed in Sections 5.2.3.1 and 5.2.3.2. Particularly the western part of the Leningradskoe Lava Field could not be clearly distinguished in most of the data pairs from the surrounding area. To be still independent of other data sources (e.g., optical imagery), the area extent of the lava flow fields was directly retrieved from the elevation difference maps. Therefore, all post-eruption elevation difference maps were used to build a mean elevation difference map which allowed to generate a mask (Fig. 5.19, lower left image). To correct for minor errors, e.g., due to vegetation or geometrical decorrelation, only significant changes in elevation were considered. Therefore, and to ensure that only the flow area was considered to calculate the area extent at each time, pixels with an elevation smaller or equal 2 m were additionally masked out. The mask then only included the flow area itself and was applied to each data pair separately. The generated mask as well as its application to a syn-eruption data pair acquired in summer and a post-eruption data pair acquired in autumn are shown in Figure 5.19. From the figure, the influence of the vegetation in the western part of the image is obvious again, highlighting the need to properly mask the flow area for calculating lava flow volume and area extent.

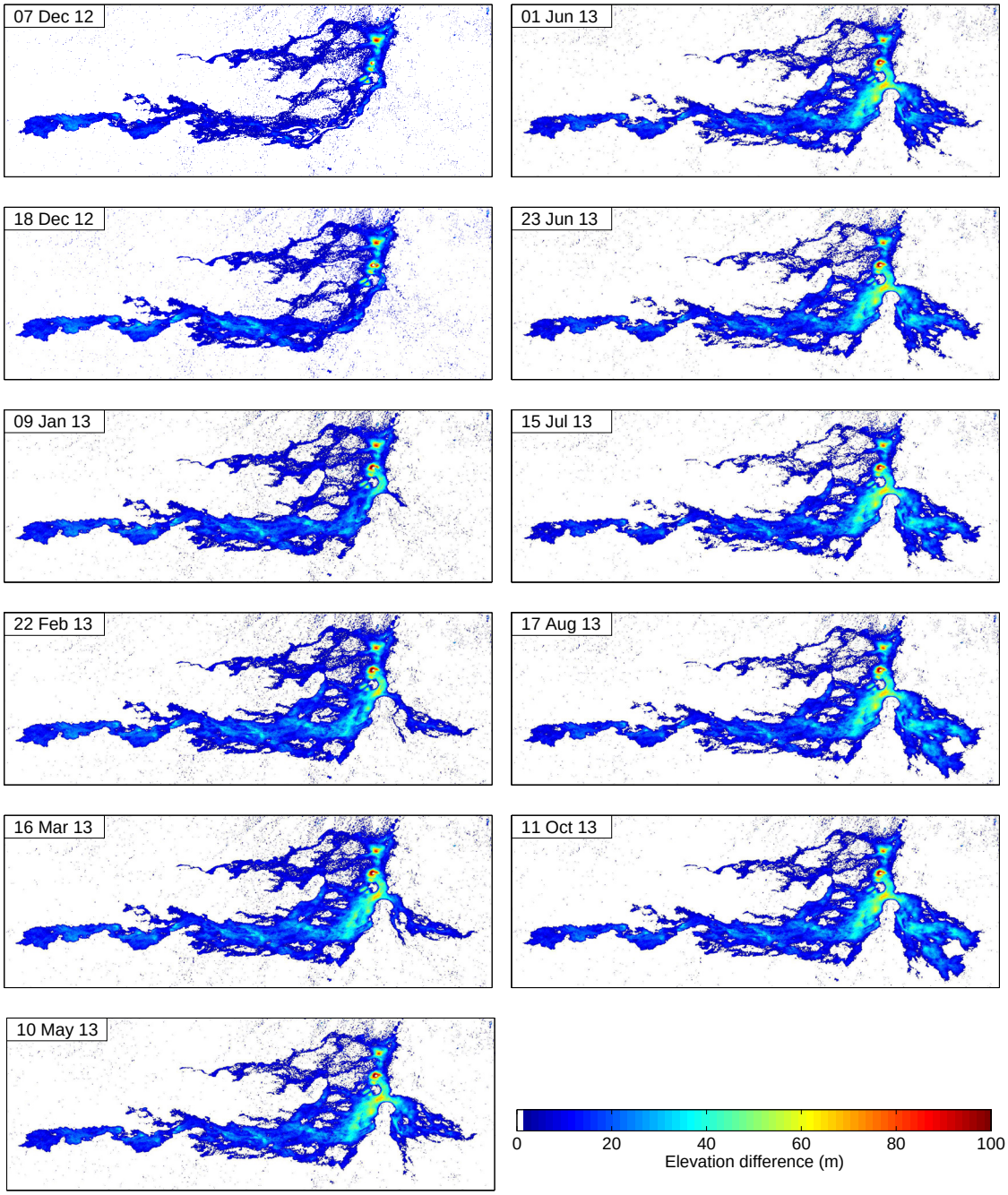

Figure 5.17 – Differential TanDEM-X results showing how the lava flows developed over time. The colors show the elevation difference between the date specified in each elevation difference and the final pre-eruption DEM.

The area covered by lava flows was identified on a pixel basis and then multiplied by the pixel size (147.84 m^2). The elevation difference of each pixel multiplied with its size results in the lava flow volume. Table 5.3 shows the calculated lava flow area and the corresponding lava flow volume. The time interval covers the days between two consecutive data pairs, with the first time interval for the 07 December 2012 data pair referring to the beginning of the eruption on 27 November 2012. The time interval combined with the lava flow volume results in the lava extrusion rate,

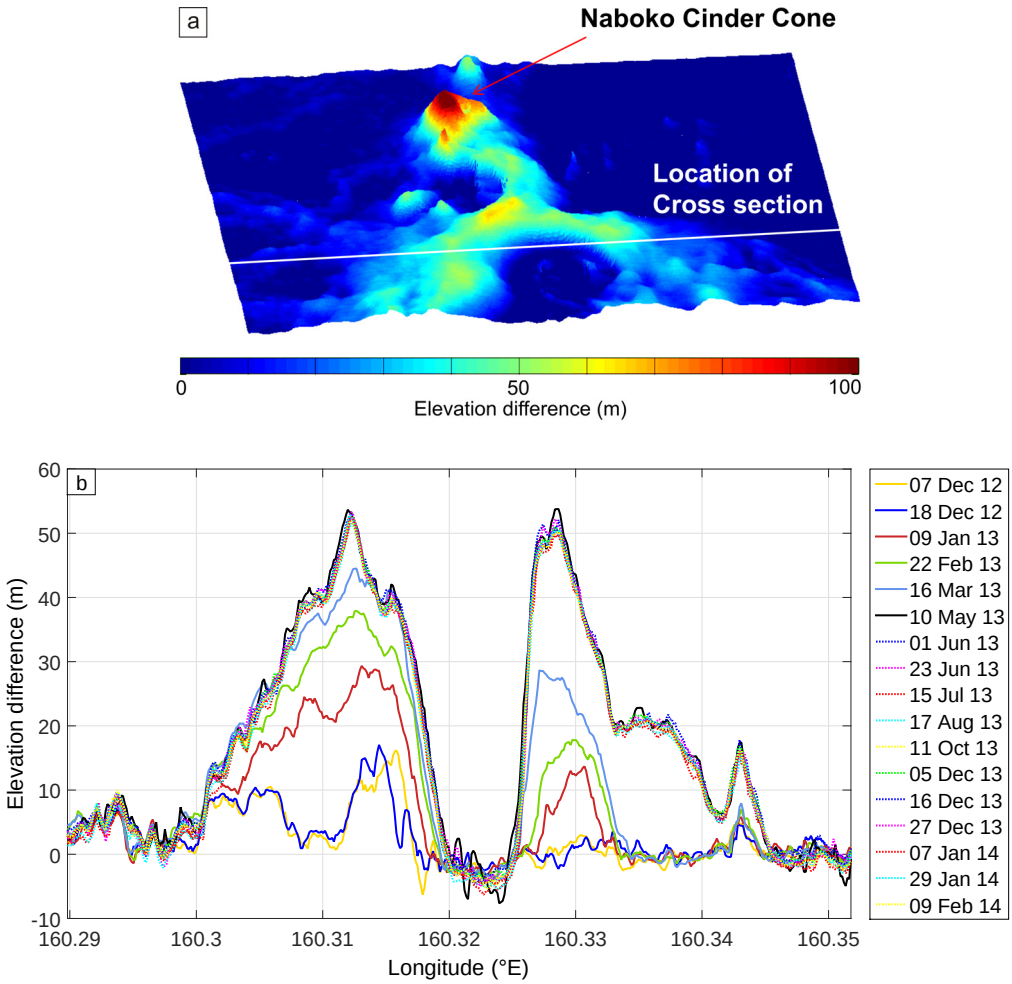

Figure 5.18 – Lava thickness over time for the Leningradskoe and Toludskoe Lava Fields close to the Naboko Cinder Cone. (a) shows a 3-D model of the Naboko Cinder Cone and the area south to it, seen from the south. The white line shows the location of the cross sections presented in (b). It extends to about 4 km and shows the elevation differences (lava flow thickness) at 55.76° E for each time interval.

which is only calculated until 17 August 2013, as the eruption ended at the end of August 2013.

The calculated area extent of new lava increased substantially in the beginning of the eruption from 07 December 2012 until 16 March 2013. However, the area related to the period between May and July 2013 is smaller than calculated for 16 March 2013. The post-eruption DEM values are again increased showing comparable values. For calculating the mean maximal extension of the area covered with lava, all estimates from 11 October 2013 until 09 February 2014 were used, resulting in 35.91 km^2. A comparable effect becomes apparent with respect to the lava flow volume. The values calculated between 10 May and 15 July 2013 show a smaller value than calculated before, however, the volume revealed by 17 August and 11 October 2013 is increased again. Calculating the final lava flow volume using all post-eruption data pairs results in 0.53 km^3. The lava extrusion rate was with 247.92 m^3/s very high in the beginning of the eruption (until 07 December 2012). The zero values calculated between 10 May 2013 and 15 July 2013 are due to the calculated decrease in lava flow volume. The results will be discussed later in this chapter.

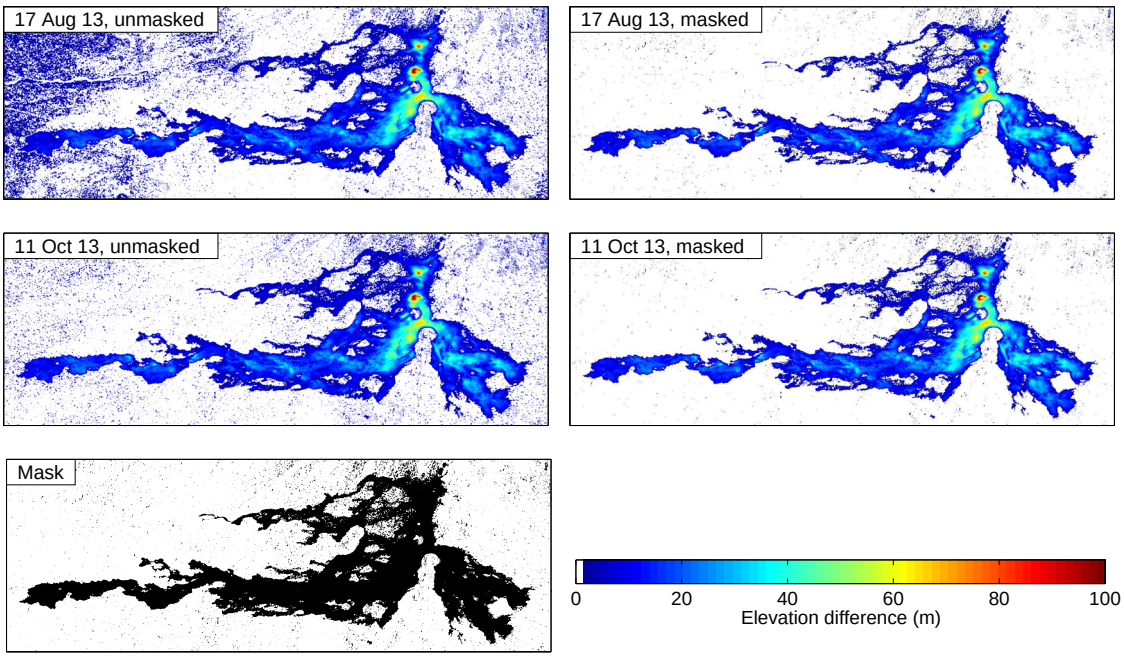

Figure 5.19 – Development of a mask to extract the lava flow area. The figures show the application of the mask (lower left image) to a summer data pair acquired on 17 August 2013 and an autumn data pair acquired on 11 October 2013.

Table 5.3 – Lava flow area, lava flow volume, and lava extrusion rates calculated using TanDEM-X elevation differences. The first dashed line separates syn-eruptive and post-eruptive results. All results are with respect to the start of the eruption on 27 November 2012.

Acquisition date	Time interval (Days)	Total lava flow area (km^2)	Total lava flow volume (km^3)	Lava extrusion rate (m^3/s)
07 Dec 2012	10	22.90	0.21	247.92
18 Dec 2012	11	25.82	0.29	81.49
09 Jan 2013	22	27.87	0.35	31.99
22 Feb 2013	44	31.74	0.42	18.97
16 Mar 2013	22	32.29	0.45	13.26
10 May 2013	55	30.22	0.42	0
01 Jun 2013	22	30.38	0.42	0
23 Jun 2013	22	29.81	0.42	0
15 Jul 2013	22	29.50	0.42	0
17 Aug 2013	33	32.73	0.47	5.02
11 Oct 2013	55	34.13	0.49	
05 Dec 2013	55	37.03	0.54	
16 Dec 2013	11	35.95	0.53	
27 Dec 2013	11	36.47	0.53	
07 Jan 2014	11	35.70	0.52	
29 Jan 2014	22	35.70	0.52	
09 Feb 2014	11	36.37	0.53	
Mean (only post-eruptive)		35.91	0.53	

5.2.5 Uncertainty estimation

To validate the accuracy of the presented results, four reference areas were chosen (see Fig. 5.20). All areas are included in the analyzed lava flow area, but are situated outside of the 2012-13 lava flows and therefore should not contain any topographic change due to the 2012-13 eruption. The uncertainty analysis was conducted without utilizing the mask presented in Figure 5.19.

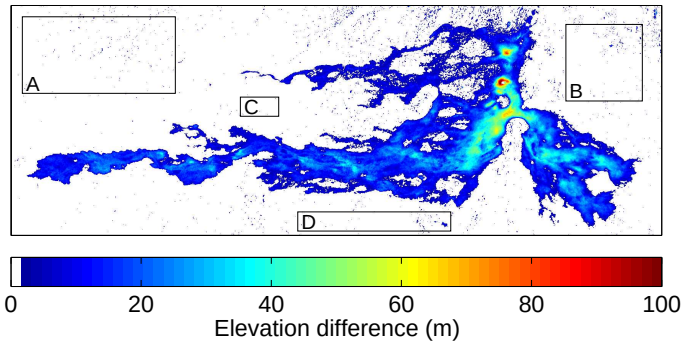

Figure 5.20 – Mean elevation of all post-eruption difference images. The black rectangles labeled with A to D show the areas that were analyzed to estimate the uncertainty of the elevation differences.

Table 5.4 – Extension of reference areas used for estimating the uncertainty of the difference maps and the lava flow volume calculations.

	Extension	
	Pixel	km^2
Area A	200 x 400 (80,000)	11.827
Area B	200 x 200 (40,000)	5.914
Area C	70 x 200 (14,000)	2.070
Area D	50 x 380 (19,000)	2.809

The areas are located around the lava flow fields. They show different characteristics and are also different in size (Tab. 5.4), which is caused by the fact that the space around the lava flow where no topographic change is expected is limited. Area A with 80,000 square pixels is the largest area. It lies north of the western end of the Leningradskoe Lava Field and is covered by vegetation. The second area, area B, is located east of the Menyailov and Naboko Vents and is barren. However, it is influenced by geometrical decorrelation as it is located on the flanks of Plosky Tolbachik. Area C is located between the Vodopadnoe and the Leningradskoe Lava Fields and is vegetated like area A. Finally, area D is south of the center of the Leningradskoe Lava Field and is barren like area B. However, it is prone to geometrical decorrelation caused by the presence of cinder cones built during the 1975-76 eruption.

To validate the generated difference maps, Figure 5.21 shows histograms of the syn- and post-eruption elevation differences for each of the reference areas. For a better

presentation of the results, the data were divided into three classes: (1) syn-eruption I, which includes the data pairs between 07 December 2012 and 16 March 2013, (2) syn-eruption II, that includes all data pairs between 10 May 2013 and 17 August 2013, and (3) post-eruption, that includes all data pairs between 11 October 2013 and 09 February 2014. The separation between syn-eruption I and II was chosen to separate winter from summer scenes. The different influences are further commented in the discussion (Sec. 5.3).

In general, three different quantities can be distinguished to analyze the difference maps. The first one is the systematic, timely variable offset $\overline{\mu}$, the second one is the reproducibility of the difference maps σ_μ (accuracy), and the third is the standard deviation σ (precision) of the single data pairs. Quantity 1 and 2 are given in Table 5.5, quantity 3 is given in Tables 5.6 to 5.9 for each difference map and each difference area. They will be described in the following with respect to the histograms shown in Figure 5.21.

Table 5.5 – Statistical analysis of height values in the chosen reference areas.

	All		Syn-eruption I		Syn-eruption II		Post-eruption	
	Mean $\overline{\mu}$ (m)	Std. σ_μ (m)	Mean $\overline{\mu}$ (m)	Std. σ_μ (m)	Mean $\overline{\mu}$ (m)	Std. σ_μ (m)	Mean $\overline{\mu}$ (m)	Std. σ_μ (m)
Area A	-0.03	1.80	-0.34	1.75	1.12	2.11	-0.63	1.62
Area B	0.13	1.69	0.65	1.62	-0.34	1.85	0.10	1.63
Area C	-0.45	1.32	0.28	1.36	-1.38	1.52	-0.31	1.14
Area D	-0.49	1.72	0.54	1.67	-2.01	2.05	-0.13	1.52
All areas	-0.21	1.63	0.28	1.60	-0.65	1.88	-0.24	1.48

Table 5.6 – Statistics for reference area A.

	Acquisition date	Min (m)	Max (m)	Mean μ (m)	Standard deviation σ (m)
	07 Dec 12	-13.69	11.57	-0.64	1.73
	18 Dec 12	-10.42	12.65	0.55	1.93
Syn-eruption I	09 Jan 13	-11.07	11.64	-0.57	1.72
	22 Feb 13	-15.05	10.50	-0.42	1.70
	16 Mar 13	-15.09	11.97	-0.59	1.69
	10 May 13	-14.51	13.16	0.41	2.10
	01 Jun 13	-12.71	14.10	1.07	2.15
Syn-eruption II	23 Jun 13	-16.69	13.56	1.53	2.22
	15 Jul 13	-14.66	12.10	0.85	2.08
	17 Aug 13	-11.57	11.74	1.75	2.00
	11 Oct 13	-11.97	9.49	-0.39	1.55
	05 Dec 13	-9.55	10.91	-0.47	1.61
	16 Dec 13	-11.30	9.50	-0.48	1.61
Post-eruption	27 Dec 13	-11.26	8.99	-0.73	1.62
	07 Jan 14	-12.23	10.05	-0.72	1.61
	29 Jan 14	-10.41	11.28	-0.56	1.64
	09 Feb 14	-14.02	9.30	-1.04	1.69
Mean		-12.72	11.32	-0.03	1.80

Table 5.7 – Statistics for reference area B.

	Acquisition date	Min (m)	Max (m)	Mean μ (m)	Standard deviation σ (m)
	07 Dec 12	-42.19	37.02	0.56	1.58
	18 Dec 12	-28.38	39.65	0.68	1.62
Syn-eruption I	09 Jan 13	-30.17	34.00	0.63	1.54
	22 Feb 13	-27.66	38.52	0.67	1.71
	16 Mar 13	-24.42	48.89	0.71	1.64
	10 May 13	-35.21	30.63	-0.32	1.97
	01 Jun 13	-29.66	33.08	-0.14	1.82
Syn-eruption II	23 Jun 13	-30.46	32.65	-0.76	1.93
	15 Jul 13	-35.22	40.01	-0.39	1.79
	17 Aug 13	-31.92	38.47	-0.08	1.72
	11 Oct 13	-31.99	36.73	-0.12	1.65
	05 Dec 13	-30.76	39.13	0.49	1.67
	16 Dec 13	-29.46	40.99	-0.03	1.60
Post-eruption	27 Dec 13	-30.76	41.40	0.25	1.63
	07 Jan 14	-28.88	40.87	0.04	1.67
	29 Jan 14	-34.34	24.44	-0.17	1.66
	09 Feb 14	-31.27	30.22	0.22	1.56
Mean		-31.34	36.87	0.13	1.69

Table 5.8 – Statistics for reference area C.

	Acquisition date	Min (m)	Max (m)	Mean μ (m)	Standard deviation σ (m)
	07 Dec 12	-7.00	6.91	0.03	1.38
	18 Dec 12	-5.72	7.34	0.48	1.50
Syn-eruption I	09 Jan 13	-6.82	6.04	0.00	1.34
	22 Feb 13	-5.16	6.37	0.44	1.30
	16 Mar 13	-6.76	6.99	0.46	1.26
	10 May 13	-8.37	5.54	-1.09	1.57
	01 Jun 13	-9.33	3.90	-1.95	1.50
Syn-eruption II	23 Jun 13	-9.19	6.33	-1.35	1.65
	15 Jul 13	-8.11	4.41	-1.68	1.54
	17 Aug 13	-7.12	5.77	-0.82	1.34
	11 Oct 13	-7.28	4.87	-1.19	1.16
	05 Dec 13	-6.12	5.80	0.04	1.15
	16 Dec 13	-6.47	5.94	-0.15	1.16
Post-eruption	27 Dec 13	-6.36	4.96	-0.19	1.11
	07 Jan 14	-6.15	4.05	-0.40	1.14
	29 Jan 14	-5.57	4.90	-0.23	1.15
	09 Feb 14	-5.43	5.33	-0.01	1.14
Mean		-6.88	5.61	-0.45	1.32

Table 5.9 – Statistics for reference area D.

	Acquisition date	Min (m)	Max (m)	Mean μ (m)	Standard deviation σ (m)
Syn-eruption I	07 Dec 12	-16.24	24.56	0.21	1.65
	18 Dec 12	-16.11	25.16	0.70	1.73
	09 Jan 13	-17.42	24.18	0.41	1.69
	22 Feb 13	-22.71	24.55	0.71	1.69
	16 Mar 13	-25.01	26.73	0.66	1.58
Syn-eruption II	10 May 13	-18.94	18.38	-1.26	2.32
	01 Jun 13	-33.15	23.04	-1.94	2.11
	23 Jun 13	-43.75	26.92	-2.41	2.43
	15 Jul 13	-21.90	17.86	-2.85	1.91
	17 Aug 13	-21.52	20.69	-1.60	1.47
Post-eruption	11 Oct 13	-20.23	21.98	-0.91	1.52
	05 Dec 13	-17.67	34.26	0.25	1.63
	16 Dec 13	-18.13	25.56	-0.03	1.52
	27 Dec 13	-24.07	23.87	0.06	1.51
	07 Jan 14	-24.52	25.42	-0.27	1.54
	29 Jan 14	-19.38	19.74	-0.11	1.42
	09 Feb 14	-25.76	19.67	0.11	1.47
Mean		-22.74	23.68	-0.49	1.72

Syn-eruption I. Regarding the histograms of the syn-eruption I scenes, it becomes obvious that the values of all elevation differences are centered around zero in all reference areas, which means that $\overline{\mu}$ is equal to 0. This can also be seen by the mean $\overline{\mu}$ given in Table 5.5. It ranges for the syn-eruption I data between -0.34 and 0.65 m. Regarding the reproducibility σ_μ, only the histogram of the elevation difference for 18 December 2012 differs slightly for reference area A (Fig. 5.21a), indicating the high reproducibility of the syn-eruption I data pairs. The standard deviation σ of all difference maps ranges between 1.26 m and 1.93 m (see Tables 5.6 to 5.9).

Syn-eruption II. The histogram values of the syn-eruption II scenes differ between the reference areas, but the scenes show a comparable behavior for each reference area. The offset $\overline{\mu}$ for reference area A with 1.12 m is slightly positive, and negative for all other reference areas, with the largest $\overline{\mu}$ for reference area D with -2.01 m. Regarding the reproducibility σ_μ, only the elevation difference of the 17 August 2013 data pair sticks out, especially for reference areas A and D. σ ranges for all data pairs between 1.34 and 2.43 m (Tab. 5.6 to 5.9).

Post-eruption. Regarding the post-eruption scenes, all differences are again centered around zero. Small negative offsets occur for all differences in reference area A, but with a mean offset $\overline{\mu}$ of -0.63 m smaller than for the syn-eruption II differences. The strongest deviation occurs here for the 11 October 2013 difference, which is slightly shifted to negative values in reference areas C and D. The standard deviation σ of the single difference maps ranges from 1.11 m to 1.69 m.

With respect to all reference areas, it becomes obvious that the elevation differences are mostly centered around zero. In addition, the reproducibility σ_μ is with 1.63 m for all reference areas and all elevation difference maps generally very high.

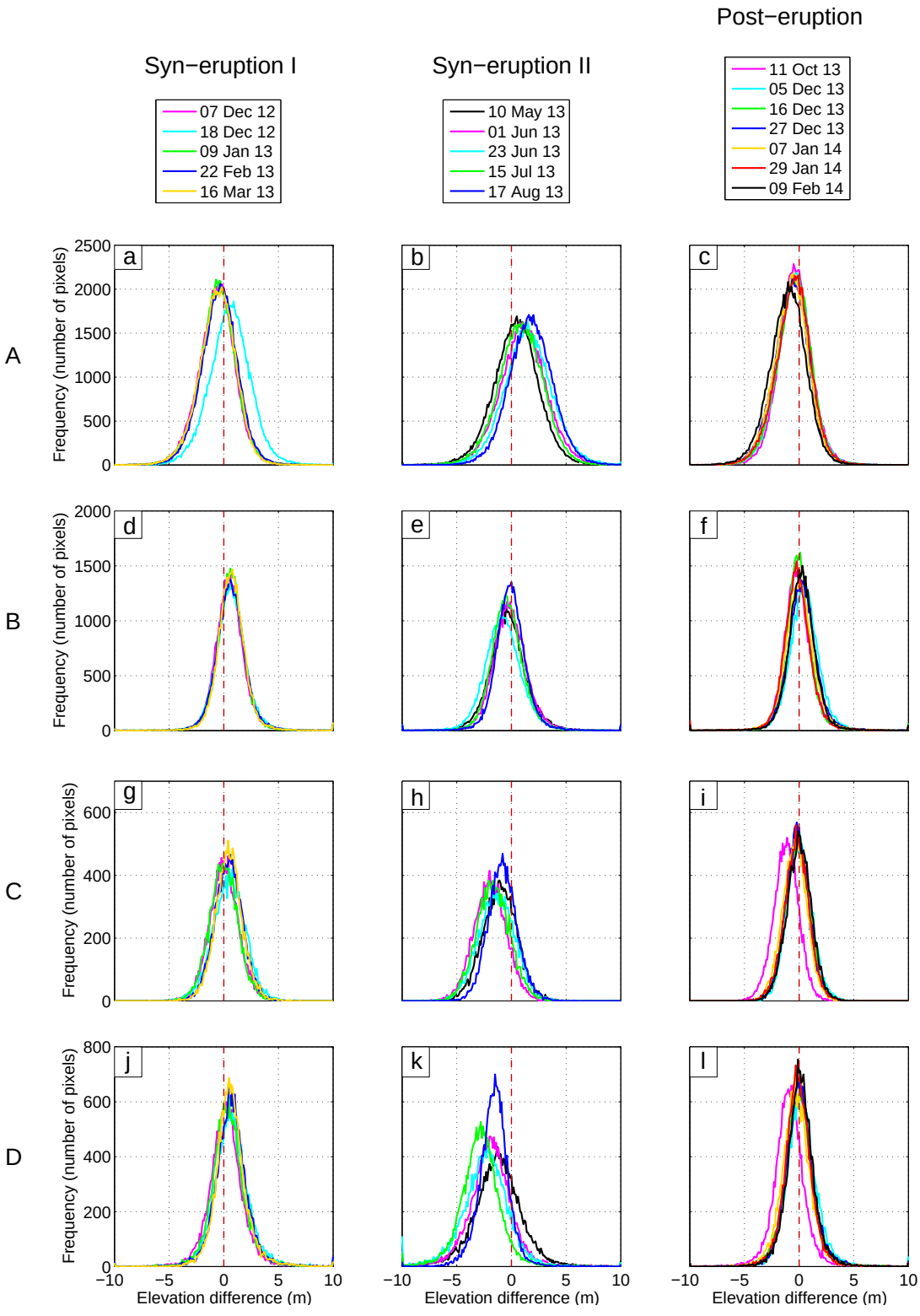

Figure 5.21 – Distribution of elevation difference values in reference areas. The first row shows the histograms for area A (a-c), the second for area B (d-f), the third for area C (g-i) and the fourth for area D (j-l). The first column shows the histograms for the elevation differences between 07 December 2012 and 16 March 2013 (syn-eruption I), the second shows the histograms for the elevation differences between 10 May 2013 and 17 August 2013 (syn-eruption II), and the third finally shows the histograms for the elevation differences between 11 October 2013 and 09 February 2014 (post-eruption). Reference is the data pair from 15 November 2012.

To analyze also the uncertainty of the volume estimates, the volume of each reference area was further calculated for each difference map using the same methodology as used for calculating the lava flow volume in Section 5.2.4. Figure 5.22 presents the results. The calculated volume for all reference areas and all difference maps is given in Table 5.10. Thereby, an independent error value was given for each volume and calculated for each time interval (see Tab. 5.3). All volumes of the four reference areas were then summed separately for each difference map. From this result, the total volume for all reference areas of all difference maps was calculated with -0.0017 km^3 and results in a standard deviation of 0.0073 km^3. This leads to a final lava flow volume of $0.53 \pm 0.0073\,km^3$.

Table 5.10 – Volume calculation in cubic kilometers for reference areas A - D.

	Acquisition date	Volume (km^3) Reference area				
		A	B	C	D	$\sum$
	07 Dec 2012	-0.0075	0.0032	0.0001	0.0006	-0.0036
	18 Dec 2012	0.0065	0.0040	0.0010	0.0019	0.0133
Syn-eruption I	09 Jan 2013	-0.0066	0.0037	0	0.0011	-0.0018
	22 Feb 2013	-0.0049	0.0039	0.0009	0.0019	0.0018
	16 Mar 2013	-0.0069	0.0041	0.0009	0.0018	-0.0001
Mean		-0.0039	0.0038	0.0006	0.0014	0.0019
	10 May 2013	0.0049	-0.0019	-0.0022	-0.0034	-0.0025
	01 Jun 2013	0.0126	-0.0008	-0.0039	-0.0052	0.0026
Syn-eruption II	23 Jun 2013	0.0179	-0.0044	-0.0027	-0.0065	0.0043
	15 Jul 2013	0.0099	-0.0022	-0.0033	-0.0077	-0.0033
	17 Aug 2013	0.0205	-0.0005	-0.0016	-0.0043	0.0141
Mean		0.0132	-0.0020	-0.0027	-0.0054	0.0031
	11 Oct 2013	-0.0045	-0.0007	-0.0024	-0.0024	-0.0100
	05 Dec 2013	-0.0055	0.0029	0.0001	0.0007	-0.0018
	16 Dec 2013	-0.0056	-0.0002	-0.0003	-0.0001	-0.0061
Post-eruption	27 Dec 2013	-0.0085	0.0015	-0.0004	0.0002	-0.0072
	07 Jan 2014	-0.0084	0.0002	-0.0008	-0.0007	-0.0097
	29 Jan 2014	-0.0065	-0.0010	-0.0004	-0.0003	-0.0082
	09 Feb 2014	-0.0121	0.0013	0	0.0003	-0.0105
Mean		-0.0073	0.0006	-0.0006	-0.0003	-0.0077
Mean all		-0.0003	0.0008	-0.0009	-0.0013	-0.0017
Standard deviation σ		0.0101	0.0026	0.0015	0.0030	0.0073

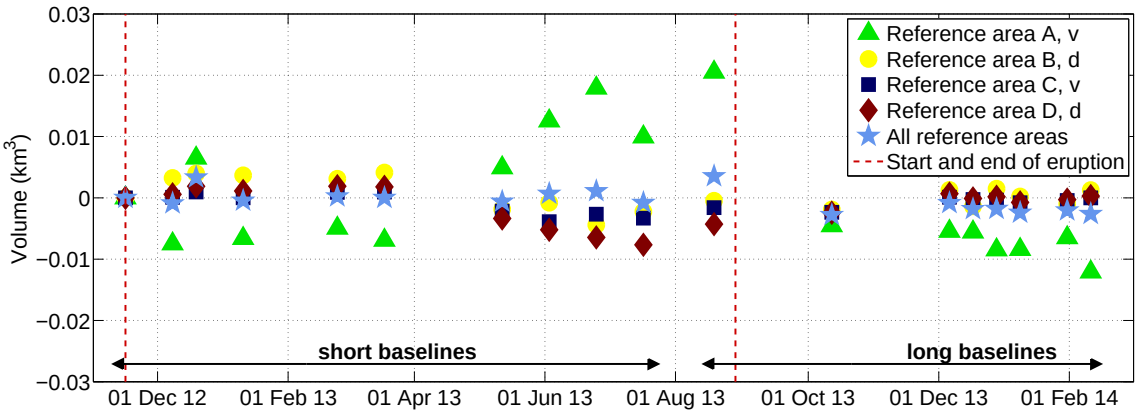

Figure 5.22 – Volume calculated for reference areas A - D where no topographic change is expected. v stands for vegetated and d for geometrical decorrelation. The light blue stars show the summed volumes of all reference areas for each difference map.

5.2.6 Comparison of TanDEM-X based results with aerophotogrammetric observations

To assess the quality of the TanDEM-X-based results, the derived parameters were compared to a study conducted by Dvigalo et al. (2014) who used aerophotogrammetric observations to study the Tolbachik 2012-13 eruption. Five data sets of different quality were generated to derive lava flow thickness and area extent throughout the eruption. The first DEM, and thus the reference elevation on which all estimates are based, was generated using aerial photographs that were acquired on 19 September 1987. Three aerial surveys were carried out during the eruption on 29 November 2012, 13 December 2012, and 05 June 2013. The images were acquired during overflights with a helicopter at 4200 m height and were afterwards stereophotogrammetrically processed, resulting in DEMs which were further used to reveal flow extension and lava flow volume (Dvigalo et al., 2014). Lava flow area as well as flow volume were further assessed on 06 March 2013 using a single satellite image from NASA's (National Aeronautics and Space Administration) EO-1 satellite. Table 5.11 shows the lava flow area, the lava flow volume, as well as the lava extrusion rates calculated by Dvigalo et al. (2014). It should be mentioned that the lava extrusion rate for the first time interval (until 29 November 2012) is given in Dvigalo et al. (2014) with 440 m^3/s. However, recalculating using the given lava flow volume of 0.072 km^3 and the time interval (time since the eruption started) of 2 days leads to a lava extrusion rate of 417 m^3/s used in the present comparison. The discrepancy is due to a more specific timing of the start of the eruption by Dvigalo et al. (2014) or due to a different amount of decimal places. The error of each DEM is given in Dvigalo et al. (2014) in percent with respect to the lava field size, and is 2 % for the DEMs from data acquired on 29 November 2012, 13 December 2012, and 05 June 2013. The error for the 06 March 2013 DEM is estimated to be 7 % with respect to the lava flow field.

As the latest aerial photogrammetric survey was conducted three months before the eruption ended, Dvigalo et al. (2014) give a probable final lava flow volume of 0.55 - 0.65 km^3 that was estimated with respect to the lava extrusion rate the

Table 5.11 – Lava flow area, lava flow volume, and lava extrusion rates observed by Dvigalo et al. (2014) using aerophotogrammetric observations.

Acquisition date	Time interval (Days)	Lava flow area (km^2)	Lava flow volume (km^3)	Lava extrusion rate (m^3/s)
29 Nov 2012	2	14.46	0.072 ± 0.00144	417
13 Dez 2012	14	22.83	0.243 ± 0.00486	140
06 Mar 2013	84	28.74	0.370 ± 0.0259	18
05 Jun 2013	91	35.23	0.520 ± 0.0104	19

authors calculated between 06 March 2013 and 05 June 2013. The final volume was recalculated by Belousov et al. (2015) to be around 0.6 km^3 non-DRE. This means that the volume of vesicles has not been subtracted for calculating the volume of magma (Schmincke, 2004).

Figure 5.23 shows the temporal distribution of the TanDEM-X scenes that were acquired throughout the eruption and includes also the effective baseline length that was used to acquire each specific image pair. It further shows the times at which the reference data used by Dvigalo et al. (2014) were acquired. The pre-eruption 1987 DEM used by Dvigalo et al. (2014) is not included in the figure.

Figure 5.24 shows the area covered by lava flows at each specific time interval calculated from TanDEM-X and determined by Dvigalo et al. (2014). Figures 5.25 and 5.26 show the same, but for the lava flow volumes and for the lava extrusion rates, respectively. It becomes obvious that the lava flow area is slightly overestimated using TanDEM-X compared to Dvigalo et al. (2014), but is underestimated for the summer month. The lava flow volume seems to be underestimated by Dvigalo et al. (2014) for the 06 March 2013 DEM. The final recalculated volume of Belousov et al. (2015) corroborate the TanDEM-X based estimates. However, Belousov et al. (2015) overestimate the volume with 0.6 km^3 (non-DRE) compared to 0.53 km^3 (non-DRE) estimated with the TanDEM-X based approach. Finally, the lava extrusion rates reveal comparable values for both studies, characterized by a very high lava extrusion in the beginning of the eruption which exponentially decreased towards its end.

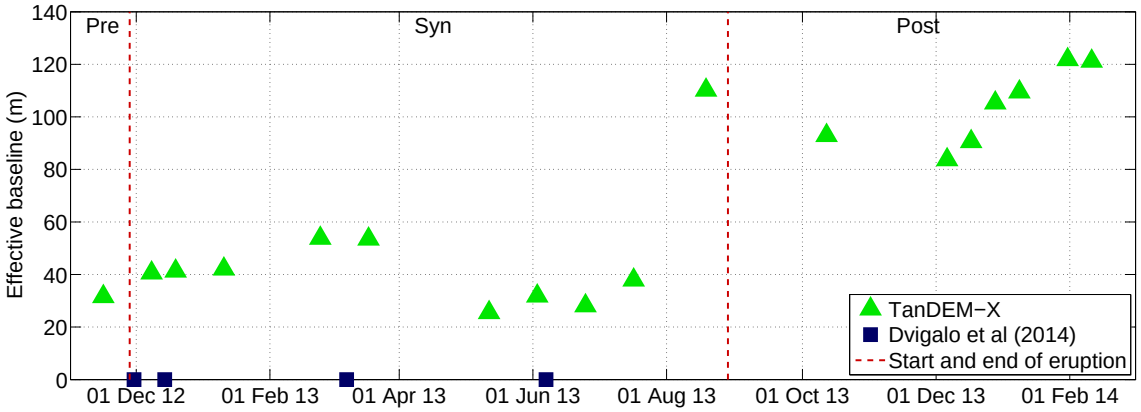

Figure 5.23 – TanDEM-X bistatic acquisitions and aerophotogrammetric surveys used by Dvigalo et al. (2014). The vertical red dashed lines mark the beginning and end of the eruption.

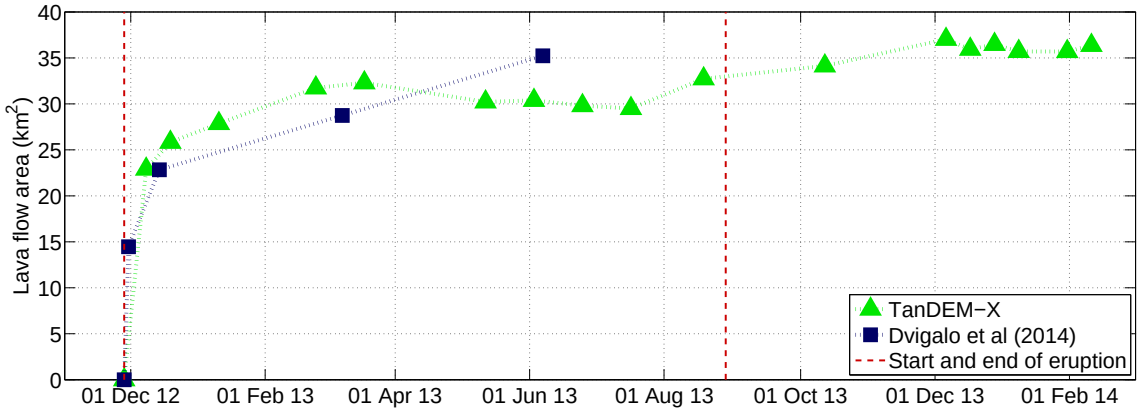

Figure 5.24 – Area covered with lava flows derived from TanDEM-X and compared to aerophotogrammetric results from Dvigalo et al. (2014).

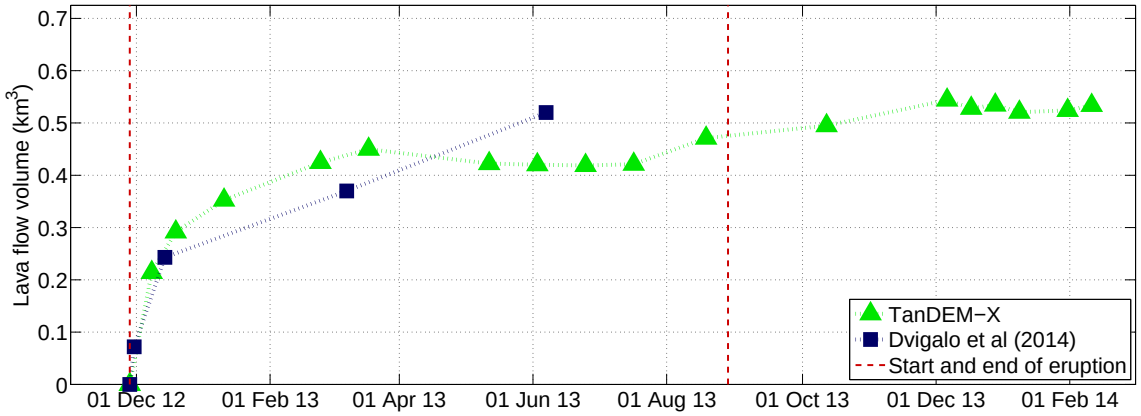

Figure 5.25 – Lava flow volume calculations derived from TanDEM-X and compared to aerophotogrammetric results from Dvigalo et al. (2014).

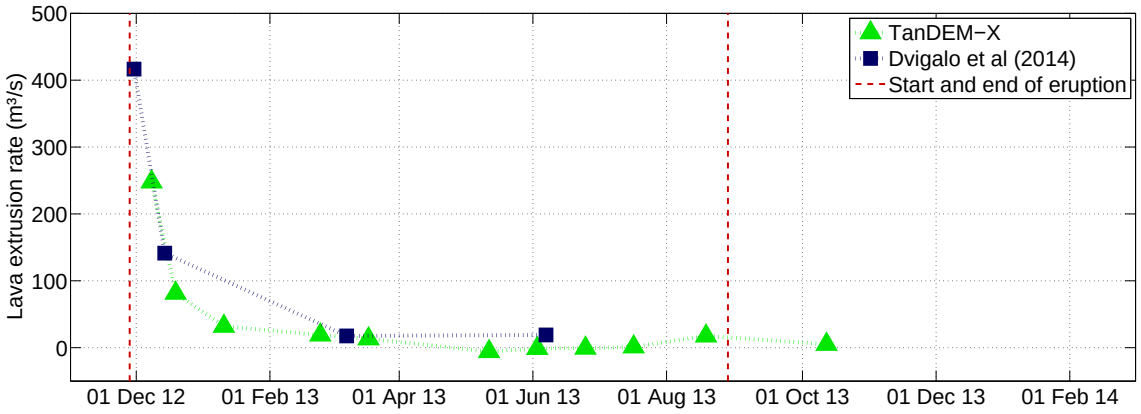

Figure 5.26 – Lava extrusion rates derived from TanDEM-X and compared to aerophotogrammetric results from Dvigalo et al. (2014).

5.2.7 Comparison of the 2012-13 and 1975-76 eruptions

The activity of Tolbachik was characterized by several small eruptions throughout the Holocene. The eruptions of the last few centuries were mostly categorized with a VEI of 1 or 2. Only the 1975-76 and 2012-13 eruptions were major eruptions and

assigned with a VEI of 4. Therefore, the following section deals with a comparison of the characteristics of both events (Tab. 5.12).

The 1975-76 eruption and related parameters were monitored continuously (Fedotov et al., 1980). Both eruptions were sourced from the same part of the fissure, south of Plosky Tolbachik. Whereas Tolbachik was active for about 17 months in 1975-76, the 2012-13 activity lasted for only about 9 months. Both eruptions were characterized by very fluid basaltic lava flows which extended about 30 km (1975-76) and 20 km (2012-13) to the south. The formation of four cinder cones occured during the 1975-76 eruption (Fedotov et al., 1980). For the 2012-13 eruption, the formation of at least five cinder cones was observed by USGS (2014). Using TanDEM-X data, the location of two cinder cones, one approximately 80 m high (cross section A - A' in Fig. 5.16), and another approximately 100 m high (cross section B - B' in Fig. 5.16) could be identified. The cinder cones of the 1975-76 eruption were estimated to be approximately 300 m high (Fedotov et al., 1980). The extruded volume of the 1975-76 eruption was estimated by Belousov et al. (2015) to be 1.18 km^3 (non-DRE), which is about twice the extruded volume of the 2012-13 eruption, calculated in this study with 0.53 km^3 (non-DRE).

It becomes obvious that although both eruptions were identified as VEI = 4, the 1975-76 eruption was larger in some characteristics. This is explained by the fact that the 1975-76 eruption produced lava flows for about twice as long as the 2012-13 eruption.

Table 5.12 – Comparison of 1975-76 and 2012-13 eruptions of Tolbachik.

	1975-76 eruption	2012-13 eruption
Duration	~17 months	~9 months
Lava flow direction and distance	About 30 km to the south	About 20 km to the south
Cinder cone formation	Four cinder cones	At least five cinder cones
Cinder cone height	Up to 300 m	Up to 100 m
Extruded volume (non-DRE)	1.18 km^3	0.53 km^3
Lava covered area	44.73 km^2	35.91 km^2
References	Fedotov et al. (1980) Gordeev et al. (2013b) Belousov et al. (2015)	USGS (2014) This study

5.2.8 From theory to near real-time estimates

The lava flow estimates presented in Section 5.2.4 require knowledge that is not available during an ongoing eruption as all available post-eruption data pairs were used to mask the lava flow area. To give evidence that the methodology could also be used in near real-time to assess hazard and risk at every stage of the eruption, a masking that is based on each single TanDEM-X difference map was further tested. Here, the elevation difference at each specific time was used to generate a lava flow mask. As undertaken previously, pixels with an elevation change smaller than or equal to a specific threshold were masked out to correct for errors. To find the

best-fitting mask, different values ranging from 0 to 7 m were tested. Figure 5.27 gives an overview of the calculated extruded lava flow volume using the different masks, while Figure 5.28 presents the calculated area extent of the flows.

Regarding the lava flow volume estimates, the volume decreases with increasing mask value, as expected. This is also observable regarding the area extent, however, with a different characteristic. The one meter as well as the two meter thresholds decrease the area extent distinctly and the higher the mask value, the less the area extent decreases. Due to the values that were calculated in Section 5.2.4, the three and four meter masks seemed to reveal the most-plausible results regarding flow volume and area extent. A value of three or four seems also plausible regarding the effect to exclude wrong height values that do not belong to the lava flow, for instance due to vegetation in the summer images. Figure 5.29 finally shows the calculated extrusion rates for the different masking alternatives, revealing that the calculated extrusion rates differ strongly in the beginning of the eruption. However, it can be seen that with smaller extrusion rates, the masking value looses its influence on the results of the calculation.

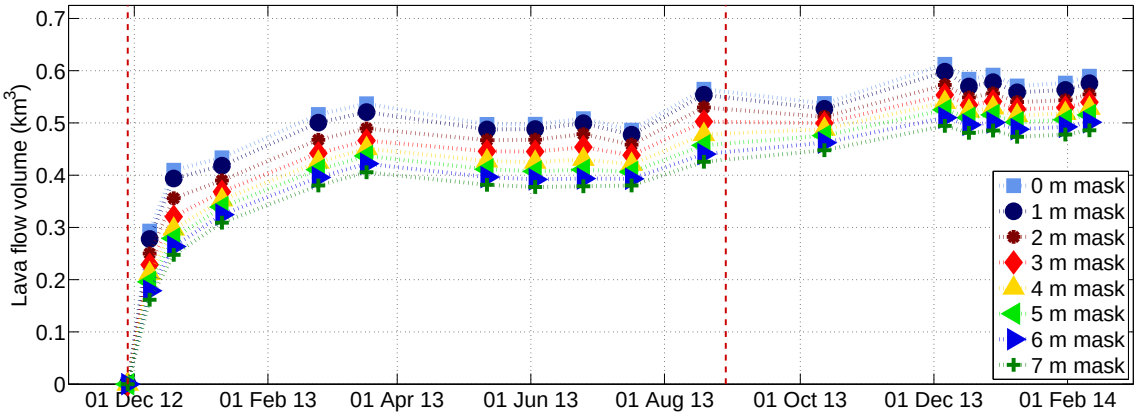

Figure 5.27 – Lava flow volume estimates based on different masks.

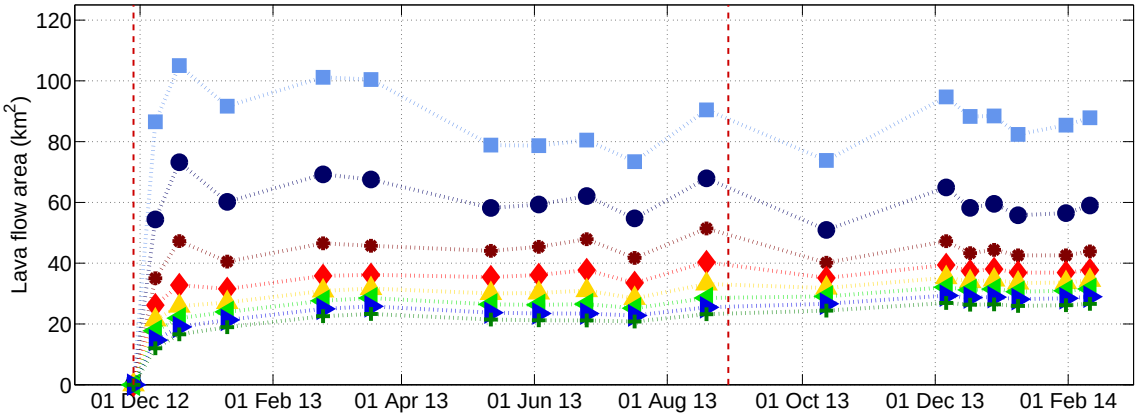

Figure 5.28 – Calculation of area covered by new lava using different masks. The legend is the same as used in Figure 5.27.

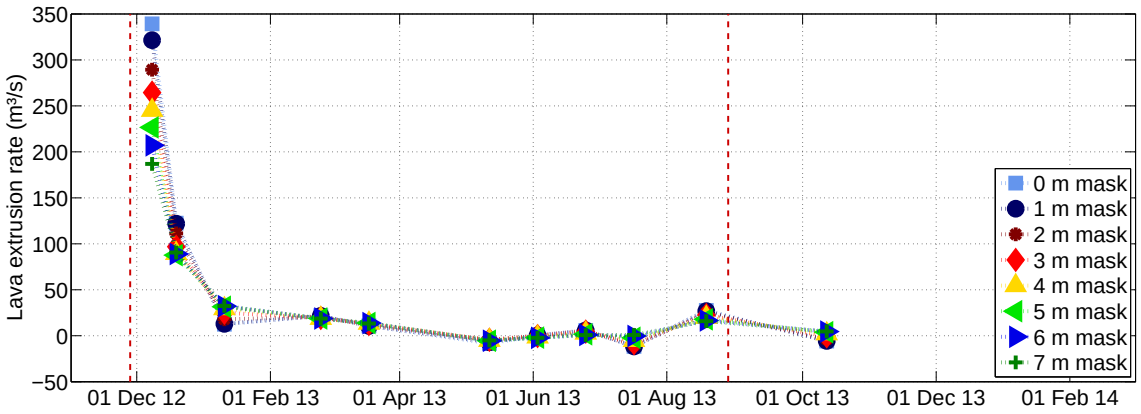

Figure 5.29 – Calculation of lava extrusion rates using different masks.

5.3 Discussion

As TanDEM-X is an innovative satellite mission, potential error sources are discussed in the following. Although the TanDEM-X-based results seem to fit aerophotogrammetric observations, the derived products are partly inconsistent (see Tab. 5.3). When the lava flow area was calculated to be 32.29 km^2 on 16 March 2013, it only amounted to between 29 to 30 km^2 between 10 May 2013 and 15 July 2013. On 17 August 2013, it increased again and after 11 October 2013, the calculated flow area seemed to be around 36 km^2 and therefore stable in all post-eruption difference images. The same statement can be made for the lava flow volume. Whereas the results derived from data pairs that were acquired during winter seem to be reliable, the mentioned inconsistencies only influence the data pairs that were acquired during summer.

In the map views depicted in Figure 5.19, a noisy pattern is present in the western part of the images generated from data recorded in summer time, i.e., from May until August 2013. The effect can also be seen in the histograms shown in Figure 5.21, where the syn-eruption I elevation differences generally show the highest standard deviation σ. This effect is easily explainable by the so-called vegetation line outlined in Figure 5.10. Whereas some kind of vegetation is present in the western part of the analyzed small section covering the lava flow, the eastern part (covering 1/3 up to 2/3 of the whole area depending on the season) is barren. Grishin (2015) described that the Leningradskoe Lava Field first passed through the alpine zone of volcanic desert, semi-desert, and subalpine zone for about 15 km; the following 8 km were intruded into forest area. Figure 5.30 shows a photography of the vegetation around the westernmost tail of the lava flow acquired on 23 June 2015. The vegetation is mainly composed of dense scrubs and taller trees. Larch and birch especially become visible, indicating that the vegetation changes with the seasons.

As the TanDEM-X data are acquired in X-band, the electromagnetic waves are reflected at the forest's canopy when trees are leaved in summer (i.e., when the larch has needles in summer), but the radiation can deeply enter the trunks to reach the ground in winter time. The same applies for the presence of scrubs. The data pair used as reference topography in the described data processing was acquired on 15 November 2012. Thus, the trees or scrubs west to the vegetation line were not leafy and the radiation could enter deep into the forest. In contrast, the data pairs recorded in summer obviously contained a leaved forest or scrub area in the west,

Figure 5.30 – Photography taken close to the westernmost tail of the Tolbachik 2012-13 lava flows on 23 June 2015. Photo courtesy of J. Krippner, University of Pittsburgh.

leading to slightly increased elevation values in the processed DEMs. This is visible in the elevation difference images (Fig. 5.19). Values for tree heights in the region is given by Grishin (2010) who studied the effect of ashfall to vegetation in different parts of the Tolbachinsky Dol due to the 1975-76 eruption. One of his sampling plots was located at an altitude of about 380 m where he found trees of up to 11 m height. Since the Leningradskoe Lava Field reached an altitude of about 300 m in its westernmost tail (Grishin, 2015), this is probably a reference value for the error influencing the western part of the summer data pairs.

In the elevation difference map shown in Figure 5.16, an elevated pattern in the northeastern part of the map not connected to any of the flow fields is observable. Due to the right-looking imaging geometry in combination with the acquisition in descending orbit, those artifacts were identified as errors due to layover effects on the steep slopes of Plosky Tolbachik. Errors due to geometrical decorrelation did not influence the lava flow field itself as the area around the flows is shallow enough to guarantee interferometric performance of the SAR satellites. However, this is likely to influence the lava flow volume calculation and the area extent, especially without using a mask to correct for errors.

Additionally, snow coverage in winter is likely to have an effect on the generated DEMs as it is probably measured as lava flow volume. The freshly fallen snow in early winter does not have a strong contribution to the total volume, but the more liquid water the snow contains, the less the radiation will penetrate. This is a probable explanation for the apparently increased lava flow volume calculated for the 16 March 2013 data pair.

For calculating the lava flow volume, only the lava flow area was chosen while employing a mask to extract the lava flow in each image. However, as the summer difference images show a slightly decreasing volume compared to the winter images,

the vegetation seems to have an effect on the deramping function employed to correct for the bistatic acquisition geometry. It is most likely that the masking used here based on the coherence has not weighted the vegetation-affected areas properly. Thus, the ramp is chosen too high in these areas and therefore a too large value is subtracted from the differential topography, resulting in the smaller volumetric value. This is also reasonable for the decreased area extension in the summer images compared to the later ones acquired in winter.

5.4 Conclusions and perspectives

The developed data processing approach shows that TanDEM-X is a suitable sensor to generate high-resolution DEMs to study the lava flows of the 2012-13 Tolbachik eruption. The final estimated lava flow area of about $36\,km^2$ as well as the extruded lava flow volume of $0.53\,km^3 \pm 0.01\,km^3$ is reasonable, especially compared to the values calculated by Dvigalo et al. (2014) and Belousov et al. (2015). This was also shown for the derived lava extrusion rates.

In addition to the mentioned error sources, the uncertainty estimation was able to clearly prove the feasibility of the developed differential DEM approach. The analysis of the four areas with different characteristics showed that independently of the time of year and location, all elevation differences were centered around zero. The mean over all elevation difference maps of all areas $\overline{\mu}$ is with -0.21 m very low, as is the mean standard deviation over the mean of all elevation differences σ_μ with 1.63 m. Only a few data pairs in reference area B showed non-reliable elevation values, which are due to the geometric decorrelation effects along the flanks of Plosky Tolbachik. Since the lava flow area itself was comparably flat, it is expected that geometrical decorrelation did not influence the lava flow volume estimates. The accuracy as well as the precision of the results prove that TanDEM-X enables to map lava flow extent and measure lava flow volume with the differential DEM approach with a high accuracy.

The accurate measurements of important volcanological parameters are very promising. The differencing algorithm between a pre-eruption and several syn-eruption and post-eruption data pairs demonstrates the potential for using bistatic TanDEM-X satellite data in volcano research and monitoring procedures. The test of using the bistatic TanDEM-X data in near real-time to monitor ongoing lava extrusion during eruptions showed promising results. However, the time delay until the data is available will be an issue.

The DEMs themselves as well as the derived volcanological parameters provide valuable information and can be used – among others – to model lava or pyroclastic flows, to assess hazard and risk of an eruption, or can be used as input for repeat-pass deformation analysis. The parameters derived in this study were already successfully used in a lava flow simulation program to reproduce the flow path of the 2012-13 Tolbachik eruption (Kubanek et al., 2015a) which again corroborated the estimated lava flow volume calculated in this study.

Since the presented results are more reliable in winter than in summer, different approaches are suggested in the following to further analyze the effects the vegetation has on the DEM differences and on the volume calculation of the lava flow:

Improve the deramping. The deramping could be improved while using only the non-vegetated area to generate the planar function to correct the phase information after unwrapping. This ramp can then be linearly filled to cover the whole scene. This will lead to better results regarding the volume calculation and calculation of area extension of the flows.

Processing of the continuously acquired TanDEM-X data of the region. The TanDEM-X time series for the Tolbachik region is long. Starting in March 2014, a data pair was acquired almost every 11 days, resulting in 17 bistatic data pairs until October 2014, where the satellite mission started acquiring data in pursuit monostatic mode. The effective baselines of the bistatic data are up to 143 m in March 2014 and decrease successively until September 2014 to about 33 m. Analyzing the data pairs throughout the year should reveal comparable volumes calculated for the so far used post-eruption data pairs. If the summer data pairs show the same trend like the syn-eruption II ones used in this study, the effect can only be explained by vegetation.

Field trip to Tolbachik volcano. The photography shown in Figure 5.30 already gives an impression about the vegetation structure around parts of the Tolbachik flow field. This indicates the importance to study the lava flow during fieldwork. A field trip to the Tolbachik region would provide a more detailed insight into the structure of the vegetation. Of major interest is, of course, the transition zone, the interaction of the lava flow with the vegetation as well as the influence of snow cover. Also multispectral images could be used additionally to classify the vegetation. The best case would obviously be to acquire a photogrammetric DEM of this post-eruptive stage to compare with the TanDEM-X data.

6. Quantification of small volumetric changes at Volcán de Colima, Mexico

Chapter 6 deals with the application of the bistatic TanDEM-X data to study small topographic changes at Volcán de Colima in Mexico. Like Merapi, Volcán de Colima is a stratovolcano with varying activity. Long terms of dome growth are intermitted by small explosions and culminate in complete dome destructions. A small explosion in June 2011 marked the end of magma ascending into the summit and stopped the ongoing building of the lava dome. Nine bistatic data pairs (two before and seven after the explosion) are analyzed to reveal the topographic and volumetric change on the western crater rim. The results are further validated using aerophotogrammetric DEMs generated by James and Varley (2012). To analyze the repeatability of the TanDEM-X-based DEMs and the derived volcanological results, further data pairs acquired between June 2011 and December 2012 are evaluated. Altogether, 26 data pairs, including the seven post-explosion data pairs mentioned above, are analyzed. As the volcano remained quiet until January 2013, it is assumed that no topographic changes occurred during this time. The results therefore give an insight into the precision of repeatedly derived TanDEM-X DEMs in different terrain types. Parts of this chapter have already been published in Kubanek et al. (2013b, 2014, 2015b).

6.1 Geological setting

Volcán de Colima (19.513° N, 103.587° W, summit 3860 m above sea level) is located approximately 30 km north of the city of Colima in western Mexico (Fig. 6.1) and composes, together with its older neighbor Nevado de Colima (19.563° N, 103.609° W, summit 4270 m above sea level), the Colima Volcanic Complex (CVC, see Fig. 6.2). While being a stratovolcano, Volcán de Colima is one of the most active volcanoes in North America.

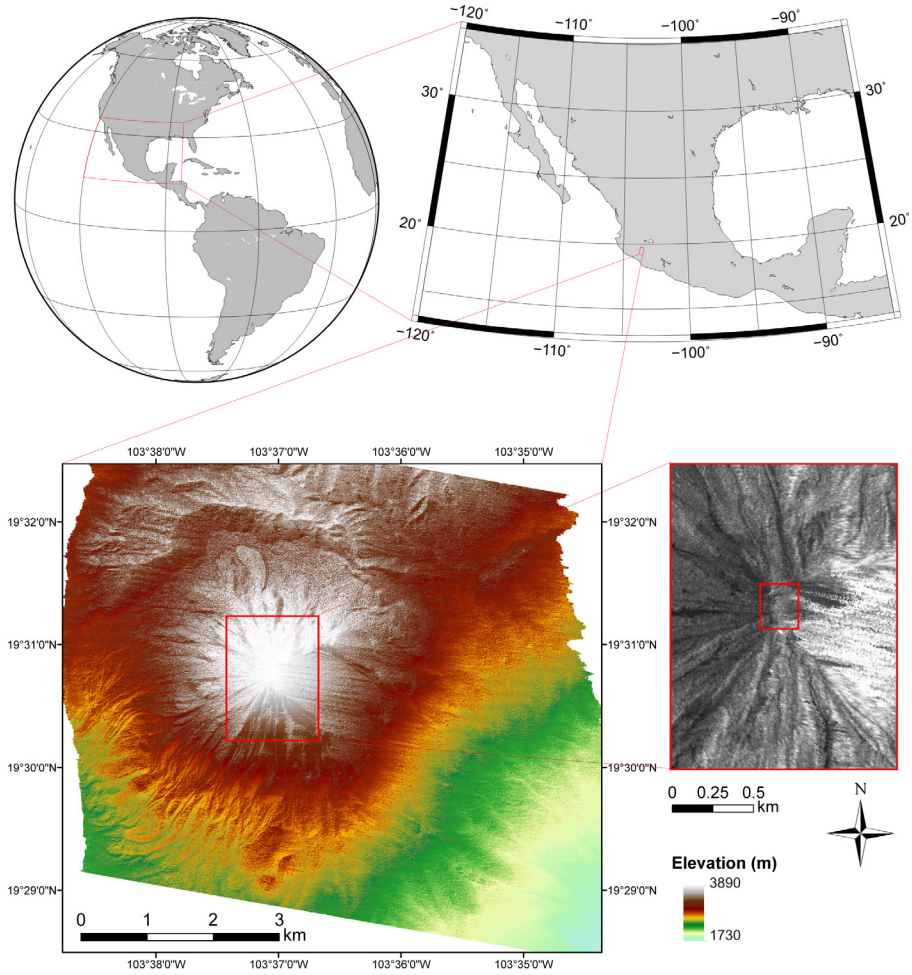

Figure 6.1 – Location of Volcán de Colima in Mexico. The upper right image shows the state of Mexico. The lower left image shows a DEM generated from TanDEM-X data. The lower right part shows an amplitude image of the summit area. The red rectangle in the lower right image indicates the section that was used for the present analysis to reveal changes of the lava dome. It has an extension of about 0.037 km^2.

6.2 Recent eruptive activity

Volcán de Colima's historical activity has been highly periodic, characterized by approximately 100-year cycles and dominated by lava dome growth and intermitted by minor-to-major eruptions with a VEI of 2 to 4, and culminating in complete dome destruction (Lavallée et al., 2012; Luhr and Carmichael, 1980). Over the last five centuries, the volcano has experienced a variety of volcanic processes culminating in explosive events with a VEI of 4 (Gonzáles et al., 2002).

The recent activity of Volcán de Colima included four phases of dome growth during 1998-1999, 2001-2003, 2004, and 2007-2011 (Savov et al., 2008). Each phase was associated with explosive activity after the growing phase (Varley et al., 2010). Among others, Hutchinson et al. (2013) studied the lava dome growth episode which started in early 2007 and continued until June 2011 using high-resolution digital photography and infrared images. Both were acquired during flights over the volcano. The infrared images were taken with hand-held thermal cameras and the photographs with digital cameras. The first and third phases of dome growth showed an effusion

rate that is typical for crater domes. In the second and last mentioned episode, however, the lava dome grew with an effusion rate of about $0.02\,m^3\,s^{-1}$, i.e., very slowly (Hutchinson et al., 2013; James and Varley, 2012). During the last extrusion phase in the end of 2009, the crater was mainly filled and the dome started to overflow the crater rim predominantly to the west (James and Varley, 2012). According to Hutchinson et al. (2013), the crater rim measured $300 \pm 20\,m$ in diameter and did not change throughout the 2007-2011 activity. The dome volume in June 2011 was measured with $1.5\text{-}2 \times 10^6\,m^3$.

On 26 June 2011, a small explosion occurred on the western crater rim, signaling the end of magma ascent to the summit (James and Varley, 2012). Subsequently, the volcano was quiet until a new episode of activity started in January 2013 (Global Volcanism Program, 2013; Salzer et al., 2014). Figure 6.2 shows a photography of Volcán de Colima acquired from the southeast. A second photography shows the lava dome in Figure 6.3. Both photographs were acquired in November 2012 during fieldwork.

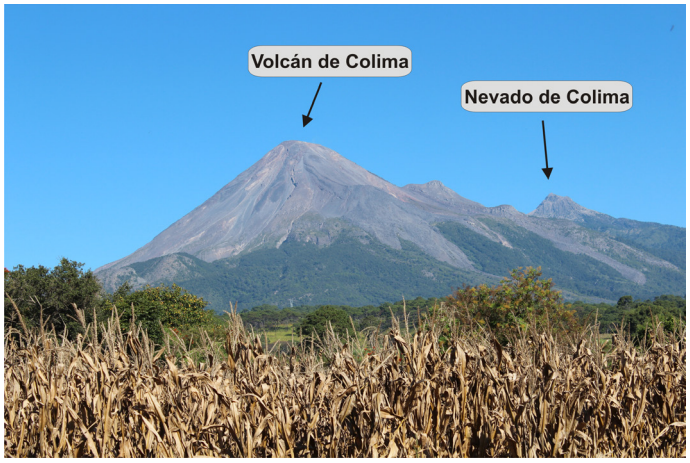

Figure 6.2 – Photography of Volcán de Colima seen from the southeast. The currently dormant neighbor Nevado de Colima is visible in the background. The photography was taken in November 2012 during fieldwork.

Figure 6.3 – Aerial photography of the summit area of Volcán de Colima taken during a flyover with a light plane in November 2012 during fieldwork. The lava dome nested in the summit crater is visible.

6.3 Measuring small topographic changes during the June 2011 explosion

Chapter 4 proved that large topographic changes at active lava domes are observable using TanDEM-X data, choosing Merapi as a case study. The same methodology was first also used to reveal insights in the meter-level topographic changes that occurred at Volcán de Colima due to the June 2011 explosion. However, data analysis without using a reference DEM phase ϕ_{topo} during processing did not reveal reliable results since the topographic changes which occurred at Volcán de Colima were by a factor of ten smaller than those at Merapi. As second approach, the methodology developed for analyzing basaltic lava flows at Tolbachik (Chap. 5) was further adapted to analyze the topographic changes due to the 2011 Colima explosion. The application and corresponding results are presented in the following.

6.3.1 Data description

Due to the side-looking acquisition geometry and the occurrence of the explosion at the western crater rim, data acquired in descending orbit seemed to reveal the most promising results. To estimate the changes in lava dome volume, nine bistatic data pairs, two of which were recorded before the explosion on 08 June 2011 and on 19 June 2011 (hereafter referred to as pre-explosion DEMs), and seven data pairs recorded from June until September 2011 (after the explosion, hereafter referred to as post-explosion DEMs) were analyzed (Tab. 6.1). All data pairs were recorded in StripMap mode. The effective baselines of the data pairs vary from 63.2 m to 87.5 m and the height of ambiguity ranges between 56.8 m and 79.1 m (Tab. 6.1), respectively. The mean incidence angle of all data pairs is 32.34°.

Table 6.1 – TanDEM-X observation times of Volcán de Colima including acquisition parameters.

Acquisition date	Effective baseline (m)	Height of ambiguity (m)	Average coherence	Mean incidence angle (°)
08 Jun 2011	87.5	56.8	0.71	32.40
19 Jun 2011	86.3	57.3	0.72	32.27
30 Jun 2011	79.0	63.0	0.75	32.40
11 Jul 2011	77.6	64.2	0.76	32.40
22 Jul 2011	73.9	67.1	0.75	32.27
02 Aug 2011	70.7	70.2	0.76	32.26
24 Aug 2011	65.2	76.2	0.78	32.28
04 Sep 2011	63.2	79.1	0.78	32.35
26 Sep 2011	80.6	61.9	0.74	32.42

6.3.2 Data processing

The processing of the Colima data pairs is closely related to the processing workflow described in Section 5.2.2 for Tolbachik volcano and consists of three steps: (1) the pre-explosion DEM processing which is further used as reference topography phase ϕ^*_{topo}, (2) the pre- and post-explosion DEM processing based on the reference topography phase ϕ^*_{topo}, and (3) the differential DEM analysis.

(1) Pre-explosion DEM processing to generate ϕ^*_{topo}
The first pre-explosion DEM from data acquired on 08 June 2011 is processed with a multilooking of 4 x 4 to generate the reference DEM ϕ^*_{topo}. During the bistatic processing, the reference phase ϕ_{ref} and the reference topography phase ϕ_{topo} are subtracted from the complex interferogram. In this case, SRTM3 is used for ϕ_{topo}. The resulting residual phase φ is filtered using spatial convolution (DORIS Manual, 2009) and unwrapped using SNAPHU (Chen and Zebker, 2001). Up to this step, the processing resembles the processing workflow applied to study the lava flows at Tolbachik volcano (Sec. 5.2.2). A change has to be made in the next processing step regarding the planar offset and phase ramp correction. Weighting the unwrapped residual phase φ_{unw} using the coherence is appropriate to correct for errors, remaining topography, and vegetation for the Tolbachik test site. However, regarding Colima volcano, another error source needs to be considered. For the reason that Volcán de Colima is a steep stratovolcano, the topography is fissured, leading to geometrical decorrelation throughout the image. To ensure that the non-reliable areas have no influence on the phase ramp calculation, the areas are masked out. The thresholds are defined independently for each interferogram based on the unwrapped residual phase φ_{unw} itself. Thereby, the threshold is manually found for each image by identifying the minimum and maximum possible values that can be set to zero masking out the geometrical decorrelated areas, but without influencing the margins of the images (Fig. 6.4b). The threshold varies between -11 rad $\leq \varphi_{\text{unw}} \geq$ 9 rad with respect to all images. In addition to the thresholding, a frame of 1000 pixels and 1500 lines at each margin of the image is set to zero to exclude, e.g., an unwrapping error present in most of the data pairs in the southeast (visible in the lower right corner of Fig. 6.4a) as well as misleading phase values in the north due to a water surface (not obvious in Fig. 6.4, but present in most of the data pairs). The same pixels of each coherence image are then set to zero to weight the phase values (Fig. 6.5d). The coherence γ itself is calculated after removal of the reference phase ϕ_{ref} and the reference topography phase ϕ_{topo}, respectively. The subsequent steps resemble the processing applied to the Tolbachik data pairs.

(2) DEM processing based on the reference topography phase ϕ^*_{topo}
The resulting 'new' reference DEM phase ϕ^*_{topo} is used as input to process all data pairs that are listed in Table 6.1. A multilooking of 2 in each direction is chosen to enable processing of the entire TanDEM-X scenes. The azimuth resolution of 3.3 m and the ground range resolution of 2.2 m combined with the multilooking of 2 in each direction leads to a pixel size of 29.04 m^2. Figure 6.4 shows the intermediate results for a post-explosion example data pair acquired on 02 August 2011. The coherence image as well as the masked coherence image are shown in Figure 6.5.

For completeness, Figure 6.5a presents an amplitude image of the same data pair, showing also the location of Volcán de Colima in the satellite scene. Figure 6.5b presents the final DEM, which is still in the slant-range radar geometry. The higher elevations north of Volcán de Colima indicate the location of its currently dormant neighbor, Nevado de Colima.

(3) Differential DEM analysis
The differential DEM analysis resembles again the processing that was applied to Tolbachik volcano. To reveal the topographic and volumetric changes in the sum-

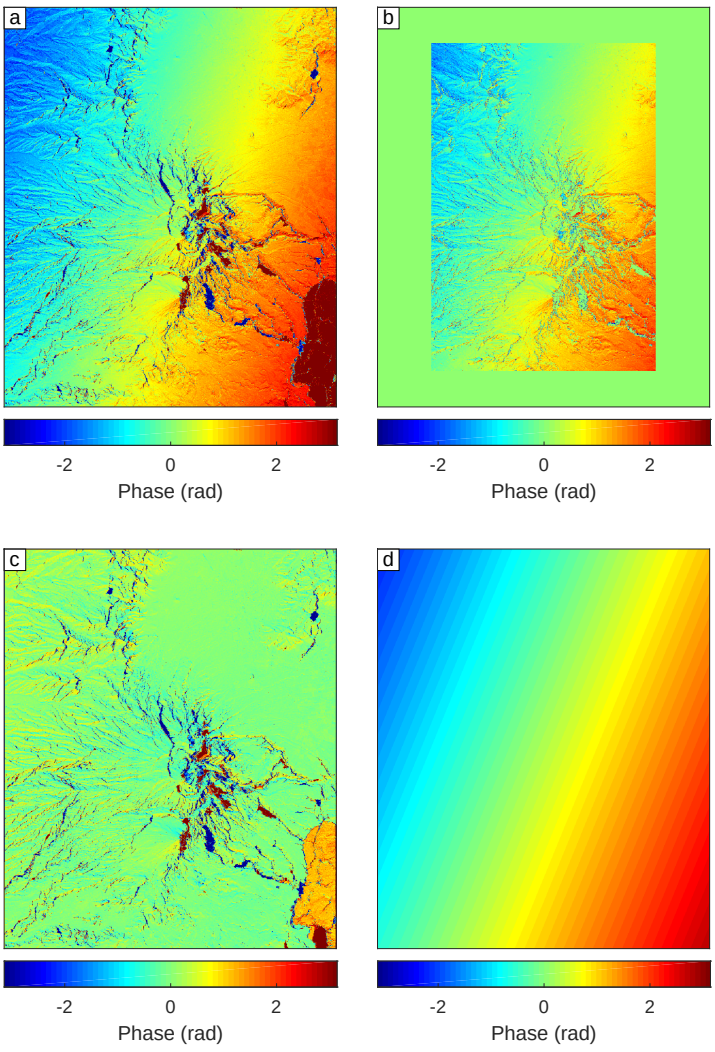

Figure 6.4 – Intermediate results of differential TanDEM-X data processing for Colima. The data pair acquired on 02 August 2011 is used as example. The images contain the entire TanDEM-X scene. (a) shows the unwrapped residual phase φ_{unw}, (b) shows the same but masked while setting $|\varphi_{\text{unw}}| \geq 3\,\text{rad}$ to zero. A frame of 1000 pixels and 1500 lines was additionally set to zero to exclude, e.g., the unwrapping error in the lower right corner in (a) and (c). (c) shows the deramped residual phase and (d) the subtracted best-fit-plane.

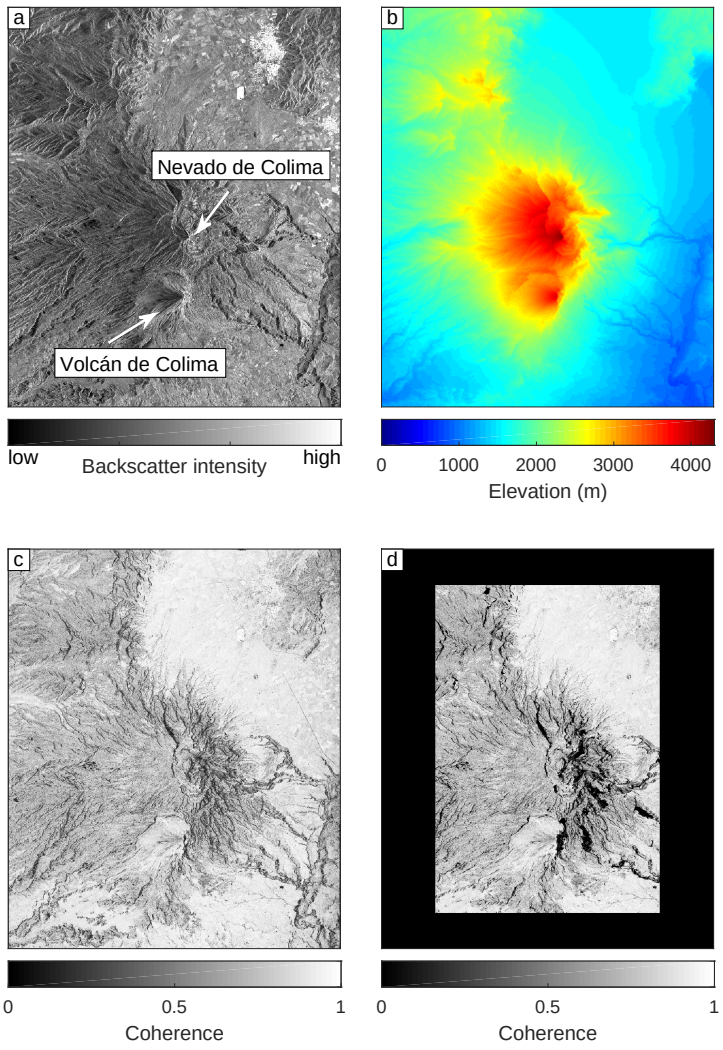

Figure 6.5 – Intermediate results of differential TanDEM-X data processing for Colima. The data pair acquired on 02 August 2011 is used again as example. The images present the entire TanDEM-X scene. (a) shows the backscatter intensity and (b) the final DEM which consists of the residual unwrapped and deramped phase and the returned reference topography phase ϕ^*_{topo}. It is still in the radar slant range geometry. (c) shows the coherence and (d) the masked coherence used to weight the unwrapped residual phase φ_{unw} for excluding unreliable areas during deramping.

mit area of Volcán de Colima, the final pre-eruption DEM is subtracted from each processed post-eruption DEM in the geocoded domain.

6.3.3 Amplitude results

Regarding the observations made at Merapi and Tolbachik volcano, the amplitude as well as the coherence images already give evidence for the topographic loss in the summit area of Merapi as well as for the newly extruded lava flows at Tolbachik. In contrast, neither the amplitude, nor the coherence images of Volcán de Colima give any sign of a topographic change occurring close to its lava dome due to the June 2011 explosion.

Figure 6.6 shows the backscatter intensity of selected data pairs, two of which were acquired before (08 and 19 June 2011) and the other two after the explosion (11 July and 26 September 2011). The images cover the larger area displayed in Figure 6.1 (big rectangle) with an area of 1.17 km^2. Dark colors indicate low backscatter whereas bright colors show a high backscatter. All images show generally the same pattern. The lava dome is visible in the center of each image as well as a pattern of very bright backscatter east of the dome. As the images were acquired in descending orbit, the high backscatter can be explained by foreshortening and layover. As the June 2011 explosion occurred at the western crater rim, the observed geometric decorrelation did not influence the results. However, it was masked out for estimating the topographic and volumetric changes in Section 6.3.5.

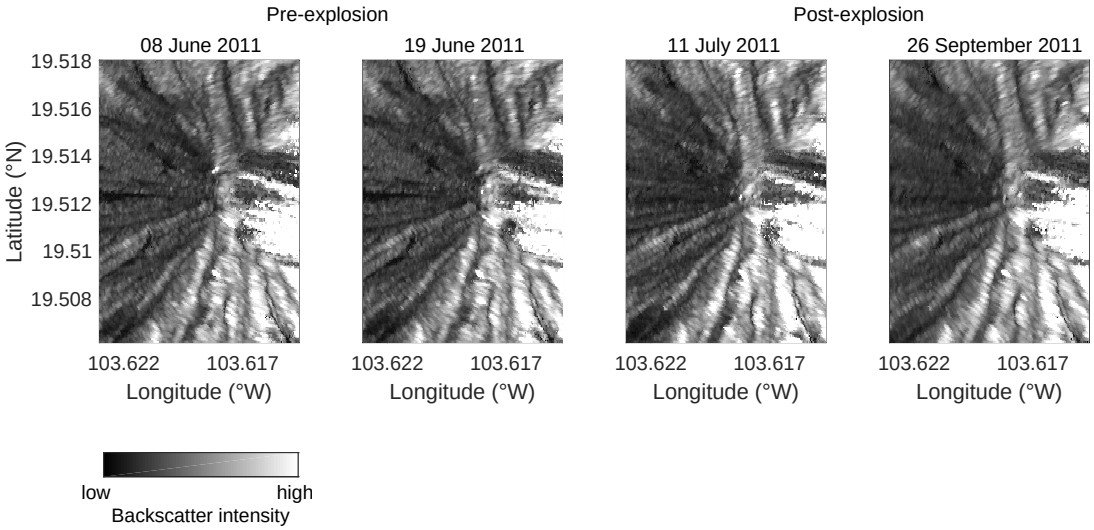

Figure 6.6 – Amplitude images: results for the two pre-explosion data pairs acquired on 08 and 19 June 2011 and for two selected post-explosion data pairs acquired on 11 July and 26 September 2011.

6.3.4 Coherence results

The coherence was calculated subtracting the reference phase ϕ_{ref} as well as the reference topography phase ϕ^{*}_{topo}. Figure 6.7 shows the coherence images of the same data pairs as used in the visual interpretations of the backscatter intensity in Figure 6.6.

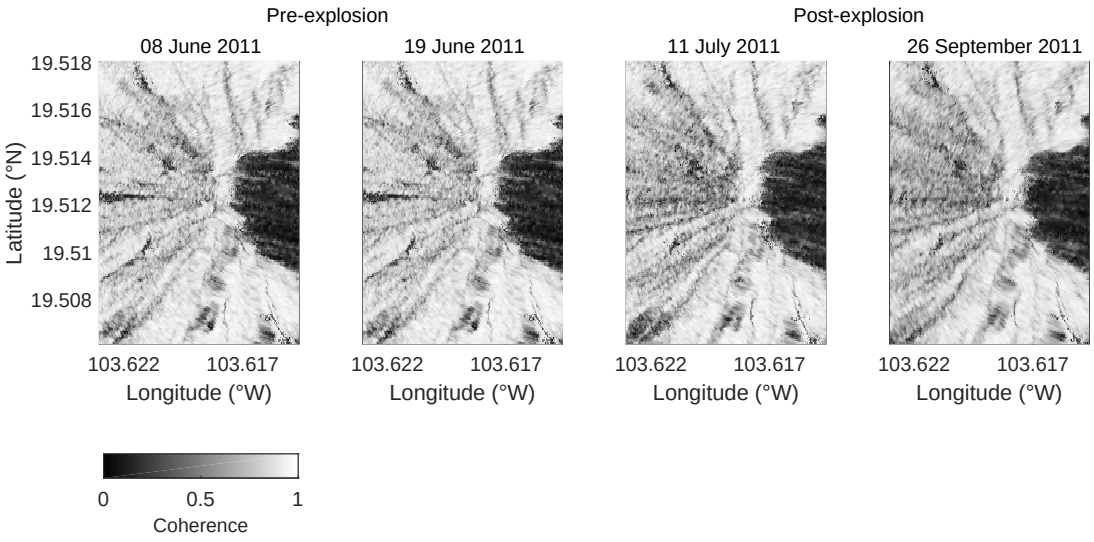

Figure 6.7 – Coherence images: results for the two pre-explosion data pairs acquired on 08 and 19 June 2011 and for two selected post-explosion data pairs acquired on 11 July and 26 September 2011.

Regarding the coherence images, dark colors indicate low and bright colors high coherence. The coherence of the whole TanDEM-X scenes is generally very high and ranges between 0.71 and 0.78 (Tab. 6.1), as shown in Section 6.3.1. No differences are apparent between pre- and post-explosion data pairs. However, the same pattern which was seen in the visual amplitude interpretation becomes obvious in all coherence images. The area east of the lava dome shows a very low coherence in all images, thus proving that layover effects are present.

6.3.5 Interferometric results

The processing of the bistatic TanDEM-X data results in nine DEMs, two of which were acquired before the explosion on 08 June 2011 and on 19 June 2011. They are in the following also referred to as first and second pre-explosion DEMs, respectively. The second pre-explosion data pair was additionally processed in the same way as all post-eruption data pairs to give a first insight into the accuracy of the presented results. After DEM generation, the first pre-explosion DEM was subtracted from the second pre-explosion DEM as well as from all post-explosion DEMs to reveal the topographic and volumetric changes due to the explosion. All results are therefore relative to the first pre-explosion data pair.

Figure 6.8 displays the results for the data pairs acquired in June and July 2011 and Figure 6.9 for the remaining data pairs acquired in August and September 2011. Column A of each figure shows the elevation differences between the date specified above each row and the reference DEM acquired on 08 June 2011. The negative topographic change is visible in all images. Additionally, also a positive topographic change is visible around the negative change, but especially north to it. It is not quantified further, however, it is also observed in aerophotogrammetric DEM differences (see Sec. 6.3.7).

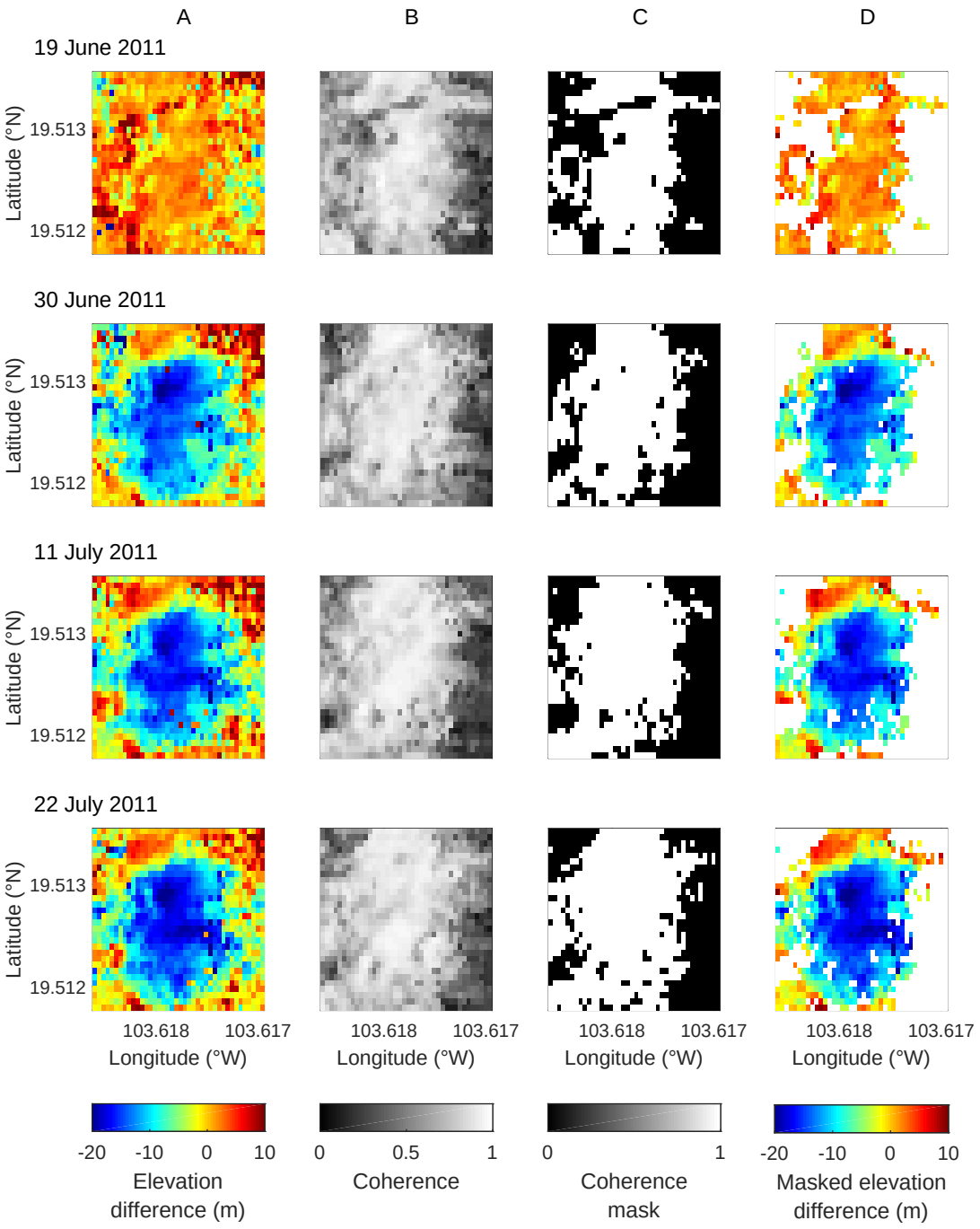

Figure 6.8 – Intermediate processing steps to extract high coherent areas: results for the data pairs acquired between June and July 2011. From left to right: (A) elevation difference, (B) coherence, (C) coherence mask, and (D) elevation difference combined with the coherence mask. Each row shows the results corresponding to the date specified above each line.

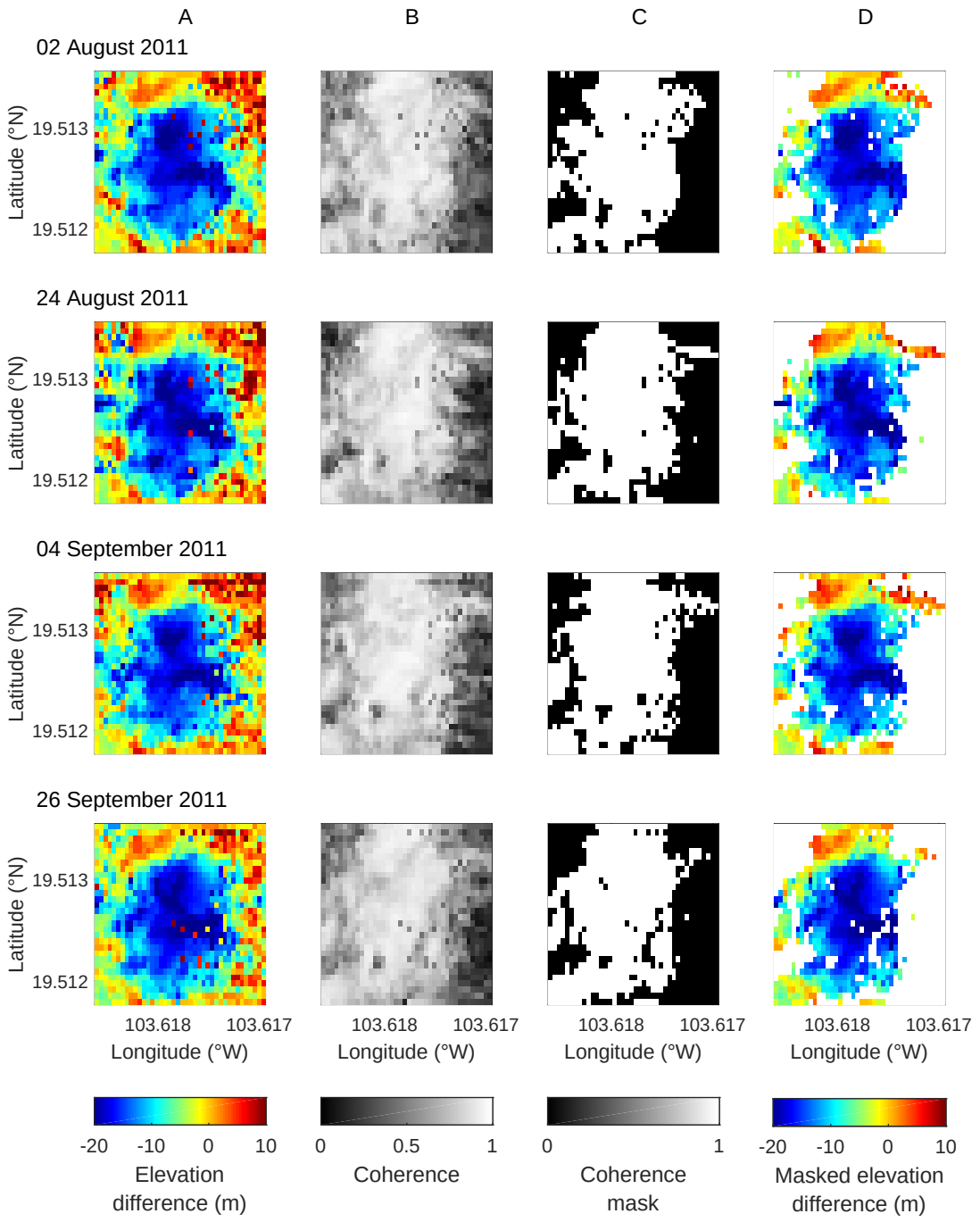

Figure 6.9 – Intermediate processing steps to extract high coherent areas: results for the data pairs acquired between August and September 2011. From left to right: (A) elevation difference, (B) coherence, (C) coherence mask, and (D) elevation difference combined with the coherence mask. Each row shows the results corresponding to the date specified above each line.

The shown section equals the small rectangle in Figure 6.1 and has an extension of 0.037 km^2. To extract only the highly coherent areas, the coherence of each corresponding data pair was used to generate a mask. Therefore, Figures 6.8 and 6.9 in column B display the coherence images of the same small section presented in column A. A threshold of 0.7 which corresponds to the mean coherence value of all images for the analyzed section was used to generate each individual mask.

Thereby, pixels with a coherence smaller or equal to 0.7 were set to zero and pixels with a value higher than 0.7 were set to 1. The result is shown for each data pair in column C. In column D, the elevation differences of column A are overlaid by the resulting coherence masks. It is clearly obvious that the noise pattern around the topographic change in the center of the image is masked out whereas the area of topographic change remains.

6.3.6 Topographic and volumetric changes

For a better presentation of the results, the elevation differences already shown in column D in Figures 6.8 and 6.9 were low-pass filtered using a moving average over a window of 3 x 3 pixel. The results are shown in Figure 6.10. In contrast to Figures 6.8 and 6.9, the coherence mask is not plotted on top of the elevation differences, but was set to zero in the images. The topographic loss is visible in all post-explosion elevation differences. The calculated mean elevation difference ranges between -4.5 m and -5.7 m for all data pairs (see Tab. 6.2).

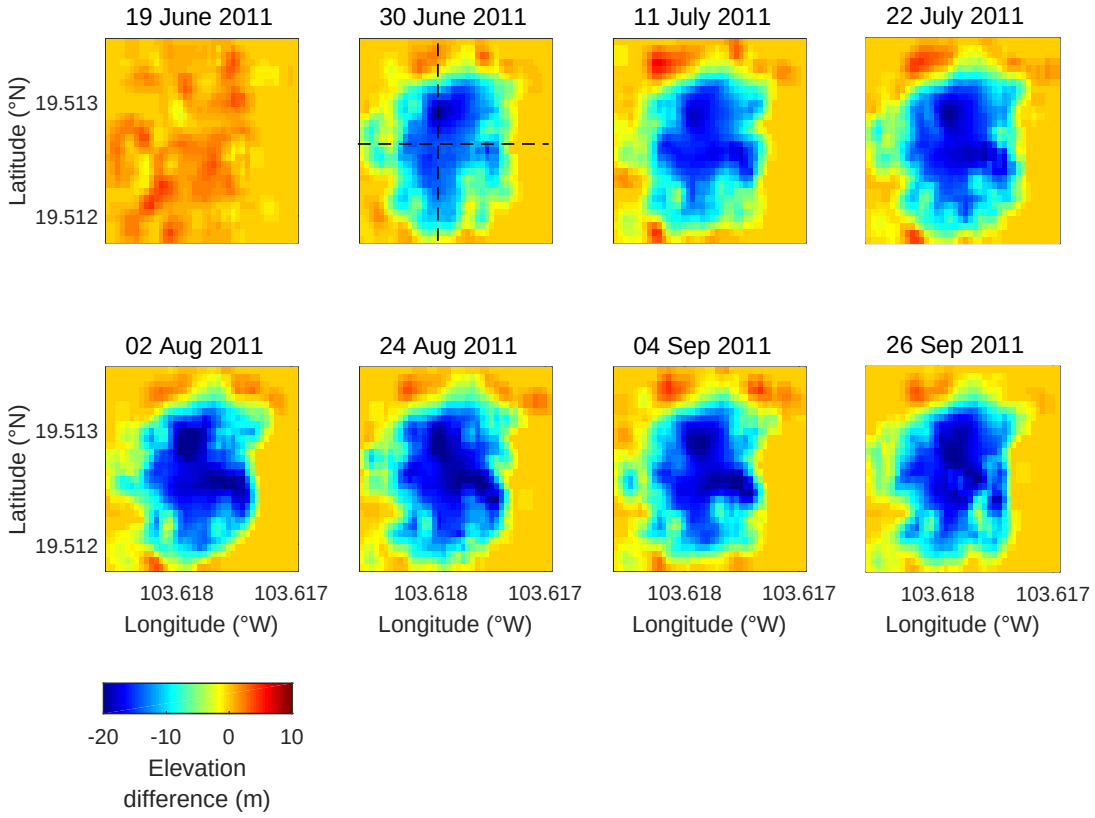

Figure 6.10 – Low-pass filtered elevation differences. The dotted lines shown in the 30 June 2011 elevation difference indicate the locations of the cross sections depicted in Figure 6.11.

The volumetric change was calculated using trapezoidal integration. The results are listed in Table 6.2, including the mean and the standard deviation σ for the elevation change and the volumetric change, respectively. The calculated volumetric change ranges between -0.166 x 10^6 m^3 and -0.210 x 10^6 m^3 for all post-explosion data pairs. The mean volumetric change was calculated with -0.189 x 10^6 m^3.

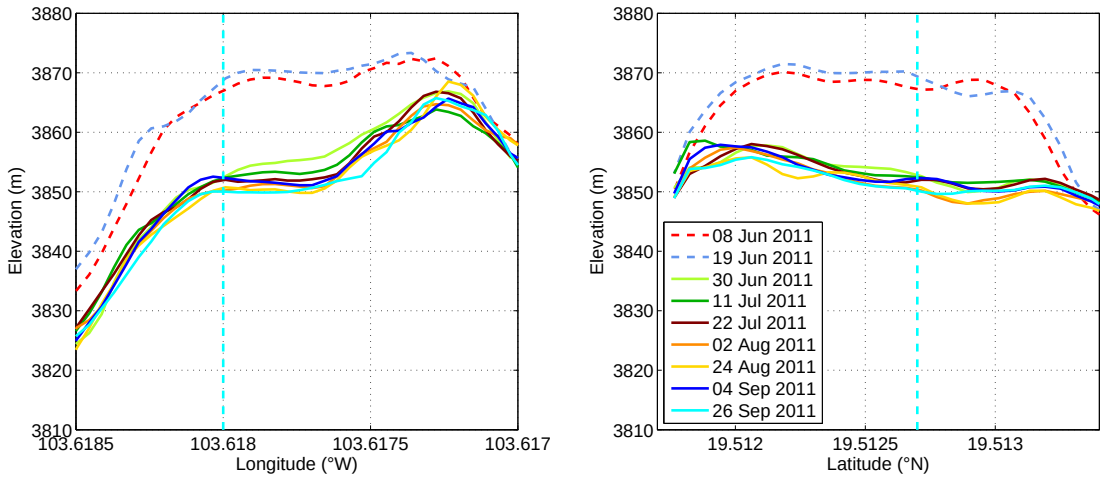

Figure 6.11 – Cross sections of the low-pass filtered DEMs. The left graphic displays the cross sections from west to east at 19.5127° N. The graphic to the right shows the cross sections from south to north at 103.6180° W. The light blue vertical line in both cross sections indicates the intersection with the other cross section, respectively.

Figure 6.11 shows cross sections of the DEMs from west to east at 19.5127° N and from south to north at 103.6180° W. Also the DEMs were low-pass filtered using a moving average over a window of 3 x 3 pixel. The locations of the cross sections are shown in Figure 6.10 as dotted lines in the 30 June 2011 elevation difference image. Although the cross sections of the pre-explosion DEMs shown as dotted lines present a small shift against each other, they fit very well and show a very similar profile in both directions. The mean elevation change between those two data pairs with -0.7 m is very low, as is the calculated volume with -24.7 m^3 (Tab. 6.2). Also the cross sections of all post-explosion DEMs show a similar profile with offsets of up to 5 m. The deviation between those data pairs is further validated in Section 6.3.8.

Table 6.2 – Calculated topographic and volumetric changes from TanDEM-X elevation differences. The volume for the difference with the second post-explosion DEM (19 June 2011) was calculated as a reference and is therefore not included in the mean $\overline{\mu}$ and the standard deviation σ.

	Acquisition date	Mean elevation change (m)	Volumetric change (x 10^6 m^3)
Pre-explosion	19 Jun 11	-0.7	-0.025
Post-explosion	30 Jun 11	-4.5	-0.166
	11 Jul 11	-4.6	-0.170
	22 Jul 11	-5.2	-0.193
	02 Aug 11	-5.4	-0.197
	24 Aug 11	-5.7	-0.210
	04 Sep 11	-5.1	-0.186
	26 Sep 11	-5.4	-0.198
	Mean $\overline{\mu}$	-5.1	-0.189
	Standard deviation σ	0.4	0.016

The difference between the cross sections of the pre-explosion DEMs and the post-explosion DEMs becomes clearly obvious in both directions and represent the change in elevation caused by the June 2011 explosion. The maximum change in elevation is about -20 m.

6.3.7 Comparison of TanDEM-X based results with aero-photogrammetric observations

To analyze the accuracy of the TanDEM-X-based topographic and volumetric change estimates, the results were compared with a study that was conducted by James and Varley (2012), who used oblique and archive photographs to study the lava dome of Volcán de Colima in the same time interval as covered by TanDEM-X acquisitions. The photographs were recorded with a consumer camera during four over-flights with a light aircraft, resulting in four DEMs with an accuracy of about 1 m in horizontal and vertical directions, respectively (James and Varley, 2012; James and Robson, 2012). James and Varley (2012) used structure-from-motion and multi-view stereo algorithms to process point clouds from each set of images. Georeferencing was performed using features identified in additional orthoimagery as well as in the image sets. The pixel resolution of the orthoimages is with one meter very high, however, the quality of their own orthorectification is unknown. Additionally, orthoimagery gives no vertical control points. James and Varley (2012) therefore defined the relative heights of the control points by rotating the point cloud until the flat upper surface of the lava dome was horizontal. The described procedure was undertaken for one set of photographs and all other DEMs were then georeferenced using the updated ground control points of the first survey. This results in four DEMs from photographies taken on 15 November 2007, 26 December 2010, 27 May 2011, and 26 December 2011. The coregistration of the DEMs guaranteed their proper alignment. Thus, it allowed to assess the dome volume as well as the change in dome volume due to the 2011 explosion.

The upper images in Figure 6.12 show three of the photogrammetric DEMs in map view, two of which were acquired before the explosion on 26 December 2010 and on 27 May 2011 and one after the explosion on 26 December 2011. The images clearly show the shape of the lava dome, which is higher than the surrounding area, as well as the crater rim to the east. The topographic change between the pre-explosion images and the post-explosion image becomes already obvious here.

For a comparison of the TanDEM-X-based results with the photogrammetric ones, the low-pass filtered TanDEM-X DEMs were converted from geographic to UTM coordinates (UTM zone 13 N) and interpolated using linear interpolation to the grid spacing of the photogrammetric DEMs, which is 1 m. The lower three images of Figure 6.12 show the two pre-explosion TanDEM-X DEMs acquired on 08 and 19 June 2011 and the post-explosion TanDEM-X DEM acquired on 04 September 2011. The shape of the lava dome becomes also obvious here, as well as the topographic change between pre- and post-explosion DEMs. Only the crater rim visible in the photogrammetric DEMs is missing in the TanDEM-X-based DEMs. This can easily be explained by the geometrical decorrelation at the eastern flank that was described in Section 6.3.5.

Figure 6.13 compares the cross sections from west to east at 2158119 N (upper two graphs) and from south to north at 645049 W (lower two graphs) from the pho-

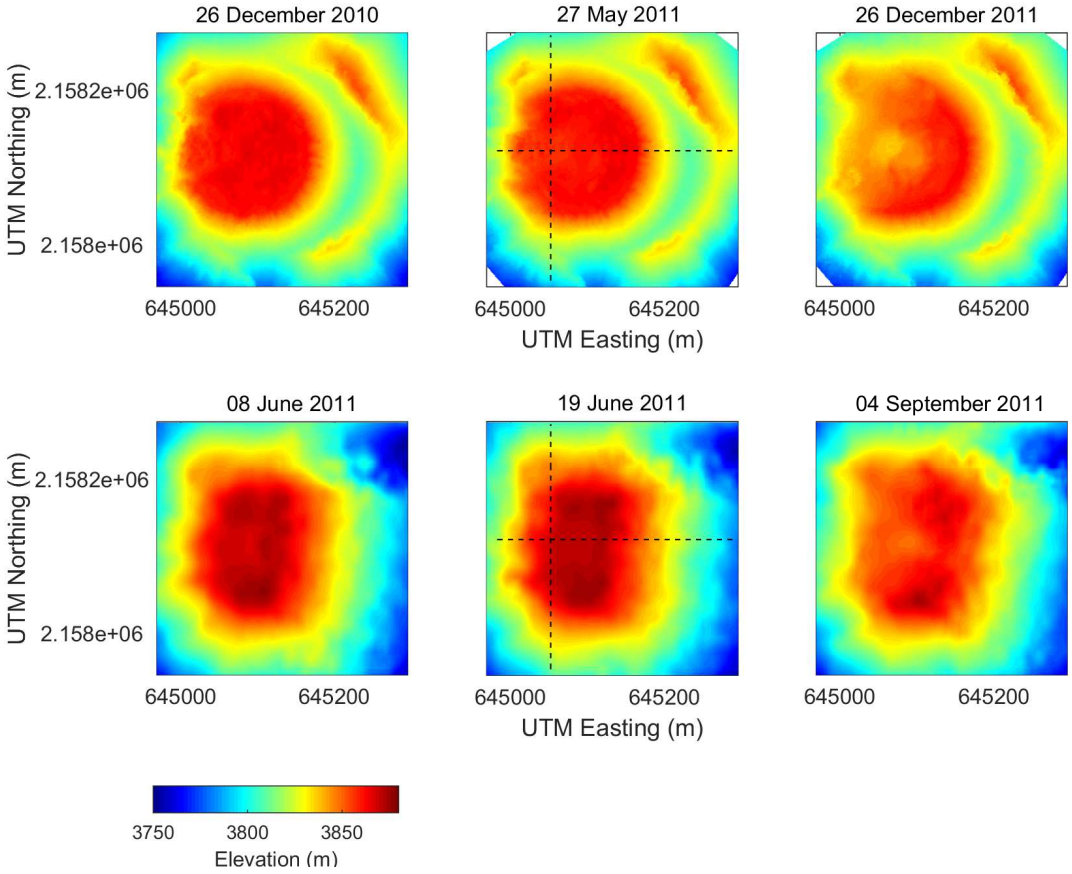

Figure 6.12 – Map view of digital elevation models. Upper images: photogrammetric DEMs, lower images: TanDEM-X DEMs. The dotted lines show the location of the cross sections depicted in Figure 6.13.

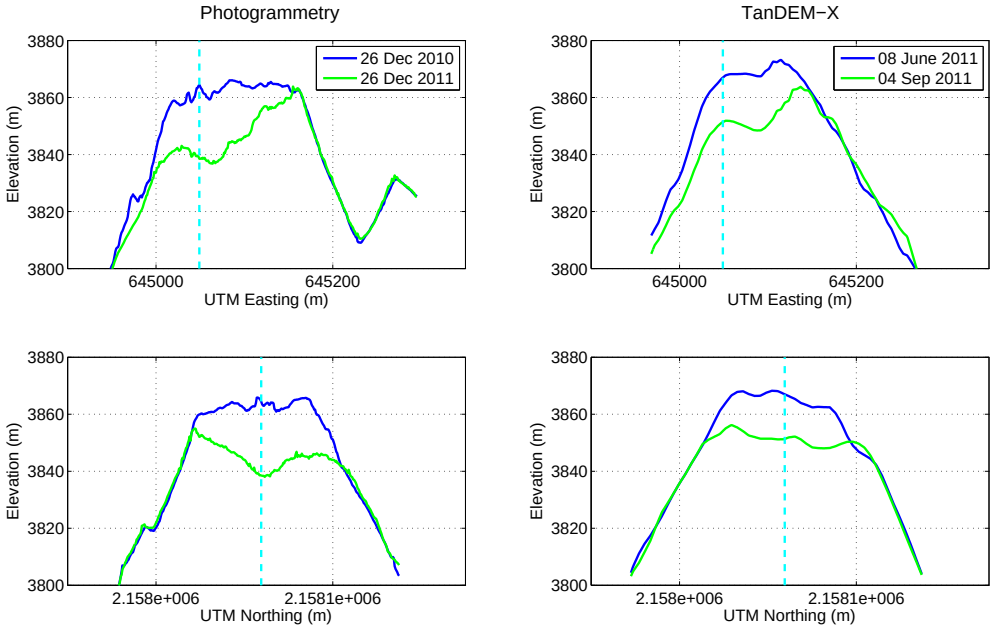

Figure 6.13 – Cross sections of photogrammetric DEMs (left) and TanDEM-X DEMs (right) in UTM coordinates (UTM zone 13 N). The upper graphs show the cross sections from west to east at 2158119 N and the lower graphs show the cross sections from south to north at 645049 W. The light blue vertical line in the cross sections shows the intersection of the other cross section.

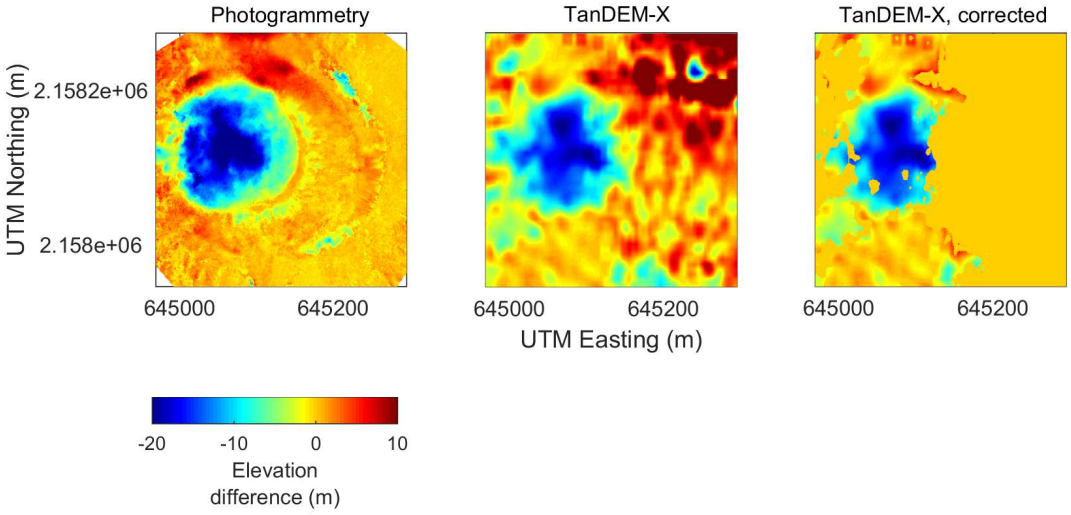

Figure 6.14 – Low-pass filtered elevation differences based on photogrammetry (left) and based on TanDEM-X (center). The image at the right is the TanDEM-X-based difference image corrected by the coherence image as described in Section 6.3.5.

togrammetric DEMs and for a TanDEM-X example, showing each time one pre-explosion DEM and a post-explosion DEM. The locations of the cross sections are shown in Figure 6.12. The cross sections of the photogrammetric DEMs and the TanDEM-X DEMs show a comparable shape. The topographic change is obvious in all cross sections and measures about -20 m at its highest points.

Finally, Figure 6.14 compares the calculated elevation differences from both image sets. The left image shows the photogrammetric result. The image in the center shows the low-pass filtered TanDEM-X result. The same elevation change is observed in both images and is represented as a blue circle. However, the area east-northeast to the elevation change is affected by geometrical decorrelation. Therefore, the right image shows the coherence corrected TanDEM-X difference map that was developed in Section 6.3.5. The error prone areas are well masked out. However, the mask also affects the topographic change at its eastern margin which is likely to result in an underestimation of the volumetric change.

A direct comparison of the DEMs is not possible as the absolute heights of the photogrammetric DEMs differ compared to those of the TanDEM-X DEMs. This is apparent in Figures 6.12 and 6.13. Additionally, the data pairs from aerophotogrammetry and TanDEM-X are slightly shifted against each other, so that it was not possible to compare the different DEMs directly.

The volumetric changes calculated in both studies are quite similar. Using aerophotogrammetric DEMs, James and Varley (2012) result in a volumetric change of -0.190×10^6 m^3. This was also found by the TanDEM-X double differential approach considering all post-explosive TanDEM-X images (see Tab. 6.2). The mean volumetric change calculated with TanDEM-X is -0.189×10^6 m^3.

6.3.8 Uncertainty estimation for TanDEM-X elevation differences in mountainous terrain

The Merapi as well as the Colima test sites have clearly demonstrated the difficulties to generate DEMs in steep mountainous terrain. This section therefore analyzes the

quality of a series of DEMs from data acquired between end of June 2011 and December 2012. During this time, no volcanic activity was recorded at Volcán de Colima. The available data pairs are optimal for validating the DEM repeatability. Table 6.3 gives an overview of the data pairs and their acquisition parameters used in addition to the post-explosion data pairs from Table 6.2. Altogether, 26 data pairs were analyzed. The effective baselines of all data pairs range between 47.4 m and 160.3 m, and the height of ambiguity is between 31.0 m and 108.3 m. The mean coherence of the data pairs varies between 0.61 and 0.78 and the incidence angle amounts to around 32.38°.

Table 6.3 – TanDEM-X observation times of Volcán de Colima for the validation data pairs including acquisition parameters.

Acquisition date	Effective baseline (m)	Height of ambiguity (m)	Average coherence	Mean incidence angle (°)
11 Apr 2012	161.9	30.7	0.61	32.39
22 Apr 2012	159.1	31.2	0.61	32.39
03 May 2012	155.1	32.0	0.62	32.39
14 May 2012	154.3	32.2	0.61	32.39
25 May 2012	152.3	32.6	0.62	32.39
08 Jul 2012	141.9	35.0	0.65	32.39
19 Jul 2012	138.2	35.9	0.65	32.39
30 Jul 2012	137.3	36.1	0.66	32.38
21 Aug 2012	132.4	37.5	0.67	32.39
01 Sep 2012	131.3	37.8	0.66	32.38
12 Sep 2012	125.3	39.6	0.67	32.39
04 Oct 2012	115.9	42.8	0.67	32.39
15 Oct 2012	112.7	44.0	0.66	32.39
26 Oct 2012	108.4	45.8	0.69	32.39
06 Nov 2012	86.0	58.8	0.71	32.37
17 Nov 2012	76.1	66.1	0.73	32.37
28 Nov 2012	69.0	73.1	0.73	32.39
20 Dec 2012	52.2	97.8	0.76	32.38
31 Dec 2012	47.4	108.3	0.76	32.38

The processing applied for the uncertainty analysis resembles the processing described in Section 6.3.2. However, since the main interest is not in deriving topographic changes, a different data pair was processed first to be used as reference topography phase ϕ^*_{topo} and all data pairs, including the post-explosion data pairs listed in Table 6.1, were processed again based on this reference topography. This time, the data pair acquired on 24 August 2011 was arbitrarily chosen as reference topography to produce 26 DEMs with a pixel spacing of about 6 m in each direction.

Since a DEM differencing approach was employed for studying topographic and volumetric changes at Volcán de Colima, also elevation differences were analyzed. For estimating the accuracy of the elevation differences, three reference areas were chosen. Figure 6.15 shows a mean amplitude image of Volcán de Colima calculated using the post-explosion data pairs listed in Table 6.2, in which the locations of the reference areas are marked. Each of the areas has an extension of 0.037 km^2 (31 x 41 pixel), which is the same size as for analyzing the lava dome changes in Section 6.3.6.

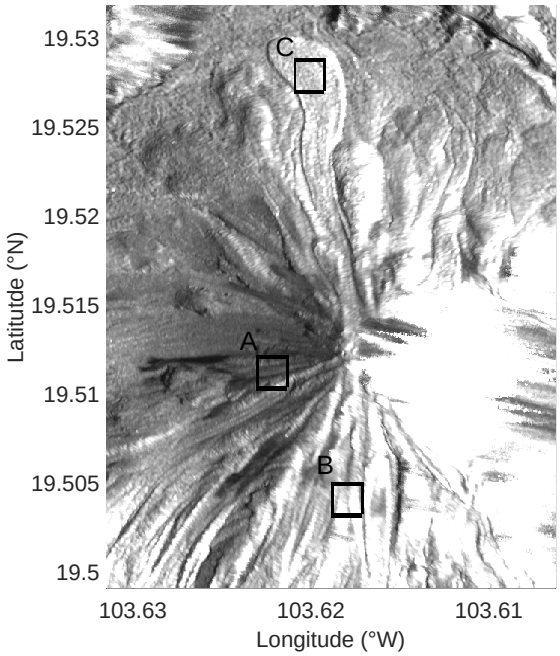

Figure 6.15 – Mean amplitude image of Volcán de Colima which shows the location of the reference areas A to C.

Table 6.4 – Elevation values of the reference areas from a mean DEM of all data pairs.

	Mean Elevation (m)	Minimum Elevation (m)	Maximum Elevation (m)	Elevation difference (m)
Area A	3549	3468	3633	165
Area B	3255	3183	3322	139
Area C	3123	3112	3136	24

All reference areas are located within a radius of about 2 km around the summit. The crater area itself was not chosen for validation because although Volcán de Colima remained quiet in the analyzed time interval, smaller activity like rockfall or landslides may have altered the topography. Only areas in the north, south, and west of the crater are appropriate for validation procedures because the eastern slopes of the volcano are affected by foreshortening and layover in descending orbit.

The major difference between the reference areas is their elevation as well as their gradient. To achieve trustworthy elevation values, all 26 DEMs were used to calculate a mean DEM. Table 6.4 gives an overview of the elevation values of each reference area for the calculated mean DEM.

Reference area A shows with 3549 m the highest mean elevation and reference area C with 3123 m the lowest elevation with respect to all reference areas. Also regarding the elevation difference between maximum and minimum elevation, reference area A shows with 165 m the highest value and reference area C with only 24 m the lowest.

The present research focuses on elevation differences analyzed in Section 6.3.6 to investigate lava dome changes at Volcán de Colima. Therefore, the uncertainty

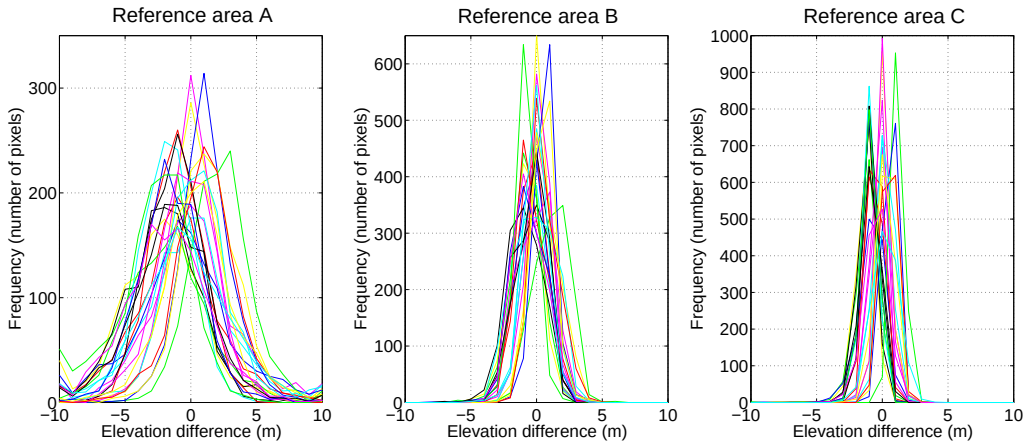

Figure 6.16 – Histograms of the elevation differences for reference areas A to C. Each color represents the values for one elevation difference with respect to the reference DEM acquired on 19 July 2012.

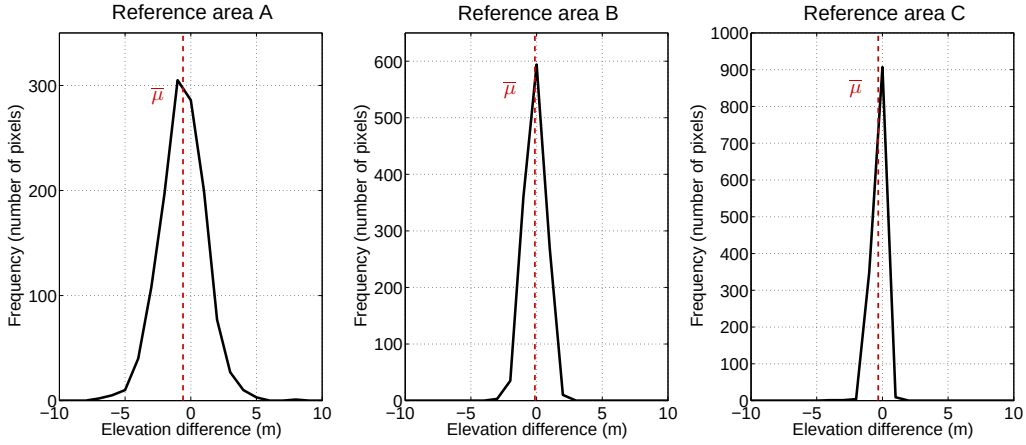

Figure 6.17 – Histograms of the mean elevation differences from all elevation differences for reference areas A to C. The mean over all elevation differences $\overline{\mu}$ is shown in each graph with the dotted red vertical line.

estimation also deals with elevation differences. First, the data pair for 24 August 2011 used for the calculation of the reference topography phase ϕ^*_{topo} was tested to build elevation differences. However, since the calculated DEM differences revealed an offset of about 2 m compared to most of the other DEMs, the data pair acquired on 19 July 2012 was randomly chosen to build elevation differences and was subtracted from each data pair in the geocoded domain. All presented results are therefore with respect to this data pair.

Figure 6.16 shows histograms for each elevation difference for reference area A (left), reference area B (center), and reference area C (right). A legend is not given as the interest is not on the individual difference images, but in their general behavior. Figure 6.17 shows the distribution of the mean elevation differences calculated separately for each of the reference areas.

Regarding the histograms, three different quantities can generally be distinguished (see Sec. 5.2.5). The first one is the mean offset over all DEMs $\overline{\mu}$. The second one considers the reproducibility, i.e., the standard deviation of the individual mean

Table 6.5 – Statistical analysis of the elevation differences in the chosen reference areas.

	Mean $\overline{\mu}$ (m)	Standard deviation σ_μ(m)
Area A	-0.59	4.16
Area B	-0.13	1.09
Area C	-0.32	0.62

over all difference maps σ_μ, and the third quantity analyzes the standard deviation σ of the individual data pairs (Fig. 6.16). Table 6.5 gives values for the first two quantities. The detailed values for the third quantity (σ), are given in Tables 6.6 to 6.8.

The histograms show that all elevation differences are centered around zero which indicates that no systematic error is existent. This can also be seen in the mean $\overline{\mu}$ given in Table 6.5 as well as in the mean for each difference image μ in Tables 6.6 to 6.8. The mean offset of $\overline{\mu}$ is -0.35 m with respect to all reference areas. The error given with σ_μ is highest for reference area A with 4.16 m and with 0.62 m lowest for reference area C. The varying reproducibility characteristic of the reference areas is displayed in Figure 6.16.

The precision of the single data pairs is given with the standard deviation σ for each elevation difference in Tables 6.6 to 6.8. The standard deviation is highest for the differences of reference area A and lowest for reference area C.

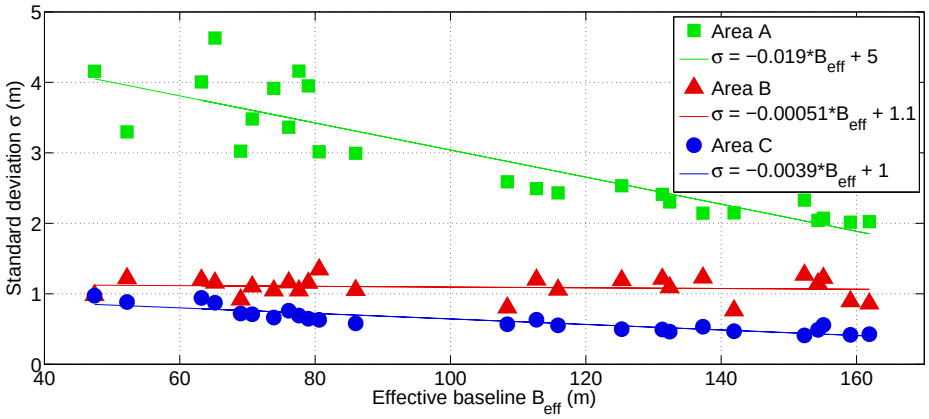

Figure 6.18 – Relationship between effective baseline and standard deviation of the elevation differences for reference areas A to C.

The characteristics of the elevation differences of the reference areas will be discussed in the following. Figure 6.18 shows how the standard deviation σ calculated for each elevation difference map correlates with the effective baselines of the corresponding data pairs. Two general relationships are observable from the figure. The first one is related to the characteristics of the reference areas. Since reference area A is the steepest area, and reference area C the flattest, one can see that the steeper the slope, the higher the standard deviation σ generally is. The second relationship can be seen considering each of the reference areas individually. From areas A and C, it

is visible that the larger the effective baseline, the smaller the standard deviations σ is. This is not significantly obvious for reference area B.

Table 6.6 – Statistics of elevation differences for reference area A. Reference is the data pair from 19 July 2012.

Acquisition date	Min (m)	Max (m)	Mean μ (m)	Standard deviation σ (m)
30 Jun 2011	-22.16	27.01	-2.14	3.95
11 Jul 2011	-28.77	32.84	0.14	4.16
22 Jul 2011	-17.03	27.74	-0.24	3.91
02 Aug 2011	-12.90	23.26	-1.07	3.48
24 Aug 2011	-26.94	63.16	-2.34	4.63
04 Sep 2011	-17.92	14.52	-0.70	4.01
26 Sep 2011	-13.95	10.87	-2.07	3.01
11 Apr 2012	-7.09	7.19	0.19	2.02
22 Apr 2012	-13.35	10.12	0.00	2.02
03 May 2012	-9.13	5.86	-1.85	2.07
14 May 2012	-10.76	4.54	-1.15	2.04
25 May 2012	-6.53	18.73	2.25	2.33
08 Jul 2012	-23.52	11.16	1.18	2.15
30 Jul 2012	-9.90	11.97	-1.33	2.14
21 Aug 2012	-8.32	9.72	1.41	2.30
01 Sep 2012	-9.83	13.75	-0.34	2.41
12 Sep 2012	-10.51	13.08	0.38	2.53
04 Oct 2012	-10.55	10.46	1.07	2.43
15 Oct 2012	-11.58	10.62	-1.51	2.49
26 Oct 2012	-10.80	30.41	-2.22	2.59
06 Nov 2012	-12.15	19.09	-1.52	2.99
17 Nov 2012	-15.64	26.43	-1.41	3.36
28 Nov 2012	-15.13	25.56	0.56	3.02
20 Dec 2012	-14.07	25.92	-1.85	3.30
31 Dec 2012	-17.68	31.69	-0.31	4.16
Mean	-14.25	19.43	-0.59	2.94

Table 6.7 – Statistics of elevation differences for reference area B. Reference is the data pair from 19 July 2012.

Acquisition date	Min (m)	Max (m)	Mean μ (m)	Standard deviation σ (m)
30 Jun 2011	-7.48	2.91	-0.85	1.15
11 Jul 2011	-2.84	4.20	0.22	1.05
22 Jul 2011	-4.64	3.10	0.09	1.05
02 Aug 2011	-5.73	3.02	-0.37	1.10
24 Aug 2011	-6.27	2.83	-0.73	1.16
04 Sep 2011	-7.60	3.43	-0.38	1.20
26 Sep 2011	-7.26	2.95	-0.89	1.34
11 Apr 2012	-2.83	3.45	0.29	0.86
22 Apr 2012	-4.86	3.19	0.06	0.89
03 May 2012	-6.31	2.79	-0.70	1.22
14 May 2012	-5.20	2.75	-0.38	1.15
25 May 2012	-2.83	5.79	1.16	1.27
08 Jul 2012	-2.70	4.36	0.62	0.76
30 Jul 2012	-5.25	3.02	-0.48	1.23
21 Aug 2012	-2.83	4.24	0.66	1.09
01 Sep 2012	-4.54	2.79	-0.21	1.21
12 Sep 2012	-2.62	3.84	0.33	1.19
04 Oct 2012	-2.73	5.43	0.61	1.06
15 Oct 2012	-5.89	2.43	-0.58	1.20
26 Oct 2012	-4.75	1.83	-0.81	0.80
06 Nov 2012	-3.69	4.00	-0.35	1.05
17 Nov 2012	-5.75	4.42	-0.39	1.16
28 Nov 2012	-3.12	4.42	0.46	0.92
20 Dec 2012	-4.74	3.97	-0.58	1.22
31 Dec 2012	-5.29	3.51	-0.06	0.98
Mean	-4.71	3.55	-0.13	1.09

Table 6.8 – Statistics of elevation differences for reference area C. Reference is the data pair from 19 July 2012.

Acquisition date	Min (m)	Max (m)	Mean μ (m)	Standard deviation σ (m)
30 Jun 2011	-6.85	0.96	-1.26	0.65
11 Jul 2011	-5.43	1.77	-0.15	0.69
22 Jul 2011	-3.91	2.11	0.01	0.66
02 Aug 2011	-4.78	1.68	-0.66	0.71
24 Aug 2011	-10.48	1.81	-1.15	0.87
04 Sep 2011	-4.49	2.75	-0.76	0.94
26 Sep 2011	-5.55	0.86	-1.18	0.63
11 Apr 2012	-3.18	1.53	0.08	0.43
22 Apr 2012	-1.24	1.86	0.06	0.42
03 May 2012	-5.79	0.59	-0.97	0.56
14 May 2012	-3.71	0.93	-0.54	0.49
25 May 2012	-0.10	2.53	1.16	0.41
08 Jul 2012	-4.02	2.36	0.61	0.47
30 Jul 2012	-7.06	0.75	-0.82	0.53
21 Aug 2012	-1.04	3.00	0.47	0.46
01 Sep 2012	-3.55	1.33	-0.28	0.49
12 Sep 2012	-1.82	2.08	0.33	0.50
04 Oct 2012	-1.16	2.70	0.49	0.55
15 Oct 2012	-9.36	1.21	-0.94	0.63
26 Oct 2012	-5.51	0.82	-0.94	0.57
06 Nov 2012	-5.17	0.90	-0.58	0.58
17 Nov 2012	-7.58	1.04	-0.89	0.76
28 Nov 2012	-8.34	2.01	0.16	0.72
20 Dec 2012	-5.38	2.42	-0.47	0.88
31 Dec 2012	-3.10	3.58	0.22	0.97
Mean	-4.75	1.74	-0.32	0.62

To analyze also the volume estimates presented in Section 6.3.6, volumes were calculated for each elevation difference map. Table 6.9 summarizes the results. The volumes should be zero since no topographic change is expected. Each value for a volume represents the error for the corresponding elevation difference.

The calculated volumes differ for each elevation difference and also in between each reference area. The mean calculated volume is with -0.004×10^6 m^3 smallest for reference area B. Figure 6.19 shows the relationship between the absolute calculated volume and the effective baseline. A linear dependency between baseline and estimated volume is not observable since the calculated volumes show a strong variation with respect to all baselines and all reference areas. However, the calculated volume is generally higher in reference area A, compared to the other two reference areas, but this does not hold for all elevation differences. This indicates that the error of the elevation differences is higher for reference area A compared to reference areas B and C, respectively.

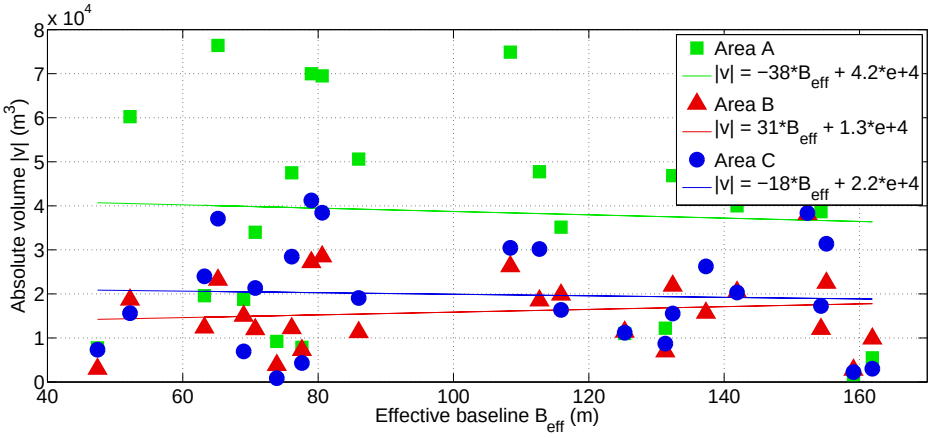

Figure 6.19 – Relationship between effective baseline and absolute calculated volume for reference areas A to C.

In Table 6.9, it is observed that the standard deviation σ is highest for the steepest reference area, area A. This can also be seen in Figure 6.19. Whereas the standard deviation σ for all calculated volumes for reference areas B and C is 0.018×10^6 m^3 and 0.021×10^6 m^3, respectively, it is with 0.042×10^6 m^3 twice as large for reference area A. Since the analyzed reference areas have the same size as the area that was analyzed to calculate the changes at the lava dome, the standard deviations of the reference areas were not accumulated like done for Tolbachik.

6.4 Discussion

The average change in dome volume due to the July 2011 explosion is estimated with -0.189×10^6 m^3. This result is corroborated by aerophotogrammetric observations with -0.190×10^6 m^3. The standard deviation of the individual mean over all elevation differences σ_μ is with 4.16 m highest for the steepest reference area A. However, σ_μ is with 1.09 and 0.62 m comparably low for reference areas B and C, respectively. This trend also holds true for the standard deviation of the calculated volumes σ, which is with 0.042×10^6 m^3 comparably high for reference area A. The standard deviation

Table 6.9 – Volume calculation for reference areas A - C. Reference is the data pair from 19 July 2012.

Acquisition date	Volume x 10^6 m^3 Reference area		
	A	B	C
30 Jun 2011	-0.07	-0.027	-0.041
11 Jul 2011	0.008	0.007	-0.004
22 Jul 2011	-0.009	0.004	0.001
02 Aug 2011	-0.034	-0.012	-0.021
24 Aug 2011	-0.076	-0.023	-0.037
04 Sep 2011	-0.020	-0.012	-0.024
26 Sep 2011	-0.070	-0.029	-0.038
11 Apr 2012	0.005	0.010	0.003
22 Apr 2012	-0.002	0.003	0.002
03 May 2012	-0.061	-0.022	-0.031
15 May 2012	-0.039	-0.012	-0.017
24 May 2012	0.073	0.038	0.038
08 Jul 2012	0.040	0.020	0.020
30 Jul 2012	-0.043	-0.016	-0.026
21 Aug 2012	0.047	0.022	0.016
01 Sep 2012	-0.012	-0.007	-0.009
12 Sep 2012	0.011	0.011	0.011
04 Oct 2012	0.035	0.020	0.016
15 Oct 2012	-0.048	-0.018	-0.030
26 Oct 2012	-0.075	-0.026	-0.030
06 Nov 2012	-0.051	-0.011	-0.019
17 Nov 2012	-0.048	-0.012	-0.028
28 Nov 2012	0.019	0.015	0.007
20 Dec 2012	-0.060	-0.019	-0.016
31 Dec 2012	-0.008	-0.003	0.007
Mean	-0.019	-0.004	-0.010
Standard deviation σ	0.042	0.018	0.021

of the volume calculated for reference areas B and C is with 0.018 and 0.021×10^6 m^3 only half of what was calculated for area A.

The calculated values for reference area A and B seem reasonable considering the high difference in elevation of 165 m within reference area A compared to the low difference in elevation of 24 m within area C. However, since the elevation difference is with 139 m also comparably high for reference area B, the calculated values should rather be close to those of area A than close to those of area C. This indicates that besides steepness, different characteristics like exposition of the slope to the satellite sensor or the roughness of the area should be considered. The elevation differences of area A are probably of worse quality since the slope is tilted away from the SAR sensor. At the same time, the material properties of areas A, B, and C could be different, leading to a decreased quality of the elevation differences in area A compared to the other areas.

Summing up, the correlation between the standard deviation of measured elevation values with the effective baseline shows a clear behavior for steep areas. Whereas the standard deviation σ is higher for small baselines, it linearly decreases for longer baselines. From this result, it can be recommended that baselines larger than 100 m should be used for generating DEMs at steep-sided stratovolcanoes. At this point, it should be mentioned that the randomly chosen reference DEM from data acquired on 19 July 2012 used as reference topography within the uncertainty estimation has been acquired with an effective baseline of 138.2 m (see Tab. 6.3), which probably has an additional effect on the results.

6.5 Conclusions and perspectives

Chapter 6 presents the application of TanDEM-X to study small topographic changes of up to -20 m at steep-sided stratovolcano Colima. The methodology developed at Tolbachik volcano to map and measure the extent and flow volume of basaltic lava flows could successfully be applied to study also dome-building volcanoes. Few changes were necessary regarding the processing of data in a more fissured terrain and are mainly due to geometric distortions in the data. Although the topography is challenging, small topographic changes are observable and volumetric changes can be calculated. The volume estimate based on TanDEM-X imagery of -0.189×10^6 m$^3 \pm 0.027 \times 10^6$ m^3 was corroborated by aerophotogrammetric observations. A visual image comparison between TanDEM-X DEMs and photogrammetric DEMs shows a good agreement of the results obtained by both methodologies.

Analyzing 26 TanDEM-X data pairs in a time period where no volcanic activity was recorded at Volcán de Colima gives a very good insight into the accuracy of the developed methodology, especially considering the quality of repeatedly generated DEMs. The mean error of the elevation differences was calculated with ± 0.35 m. The strong correlation between slope steepness and effective baselines is one explanation for errors in the DEMs and the derived volcanological products.

For continuing research at Volcán de Colima, the following topics are suggested:

DEM generation from ascending and descending acquisition geometries. The Colima example has clearly demonstrated that TanDEM-X allows for an estimate of volumetric changes at steep-sided stratovolcano Colima on a 20 m scale.

However, the identified effects due to foreshortening and layover influenced the generation of reliable DEMs which cover the whole volcanic edifice. Depending on the type of volcanic activity and its major directions, the usage of ascending and descending data pairs should be considered. Also a combination of both acquisition geometries will be helpful, but only if an ascending and a descending data pair are acquired within a short time period. Two methodologies regarding the fusion of DEMs are suggested in Section 7.2.

Repeat-pass analysis of the TanDEM-X data. Although the bandwidth is less compared to TerraSAR-X StripMap data acquired in monostatic mode, the TanDEM-X data could be used in a repeat-pass analysis to reveal deformations of the surface on a cm scale. Combined with the TanDEM-X differential approach to assess larger topographic changes on meter level, this may result in a more comprehensive analysis of lava dome changes on very different scales and will give broad insights into the volcanic behavior of Volcán de Colima.

Analyzing the new episode of activity that started in January 2013 and continues until today. After the explosive event in June 2011 analyzed in the present study, Volcán de Colima remained quiet until a new episode of volcanic activity started on 06 January 2013 with an initial vulcanian explosion followed by three further vulcanian events all of which occurred in January 2013 (Salzer et al., 2014; Zobin et al., 2015). The activity led to the formation of a new crater in the lava dome formed between 2007 and 2011. A new lava dome filled this crater in the successive activity which lasted until October 2013 (Zobin et al., 2015). The methodology presented in this chapter could be used to gain insights into this new episode of activity. Also the large amount of data pairs acquired in ascending orbit could be included. As the activity continues until today, high resolution topographic data needs to be updated very frequently, and may be used among others to assess total volumes of pyroclastic density currents, which occurred for instance on 11 July 2015.

7. Conclusions and Outlook

7.1 Conclusions

The general research question was whether TanDEM-X InSAR could be used as a basis to quantify topographic and volumetric changes in non-coherent areas around volcanoes, aiming to overcome the limitations of ground-based, optical, and repeat-pass interferometric methods.

The present thesis gives a comprehensive overview of the application of bistatic TanDEM-X data to study active volcanoes. In detail, a methodology based on a differential DEM analysis using repeatedly acquired TanDEM-X data pairs was developed. It has been tested at different sites to study various volcanological features. The most important characteristics of the developed differential DEM approach are summarized in the following.

The developed TanDEM-X-based differential DEM approach ...

- **is independent of space, time, and weather conditions.**

  Weather and time independence is per se given since radar data can be acquired during day- and nighttime and at all weather conditions. TanDEM-X also realizes a global coverage. The developed methodology was tested within this thesis in three different geographical regions at three different volcanoes at three different times. Whereas at Merapi volcano volumetric changes due to a major eruption were investigated, the study at Volcán de Colima focused on a smaller explosive event. With the lava flow development analysis of Tolbachik, the methodology could be further adapted to study a third kind of volcanic activity.

- **overcomes the limitations of ground-based, optical, and repeat-pass interferometric methods.**

  Major limitations of ground-based data collection result from the fact that people as well as equipment are probably at risk during an eruption. Using satellite

data is likely to solve this problem. The circumstance that field measurements are often very limited in space is not an issue for remote-sensing analyses. Using radar data such as TanDEM-X also overcomes the limitations of optical images which are often prone to bad viewing conditions due to cloud cover often accompanying volcanic activity. The characteristic that TanDEM-X acquires two radar images simultaneously facilitates the generation of DEMs each time a bistatic data pair is acquired. This clearly demonstrates the advantage compared to repeat-pass interferometric approaches.

- **observes different kinds of volcanic activity.**

  The examples shown at Volcán de Colima and Merapi have demonstrated that the developed methodology can be used successfully to study changing lava domes on a very broad scale. The differential DEM approach was further tested successfully to study the development of a basaltic lava flow at Tolbachik.

- **reveals topographic and volumetric changes due to volcanic activity.**

  Topographic and volumetric changes could be measured at all test sites. The measured volume estimates range from -0.189 x 10^6 m^3 for small lava dome changes at Volcán de Colima, over -18.9 x 10^6 m^3 for the large changes observed at Merapi due to the 2010 major eruption, to the extensive field of newly extruded lava at Tolbachik due to the 2012-13 eruption with 530 x 10^6 m^3. The approach therefore proved its applicability to study topographic changes on various scales and over different time periods. Whereas the explosion at Volcán de Colima was a single event and the Merapi eruption was treated as one – due to the data availability only before and after the event – the investigations at Tolbachik have shown the potential of the approach to measure a changing topography of a volcanic complex over time. The approach has further been tested to study the lava flows at Etna volcano in Sicily, Italy, that were extruded between June and October 2011 (Raible and Kubanek, 2016) as well as at Shiveluch volcano in Kamchatka, where lava flows from June 2011 to September 2014 have been investigated (Heck et al., 2016).

- **enables to derive magma ascent rates.**

  Information on the mass transport through volcanic systems can be valuable information for eruption forecasting. One important but not easily determined value is the magma ascent rate. Measurements in the field are often incomplete, and aerophotogrammetric data acquisitions in a regular interval are rare. However, using the differential DEM approach developed within this thesis, the magma ascent rates were successfully calculated for the Tolbachik 2012-13 eruption.

- **contributes to numerical flow models.**

  Any kind of flow models (lava flows, pyroclastic flows, lahars) require up-to-date and high-resolution topographical information as well as information on topographic changes that occur during an eruption. Although not tested within this thesis, the TanDEM-X approach was already used successfully to model the lava flows extruded during the 2012-13 Tolbachik eruption. The methodology and results have been published in Kubanek et al. (2015a). It is

mentioned here to show the wide impact of the TanDEM-X methodology and derived results.

- **produces reliable results.**

  This is probably the most interesting point with respect to the scientific community. The present research has clearly demonstrated the applicability to study active volcanism with the bistatic differential DEM approach.

  Validating the results at Merapi was very challenging. However, a rough comparison to amplitude-based interpretations conducted to assist in evacuation procedures during the 2010 eruption corroborated the TanDEM-X estimates. A comparison of the elevation of the different DEMs with data from permanent GPS stations around Merapi's summit gave further insight into the quality of the dome-change estimates due to the eruption. Using the two post-eruption DEMs, the average change in dome volume was calculated with $-18.9 \times 10^6\,m^3$. The standard deviation σ for the elevation difference between the two post-eruption DEMs was calculated with 14.79 m, and the difference in dome volume estimates using the two post-eruption DEMs amounted to $\pm 0.4 \times 10^6\,m^3$, which is 2 % of the average dome volume change.

  At Tolbachik, a total of 18 bistatic TanDEM-X data pairs were analyzed, resulting in a total volume of the extruded lava flow of $530 \times 10^6\,m^3$. The validation was done using the same data pairs used to map and measure the extruding lava flows. Using four reference areas around the flow field where no topographic change was expected resulted in a standard deviation σ of $7.3 \times 10^6\,m^3$ for the volumetric change estimates, which is about 1.4 % of the calculated lava flow volume. The mean error for the elevation differences was calculated with ± 0.21 m and the mean standard deviation over all areas and different maps σ_μ amounted to ± 1.63 m.

  At Volcán de Colima, nine data pairs were used to investigate the lava dome changes due to the June 2011 explosion, resulting in a volumetric change of $-0.189 \times 10^6\,m^3$. The topographic and volumetric changes revealed from TanDEM-X imagery were compared to aerophotogrammetric estimates from James and Varley (2012). The results correlate very well. The quality of the TanDEM-X-based approach and results was further estimated using 26 data pairs from a period when no volcanic activity occurred. Analyzing elevation differences in three reference areas led to a mean standard deviation of $0.027 \times 10^6\,m^3$ for the volumetric change estimates. This is about 14 % of the calculated volumetric change due to the June 2011 explosion. The mean error of the elevation differences was calculated with ± 0.35 m, and the mean standard deviation σ_μ with ± 1.96 m.

The developed data processing approach demonstrates the great potential of the bistatic TanDEM-X data to study active volcanism. The differential TanDEM-X DEM analysis revealed topographic and volumetric changes around active volcanoes ranging from a ten meter scale to several hundred meters of height changes. Within this study – and this is probably one of the major differences compared to other studies – InSAR was used as an independent methodology to quantitatively assess large topographic changes produced during the rapidly changing morphologies of volcanoes during eruptions. Assuming that the TanDEM-X data are provided

without delay after data acquisition, the developed methodology could be used in near real-time to observe topographic changes along volcanoes during eruptions. The repeat interval of 11 days sounds long at first. However, considering that both acquisition geometries (ascending and descending) as well as different incidence angles are theoretically usable for one test site, the TanDEM-X data could give valuable information on changing topography during an ongoing eruption. The fact that volcanic activity often lasts for several days, weeks, or even years, makes TanDEM-X a good additional source for collecting information during recent eruptions and the data has great potential to assist in decision making for evacuation procedures. Furthermore, high-resolution DEMs have a great value in various applications, in particular when modeling volcanic deposits. In addition, repeat-pass differential InSAR studies require actual, high-resolution DEMs, which underscores the potential of utilizing data of the TanDEM-X mission to generate up-to-date and high-resolution DEMs.

7.2 Outlook

The main problems and challenges of the developed TanDEM-X-based differential DEM approach result from (1) problems due to the presence of vegetation, which was discovered during the time-series analysis conducted at Tolbachik volcano, and (2) the side-looking imaging geometry of SAR systems, especially when using the data in strongly fissured terrain, i.e., when analyzing steep-sided stratovolcanoes like Merapi or Volcán de Colima. Some approaches are discussed in the following to overcome the discovered limitations of the developed approach.

To overcome the limitations of the TanDEM-X-based differential DEM approach, ...

- **the vegetation and its structure could be further analyzed.**

  The vegetation was discovered as one of the major issues regarding the Tolbachik test site and influenced the analysis in two different ways. The first one was due to the problems concerning volume scattering that hindered the extraction of the real flow area, which would have been possible without the vegetation influence from the backscatter intensity or from the coherence. The second influence was due to the vegetation that led to misleading elevation values in the summer data pairs and thus had a negative effect on the deramping function used to correct the unwrapped phase. Considering only the utilization of the non-vegetated area for deramping is likely to improve the best-fit-plane correction. Another way would be to distinguish between 'positive' and 'negative' lava flows. Flows are called positive, when no vegetation is present and the flows become obvious in the differencing approach. The negative flows are those that are not displayed properly due to vegetation. Different cases need to be distinguished. They are firstly related to the presence of vegetation in the different data pairs, especially with respect to the pre-eruption and syn-/post-eruption data pairs and secondly related to the interaction between flow and vegetation. Then, the positive and negative flows can be treated separately, to catch up with a special analysis of the negative flows. Dealing with the negative flows will have to be studied in more detail. Interesting questions are, how the backscatter will change if the flow enters a forest but

the vegetation persists, or what will happen if the pre-eruption DEM contains vegetation destroyed by a flow in the post-eruption DEM.

- **the radar shadow could be used to improve DEM generation.**

  Eineder and Suchandt (2003) developed an approach in which the random phase values in the shadow zones are replaced by a constant value to facilitate phase unwrapping and DEM reconstruction. The unwrapped phase will provide a maximum estimation of the topographic heights in the shadow area. Differencing two interferograms including one of which was corrected will lead to a minimal estimation of the volume. Eineder and Suchandt (2003) achieve reasonable results for an explosion crater in Tschad. The main difference to the Merapi data pairs is that this crater is surrounded by a flat area. Merapi has the aforementioned layover areas located directly besides the shadow area, which will have to be considered when adapting the approach of Eineder and Suchandt (2003) at steep-sided stratovolcanoes. However, reprocessing of the Merapi data pairs with first subtracting the topographic phase ϕ^*_{topo} during processing will result in a better basis to implement the approach of Eineder and Suchandt (2003).

- **data from ascending and descending orbits could be fused into a single DEM.**

  Combining data from ascending and descending orbits, especially for the Merapi and Volcán de Colima test sites, but also for any other stratovolcano, will improve the quality of the DEMs and thus the volume estimates. Both examples have clearly demonstrated the problems due to geometrical decorrelation which are most likely to occur along stratovolcanoes. Regarding Merapi, the direct transition from layover to shadow-affected areas along the walls of the crater built during the 2010 eruption can cause severe unwrapping errors. The application of shadow masks for calculating the volumetric loss due to the eruption was a first attempt to improve the estimates. However, also data acquired in ascending orbit can help here. In the optimal case, areas that are displayed properly in the ascending data pair will be decorrelated in the descending data pair and vice versa, as shadow and layover areas are contrarily distributed in the DEMs of the opposite acquisition geometries. In addition, also data pairs acquired in the same orbit, but with varying incidence angles may be used.

  Although there is no pre-October 2010 ascending data pair available for Merapi, several post-October 2010 data pairs (starting in June 2011) can be analyzed to reduce the errors resulting from geometrical decorrelation. Regarding Volcán de Colima, several data pairs in ascending orbit exist as well, which are very helpful for the suggested analysis of the post-January 2013 activity of the volcano. A helpful characteristic is that ascending and descending data pairs are acquired on consecutive days, which facilitates DEM generation of the volcano without topographic changes in between.

  For the fusion, two different approaches can generally be considered, which are (1) mosaicking (Pasquali et al., 1994; Knöpfle et al., 1998) and (2) the probability density approach of Eineder and Adam (2005).

Besides its limitations, the developed differential DEM approach has shown great potential to study active volcanoes at different scales. Nevertheless, various research questions remain that should be addressed in the future.

Open research questions are:

- **Will the implementation of the exact bistatic acquisition geometry in the open-source software DORIS significantly improve the results?**

  The described usage of half the length of the perpendicular baseline (the effective baseline) for the TanDEM-X data is hitherto a rough approximation of the real bistatic acquisition geometry.

  In monostatic mode, the backscattered signal is received by the same satellite that emitted the electromagnetic wave before, and the motion of the satellite between emitting and receiving is considered in the calculation. In bistatic mode, the active satellite emits the signal and both – the active and the passive satellite – receive it. There is no change for the active satellite compared to the monostatic mode. In contrast, an additional signal propagation delay caused by the varying distance between the active and the passive satellites has to be considered for the passive satellite with respect to a pixel on the ground (Duque et al., 2012).

  To corroborate the approximation of the bistatic acquisition geometry implemented in DORIS reveals reliable results, two TanDEM-X data pairs were processed using the commercial software GAMMA developed by the GAMMA Remote Sensing and Consulting AG. The comparison was successful as both softwares reveal comparable results for the topographic change caused by a developing lava flow.

  Another way would be to compare the results obtained with the DORIS software package with results obtained by processing the data with the InSAR software system GENESIS developed at DLR.

- **Can the developed approach reveal lava dome growth?**

  Lava domes are one of the most hazardous volcanic phenomena, but are at the same time only imperfectly understood. The highly viscous magma of andesitic volcanoes often does not extrude visibly at the surface, but emerges from a vent hidden beneath a growing/changing lava dome. The magma ascent rate can therefore only be estimated by monitoring the changing shape of the volcano summit.

  As no dome growth took part at any of the volcanoes in the analyzed time period, the important question concerning the applicability of the developed methodology to study a growing lava dome remains open. A first approach has been tested by Heck et al. (2016), who used the developed approach to study lava flows and lava dome changes over time at Shiveluch volcano, Kamchatka.

- **Can the bistatic data be used in repeat-pass mode to reveal deformation on a cm scale?**

  The TanDEM-X data can probably be utilized within a repeat-pass analysis to reveal cm changes of the investigated volcano. Processing the data like it was

acquired in monostatic mode, the radar image from the active satellite should be used. One major advantage is that the bistatic data can be used at the same time to reveal a DEM, which can help in the repeat-pass processing to remove the topographic phase component. The results from the repeat-pass analysis may be used when very small displacements are observable. In times when the deformation is too large causing decorrelation in the repeat-pass analysis, the differential DEM approach will still give insights into the larger topographic changes.

- **Can the developed approach also be applied to study topographic changes that are not related to volcanology?**

  The developed approach can probably be used to analyze processes in different target regions with moderate topographic changes that are not related to volcanoes. Examples are manifold, reaching from landslide observations over glacial retreat to mining activities. The only requirement here is that the topographic displacements are – depending on the slope – larger than a few meters to achieve reasonable results.

Appendix

A. Additional material for Tolbachik volcano

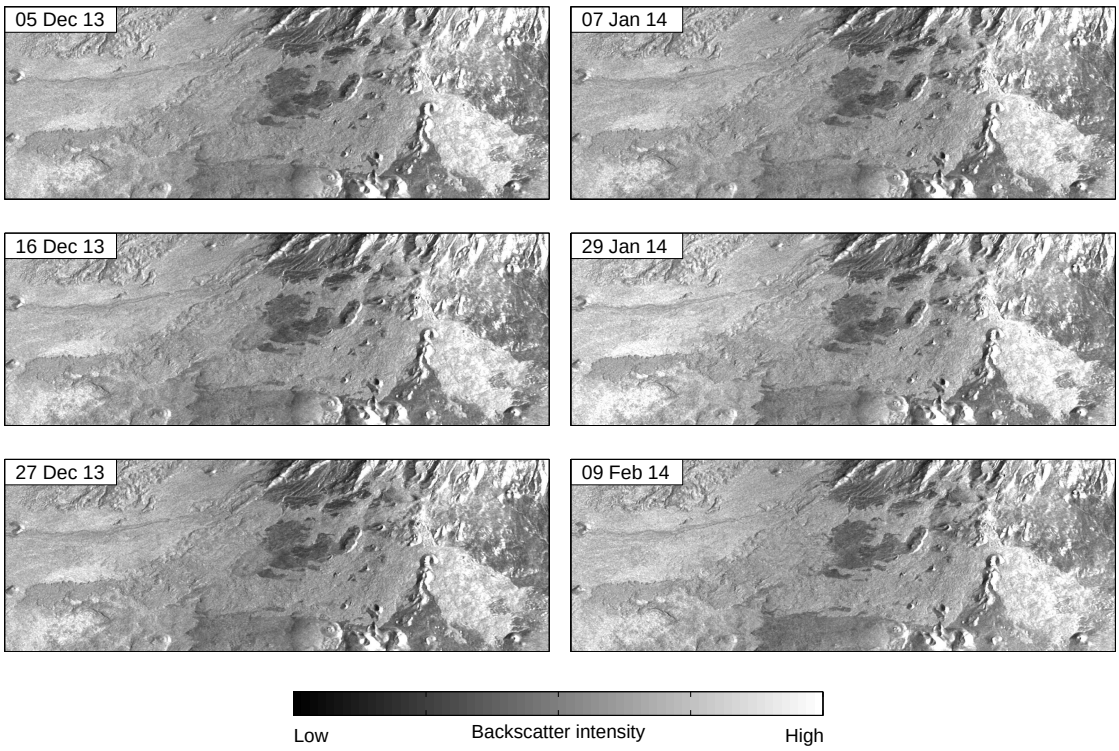

Figure A.1 – Amplitude images: results for the post-eruption data pairs acquired between December 2013 and February 2014.

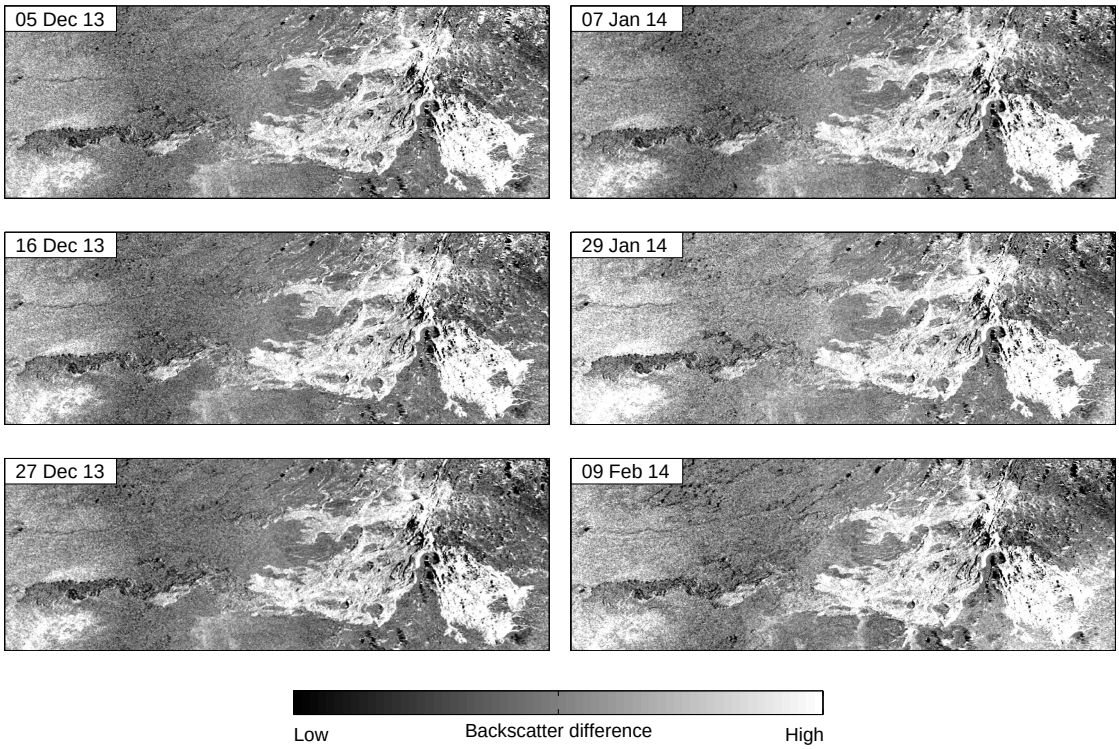

Figure A.2 – Amplitude difference images of the post-eruption data pairs acquired between December 2013 and February 2014 with respect to the pre-eruption data pair acquired on 15 November 2012.

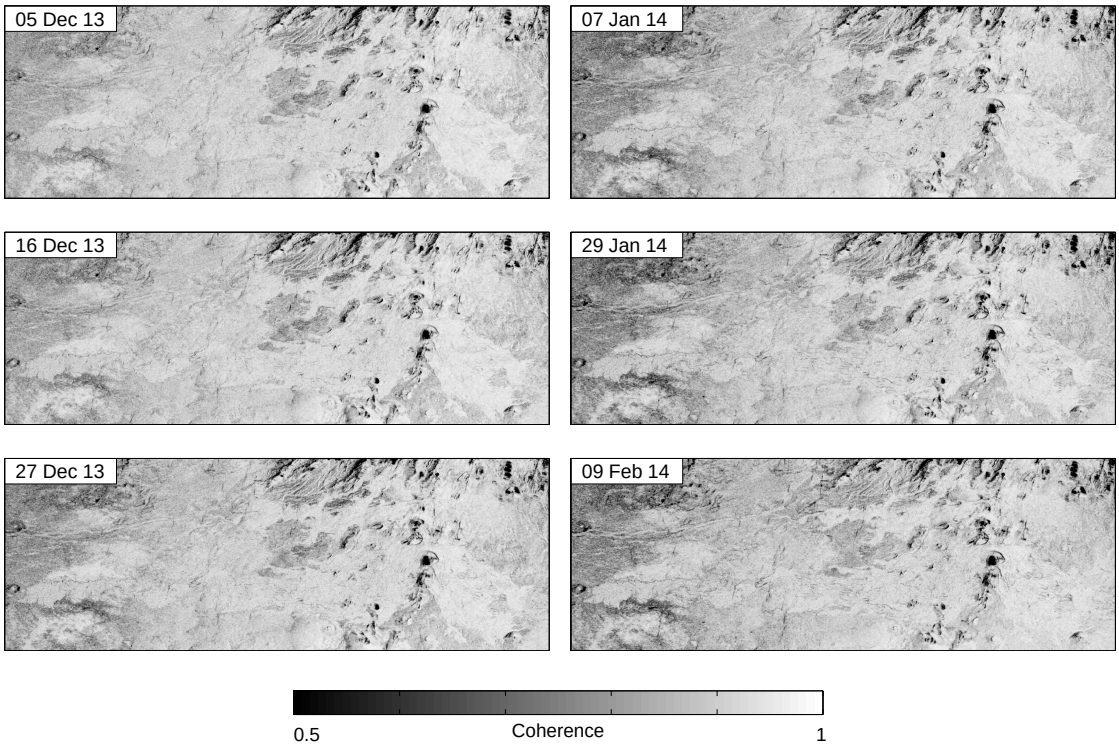

Figure A.3 – Coherence images: results for the post-eruption data pairs acquired between December 2013 and February 2014.

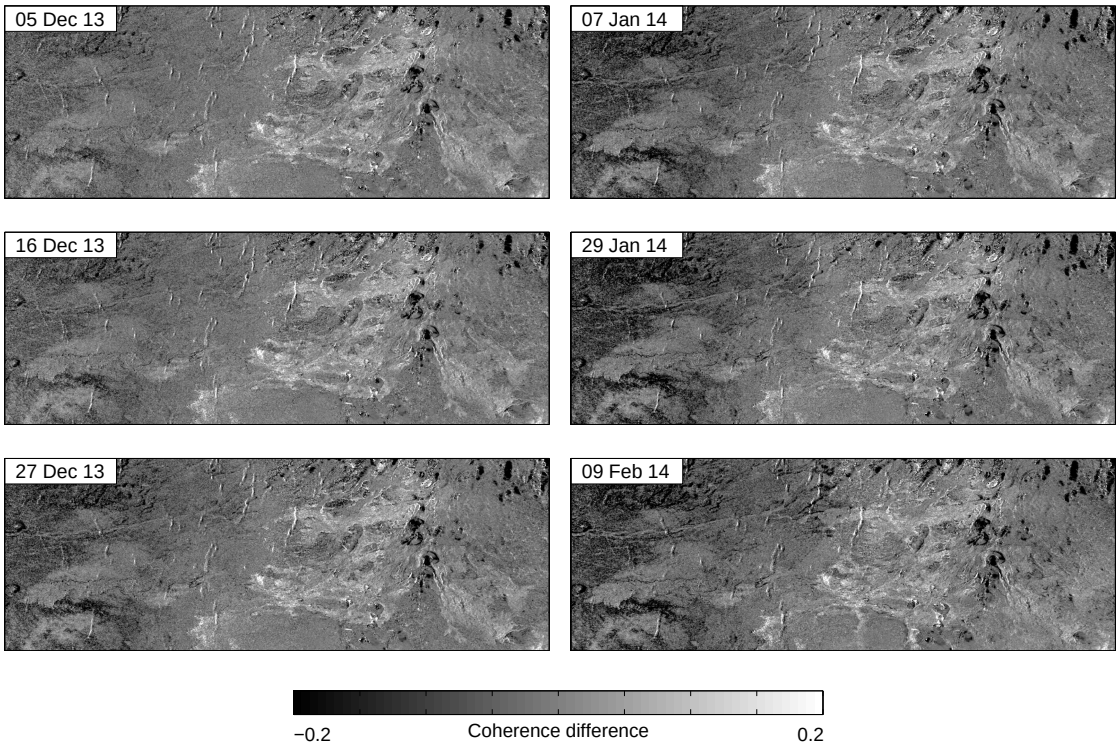

Figure A.4 – Coherence difference images of the post-eruption data pairs acquired between December 2013 and February 2014 with respect to the pre-eruption data pair acquired on 15 November 2012.

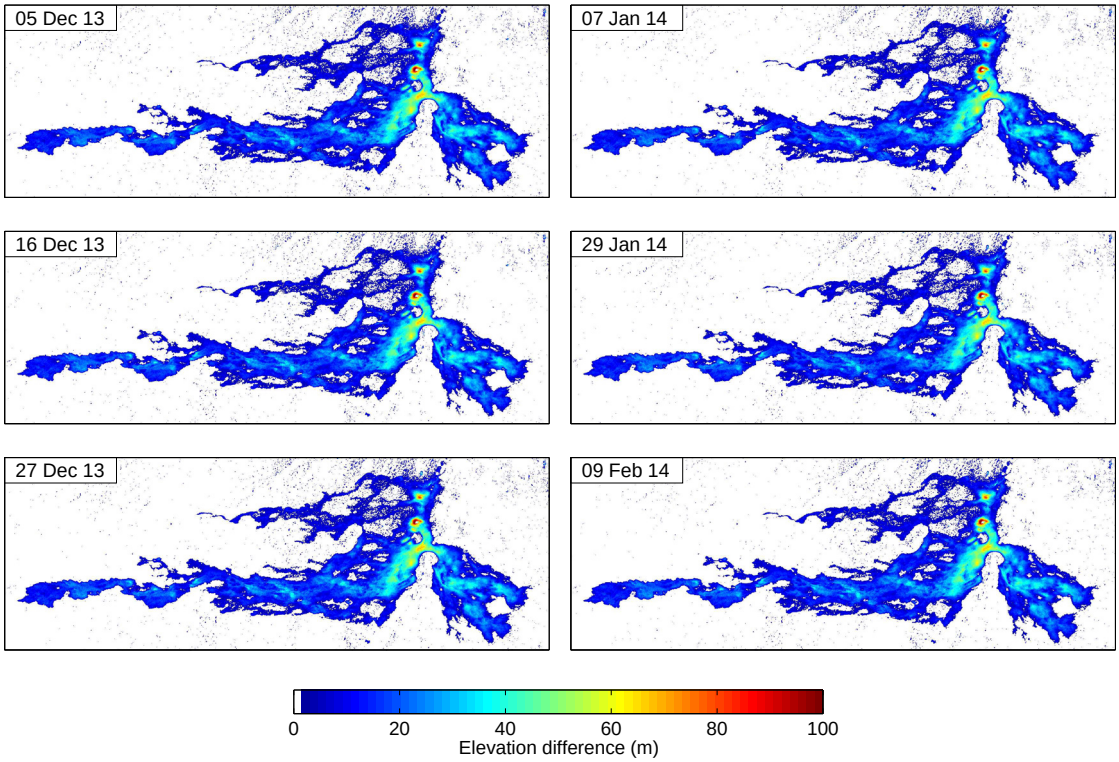

Figure A.5 – Differential TanDEM-X results showing the lava flows in the post-eruption images acquired between December 2013 and February 2014. The colors show the elevation difference between the reference topography and the date specified in each elevation difference.

Bibliography

Abdurachman EK, Bourdier JL, Voight B (2000) Nuées ardentes of 22 November 1994 at Merapi volcano, Java, Indonesia. Journal of Volcanology and Geothermal Research 100:345–361, DOI 10.1016/S0377-0273(00)00144-X

Albertz J (2009) Einführung in die Fernerkundung. Grundlagen der Interpretation von Luft- und Satellitenbildern. Wissenschaftliche Buchgesellschaft Darmstadt, Germany

Albino F, Semets B, d'Oreye N, Kervyn N (2015) High-resolution TanDEM-X DEM: An accurate method to estimate lava flow volumes at Nyamulagira Volcano (D. R. Congo). Journal of Geophysical Research: Solid Earth 120:4189–4207, DOI 10.1002/2015JB011988

Aubert M, Dana I IN, Gourgaud A (2000) Internal structure of the Merapi summit from self-potential measurements. Journal of Volcanology and Geothermal Research 100:337–343, DOI 10.1016/S0377-0273(00)00143-8

Bähr H (2013) Orbital effects in spaceborne synthetic aperture radar interferometry. PhD thesis, German Geodetic Commission (Deutsche Geodätische Kommission, DGK), series C 719. Bavarian Academy of Sciences and Humanities, Munich, Germany.

Baldi P, Fabris M, Marsella M, Monticelli R (2005) Monitoring the morphological evolution of the Sciara del Fuoco during the 2002-2003 Stromboli eruption using multi temporal photogrammetry. ISPRS Journal of Photogrammetry and Remote Sensing 59:199–211, DOI 10.1016/j.isprsjprs.2005.02.004

Bamler R (2000) Principles of synthetic aperture radar. Surveys in Geophysics 21:147–157, DOI 10.1023/A:1006790026612

Bamler R, Hartl P (1998) Synthetic aperture radar interferometry. Inverse Problems 14:R1–R54, DOI 0266-5611/98/040001+54$19.50

de Bélizal E, Lavigne F, Hadmoko DS, Degeai JP, Dipayana GA, Mutaqin BW, Marfai MA, Coquet M, Le Mauff N, Robin AK, Vidal C, Cholik N, Aisyah N (2013) Rain-triggered lahars following the 2010 eruption of Merapi volcano, Indonesia: A major risk. Journal of Volcanology and Geothermal Research 261:330–347, DOI 10.1016/j.jvolgeores.2013.01.010

Belousov A, Belousova M, Ewards B, Volynets A, Melnikov D (2015) Overview of the precursors and dynamics of the 2012-13 basaltic fissure eruption of Tolbachik volcano, Kamchatka, Russia. Journal of Volcanology and Geothermal Research 299:19–34, DOI 10.1016/j.jvolgeores.2015.04.009

Berger M, Moreno J, Johannessen JA, Levelt PF, Hanssen RF (2012) ESA's sentinel missions in support of Earth system science. Remote Sensing of Environment 120:84–90, DOI 10.1016/j.rse.2011.07.023

Bianchessi N, Righini G (2008) Planning and scheduling algorithms for the COSMO-SkyMed constellation. Aerospace Science and Technology 12:535–544, DOI 10.1016/j.ast.2008.01.001

Bignami C, Ruch J, Chini M, Neri M, Buongiorno MF, Hidayati S, Sayudi DS, Surono (2013) Pyroclastic density current volume estimation after the 2010 Merapi volcano eruption using X-band SAR. Journal of Volcanology and Geothermal Research 261:236–243, DOI 10.1016/j.jvolgeores.2013.03.023

Borla Tridon D, Bachmann M, Schulze D, Ortega-Míguez C, Donata Polimeni M, Martone M, Böer J, Zink M (2013) TanDEM-X: DEM acquisition in the third year era. International Journal of Space Science and Engineering 1:1–14, DOI 10.1504/IJSPACESE.2013.059270

Brenguier F, Shapiro N, Campillo M, Ferrazzini V, Duputel Z, Coutant O, Nercessian A (2008) Towards forecasting volcanic eruptions using seismic noise. Nature Geoscience 1:126–130, DOI 10.1038/ngeo104

Bürgmann R, Rosen P, Fielding E (2000) Synthetic Aperture Radar Interferometry to measure Earth's surface topography and its deformation. Annual Review of Earth and Planetary Sciences 28:169–209, DOI 10.1146/annurev.earth.28.1.169

Calder ES, Luckett R, Sparks RSJ, Voight B (2002) Mechanisms of lava dome instability and generation of rockfalls and pyroclastic flows at Soufrière Hills Volcano, Montserrat. In: Druitt T, Kokelaar B (eds) The eruption of Soufrière Hills Volcano, Montserrat, from 1995 to 1999, Geological Society, London, Memoirs 21, pp 173–190

Calvari S, Neri M, Pinkerton H (2003) Effusion rate estimations during the 1999 summit eruption on Mount Etna, and growth of two distinct lava flow fields. Journal of Volcanology and Geothermal Research 119:107–123, DOI 10.1016/S0377-0273(02)00308-6

Casadevall T, Rose W, Gerlach T, Greenland LP, Ewert J, Wunderman R, Symonds R (1983) Gas emissions and the eruptions of Mount St. Helens through 1982. Science 221(4618):1383–1385, DOI 10.1126/science.221.4618.1383

Charbonnier SJ, Gertisser R (2008) Field observations and surface characteristics of pristine block-and-ash flow deposits from the 2006 eruption of Merapi Volcano, Java, Indonesia. Journal of Volcanology and Geothermal Research 177:971–982, DOI 10.1016/j.jvolgeores.2008.07.008

Chen CW, Zebker HA (2001) Two-dimensional phase unwrapping with use of statistical models for cost functions in nonlinear optimization. Journal of the Optical Society of America A 18(2):338–351, DOI 10.1364/JOSAA.17.000401

Coppola D, James MR, Staudacher T, Cigolini C (2010) A comparison of field- and satellite-derived thermal flux at Piton de la Fournaise: implications for the

calculation of lava discharge rate. Bulletin of Volcanology 72:341–356, DOI 10.1007/s00445-009-0320-8

Covello F, Battazza F, Coletta A, Lopinto E, Fiorentino C, Pietranera L, Valentini G, Zoffoli S (2010) COSMO-SkyMed an existing opportunity for observing the Earth. Journal of Geodynamics 49:171–180, DOI 10.1016/j.jog.2010.01.001

Curlander JC, McDonough RN (1991) Synthetic aperture radar: Systems and signal processing. Wiley

Diefenbach A, Crider J, Schilling S, Dzurisin D (2012) Rapid, low-cost photogrammetry to monitor volcanic eruptions: an example from Mount St. Helens, Washington, USA. Bulletin of Volcanology 74:579–587, DOI 10.1007/s00445-011-0548-y

Diefenbach AK, Bull KF, Wessels RL, McGimsey RG (2013) Photogrammetric monitoring of lava dome growth during the 2009 eruption of Redoubt Volcano. Journal of Volcanology and Geothermal Research 259:308–316, DOI 10.1016/j.jvolgeores.2011.12.009

DORIS Manual (2009) Delft Object-oriented Radar Interferometric Software User's manual and technical documentation Version: v4.02. Delft University of Technology, Delft, The Netherlands, URL http://doris.tudelft.nl.

Doubik P, Hill BE (1999) Magmatic and hydromagmatic conduit development during the 1975 Tolbachik eruption, Kamchatka, with implications for hazards assessment at Yucca Mountain, NV. Journal of Volcanology and Geothermal Research 91:43–64, DOI 10.1016/S0377-0273(99)00052-9

Duque S, Balss U, Rossi C, Fritz T, Balzer W (2012) TanDEM-X Payload Ground Segment. CoSSC Generation and Interferometric Considerations. Tech. rep., Remote Sensing Technology Institute, TD-PGS-TN-3129.

Dvigalo VN, Svirid IY, Shevchenko AV (2014) The first quantitative estimates of parameters for the Tolbachik fissure eruption of 2012-2013 from aerophotogrammetric observations. Journal of Volcanology and Seismology 8(5):3–11, DOI 10.1134/S0742046314050029

Dvorak JJ, Dzurisin D (1997) Volcano geodesy: the search for magma reservoirs and the formation of eruptive vents. Reviews of Geophysics 35:343–384, DOI 10.1029/97RG00070

Ebmeier SK, Biggs J, Mather TA, Ellitott JR, Wadge G, Amelung F (2012) Measuring large topographic change with InSAR: Lava thicknesses, extrusion rate and subsidence at Santiaguito volcano, Guatemala. Earth and Planetary Science Letters 335-336:216–225, DOI 10.1016/j.epsl.2012.04.027

Eineder M (2003) Problems and solutions for InSAR digital elevation model generation of mountainous terrain. In: Proc. of Fringe 2003 Workshop, Frascati, Italy, 1.-5. Dec. 2003

Eineder M, Adam N (2005) A maximum-likelihood estimator to simultaneously unwrap, geocode, and fuse SAR interferograms from different viewing geometries into one digital elevation model. IEEE Tansactions on Geoscience and Remote Sensing 43(1):24–36, DOI 10.1109/TGRS.2004.838389

Eineder M, Suchandt S (2003) Recovering radar shadow to improve interferometric phase unwrapping and DEM reconstruction. IEEE Tansactions on Geoscience and Remote Sensing 41(12):2959–2962, DOI 10.1109/TGRS.2003.821266

Elias T, Sutton AJ (2012) Sulfur dioxide emission rates from Kilauea Volcano, Hawaii, 2007-2010. Tech. rep., U.S. Geological Survey

Fedotov SA, Chirkov AM, Gusev NA, Kovalev GN, Slezin Y (1980) The large fissure eruption in the region of Plosky Tolbachik Volcano in Kamchatka, 1975-1976. Bulletin of Volcanology 43(1):47–60, DOI 10.1007/BF02597610

Ferretti A, Monti-Guarnieri A, Prati C, Rocca F, Massonnet D (2007a) InSAR principles: Guidelines for SAR Interferometry. Processing and interpretation. Part A Interferometric SAR image processing and interpretation. Tech. rep., ESA Publications, ESTEC, The Netherlands

Ferretti A, Monti-Guarnieri A, Prati C, Rocca F, Massonnet D (2007b) InSAR principles: Guidelines for SAR Interferometry. Processing and interpretation. Part B InSAR processing: a practical approach. Tech. rep., ESA Publications, ESTEC, The Netherlands

Fritz T, Bräutigam B, Krieger G, Zink M (2012) TanDEM-X Ground Segment. TanDEM-X Experimental Product Description. Tech. rep., Remote Sensing Technology Institute, TD-GS-PS-3028

Fu LL, Holt B (1982) Seasat views oceans and sea ice with synthetic aperture radar. Tech. rep., Jet Propulsion Laboratory (JPL)

Gertisser R, Charbonnier SJ, Troll VR, Keller J, Preece K, Chadwick JP, Barclay J, Herd RA (2011) Merapi (Java, Indonesia): anatomy of a killer volcano. Geology Today 27(2):57–62, DOI 10.1111/j.1365-2451.2011.00786.x

Geudtner D (1995) Die interferometrische Verarbeitung von SAR-Daten des ERS-1 (in German). PhD thesis, Forschungsbericht 95-28, Deutsche Forschungsanstalt für Luft- und Raumfahrt (DLR), Oberpfaffenhofen, Germany

Ghiglia DC, Pritt MD (1998) Two-dimensional phase unwrapping: theory, algorithms, and software. John Wiley & Sons, New York, USA

Global Volcanism Program (2013) Report on Colima (Mexico). In: Wunderman R (ed) Bulletin of the Global Volcanism Network, vol 38, Smithsonian Institution, DOI 10.5479/si.GVP.BGVN201304-341040.

Goldstein R (1995) Atmospheric lilmitations to repeat-track radar interferometry. Geophysical Research Letters 22:2517–2520, DOI 10.1029/95GL02475

Goldstein R, Werner C (1998) Radar interferogram filtering for geophysical applications. Geophysical Research Letters 25:4035–4038, DOI 10.1029/1998GL900033

Goldstein RM, Engelhardt H, Kamb B, Frolich RM (1993) Satellite radar interferometry for monitoring ice sheet motion: Application to an Antarctic ice stream. Science 262:1525–1530, DOI 10.1126/science.262.5139.1525

Gonzáles JH, Bachmann M, Krieger G, Fiedler H (2010) Development of the TanDEM-X calibration concept: Analysis of systematic errors. IEEE Transactions on Geoscience and Remote Sensing 48(2):716–726, DOI 10.1109/TGRS.2009.2034980

Gonzáles MB, Ramírez JJ, Navarro C (2002) Summary of the historical eruptive activity of Volcán de Colima, Mexico 1519-2000. Journal of Volcanology and Geothermal Research 117:21–46, DOI 10.1016/S0377-0273(02)00233-0

Gordeev EI, Murav'ev YD, Samoilenko SB, Volynets AO, Mel'nikov DV, Dvigalo VN (2013a) The Tolbachik fissure eruption of 2012-2013: Preliminary results. Doklady Earth Sciences 452(2):1046–1050, DOI 10.1134/S1028334X13100103

Gordeev EI, Muravyov YD, Samoylenko SB, Volynets AO, Melnikov DV, Dvigalo VN, Melekestsev IV (2013b) First results from the 2012-2013 Tolbachik fissure eruption. Bulletin of the Volcanological Society of Japan 58(2):1–8

Grishin SY (2010) Vegetation changes under the impact of volcanic ashfall (Tolbachinsky Dol, Kamchatka). Russian Journal of Ecology 41(5):436–439, DOI 10.1134/S1067413610050127

Grishin SY (2015) Tolbachik eruption in 2012-2013 in Kamchatka, Russia. DIWPA News Letter (32):12–15

Grotzinger J, Jordan TH, Press F, Siever R (2008) Allgemeine Geologie (in German). Spektrum akademischer Verlag Berlin Heidelberg, Germany

Hajnsek I, Busche T (2013) 4th TDM Science Team Meeting: Organizational Issues. In: Presentation at TerraSAR-X/TanDEM-X Science Team Meeting. Oberpfaffenhofen, Germany, 10.-14. Jun. 2013

Hajnsek I, Busche TE, Krieger G, Zink M, Moreira A (2014) TanDEM-X Ground Segment. Announcment of Opportunity: TanDEM-X Science Phase. Tech. rep., Microwaves and Radar Institute

Hanssen RF (2001) Radar interferometry. Data interpretation and error analysis. Kluwer Academic Publishers Dordrecht, The Netherlands

Hanssen RF, Bamler R (1999) Evaluation of interpolation kernels for SAR interferometry. IEEE Transactions on Geoscience and Remote Sensing 37:318–321, DOI 10.1109/36.739168

Harris AJL, Dehn J, Calvari S (2007) Lava effusion rate definition and measurement: a review. Bulletin of Volcanology 70:1–22, DOI 10.1007/s00445-007-0120-y

Heck A, Kubanek J, Westerhaus M, Gottschämmer E, Heck B, Wenzel F (2016) Lava emplacements at Shiveluch volcano (Kamchatka) from June 2011 to September 2014 observed by TanDEM-X SAR-Interferometry. In: General Assembly of the European Geosciences Union. Geophysical Research Abstracts. 17.-22. April 2016, Vienna, Austria, EGU2016-4401

Heck B (2003) Rechenverfahren und Auswertemodelle in der Landesvermessung. Klassische und moderne Methoden (in German). Wichmann Verlag Heidelberg, Germany

Hein A (2004) Processing of SAR data. Fundamentals, signal processing, interferometry. Springer-Verlag Berlin Heidelberg, Germany

Hooper A, Zebker H, Segall P, Kampes B (2004) A new method for measuring deformation on volcanoes and other natural terrains using InSAR persistent scatterers. Geophysical Research Letters 31:1–5, DOI 10.1029/2004GL021737

Hutchinson W, Varley N, Pyle DM, Mather TA, Stevenson JA (2013) Airborne thermal remote sensing of the Volcán de Colima (Mexico) lava dome eruption from 2007 to 2010. In: Pyle D, Mather T, Biggs J (eds) Remote-sensing of volcanoes and volcanic processes: integrating observation and modelling, vol 380, Geological Society Special Publication, DOI 10.1144/SP380.8

Inbar M, Gilichinsky M, Melekestsev I, Melnikov D, Zaretskaya N (2011) Morphometric and morphological development of Holocene cinder cones: A field and remote sensing study in the Tolbachik volcanic field, Kamchatka. Journal of Volcanology and Geothermal Research 201:301–311, DOI 10.1016/j.jvolgeores.2010.07.013

James MR, Robson S (2012) Straightforward reconstruction of 3D surfaces and topography with a camera: Accuracy and geoscience application. Journal of Geophysical Research 117:F03,017, DOI 10.1029/2011JF002289

James MR, Varley N (2012) Identification of structural controls in an active lava dome with high resolution DEMs: Volcán de Colima, Mexico. Geophysical Research Letters 39:L22,303, DOI 10.1029/2012GL054245

Kampes BM, Hanssen RF, Perski Z (2003) Radar interferometry with public domain tools. In: Fringe 2003 Workshop, Frascati, Italy, 1.-5. Dec. 2003

Knöpfle W, Strunz G, Roth A (1998) Mosaicking of digital elevation models derived by SAR interferometry. In: International Archives of Photogrammetry and Remote Sensing, 32, Part 4. ISPRS Commission IV Symposium, Stuttgart, 7.-10. Sept. 1998., pp 306–313

Krieger G, Moreira A, Fiedler H, Hajnsek I, Werner M, Younis M, Zink M (2007) TanDEM-X: A satellite formation for high resolution SAR interferometry. IEEE Tansactions on Geoscience and Remote Sensing 45(11):3317–3340, DOI 10.1109/TGRS.2007.900693

Kubanek J, Westerhaus M, Heck B (2013a) On the potential of TanDEM-X to assess complex topography. In: Proc. of ESA Living Planet Symposium, 9.-13. Sep. 2013, Edinburgh, Scotland

Kubanek J, Westerhaus M, Heck B (2013b) Topographic changes at Volcán de Colima observed by double differential InSAR using TanDEM-X. In: Proc. of ESA Living Planet Symposium, 9.-13. Sep. 2013, Edinburgh, Scotland

Kubanek J, Westerhaus M, Varley N, James MR, Heck B (2014) On using bistatic TanDEM-X data for volcano monitoring. In: Proc. of 10th European Conference on Synthetic Aperture Radar (EUSAR), 3.-5. June 2014, Berlin, Germany

Kubanek J, Richardson JA, Charbonnier SJ, Connor LJ (2015a) Lava flow mapping and volume calculations of the 2012-13 Tolbachik, Kamchatka fissure eruption using bistatic TanDEM-X InSAR. Bulletin of Volcanology 77(106):1–13, DOI 10.1007/s00445-015-0989-9

Kubanek J, Westerhaus M, Heck B (2015b) On the use of bistatic TanDEM-X images to quantify volumetric changes of active lava domes. In: International Association of Geodesy Symposia, Springer International Publishing Switzerland, DOI 10.1007/1345_2015_172

Kubanek J, Westerhaus M, Schenk A, Aisyah N, Brotopuspito KS, Heck B (2015c) Volumetric change quantification of the 2010 Merapi eruption using TanDEM-X InSAR. Remote Sensing of Environment 164:16–25, DOI 10.1016/j.rse.2015.02.027

Kugaenko Y, Titkov N, Saltykov V (2015) Constraints on unrest in the Tolbachik volcanic zone in Kamchatka prior the 2012-13 flank fissure eruption of Plosky Tolbachik volcano from local seismicity and GPS data. Journal of Volcanology and Geothermal Research 307:38–46, DOI 10.1016/j.jvolgeores.2015.05.020

Lachaise M, Eineder M, Fritz T (2007) Multi baseline SAR acquisition concepts and phase unwrapping algorithms for the TanDEM-X mission. Geoscience and Remote Sensing Symposium, 2007 IGARSS pp 5272–5276

Lavallée Y, Varley NR, Alatorre-Ibargüengoitia MA, Hess KU, Kueppers U, Mueller S, Richard D, Scheu B, Spieler O, Dingwell DB (2012) Magmatic architecture of dome-building eruptions at Volcán de Colima, Mexico. Bulletin of Volcanology 74:249–260, DOI 10.1007/s00445-011-0518-4

Li Z, Bethel J (2008) Image coregistration in SAR interferometry. In: The International Archives of the Photogrammetry, Remote Sensing and Spatial Information Sciences, vol XXXVII. Part B1.

Lu Z, Dzurisin D (2014) InSAR imaging of Aleutian volcanoes. Monitoring a volcanic arc from space. Springer-Verlag Berling Heidelberg, Germany, DOI 10.1007/978-3-642-00348-6

Lu Z, Freymueller JT (1998) Synthetic aperture radar interferometry coherence analysis over Katmai volcano group, Alaska. Journal of Geophysical Research 103:29,887–29,894, DOI 10.1029/98JB02410

Lu Z, Masterlark T, Dzurisin D (2005) Interferometric synthetic aperture radar study of Okmok volcano, Alaska, 1992-2003: Magma supply dynamics and postemplacement lava flow deformation. Journal of Geophysical Research 110:1–18, DOI 10.1029/2004JB003148

Luckett R, Loughlin S, De Angelis S, Ryan G (2008) Volcanic seismicity at Montserrat, a comparison between the 2005 dome growth episode and earlier dome growth. Journal of Volcanology and Geothermal Research 177:894–902, DOI 10.1016/j.jvolgeores.2008.07.006

Luhr JF, Carmichael ISE (1980) The Colima Volcanic Complex, Mexico. Contributions to Mineralogy and Petrology 71:343–372, DOI 10.1007/BF00374707

Lundgren P, Berardino P, Coltelli M, Fornaro G, Lanari R, Puglisi G, Sansosti E, Tesauro M (2003) Coupled magma chamber inflation and sector collapse slip observed with synthetic aperture radar interferometry on Mt. Etna volcano. Journal of Geophysical Research 108:1–15, DOI 10.1029/2001JB000657

Martone M, Bräutigam B, Krieger G (2012a) Decorrelation effects in bistatic TanDEM-X data. In: Geoscience and Remote Sensing Symposium (IGARSS), IEEE International, 22.-27. July 2012, Munich, Germany, DOI 10.1109/IGARSS.2012.6352346

Martone M, Bräutigam B, Rizzoli P, Bachmann M, Krieger G (2012b) Coherence evaluation of TanDEM-X interferometric data. ISPRS Journal of Photogrammetry & Remote Sensing 73:21–29, DOI 10.1016/j.isprsjprs.2012.06.006

Massonnet D, Rossi M, Carmona C, Adragna F, Peltzer G, Feigel K, Rabaute T (1993) The displacement field of the Landers earthquake mapped by radar interferometry. Nature 364:138–142, DOI 10.1038/364138a0

Massonnet D, Briole P, Arnaud A (1995) Deflation of Mount Etna monitored by spaceborne radar interferometry. Nature 375:567–570, DOI 10.1038/375567a0

Montenbruck O, Wermuth M, Kahle R (2011) GPS based relative navigation for the TanDEM-X mission – First flight results. Navigation 58(4):293–304, DOI 10.1002/j.2161-4296.2011.tb02587.x

Moreira A (2000) Radar mit synthetischer Apertur. Grundlagen und Signalverarbeitung (in German), Habilitationsschrift, Universität Friedericiana zu Karlsruhe (TH), Germany

Moreira A, Krieger G, Mittermayer J (2003) Satellite configuration for interferometric and/or tomographic remote sensing by means of synthetic aperture radar (SAR), U.S. Patent 6 677 884, U.S. Off. Pat. Office, Washington, DC, July 2002

Olmsted C (1993) Alaska SAR Facility Scientific User's Guide. Available at: http://nsidc.org/data/radarsat/pdfs/SciSARuserGuide.pdf

Osmanoglu B (2012) A new open-source tool for education of SAR interferometry: ADORE-DORIS. In: American Geophysical Union, Fall Meeting 2012, Abstract #ED21A-0701

Pallister J, Schneider DJ, Griswold JP, Keeler RH, Burton WC, Noyles C, Newhall CG, Ratdomopurbo A (2013) Merapi 2010 eruption — Chronology and extrusion rates monitored with satellite radar used in eruption forecasting. Journal of Volcanology and Geothermal Research 261:144–152, DOI 10.1016/j.jvolgeores.2012.07.012

Parks MM, Biggs J, England P, Mather TA, Nomikou P, Palamartchouk K, Papanikolaou X, Paradissis D, Parsons B, Pyle DM, Raptakis C, Zacharis V (2012) Evolution of Santorini Volcano dominated by episodic and rapid fluxes of melt from depth. Nature Geoscience 5:749–754, DOI 10.1038/NGEO1562

Pasquali P, Pellegrini R, Prati C, Rocca F (1994) Combination of interferograms from ascending and descending orbits. In: Geoscience and Remote Sensing Symposium, IGARSS '94. Surface and Atmospheric Remote Sensing: Technologies, Data Analysis and Interpretation, DOI 10.1109/IGARSS.1994.399244

Pierson TC, Janda RJ, Thouret JC, Borrero CA (1990) Perturbation and melting of snow and ice by the 13 November 1985 eruption of Nevado del Ruiz, Colombia, and consequent mobilization, flow and deposition of lahars. Journal of Volcanology and Geothermal Research 41:17–66, DOI 10.1016/0377-0273(90)90082-Q

Poland MP (2014) Time-averaged discharge rate of subaerial lava at Kilauea, Hawai'i, measured from TanDEM-X interferometry: Implications for magma supply and storage during 2011-2013. Journal of Geophysical Research: Solid Earth 119:5464–5481, DOI 10.1002/2014JB011132

Pritchard M, Simons M (2002) A satellite geodetic survey of large-scale deformation of volcanic centres in the central Andes. Nature 418:167–171, DOI 10.1038/nature00872

Rabus B, Eineder M, Roth A, Bamler R (2003) The shuttle radar topography mission – A new class of digital elevation models acquired by spaceborne radar. ISPRS Journal of Photogrammetry & Remote Sensing 57:241–262, DOI 10.1016/S0924-2716(02)00124-7

Raible B, Kubanek J (2016) Application of bistatic interferometry to study lava flows at Etna volcano in Italy. Tech. rep., KIT Scientific Reports, KIT Scientific Publishing (in preparation)

Rao K, Al-Jassar H, Phalke S, Rao Y, Muller JP, Li Z (2006) A study on the applicability of repeat-pass SAR interferometry for generating DEMs over several Indian test sites. International Journal of Remote Sensing 27:595–616, DOI 10.1080/01431160500239248

Ryan GA, Loughlin SC, James MR, Jones LD, Calder ES, Christopher T, Strutt MH, Wadge G (2010) Growth of the lava dome and extrusion rates at Soufrière Hills Volcano, Montserrat, West Indies: 2005-2008. Geophysical Research Letters 37:L00E08, DOI 10.1029/2009GL041477

Saepuloh A, Urai M, Aisyah N, Sunarta, Widiwijayanti C, Subandriyo, Jousset P (2013) Interpretation of ground surface changes prior to the 2010 large eruption of Merapi volcano using ALOS/PALSAR, ASTER TIR and gas emission data. Journal of Volcanology and Geothermal Research 261:130–143, DOI 10.1016/j.jvolgeores.2013.05.001

Salzer JT, Nikkhoo M, Walter TR, Sudhaus H, Reyes Dávila G, Bréton M, Arámbula R (2014) Satellite radar data reveal short-term pre-explosive displacements and a complex conduit system at Volcán de Colima, Mexico. Frontiers in Earth Science 2:1–11, DOI 10.3389/feart.2014.00012

Savov IP, Luhr JF, Navarro-Ochoa C (2008) Petrology and geochemistry of lava and ash erupted from Volcán Colima, Mexico, during 1998-2005. Journal of Volcanology and Geothermal Research 174:241–256, DOI 10.1016/j.jvolgeores.2008.02.007

Schilling SP, Thompson RA, Messerich JA, Iwatsubo EY (2008) Use of digital aerophotogrammetry to determine rates of lava dome growth, Mount St. Helens, Washington, 2004-2005. In: A volcano rekindled: The renewed eruption of Mount St. Helens, 2004-2006, U.S. Geological Survey Professional Paper, vol 1750, Sherrod, D.R. and Scott, W.E. and Stauffer, P.H., pp 145–167.

Schmincke HU (2004) Volcanism. Springer-Verlag Berlin Heidelberg, Germany

Schowengerdt RA (1983) Techniques for Image Processing and Classifications in Remote Sensing. Academic Press New York, USA

Schwäbisch M (1995) Die SAR-Interferometrie zur Erzeugung digitaler Geländemodelle (in German). Tech. rep., Deutsche Forschungsanstalt für Luft- und Raumfahrt e.V., Deutsches Fernerkundungszentrum (DFD) Oberpfaffenhofen, Germany

Senyukov SL, Nuzhdina IN, Droznina SY, Garbuzova VT, Kozhevnikova TY, Sobolevskaya OV, Nazarova ZA, Bliznetsov VE (2015) Reprint of "Seismic monitoring of the Plosky Tolbachik eruption in 2012-2013 (Kamchatka Peninsula Russia)". Journal of Volcanology and Geothermal Research 307:47–59, DOI 10.1016/j.jvolgeores.2015.07.026

Solikhin A, Thouret JC, Gupta A, Sayudi DS, Oehler JF, Liew SC (2015) Effects and behavior of pyroclastic and lahar deposits of the 2010 Merapi eruption based on high-resolution optical imagery. Journal of Volcanology and Geothermal Research 12:1–10, DOI 10.1016/j.proeps.2015.03.002

Sparks RSJ, Young SR, Barclay J, Calder ES, Cole P, Darroux B, Davies MA, Druitt TH, Harford C, Herd R, James M, Lejeune AM, Loughlin S, Norton G, Skerrit G, Stasiuk MV, Stevens NS, Toothill J, Wadge G, Watts R (1998) Magma production and growth of the lava dome of the Soufrière Hills Volcano, Montserrat, West Indies: November 1995 to December 1997. Geophysical Research Letters 25:3421–3424, DOI 10.1029/98GL00639

Stevens NF, Wadge G (2004) Towards operational repeat-pass SAR interferometry at active volcanoes. Natural Hazards 33:47–76, DOI 10.1023/B:NHAZ.0000035005.45346.2b

Stevens NF, Wadge G, Murray JB (1999) Lava flow volume and morphology from digitised contour maps: a case study at Mount Etna, Sicily. Geomorphology 28:251–261, DOI 10.1016/S0169-555X(98)00115-9

Stevens NF, Wadge G, Williams CA (2001) Post-emplacement lava subsidence and the accuracy of ERS InSAR digital elevation models of volcanoes. International Journal of Remote Sensing 22:819–828, DOI 10.1080/01431160051060246

Surono, Jousset P, Pallister J, Boichu M, Buongiorno MF, Budisantoso A, Costa F, Andreastuti S, Prata F, Schneider D, Clarisse L, Humaida H, Sumarti S, Bignami C, Griswold J, Carn S, Oppenheimer C, Lavigne F (2012) The 2010 explosive eruption of Java's Merapi volcano – a '100-year' event. Journal of Volcanology and Geothermal Research 241-242:121–135, DOI 10.1016/j.jvolgeores.2012.06.018

Sutton AJ, Elias T, Gerlach TM, Stokes JB (2001) Implications for eruptive processes as indicated by sulfur dioxide emissions from Kilauea Volcano, Hawai'i, 1979-1997. Journal of Volcanology and Geothermal Research 108:283–302, DOI 10.1016/S0377-0273(00)00291-2

Sutton AJ, Elias T, Kauahikaua J (2003) Lava-effusion rates for the Pu'u 'Ö'ö-Küpaianaha eruption derived from SO_2 emissions and very low frequency (VLF) measurements. In: The Pu'u 'Ö'ö-Küpaianaha Eruption of Kilauea Volcano, Hawai'i: The First 20 Years, U.S. Geological Survey Professional Paper 1676

Tokarev PI (1978) Prediction and characteristics of the 1975 eruption of Tolbachik volcano, Kamchatka. Bulletin of Volcanology 41-3:251–258, DOI 10.1007/BF02597226

Torres R, Snoeij P, Geudtner D, Bibby D, Davidson M, Attema E, Potin P, Rommen B, Floury N, Brown M, Nava Traver I, Deghaye P, Duesmann B, Rosich B, Miranda N, Bruno C, L'Abbate M, Croci R, Pietropaolo A, Huchler M, Rostan F (2012) GMES Sentinel-1 mission. Remote Sensing of Environment 120:9–24, DOI 10.1016/j.rse.2011.05.028

Tursa J (2009) IEEE 754r half precision floating point converter. Available at: http://www.mathworks.com/matlabcentral/fileexchange/23173-ieee-754r-half-precision-floating-point-converter

USGS (2014) Global Volcanism Program: Tolbachik summary and monthly reports. Available at: http://www.volcano.si.edu/volcano.cfm?vn=300240. Smithsonian Institution. Accessed 24. June 2014

Vallance JW, Schneider DJ, Schilling SP (2008) Growth of the 2004-2006 lava-dome complex at Mount St. Helens, Washington. In: A volcano rekindled: The renewed eruption of Mount St. Helens, 2004-2006, U.S. Geological Survey Professional Paper, vol 1750, Sherrod, D. R. and Scott, W. E. and Stauffer, P. H., pp 169–208

Varley N, Arambula-Mendoza R, Reyes-Davila G, Sanderson R, Stevenson J (2010) Generation of vulcanian activity and long-period seismicity at Volcán de Colima, Mexico. Journal of Volcanology and Geothermal Research 198:45–56, DOI 10.1016/j.jvolgeores.2010.08.009

Voight B, Constantine EK, Siswowidjoyo S, Torley R (2000) Historical eruptions of Merapi Volcano, Central Java, Indonesia, 1768-1998. Journal of Volcanology and Geothermal Research 100:69–138, DOI 10.1016/S0377-0273(00)00134-7

Wadge G (2003) Measuring the rate of lava effusion by InSAR. In: Proc. of Fringe 2003 Workshop, Frascati, Italy, 1.-5. Dec. 2003

Wadge G, Macfarlane DG, Odbert HM, James MR, Hole JK, Ryan G, Bass V, De Angelis S, Pinkerton H, Robertson DA, Loughlin SC (2008) Lava dome growth and mass wasting measured by a time series of ground-based radar and seismicity observations. Journal of Geophysical Research 113:B08,210, DOI 10.1029/2007JB005466

Wadge G, Herd R, Ryan G, Calder ES, Komorowski JC (2010) Lava production at Soufrière Hills Volcano, Montserrat: 1995-2009. Geophysical Research Letters 37:L00E03, DOI 10.1029/2009GL041466

Wadge G, Cole P, Stinton A, Komorowski JC, Stewart R, Toombs AC, Legendre Y (2011) Rapid topographic change measured by high-resolution satellite radar at Soufrière Hills Volcano, Montserrat, 2008-2010. Journal of Volcanology and Geothermal Research 199:142–152, DOI 10.1016/j.jvolgeores.2010.10.011

Walter TR, Subandriyo J, Kirbani S, Bathke H, Suryanto W, Aisyah N, Darmawan H, Jousset P, Lühr BG (2015) Volcano-tectonic control of Merapi's lava dome splitting: The November 2013 fracture observed from high resolution TessaSAR-X data. Tectonophysics 639:23–33, DOI 10.1016/j.tecto.2014.11.007

Wermuth M, Hauschild A, Montenbruck O, Jäggi A (2009) TerraSAR-X rapid and precise orbit determination. In: Proc. of 21st International Symposium on Space Flight Dynamics, 28. Sep. - 2. Oct. 2009, Toulouse, France

Werninghaus R (2004) TerraSAR-X Mission. In: Proc. SPIE 5236, SAR Image Analysis, Modeling, and Techniques VI, 9, 8. Sep. 2003, Barcelona, Spain, DOI 10.1117/12.511500

Wessel P, Smith WHF, Scharroo R, Luis JF, Wobbe F (2013) Generic Mapping Tools: Improved version released. EOS Transactions, American Geophysical Union 94:409–410

Xu W, Jónsson S (2014) The 2007-8 volcanic eruption on Jebel at Tair island (Red Sea) observed by satellite radar and optical images. Bulletin of Volcanology 76(795):1–14, DOI 10.1007/s00445-014-0795-9

Yoon Y, Eineder M, Yague-Martinez N, Montenbruck O (2009) TerraSAR-X precise trajectory estimation and quality assessment. IEEE Tranactions on Geoscience and Remote Sensing 47:1859–1868, DOI 10.1109/TGRS.2008.2006983

Zebker H, Villasenor J (1992) Decorrelation in interferometric radar echoes. IEEE Transactions on Geoscience and Remote Sensing 30:950–959, DOI 10.1109/36.175330

Zebker H, Rosen P, Hensley S (1997) Atmospheric effects in interferometric synthetic aperture radar surface deformation and topographic maps. Journal of Geophysical Research 102:7547–7563, DOI 10.1029/96JB03804

Zelenski M, Malik N, Taran Y (2014) Emissions of trace elements during the 2012-2013 effusive eruption of Tolbachik volcano, Kamchatka: enrichment factors, partition coefficients and aerosol contribution. Journal of Volcanology and Geothermal Research 285:136–149, DOI 10.1016/j.jvolgeores.2014.08.007

Zink M (2014) TanDEM-X: Key features and mission status. In: Proc. of 10th European Conference on Synthetic Aperture Radar (EUSAR), 3.-5. June 2014, Berlin, Germany

Zobin MV, Arámbula R, Bréton M, Reyes G, Plascencia I, Navarro C, Téllez A, Campos A, Gonzáles M, León Z, Martínez A, Ramírez C (2015) Dynamics of the January 2013 – June 2014 explosive-effusive episode in the eruption of Volcán de Colima, México: insights from seismic and video moning. Bulletin of Volcanology 77(31):1–13, DOI 10.1007/s00445-015-0917-z

List of Symbols

B	Baseline
B_{eff}	Effective baseline
$B_{\parallel}$	Parallel baseline
$B_{\parallel\text{err}}$	Baseline determination error in the line-of-sight of the satellite
$B_{\perp}$	Perpendicular baseline
$B_{\perp\text{err}}$	Baseline determination errors perpendicular to the line-of-sight of the satellite
$E\{.\}$	Expectation operator
f	Geometrical flattening of the ellipsoid
f_{DC}	Doppler centroid frequency
h	Height above the reference surface or ellipsoid
h_{amb}	Height of ambiguity
h_{err}	Terrain height error
H	Sensor altitude
i, j	Slant range coordinates
P_1/P_2	Points on the reference surface
r	Ground range
R	Slant range
R_e	Earth radius at the equator
$\boldsymbol{R_s}$	Sensor positioning vector
$\boldsymbol{R_t}$	Target positioning vector
S	Sensor
T	Target on the ground
v	Velocity
$\boldsymbol{V_s}$	Sensor velocity vector
x, y, z	Cartesian coordinates
X	Easting
y_1/y_2	Complex SAR images
$y_1 y_2^*$	Complex interferogram
Y	Northing

α	Gradient of slope directed towards the sensor
β	Gradient of slope directed away from the sensor
γ	Coherence; in Chapter 5 and 6 used as phase and topography corrected estimated coherence
$\hat{\gamma}$	Estimated coherence
$\hat{\gamma}_{\mathrm{pc}}$	Phase corrected estimated coherence
ΔR	Slant range difference
Δs	Distance in ground range based on a reference point
ϵ_{tilt}	Tilt of the terrain in ground range
θ	Look angle
θ_{inc}	Incidence angle
θ_{loc}	Local incidence angle
λ	Radar wavelength
Λ	Geographic longitude
μ	Mean
$\overline{\mu}$	Mean offset
σ	Standard deviation
σ_{μ}	Standard deviation of individual mean
ϕ	Interferometric phase
$\phi^{(n)}$	Systematic phase component
ϕ_{atm}	Phase contribution due to atmospheric effects
ϕ_{bs}	Phase contribution due to the backscattering properties on the ground
ϕ_{def}	Phase change due to the displacement of the ground scatterer in the satellite line-of-sight
ϕ_{noise}	Phase contribution due to noise
ϕ_{orb}	Phase contribution due to orbit errors
ϕ_{ref}	Reference phase
ϕ_{topo}	Topographic phase (based on SRTM)
ϕ^{*}_{topo}	Topographic phase (based on TanDEM-X)
ϕ_{unw}	Unwrapped phase
Φ	Geographic latitude
φ	Residual wrapped phase after subtracting the reference phase ϕ_{ref} and the reference topography ϕ_{topo} / ϕ^{*}_{topo}
φ_{unw}	Filtered and unwrapped residual phase
ψ	Phase value (rad)
ψ_{scat}	Contribution of scattering to the phase value (rad)

List of Acronyms

ADORE-DORIS	Automated Delft Object-oriented Radar Interferometric Software Environment
ALI	Advanced Land Imager
ALOS	Advanced Land Observing Satellite
COSMO-SkyMed	Constellation of small Satellites for Mediterranean basin Observation
CoSSC	Coregistered Single look Slant range Complex
CVC	Colima Volcanic Complex
DEM	Digital Elevation Model
DLR	German Aerospace Center (Deutsches Zentrum für Luft- und Raumfahrt)
DORIS	Delft Object-oriented Radar Interferometric Software
DRE	Dense-Rock Equivalent
DTED	Digital Terrain Elevation Data
EDM	Electronic Distance Measurement
EO-1	Earth Observing-1
ERS	European Remote Sensing Satellites
ESA	European Space Agency
GMT	Generic Mapping Tools
GPS	Global Positioning System
HRTI	High-Resolution Terrain Information
IAVCEI	International Association of Volcanology and Chemistry of the Earth's Interior
InSAR	Synthetic Aperture Radar Interferometry
ITRF	International Terrestrial Reference Frame
IVS FEB RAS	Institute of Volcanology and Seismology of the Far Eastern Branch of the Russian Academy of Sciences
KVERT	Kamchatka Volcanic Eruption Response Team
LiDAR	Light Detection And Ranging
LOS	Line-Of-Sight
NASA	National Aeronautics and Space Administration
PRF	Pulse Repetition Frequency

SAR	Synthetic Aperture Radar
SNAPHU	Statistical-Cost, Network-Flow Algorithm for Phase Unwrapping
SNR	Signal-to-noise ratio
SRTM	Shuttle Radar Topography Mission
TanDEM-X	TerraSAR-X Add-on for Digital Elevation Measurements
TDX	TanDEM-X satellite
TSX	TerraSAR-X satellite
UTM	Universal Transverse Mercator
VEI	Volcanic Explosivity Index
WGS 84	World Geodetic System 1984

Acknowledgments

I would like to start by acknowledging the German Aerospace Center for providing the TanDEM-X data and for funding the study under contract no. 50 EE0957 with funds from the German Federal Ministry for Economic Affairs and Energy (BMWi) due to a Decision of the German Bundestag. Without this, the present research could not have been conducted.

I would further like to express my deepest gratitude to my supervisor Prof. Bernhard Heck, who gave me the opportunity to do my PhD in his department. I owe him many thanks for his trust, as well as his mental and financial support. A big thank goes also to both of my Co-reviewers, Priv. Doz. Thomas Walter and Prof. Alberto Moreira, for great ideas and very helpful discussions. Thank you, Thomas, for taking me to the field and for letting me be a part of your working group. At this point I would also like to thank Andreas Schenk not only for his critical comments when proofreading my manuscript, but also for introducing me to the topic at the very start. Malte, I thank you for the idea of my TanDEM-X research project. Without both of you, Malte and Andreas, I would never have been able to understand the psychedelic rainbow-colored InSAR data. I will never forget us three sitting in my office and staring at the first TanDEM-X interferograms I processed – simply wonderful! I will for real create a memory game out of it at some point...

Thank you, Maren Daniell, Clémence Dubois, and Christine Weiß for the last-minute corrections of the manuscript. At this point I would also like to thank Dr. Mike James from Lancaster University for providing the aerophotogrammetric data of Volcán de Colima as well as Janine Krippner from University of Pittsburgh for sharing the photographs of Tolbachik.

A big thanks goes further to my Post-colleagues, for wonderful funny coffee breaks but also for the constructive criticism. Michael, I thank you for keeping track of what was going on in our working group, and for very good face-to-face conversations. I very much appreciated that I could talk to you whenever necessary.

I would also like to thank KIT for giving me a good framework around my PhD. Participating in the X-Ment Program was a very nice add-on to my usual working day – and I still enjoy and profit a lot from the network it enabled me to built.

Within this network, I would like to acknowledge the fruitful conversations with my mentor Frank Martin Seifert from ESA-ESRIN. It always felt so good to have somebody to talk to from the outside but who was still in the loop. Big thanks also go to the Graduate School for Climate and Environment (GRACE) from KIT for funding my research stay in Miami, but also for letting me build a great network of other PhD students.

I am also deeply grateful to my friends, who make work as well as living so very enjoyable in Karlsruhe.

Mein ganz besonderer Dank gilt schließlich meiner Familie. Danke, dass ihr immer an mich geglaubt habt und immer für mich da wart. Ihr seid einfach die Besten!

There is more to be seen than can ever be seen
more to do than can ever be done.

(Elton John, Circle of Life)